OPTIMIZATION OF A MAGNETICALLY SATURABLE INTERIOR PERMANENT-MAGNET SYNCHRONOUS MACHINE DRIVE

By

EDWARD CARL FRANCIS LOVELACE

Submitted to the Department of Electrical Engineering and Computer Science in partial
fulfillment of the requirements for the degree of

DOCTOR OF PHILOSOPHY IN ELECTRICAL ENGINEERING AND COMPUTER SCIENCE

at the

MASSACHUSETTS INSTITUTE OF TECHNOLOGY

June 2000

Signature of Author..
Department of Electrical Engineering and Computer Science
May 19, 2000

Certified by..
Jeffrey H. Lang
Professor, Department of Electrical Engineering and Computer Science
Thesis Supervisor

Certified by..
Thomas M. Jahns
Professor, Department of Electrical and Computer Engineering
University of Wisconsin-Madison
Thesis Supervisor

Accepted by..
Arthur C. Smith,
Department of Electrical Engineering and Computer Science
Chairman, Departmental Committee on Graduate Students

OPTIMIZATION OF A MAGNETICALLY SATURABLE INTERIOR PERMANENT-MAGNET SYNCHRONOUS MACHINE DRIVE

By

EDWARD CARL FRANCIS LOVELACE

Submitted to the Department of Electrical Engineering and Computer Science on May 19th, 2000 in partial fulfillment of the requirements for the degrees of Doctor of Philosophy in Electrical Engineering and Computer Science

ABSTRACT

Interior permanent magnet (IPM) synchronous machines are attractive because they can achieve constant-power operation over a wide speed range with limited magnet strength requirements and reduced power electronics cost. These characteristics provide the IPM machine with advantages over alternative machine types in applications such as spindle and traction drives. An important challenge for high-performance IPM machine design is to model the magnetic saturation of the core in a manner that is accurate, flexible, and computationally fast for design optimization.

A magnetically-saturable lumped parameter model (LPM) is developed for the optimized design of high-performance IPM synchronous machine drives. Using equivalent magnetic circuit analyses, the *dq*-frame inductances and magnet flux linkage are calculated for transversely-laminated IPM machines. The lumped parameters are employed to predict machine drive system performance for both rated-torque and constant-power operation. The results of saturable model calculations and finite element analysis (FEA) match very closely for the machine inductances, magnet flux linkage, and converted torque. Further validation is presented by comparing measurements of existing experimental machines to predictions from the saturable lumped parameter model. Agreement of measurements and predictions for the highly nonlinear saturable *q*-axis inductance is within 5% in the saturated excitation range.

The utility of the saturable LPM is then demonstrated by developing a cost-optimized design for an automotive integrated starter/generator (ISG) that is rated at 4 to 6 kW during generating operation. This ISG machine is mounted in a direct-drive mechanical configuration on the engine crankshaft. Agreement between the saturable LPM and FEA calculations for *q*- and *d*- axis inductances and PM flux linkage are all within 5% for the entire excitation range. Results of this model have been combined with structural FEA and demagnetization studies to produce a machine design that is predicted to meet all key ISG performance requirements. For this application and the chosen cost model, it is shown that optimizing the combined machine and drive system versus optimizing only the machine reduces the overall cost prediction by 12%.

Supervisors: Jeffrey H. Lang, Professor of Electrical Engineering
Massachusetts Institute of Technology
Thomas M. Jahns, Professor of Power Electronics and Electric Machines
University of Wisconsin-Madison

ACKNOWLEDGMENTS

I would first like to thank my thesis committee including Professor James L. Kirtley Jr. and Dr. Thomas Keim, and in particular, my co-advisors Professor Jeffrey. H. Lang and Professor Thomas Jahns (University of Wisconsin-Madison) for their guidance, patience, and support during these years. My family, Susan my wife, and my two sons, Connor and Patrick, have been critical to my survival and well-being while being a doctoral student.

For their financial support and affording me the opportunity to work in this exciting and challenging field, I thank the Department of Transportation, Federal Highway Administration's Universities and Grants Program for awarding me the Eisenhower Fellowship. Likewise, I thank the MIT/Industry Consortium on Advanced Automotive Electronics/Electrical Components and Systems, and Professor John Kassakian in particular, for their continued support and the active forum they have provided to gain exposure and experience developing and communicating advanced technical solutions.

I would also like to thank Dr. Wen L. Soong, University of Adelaide, for providing the experimental machine data that was vital to completing this dissertation. I also appreciate the participation from and communications with Professor Alfredo Vagati, Professor Morimoto, Dr. Yukio Honda, and Dr. Ronald Krefta.

Dr. John Miller, Ford Research Laboratory, and Jerry Brown, Kollmorgen Corporation, for the enthusiasm about prototyping interior PM machines. Kollmorgen Corporation also donated substantial drive stand equipment that will be used to test the system that is developed as a result of this research.

And finally, I have truly enjoyed my time at the Massachusetts Institute of Technology's Laboratory for Electromagnetic and Electronic Systems. The staff including Vivian, Karin, and recently Kiyomi as well as the other students have made it a pleasure to work and learn there.

Contents

List of Figures

List of Tables

List of Symbols

α_k	electrical angular distance from *d*-axis to kth segment
A_a	conductor cross-sectional area
A_{bk}	cross-sectional area of kth bridge
A_{gk}	cross-sectional area of kth airgap section
A_{mk}	cross-sectional area of kth magnet
A_{reqk}	kth equivalent 'reluctance' cross-sectional area
A_s	airgap surface area of one tooth pitch
A_{seqk}	kth equivalent 'saturated core' cross-sectional area
B_{ag}	RMS fundamental total airgap flux density
B_B	core loss base flux density
B_{db}	average back iron flux density
B_h	slot harmonic flux density
B_{gk}	average flux density of kth airgap section
B_r	PM reluctance
B_s	core saturation constant
B_t	average tooth flux density
B_1	RMS fundamental PM airgap flux density
d_s	slot depth
d_b	stator back iron depth
d_o	slot opening depth
d_t	tooth tip depth
d_{rk}	kth rotor section depth
d_{mk}	kth magnet section depth
d_{bk}	kth bridge depth
d_{ck}	kth center post depth
δ	torque angle
δ_c	rotor skin depth
ε_b	core loss flux density exponent
ε_f	core loss frequency exponent
$\Delta\alpha_k$	electrical angle between k-1th and kth segments
E_z	rotor surface electric field
E_a	PM back emf
f	mechanical frequency [Hz]
f_e	electrical frequency [Hz]
f_{dsk}	per-unit *d*-axis kth stator mmf
f_{drk}	per-unit *d*-axis kth rotor mmf
$\mathcal{F}_i$	mmf across ith element
$\mathcal{F}_{dsk}$	mmf source for kth stator element
ϕ	power factor angle
ϕ_i	per-unit flux of ith source
Φ_{bk}	flux source of kth bridge
Φ_d	flux along *d*-axis
Φ_{mk}	flux source of kth magnet
Φ_q	flux along *q*-axis
g	airgap width
g'	airgap width corrected for stator slot openings (Carter coefficient)
γ	current vector control angle
h_k	height of kth element
i	general purpose index
i_a	per-unit phase current
I_a	phase RMS terminal current
I_b	base current
i_d	per-unit *d*-axis current
I_d	*d*-axis current (RMS-defined)
I_{d0}	corner speed d-axis current
I_0	rated current
i_q	per-unit *q*-axis current
I_q	*q*-axis current (RMS-defined)

I_{q0}	corner sped q-axis current
j	imaginary plane operator ($\sqrt{-1}$)
k	general purpose index
k_{an}	nth harmonic winding factor
k_{abz}	backward zigzag winding factor
k_{afz}	forward zigzag winding factor
k_{bn}	nth harmonic breadth factor
k_{bbz}	backward zigzag breadth factor
k_{bfz}	forward zigzag breadth factor
k_{cs}	stator Carter coefficient
k_{pn}	nth harmonic pitch factor
k_{pbz}	backward zigzag pitch factor
k_{pfz}	forward zigzag pitch factor
k_{sn}	nth harmonic skew factor
k_{sbz}	backward zigzag skew factor
k_{sfz}	forward zigzag skew factor
k_{ssp}	slot short pitch factor
K_z	rotor surface current density
K	number of magnet cavity layers
l	active length
l_a	phase winding length
l_{bk}	length of kth bridge
l_{e1}	axial end turn length
l_{e2}	azimuthal end turn length
l_{mk}	length of kth magnet
l_{out}	overall machine length
L_a	phase inductance
L_{ag}	airgap magnetizing inductance
L_{bzig}	backward zig-zag harmonic inductance
L_{end}	armature end turn leakage inductance
L_d	d-axis synchronous inductance
L_{dc}	d-axis circulating inductance
L_{dm}	d-axis magnetizing inductance
L_{dt}	d-axis through inductance
L_{fzig}	forward zig-zag space harmonic inductance

L_l	leakage inductance
L_q	q-axis synchronous inductance
L_{qm}	q-axis magnetizing inductance, non-saturable
L_{qms}	q-axis magnetizing inductance, saturable
L_s	round rotor synchronous inductance
L_{slot}	stator slot leakage inductance
L_{5belt},	5th space harmonic (belt leakage) inductance
L_{7belt}	7th space harmonic (belt leakage) inductance
L_{qms}	saturable q-axis magnetizing inductance
λ_{PM}	permanent-magnet flux linkage
λ_d	d-axis flux linkage
λ_q	q-axis flux linkage
λ_{PM}	PM flux linkage
λ_{ssp}	short slot pitch ratio
m_a	slot distribution
m_{db}	mass of back iron
m_t	mass of the teeth
μ	permeability
μ_0	permeability of free space
μ_r	relative permeability
m_k	mass of kth core section
n	harmonic order
n_{bz}	backward zigzag harmonic
n_{fz}	forward zigzag harmonic
n_s	number of slots per machine
n_{sp}	number of slots per pole
n_{ssp}	number of slots short pitched
N_a	series turns per phase
Ω	mechanical speed [rpm]
p	pole-pairs
p_B	specific power (core) loss
P_a	armature power loss
P_c	core loss

P_{ci}	core loss of ith core section
P_l	leakage power
P_{sh}	slot harmonic core loss
P_{shaft}	shaft power
P_{te}	converted power
$\mathcal{P}_s$	slot leakage permeance
Ψ_d	d-axis flux linkage
Ψ_q	q-axis flux linkage
θ_{mik}	ith magnet inner span
θ_{mok}	ith magnet outer span
θ_o	slot opening pitch
θ	rotor angular position
θ_p	pole pitch
θ_{ssp}	short slot pitch angle
θ_{sk}	skew angle
θ_t	tooth pitch
Φ	flux through ith element
q	number of phases
r	stator inner radius
r_{bk}	per-unit reluctance of bridge
r_{gk}	per-unit airgap reluctance kth element
r_{mk}	per-unit magnet cavity reluctance kth element
r_{ri}	rotor inner radius
r_{ro}	rotor outer radius
r_{si}	stator inner radius
r_{so}	stator outer radius
R	rotor outer radius
R_a	phase resistance
R_s	rotor surface resistance
$\mathcal{R}_{gk}$	kth airgap section reluctance element
$\mathcal{R}_{mk}$	kth magnet cavity reluctance element
S_r	saliency ratio
σ_a	armature conductivity
σ_c	rotor surface conductivity

t_e	per-unit torque of electrical origin
T_e	torque of electrical origin
T_{shaft}	shaft torque
V_a	phase RMS terminal voltage
V_{ag}	airgap voltage
V_b	base voltage
V_d	*d*-axis voltage (RMS-defined)
V_0	rated voltage
V_q	*q*-axis voltage (RMS-defined)
w_{bk}	ith bridge width
w_{ck}	ith center post width
w_f	tooth face width
w_i	width of ith element
w_o	slot opening width
w_{sa}	slot average width
w_{sb}	slot bottom width
w_{st}	slot top width
w_t	tooth width
ω	mechanical frequency [rad/sec]
ω_B	core loss base frequency [rad/sec]
ω_e	electrical frequency [rad/sec]
ω_h	slot harmonic frequency [rad/sec]
X_a	phase reactance
x_d	per-unit *d*-axis reactance
X_d	*d*-axis reactance
x_q	per-unit *q*-axis reactance
X_q	q-axis reactance
Z_s	rotor surface impedance

Chapter 1

INTRODUCTION

1.1 Introduction

This thesis studies the optimized design of interior permanent-magnet (IPM) machine drives which appear advantageous to many applications for their ability to operate at constant power over a wide speed range. IPM machine characteristics are contrasted with closely related AC synchronous machine. The attributes and optimized design challenges that are particular to IPM machines are presented in terms of the previous work published on the subject. That discussion motivates the development of a saturable lumped parameter model (LPM) that is capable of accurately analyzing or being incorporated in the design process of IPM machine drives. The LPM is validated using electromagnetic finite element analysis (FEA) applied to proposed designs and existing experimental machine drive data. The second half of the thesis deals with the application of the LPM tools to the cost-optimized design an integrated starter/generator (ISG). A combined Monte Carlo and gradient optimization method is proposed that is useful for complex system optimization problems characterized by wide design variable spaces and multiple constraints. The design specifications are presented, then a discussion of ancillary issues (structural integrity and demagnetization) follows, and the thesis concludes with a presentation of the optimized ISG design.

In this chapter the need for cost-optimized machine drives that are well suited for constant power operation over wide speed ranges is demonstrated by the example of future automotive starting and generation systems. Then, based on the assumption of rising electrical generation requirements, an integrated starter/generator (ISG) is described as an attractive alternative to conventional automotive starting and generation systems. The general characteristics of IPM synchronous machines are then outlined with respect to their suitability for such an application. With this motivation, the rationale for and the technical challenges associated with analytical design of IPM machines are then described. The concept of a lumped parameter model (LPM) machine that accounts for magnetic saturation is introduced, and the methodology for optimized IPM machine design with particular attention to the cost-optimized integrated starter/generator (ISG) application is proposed. The chapter ends by outlining the following remainder of the thesis.

1.2 Motivation

The motivation that resulted in the decision to study the optimized design of IPM machines is the problem of rising electrical generation requirements in automotive applications. The increased electrical loading is resulting in the consideration of alternative starting and generation systems by the automotive industry that may be preferable from either a cost or functionality standpoint. This section describes this motivation and the following sections outlines why an IPM machine drive is an attractive alternative to consider for applications which have the common requirement of constant power operation over a wide speed range and the associated challenges of optimized design.

1.2.1 Conventional Automotive Starters and Alternators

In present day vehicles the typical starter is a DC motor that drives a pinion gear connected to a toothed flywheel ring on the main crankshaft. The flywheel is mounted where the crankshaft exits the internal combustion engine (ICE) casing and functions to smooth out the torque pulsations caused by the individual cylinder firings. The starter must provide high-torque at the crankshaft (100 to 300 Nm) for a short duration from standstill up to the cranking speed at which point the ICE is capable of sustaining operation and accelerating up to the vehicle idle speed. The physical location of the starter subjects the machine to a severe operating environment in terms of debris, vibration, and particularly temperature (in excess of 100° C). The 10:1 gear ratio between the starter pinion and the crankshaft allows a lower torque, higher-speed electrical machine to be selected and still provide the high starting torque when reflected through this mechanical transformer. The starter is driven from the energy stored in the vehicle battery using a mechanical commutator to convert the DC power provided by the battery. According to industry sources, a conventional DC starter costs roughly $25 to manufacture [1]. For our purposes, this unit production cost is defined as the cost of materials, manufacturing, and overhead to produce an additional unit at high volume.

The present day automotive alternator provides the electrical generation necessary to power all the vehicle electrical loads when running. In addition, it must maintain the charge balance in the battery over a specified minimum drive cycle of the vehicle [2]. Typically the alternator is a wound-field synchronous generator that is driven by the engine through a 3:1 pulley-belt transmission at the opposite end of the ICE from the crankshaft. The rotor uses a claw-pole configuration constructed from solid steel to reduce manufacturing costs. This design is widely referred to as a Lundell alternator [2]. The alternator must generate from idle through to the maximum engine speed. This is roughly 600 to 6000 rpm at the crankshaft but is 1800 to 18000 rpm at the alternator shaft when reflected through the belted transmission. Though the alternator power output capability drops below its rated value at low engine speeds, the electrical machine still provides a relatively wide speed range (approximately 4:1) with constant power output. The alternator power is generated by three phase windings and converted to the battery's DC bus voltage by a rectifier circuit with a field winding controller. A typical alternator unit production cost is in the vicinity of $75 for an alternator rated at 1.2kW including the rectifier [1].

The above description demonstrates that automotive applications present a unique combination of performance, environmental, interfacing, and cost requirements for electrical drive and generation systems. This must all be achieved with a minimum of manufacturing cost thus severely limiting the choices for selecting electric machine technologies to those that require only the most basic power electronics and use inexpensive magnetic and electrical materials.

1.2.2 A Future Alternative: An Integrated Starter/Generator (ISG)

This section shows why one competitive alternative to the present starting and generation system for meeting the increasing generation requirements is an integrated starter/generator (ISG). The specific application that will be referenced throughout this thesis is an integrated starter/generator (ISG) system that meets the expected performance requirements of a typical 'high-end' vehicle that would be in production between 2005 and 2010. The present day base vehicle that is used for all comparisons in this research is a typical 'high-end' mid-size North American market sedan (e.g. Mercury Sable) [3]. The chief reason for considering ISG machines is to simplify the vehicle starting and generation system. The resulting simplification offers a number of potential advantages compared to a separate high-power alternator and conventional starter, including:

- lower total size and weight;
- simplified engine compartment layout;
- fewer parts to maintain or possibly fail;
- potential for lower unit production cost.

The MIT/Industry Consortium on Advanced Automotive Electrical/Electronic Components and Systems which is represented by knowledgeable professionals from the automotive industry provided recommendations on appropriate application requirements [3]. The three broad application requirements that were adopted are as follows:

1. Starting torque will be similar to today's vehicles but generation requirements will increase significantly. A 42 VDC battery system will be implemented in order to manage the vehicle's electrical network and loads more effectively.
2. The generating system must be significantly more efficient than conventional alternators that typically achieve only 50 to 60% shaft-to-output efficiency.
3. The system must be cost-optimized to achieve the lowest initial manufacturing cost within the constraints of all the other detailed performance requirements.

Figure 1.1 and Figure 1.2 show the performance requirements recommended by the Consortium [3]. The 6 kW rated power level at 6000 rpm shown in Figure 1.2 is approximately five times the rated power required from a conventional alternator. This does not assume a specific set of new or increased electrical loads on the vehicle but does presume that the average vehicle electrical load will increase significantly during the coming years [4]. The linear power increase from 4 kW at idle speed to 6 kW at maximum engine speed corresponds to the expected requirements of electrically-actuated engine valves that are likely to be available in future 'high-end' vehicles.

Figure 1.1 also shows data markers representing the equivalent crankshaft torque at idle speed of both the new high-power starter/generator and a conventional alternator. This is important because the required shaft torque largely determines the physical size and weight of an electric machine. As a result, two conclusions can be drawn from the Figure 1.1 starting performance requirements.

1. The equivalent shaft torque requirements of the high-power alternator come closer to matching the starting torque requirements than the equivalent shaft torque requirements of a conventional alternator. Therefore consideration of an ISG machine becomes progressively more attractive.
2. The machine sizing for the 6 kW starter/generator system will still be dominated by the starting rather than the generating requirements since there is still roughly a 2:1 torque mismatch.

The two above conclusions are somewhat at odds. Though the high generating requirements have closed the gap between starter and alternator machine sizing, there is still some mismatch. Vehicle starting, though, is time-limited and so transient current limits can be employed since the machine will not reach thermal steady state in the 5 to 15 seconds required at rated starting torque. The higher starting current limit will reduce the machine-sizing mismatch further making an ISG even more appealing to consider for such future vehicles. ISGs are already being seriously being considered by the automotive industry because of the rising generation requirements but also because of additional system capabilities that it affords such as quick start/stop at traffic lights, active torque damping, and eliminated unnecessary accessories [5].

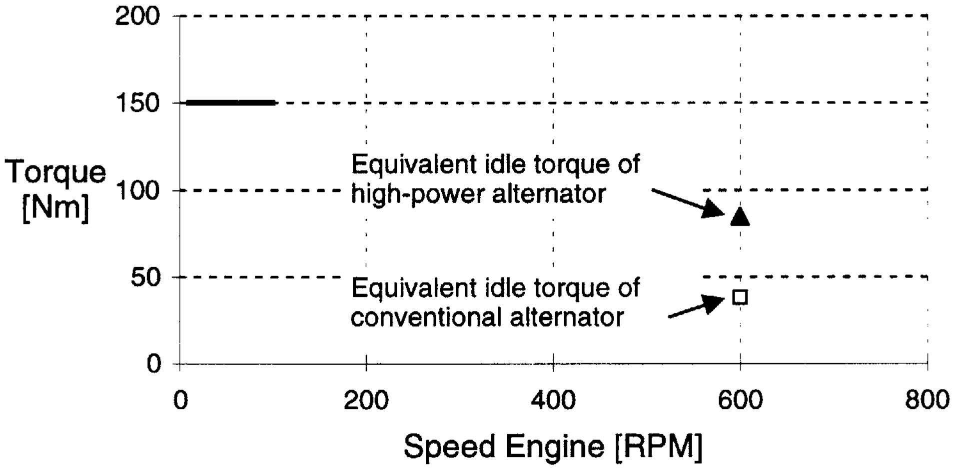

Figure 1.1: Starting requirements for the high-power starter/generator.

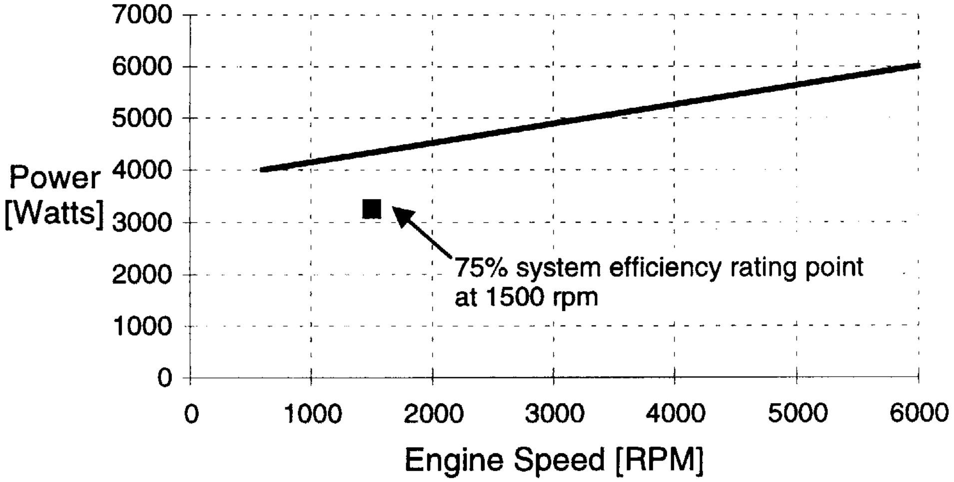

Figure 1.2: Generating requirements for the high-power starter/generator.

1.2.3 ISG Challenges

One of the most important challenges in developing a practical starter/generator system is unit production cost. Life cycle and repair costs are secondary considerations to the initial production cost in the highly cost-competitive automotive world. A major contributor to the unit production cost of an ISG is the power electronics required for interfacing a combined machine to the 42VDC bus. At these power levels the cost of power semiconductor switches is significant, and all of the combined machine options require controlled switches.

A conventional alternator requires only one electrical switch for the field winding since rectification can be accomplished using only relatively inexpensive power diodes. Similarly, a conventional DC starter motor does not require semiconductor switches because the switching of currents is accomplished mechanically by the commutator. However, an ISG machine requires a number of relatively expensive power switches unless a DC machine is used. There is also measurable cost associated with all of the ancillary components necessary to complete a controlled switch converter for the machine. A popular rule of thumb for switching power converters is an estimated production cost of US$0.10 per Watt, so that a 6 kW power converter can be expected to have a base cost of approximately $600 without even including the rotating machine.

Another notable feature of the generating requirements is the wide constant-power speed range as discussed in the previous section. This is an extremely demanding requirement for the machine-converter system from a system design standpoint. It requires either oversizing the machine and the converter to be capable of simultaneously delivering the maximum torque (converter current limit) at the maximum speed (converter voltage limit), or selection of a system that can take advantage of flux-weakened operation at the higher speeds [6]. Some machine topologies are inherently capable of flux weakening operation and, as such, can deliver roughly constant power up to a top speed typically 2 to 5 times higher than the design corner speed (the lowest voltage and current limited speed). Achieving constant power speed ranges (CPSR) as high as the 10:1 range required by this application is extremely difficult using any conventional types of machines unless the machine and power converter are purposely oversized. An IPM machine is theoretically capable of design for an infinite CPSR [7, 8]. Taking into account realistic considerations including magnetic saturation, losses, and other system limitations, the IPM machine offers a very competitive chance of achieving or approaching this 10:1 CPSR goal [9].

1.3 A Crankshaft IPM Machine Drive as an ISG Solution

1.3.1 Tradeoff Comparison

After examining the electrical power system requirements of future internal combustion engine (ICE) vehicles, it was determined that the interior PM machine drive represents an attractive candidate for meeting the starting and generating requirements of these vehicles. This is primarily due to the IPM machine's suitability for wide CPSR operation when compared to other classes of rotating machines. The system requirements and desired features described above resulted in numerous machine design and system configuration decisions, some of which were accomplished automatically by the design optimization process and some of which were made in consultation with the Consortium [3]. This section describes in more detail how these selections were made.

A tradeoff study was conducted to evaluate alternative machine-converter combinations for the starter/alternator application in order to select the most promising candidate for further investigation. The tradeoff study evaluated key attributes of several cost-optimized machine-converter systems and mechanical configurations. The methodology of the tradeoff study was to develop cost-optimized designs of alternative machine drive systems in different mechanical configurations, and to estimate the chief mechanical and electrical performance characteristics of each design. Equivalent magnetic circuit modeling techniques were used to develop the machine designs and to predict the performance characteristics for each machine. The equivalent circuit models used in this preliminary study, particularly for the IPM machine, were significantly simpler than those developed in the following chapters of the thesis.

The machines that were chosen for the study are shown in Table 1.1, including a discussion of key electrical and mechanical characteristics. The machine-converter system designs were constrained by the requirements and features outlined in the preceding section. In particular, DC machines were not considered in the tradeoff study due to concerns over brush life during continuous operation as a starter/alternator in contrast to the DC starter, which is disengaged after the vehicle is started. Lundell machines were also not considered primarily because these machines do not scale well to higher power levels and larger sizes [10].

The mechanical configurations considered in this study are shown in Table 1.2. Three gearing configurations (direct-drive, offset-coupled, and two-speed offset-coupled) and two starting torque levels (150 Nm and 300 Nm) were investigated. The case of 300 Nm starting torque was considered as an option to obtain data on the sensitivity of the results in this key specification. Also there is considerable uncertainty in automotive starting

Table 1.1: List of the tradeoff study machines and their major characteristics.

Machine	**Electrical Characteristics**	**Mechanical Characteristics**
Induction Machine (IM)	Widely used asynchronous machine that operates at a small 'slip' speed difference from the synchronous speed. This machine has a limited constant power speed region followed by a constant torque-speed-squared region, i.e., $T_{em}\omega_e^2 = \text{const}$; requires a 3-phase full wave bridge converter	Mature squirrel-cage manufacturing technology capable of achieving low cost in high volumes
Interior PM (IPM) Machine	Hybrid PM and salient-pole synchronous machine that is capable of very high constant power speed ranges with purpose-built designs; requires a 3-phase full wave bridge converter	A more complicated rotor design with imbedded magnets that poses high-speed structural design challenges; Limited high-volume manufacturing experience.
Surface PM (SPM) Machine	Non-salient PM synchronous machine in which the back-emf voltage is directly proportional to speed. Requires extra power electronics in addition to a 3-phase full wave bridge converter to hold output voltage constant over 10:1 speed range.	Uses surface-mounted magnets that present high-speed structural design challenges, typically requiring a high-strength retaining sleeve wrapped around the rotor
Variable, or Switched, Reluctance Machine (VRM)	Doubly salient reluctance machine that typically produces significant torque pulsations when operated over a wide CPSR. Requires two switches per phase with the opportunity to reduce torque pulsations by adding phases and therefore more power switches.	Robust rotor construction using cruciform iron lamination stack. Limited high-volume manufacturing experience.

torque requirements both present and future. The offset-coupled case is similar to the mechanical configuration of a conventional alternator with the separate starter machine eliminated. The dual-speed system was investigated for the 300 Nm starting case as a 'torque leveling' option so that torque requirements for starting and generating would be equivalent. For 150 Nm starting, this case was not pursued because the torque mismatch is considerably smaller and therefore did not warrant the additional complexity of a clutched mechanism for changing gearing ratios. The actual gearing mechanism was also not specified and left as a manufacturer's option to decide how to best provide the speed transformation. The direct-drive configuration is depicted in Figure 1.3. The machine is located where the engine flywheel is normally located and the machine rotor performs the same function of inertial torque damping. Other eliminated parts are also noted.

Figure 1.4 plots the estimated motor-plus-converter system cost results from the tradeoff study for the direct drive mechanical configuration for each of the four machine candidates. The relative system costs for the other mechanical configurations were similar, with the two-speed offset-coupled case producing marginally lower costs than the direct drive case. Attention was eventually focused on the direct-drive mechanical configuration because of the net advantages it offers compared to the offset-coupled designs as explained in the following discussion.

Based on the results of this tradeoff study, the IPM synchronous machine was selected for further investigation. Both the IM and the IPM machines resulted in significantly lower system costs than the VRM and SPM machines. Although the VRM and SPM machines alone were less expensive, they required substantially more costly converters resulting in the higher overall system costs. Although the IM is a close competitor, the IPM machine was selected because it offers potential to achieve higher efficiency and lower weight and/or inertia for comparable cost to the IM. The other important characteristics that are desirable and available in the IPM machine are its brushless design, high power- and torque density, low magnet strength requirements, and excellent flux-weakening capability. The IPM machine-converter system was selected for these desirable characteristics while recognizing that the anisotropic, or salient, rotor with imbedded magnets presents manufacturing complications as discussed in the following section.

The relative cost results for the different systems can be explained primarily by examining the cost of the electrical converter. Using a converter cost estimate of US$0.10/Watt, generation applications over 5 kW may have converter-to-machine cost ratios in excess of 10:1 as demonstrated by Figure 1.4. Minimizing system cost then becomes primarily an issue of choosing machine types that use lower-cost converter topologies. Since the automotive electrical environment is relatively low voltage, three-phase full bridge converters employing MOSFET switches become the least expensive option. The VRM and SPM machines require more power switches as noted in Table 1.1 (and higher voltage IGBTs in the case of the SPM machine) and therefore the base cost of their converters increases significantly. Though IPM and induction machines both employ the basic six-switch bridge converter, the IPM machine topology offers greater potential for higher torque and power densities. Based on these results alone one would expect that if a dramatic reduction in converter costs were to occur, the SPM would become more attractive. This is not foregone conclusion, though, because each of the machines would reoptimize around a different point in the design variable space. It would be a point that weighed the cost of the machine more heavily than the cost of the converter and current requirements. All that really can be noted is that the relative costs of the different machine systems would become much closer.

Table 1.2: List of tradeoff study mechanical configurations.

Mechanical Configuration	Description	Starting Speed Ratio	Generating Speed Ratio
Direct-Drive, 150 Nm	Located where the crankshaft exits the engine casing replacing the flywheel (machine rotor performs the same function)	1:1	1:1
Offset-Coupled, 150 Nm	Located in the conventional alternator location	3:1	3:1
Offset-Coupled, 300 Nm	Located in the conventional alternator location	5:1	5:1
Two-Speed Offset-Coupled, 300Nm	Located in the conventional alternator location with a clutching mechanism to switch speed ratio between starting and generating	3:1	15:1

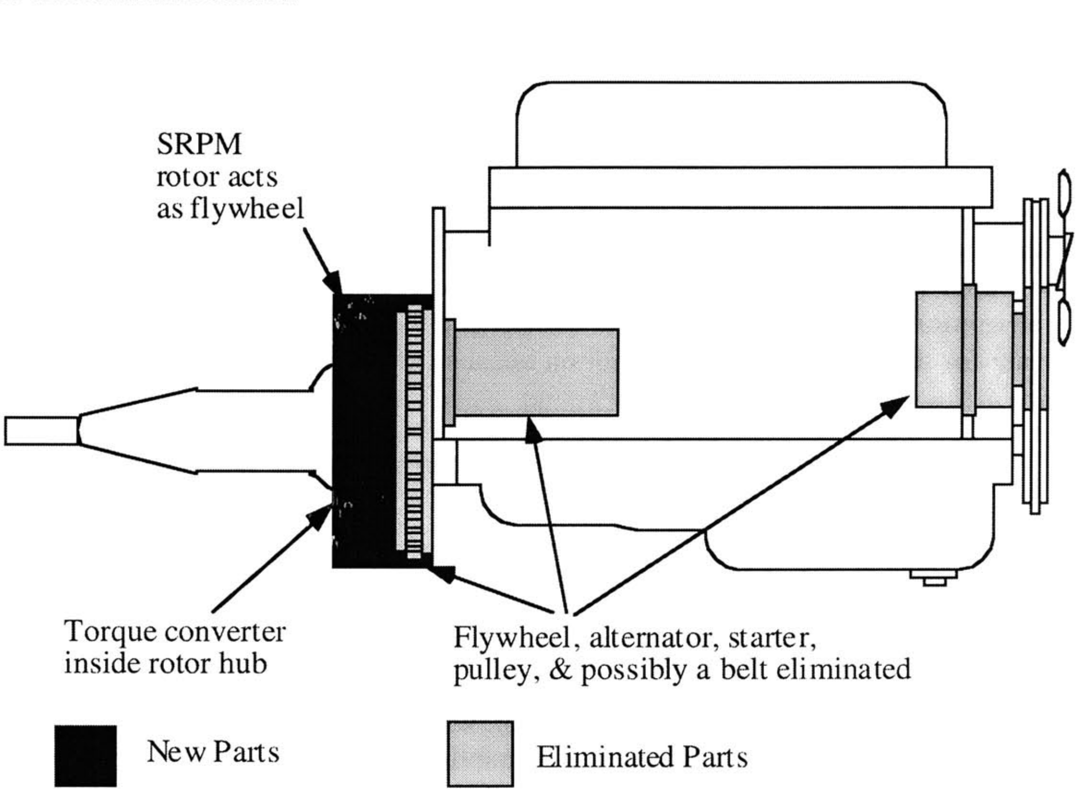

Figure 1.3: Drivetrain cross-section showing conventional starter, alternator, and a replacement direct-drive ISG.

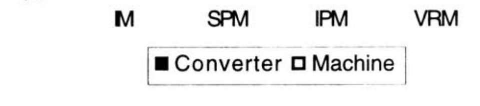

Figure 1.4: Tradeoff study system cost comparison results for the direct-drive configuration.

The other major tradeoff study conclusion was the choice of direct drive as the mechanical configuration. This system did not result in the least expensive machine converter alternative but did afford the greatest degree of simplification to the overall starting and generating system. It eliminates the alternator belt, pulley system, and the flywheel, and therefore offers the potential for the lowest starter/alternator system cost. In addition, it also makes it possible to use the starter/alternator machine to provide active damping of the torque variations caused by the cyclical piston action. On the negative side, the direct-drive configuration results in an increase in the overall length of the engine-starter-alternator group, and the temperature environment is more severe than in the conventional alternator location. Furthermore, high reliability is particularly important for the direct-drive configuration because of the relative inaccessibility of the machine.

1.3.2 Physical and Electromagnetic Characteristics of an IPM Machine

Figure 1.5 shows a cross-section of a 12-pole IPM machine. Figure 1.6 shows a close up of one rotor pole of this example IPM machine. In this configuration, each rotor pole contains two buried permanent magnet layers which are magnetized across their shorter dimensions to produce the air-gap PM flux. The definitions of the *dq*-frame axes of the machine, which are discussed in more detail in Chapter 2, are also shown. The PM cavities also create flux barriers within the rotor, which increases the effective air gap in a flux direction that crosses the cavities. This establishes the magnetic saliency of the IPM machine.

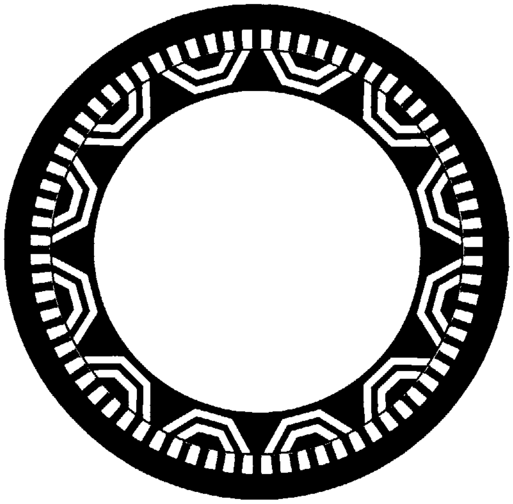

Figure 1.5: Cross-section of a 12-pole IPM machine.

The PM cavities are constructed by punching unitary annular laminations so that the rotor is assembled from a conventional stack of laminations. The unitary structure is maintained by a thin bridge of core material left by the punching at the rotor periphery. The bridges are designed to provide the required structural integrity while saturating magnetically to minimize their negative impact on the machine's electromagnetic performance.

The stator of the IPM machine is a typical AC design incorporating three-phase distributed windings in slots to produce the characteristic synchronously rotating, approximately sinusoidal, m.m.f. wave. Though a 12-pole, conventionally laminated, two-barrier machine is shown, IPM machines can be designed in many different configurations including axially-laminated machines with many more PM layers as discussed in the following chapter.

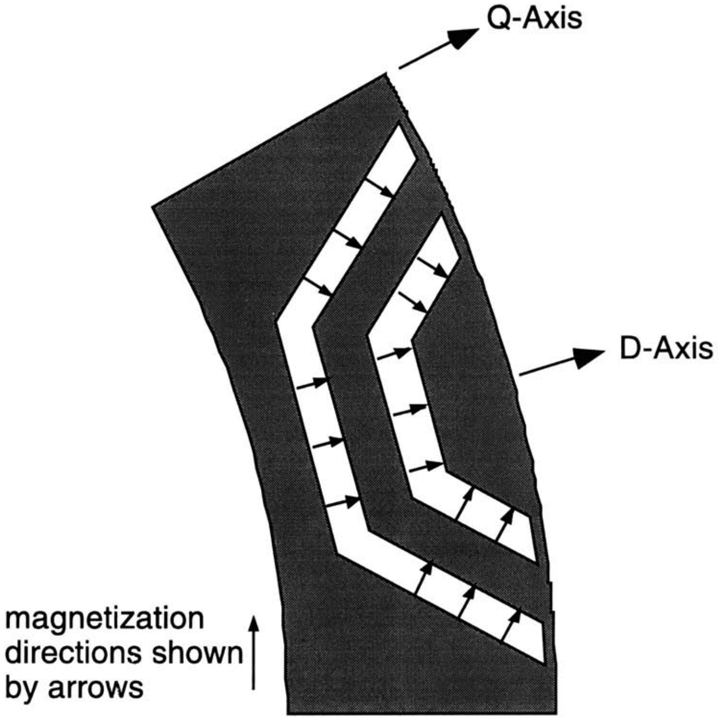

Figure 1.6: Cross-section of a single pole of an IPM machine.

Torque production is the result of a combination of reluctance and magnet field alignment components. The PM layers within the rotor produce the field necessary for the alignment torque component. The rotor cavities themselves create the electromagnetic saliency necessary for the reluctance torque. The combination of the two components creates a machine that can be designed for constant power operation over a wide speed range with a high base torque. This is ideally suited to the high-power starter/alternator application as shown in Figure 1.7. As a result, a relatively minimal amount of machine oversizing is likely to be necessary to meet the ISG torque requirements.

1.4 Thesis Objectives and Proposed Design Methodology

As the previous section outlined, the idealized torque-speed characteristics and converter requirements of an IPM machine make this machine attractive for constant power operation over wide speed ranges. To approach these characteristics, though, the design must be optimized. The optimization investigated in this thesis is briefly introduced here while further research background and development is the subject of the following chapters.

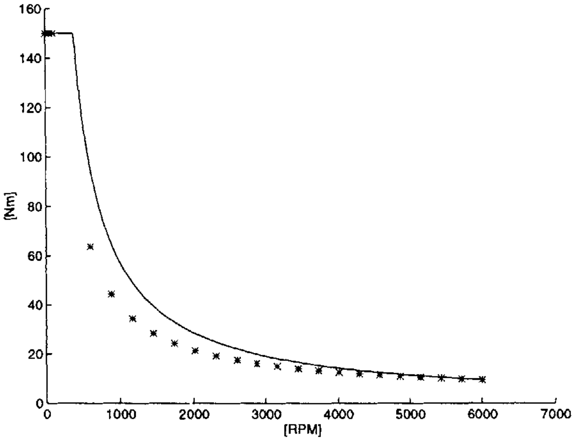

Figure 1.7: Torque-speed characteristic of an idealized IPM (solid line) overlaid on the torque requirements for the ISG application (stars, *).

The possible design methods can be broadly divided into analytical, numerical, and experimental methods. Experimental methods are appropriate for incremental changes in machine design, or where the machine class is highly developed and therefore optimal design characteristics are largely understood such as with induction machines. Numerical design tools such as finite element analysis (FEA), both the software and the computation hardware have progressed to the stage where design optimization can be accomplished in a reasonable time frame. This method, though, quickly becomes impractical as the number of design variables increases. Also the achievable design space for rotating machines is likely to have many local optima due primarily to the integer values of several of the design variables such as the number of turns, poles, and slots.

Since the IPM machine class has been sparsely explored when compared to other major machines (induction, surface PM, switched reluctance, wound synchronous) and because optimization can introduce many design variables, an analytic method has been selected here for investigating the IPM machine. Numerical and experimental methods can certainly accurately model magnetic saturation for a single high-performance design, but are not reasonable solutions (computation and manufacturing time or financial resources) when a wide design space search is desired. Analytic models can be directly related to machine geometry and specifications to more readily understand the effects of an individual variable change on a particular machine design's capability. Using analytic methods a single design can be computed almost instantly, and so by employing Monte Carlo synthesis a wide design space covering multiple variables can be searched in a reasonable time span. The designs that are most attractive (i.e. approach the optimization criteria closest and have reasonable manufacturable cross-sections) can then be further refined using local gradient optimization of the design variables. Figure 1.8 shows an overview of this optimal design methodology.

Given that an analytic design method is desirable from the standpoint of optimization over a wide design space, there is still the major problem of determining the analytic design model. A common characteristic of many analytic machine models is the use of equivalent magnetic circuits to represent the machine's electromagnetic behavior. The equivalent circuits are comprised of MMF sources, flux sources, and reluctance elements in various levels of complexity. One way to classify the different types of equivalent circuit models is by how the principal machine materials are treated. The MMF sources in an IPM machine include the copper windings and permanent magnets; the flux-carrying reluctance elements represent the airgap, the magnet cavities, and the iron core.

Flux crossing the windings between adjacent stator teeth is often treated as a second-order fringing effect. The permeability of magnets is typically very close to that of air and is often treated in simpler models as an equivalent airgap. For practical machine design it may be reasonable to treat the windings, magnets, and airgap using simple linear isotropic models, but how closely the core model represents the magnetic saturation of real machine steel can have a dramatic effect its resulting performance predictions.

In this thesis the interest is in optimized design, and much of the core at rated excitation for optimal designs will operate right at the knee of an actual machine steel's BH curve where saturation onsets. Qualitatively this should make sense because below the knee there is a significant gain between excitation and the induced flux while above the knee the incremental flux that can be induced in the machine is reduced by a factor of 5000 to 10000 times. Therefore for optimal design it would be preferable to model the real BH curve more precisely.

This is the basis for the magnetically saturable models that are developed in the following chapters for optimized design of IPM machines. The cross-section of an IPM machine introduces additional complexities due to wide geometrical variation of the rotor flux paths. Equivalent circuit models that account for these localized magnetic behaviors are explored more fully in the following chapters with the goal of producing an electromagnetic model that can successfully predict performance of saturated IPM machines and be incorporated into the optimization process outlined above.

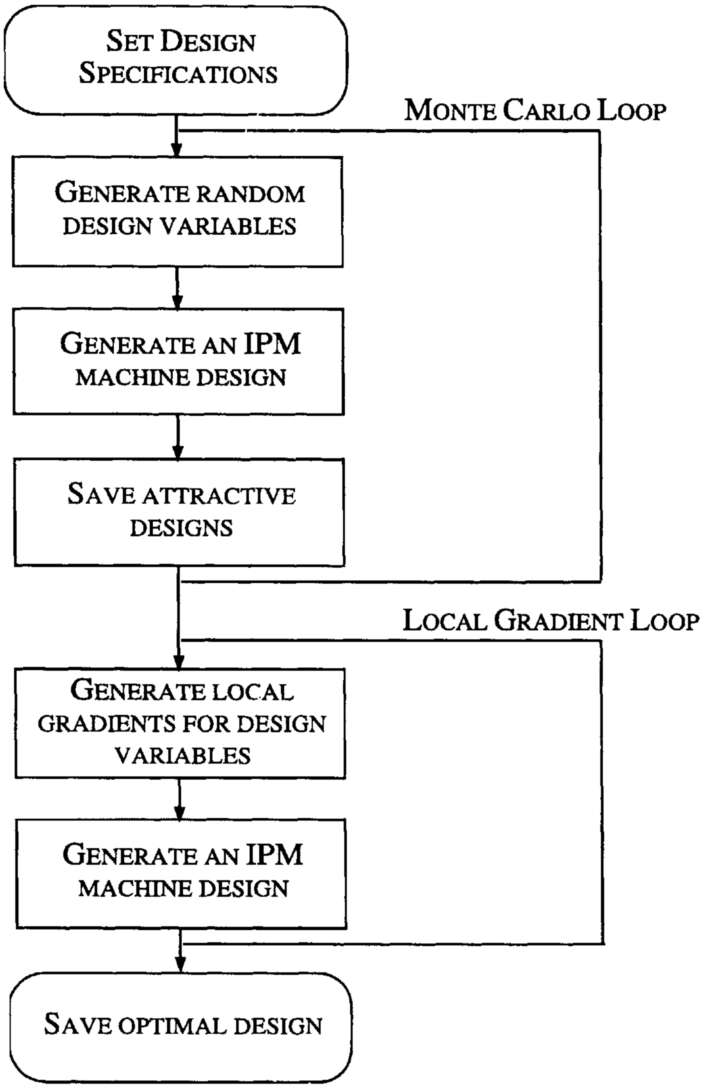

Figure 1.8: IPM machine drive design flow.

As described in Section 1.2, the primary application that motivated the study of IPM machine optimal design is the design and optimization of an automotive crankshaft-mounted integrated starter/generator. Though the initial tradeoff study indicated that the IPM machine is a promising candidate more thorough magnetically saturable models are necessary to accurately predict the capabilities of a properly optimized machine design.

So following the development of the general design and optimization methods in the next chapters, the automotive ISG application is revisited and the tools developed and validated earlier are then applied to design a cost-optimized ISG drive system.

1.5 Thesis Organization

Figure 1.9 depicts the organization of the thesis by chapter. The work can be divided into two parts: IPM machine design theory and application.

In the first part, the machine design theory is developed. IPM machines are described in more detail, and in particular, the conventionally laminated versions that the models developed in the thesis apply to. The applicable work by other authors is presented and contrasted with this work. Building on this background, Chapter 3 develops the IPM machine models with increasing complexity to motivate the final magnetically saturable equivalent circuit model that is the basis for the machine design. Chapter 4 presents the design method verifications using finite element analyses and existing similar experimental machines.

In second part, the specific automotive ISG application is revisited. The cost-optimized ISG drive system requirements and the optimization methods to achieve them are fully presented in Chapter 5. Chapter 6 presents additional design challenges, structural integrity and demagnetization, and the methods used to design to meet these ancillary but necessary conditions. Following this, the ISG drive optimization results are presented in Chapter 7.

In Chapter 8, the machine design methods are presented again in terms of their wider applicability. Opportunities for further study are suggested. And in particular, opportunities for further variations of the automotive ISG application are highlighted.

1.6 Summary

This chapter introduced the motivation for this thesis and presented the rationale for developing a magnetically saturable analytical model for optimized IPM machine drive design that is presented in this thesis. The motivation is the need for optimized design methods for IPM machine drives that can optimize over a wide design space with reasonable computation time while accurately predicting capabilities in the presence of magnetic saturation. The IPM machine drive in particular is shown to be attractive for applications that require wide constant power operating regions and need to be cost-optimized. The requirements for optimal design of an automotive crankshaft-mounted integrated starter/generator are developed as a real world example that could benefit from the design techniques presented in the thesis.

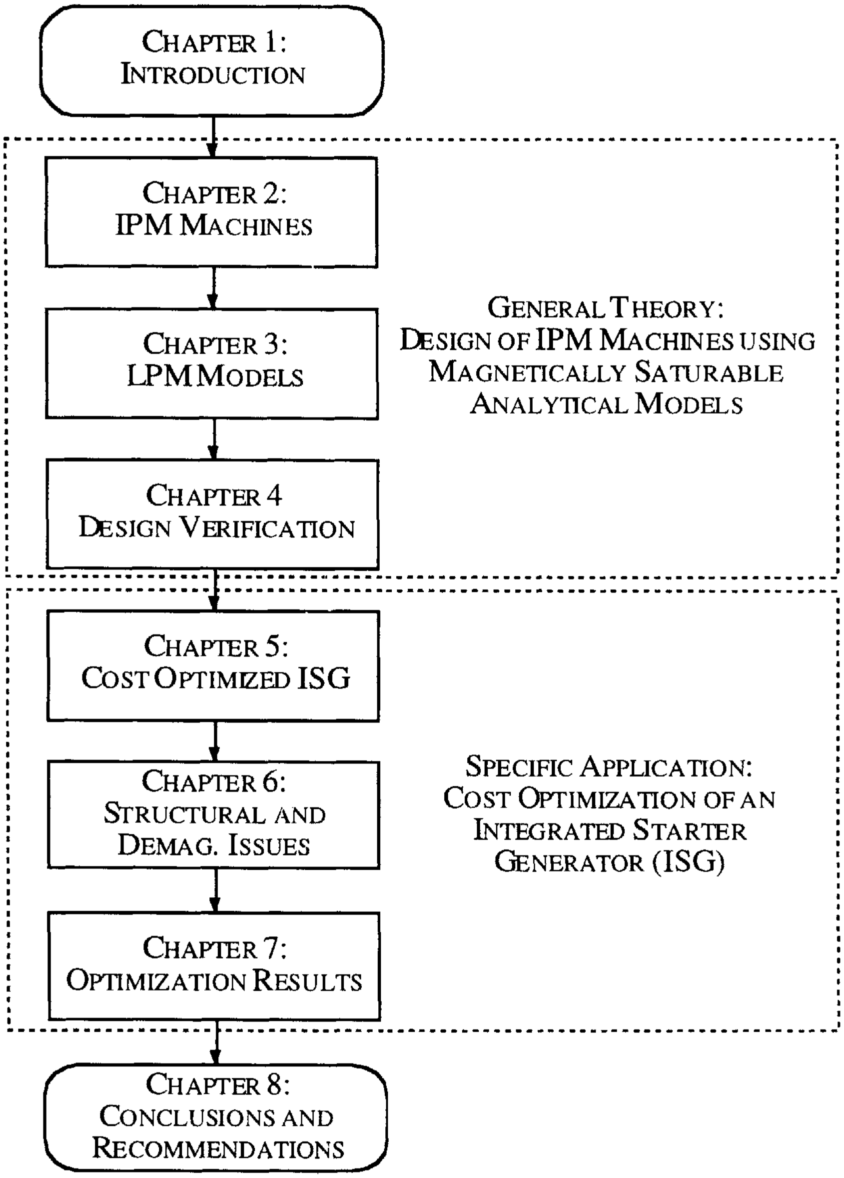

Figure 1.9: Thesis organization by chapter.

Chapter 2

INTERIOR PERMANENT-MAGNET MACHINES

2.1 Introduction

This chapter describes IPM machine drive characteristics and the applicable literature regarding the design and modeling of IPM machines. First, a generalized IPM machine is described to distinguish it from other common machines. Then the specific subclass of IPM machines that is being investigated in this thesis is presented. Published studies conducted by other researchers are summarized and the pertinent contributions are contrasted to the work of this thesis. This lays the groundwork for the development of the analytical IPM machine models in the following chapter.

2.2 Interior PM Machine Description

The IPM machine was briefly introduced in Chapter 1. IPM machine drive systems were described as particularly applicable to applications requiring high power density, starting and generation, constant power operation over wide speed ranges, and cost optimization. This section examines the IPM machine drive class to demonstrate, in the context of similar machines, how the selected IPM machine subclass can achieve these characteristics. The section also lays the analytical groundwork for the design models developed in the following chapter.

2.2.1 Permanent Magnet and Saliency Characteristics

IPM machines are synchronous machines that use both permanent magnets and mechanical rotor saliency for electromechanical energy conversion. Machine theory explains that there are two sources of electromechanical energy conversion, or equivalently, average torque production: torque due to interaction of stator magnetomotive force (MMF) with a rotor magnetic field and torque due to the interaction of stator MMF with rotor electromagnetic saliency [11]. The rotor field source may be a permanent magnet (PM) or electromagnet (i.e. a winding). Due to improvements in PM materials, manufacturing methods, and converter control capabilities, PM field production has gradually been replacing wound fields in many synchronous machine applications. Some of the exceptions are very large power generators and applications with extreme temperature environments.

The permanent magnets produce a DC field that rotates synchronously with the rotor with alternating polarity at each magnetic pole. The second source of torque production, electromagnetic saliency, is most commonly built mechanically into the machine geometry. This means that the equivalent inductance that a stator winding would exhibit as the rotor sweeps by changes with rotor position. This can be accomplished by changing the mean airgap as a function of rotor position, or by changing the effective airgap due to features in the interior of the rotor. The machine can be doubly-salient, where the stator reluctance also changes significantly around the airgap periphery, or singly-salient when there is only rotor saliency. Like the PM field the saliency profile also rotates synchronously, but with symmetry that repeats every pole since saliency is not directionally dependent (i.e. not magnetically polarized).

Figure 2.1 sketches the shape of the PM airgap flux, Φ_{PM}, and self-inductance of a phase winding, L_a, versus position along the airgap, θ, for rotors with magnets or mechanical saliency. Figure 2.2 shows the effect when the rotor design includes both PM material and saliency. Note that for each, axes of symmetry are defined as the d-axis and q-axis of the machine. There is a useful well-developed theory of both machine analysis and control, the Blondel-Park Transform, that was extended from a general mathematical transform [12]. It defines these two axes with the purpose of performing calculations in a coordinate frame that rotates with arbitrary speed. It is often employed with a rotation transform index that moves in synchronism with the rotor [13, 14]. The usefulness comes from the fact that analyses and control can be performed using defined machine parameters that are constants instead of using the stationary frame quantities, such as Φ_{PM} and L_s, which are functions of θ.

It is evident from Figure 2.2 that by using appropriate control, average torque can be developed using both the PM field and saliency of the rotor designs. Furthermore, two orientation options are shown: in (a) the magnets are aligned with the axis having a higher inductance, and in (b) the magnets are aligned with the low-inductance axis. There are multiple conventions with respect to how to define the d and q axes. Though these particular designs may not be practical, they do simply illustrate the characteristics of different rotors.

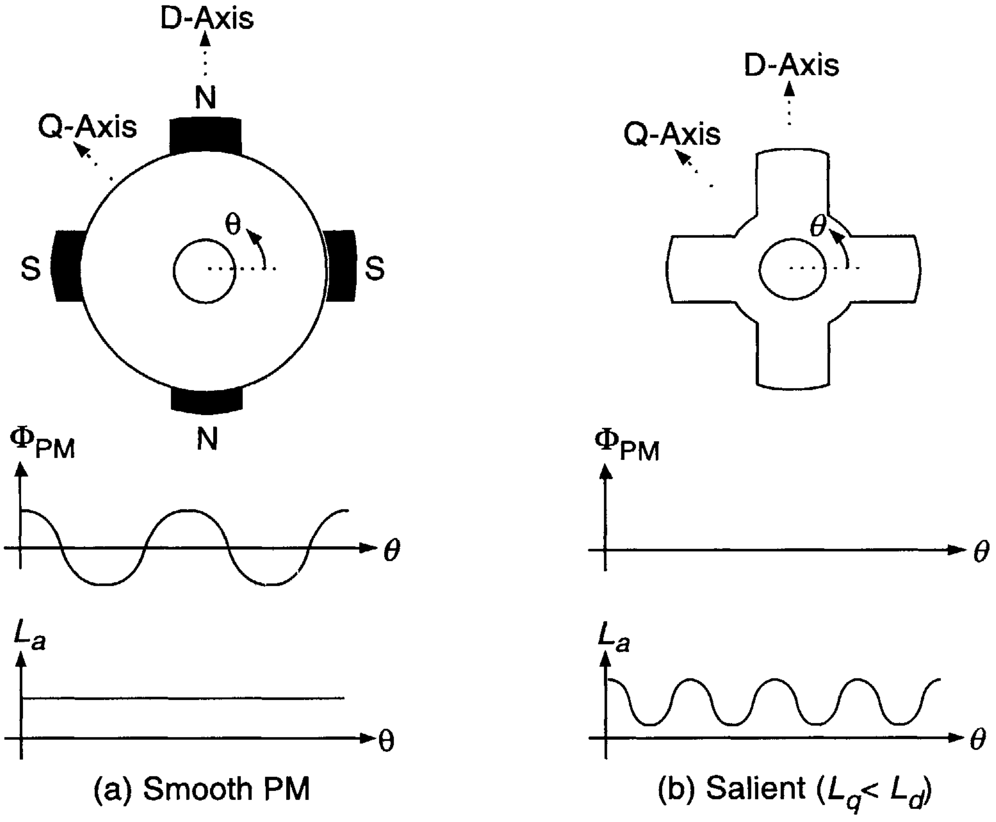

(a) Smooth PM (b) Salient ($L_q < L_d$)

Figure 2.1: PM field and synchronous inductance associated with PM or salient rotors.

The convention used throughout this thesis is to define the d-axis to be aligned with the PM field, and in designs without magnets, the d-axis is defined to be aligned with the high-inductance axis. Furthermore, a right-handed coordinate system is assumed with the positive q-axis 90 electrical degrees advanced in the positive (counterclockwise) angular direction from the positive d-axis as indicated in Figure 2.2.

There are both advantages and disadvantages to constructing a PM synchronous machine to incorporate saliency. The chief benefits are increased constant-power speed range (CPSR) capability, and reduced magnet size for a given torque requirement [7-9, 15-17]. The major disadvantages are increased manufacturing costs and decreased structural strength. The rotors in Figure 2.1 are visibly simpler than the rotors Figure 2.2 which would tend to have higher manufacturing costs due to both cutting the rotor lamination features, and mounting the magnets. With experience, though, perhaps this difference becomes more marginal. The structural strength issue becomes increasingly important as the rotor tip speed increases where it is more difficult to ensure securely adhered magnets. This becomes even more significant in the later discussion of the ISG IPM machine where the magnets are mounted in cavities cut in the rotor laminations.

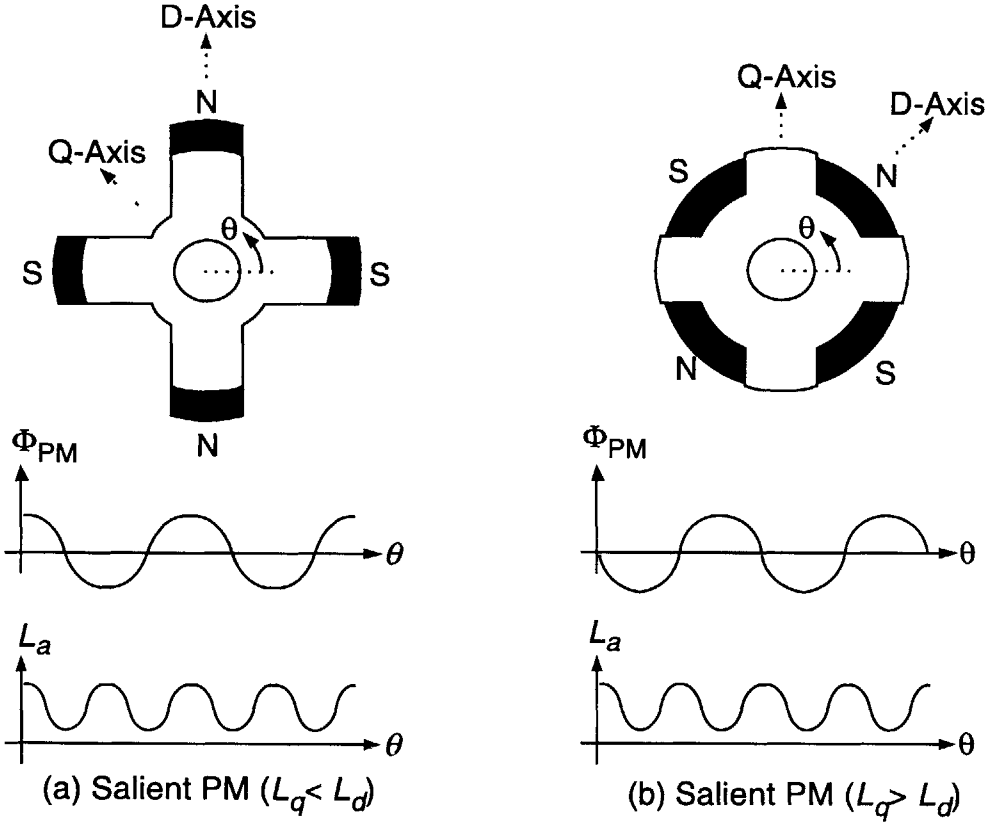

(a) Salient PM ($L_q < L_d$)

(b) Salient PM ($L_q > L_d$)

Figure 2.2: PM field and synchronous inductance associated with rotors that are both PM and salient.

The potential for hybrid torque production can be observed by starting with the formula for the average torque of electrical origin

$$T_e = qp\left(\Psi_d I_q - \Psi_q I_d\right) \tag{2.1}$$

which is valid for any q-phase, p-pole-pair, rotating machine [14]. Ψ_d and Ψ_q, and I_d and I_q, are defined as the flux linkages and currents along the d and q axes respectively. The dq-frame flux linkages and currents are defined with respect to the respective RMS, not peak, phase quantities. Recognizing that the flux linked in each axis can be broken down into the flux linkage due to the PM field, λ_{PM}, and a portion due to the self-inductance, the following definitions are made

$$\Psi_d = \lambda_{PM} + L_d I_d \tag{2.2}$$

$$\Psi_q = L_q I_q \tag{2.3}$$

where the salient synchronous inductances, L_d and L_q, are defined as independent machine parameters along each axis. It has already been noted above that the *dq*-frame inductances are independent of angle in the rotating reference frame, but there is no requirement that they are constant with respect to other parameters, most notably the excitation level (I_d, I_q). Equation (2.1) is next rewritten using (2.2) and (2.3) in the common form

$$T_e = qp\left(\lambda_{PM} - \left(L_q - L_d\right)I_d\right)I_q \tag{2.4}$$

and then, after rearranging the terms,

$$T_e = qp\lambda_{PM} I_q - qp\left(L_q - L_d\right)I_d I_q \tag{2.5}$$

The first term in (2.5) is the torque due to the PM field and the second is the contribution from the saliency, $L_q - L_d$. Note that I_d only contributes to the saliency torque component. A term that is often used in the discussion of IPM machines is the saliency ratio, which is defined here as

$$S_r = \frac{L_q}{L_d} \tag{2.6}$$

For rotors in Figure 2.2 (a) where the high-inductance axis is the *d*-axis $S_r < 1$; for rotor (b) $S_r > 1$. The chief implication for this distinction is that the sign of I_d that is required to increase the available torque is positive for a machine with rotor (a) and negative with rotor (b) as observed in (2.4) or (2.5). Furthermore, in the second case with $S_r > 1$, (2.2) shows that the negative I_d is in a direction that reduces the flux linked along the *d*-axis. This is called flux weakening. The term field weakening is reserved for dc and ac synchronous machines with wound, instead of PM, fields that can be reduced in strength from the field terminals as the speed is increased beyond base speed [18].

This discussion is not to suggest that adding saliency would give a machine designer something for nothing regarding torque capability. There are inherent limits in the torque capability of a machine of a given design and rotor surface area that have little to do with the field source or saliency, notably the RMS airgap flux density, B_{ag}, and RMS surface current density, K_s [11]. These quantities determine the average shear stress in the airgap

$$\langle \tau \rangle \propto B_{ag} K_s \tag{2.7}$$

which in turn is related to the torque capability for a given rotor volume, V_r, by

$$\frac{T_e}{V_r} = 2\langle \tau \rangle \tag{2.8}$$

B_{ag} is limited by magnetic saturation in the core so a surface PM rotor could possibly be designed that substantially saturates the machine iron, thus there may be limited torque capability increase for an IPM machine design if the rotor diameter and volume remained the same when saliency is introduced. For reference, K_s is limited by manufacturing capabilities (to increase the winding packing factor at the airgap) and the thermal limitations dictated by the stator cooling capabilities and the insulation characteristics of the wire.

Hybrid torque production does, though, produce other benefits. Most notable is the opportunity to design salient PM machines with a combination of a higher CPSR with good power factor. And this can be accomplished with lower magnet strength or size rather than artificially increasing leakage inductance as the following discussion indicates.

The detailed CPSR analyses are well-documented [7, 17-19]. Figure 2.3 and Figure 2.4 show the *dq*-current (i.e. vector control) plane focussing on the motoring quadrant and the associated torque versus speed sketches for idealized surface PM (SPM) and salient PM machine drives. It is assumed that the drive systems represented in both figures are operating with the same converter ratings (I_0, V_0), but that the machine design details are necessarily different. The operating limits imposed by the converter are shown as a current limit circle (I_0) and as voltage limit ellipses (V_0). The voltage limit ellipses collapse to a circle for SPM machine drives because of the lack of saliency. The voltage limitation shrinks with increasing speed towards the center of the ellipse or circle at the 'infinite speed point'

$$I_d\big|_{\substack{\text{inf.}\\ speed}} = -\frac{\lambda_{PM}}{L_d} \tag{2.9}$$

where this point can be designed inside or outside the current limit circle. The figures show graphically that having a machine drive with appropriate magnet design and vector control can, neglecting losses and mechanical limitations, produce a system with an infinite CPSR. This is possible when the center of the voltage limit ellipse is inside the current circle, and the power factor in the CPSR is maximized when this point is right on the current circle as shown [7]. What is implied, but perhaps not obvious from these figures, is that flux weakening operation achieves the constant-power operation with a given power converter rating (I_0, V_0) by limiting the developed back-emf voltage by the injection of current along the negative d-axis.

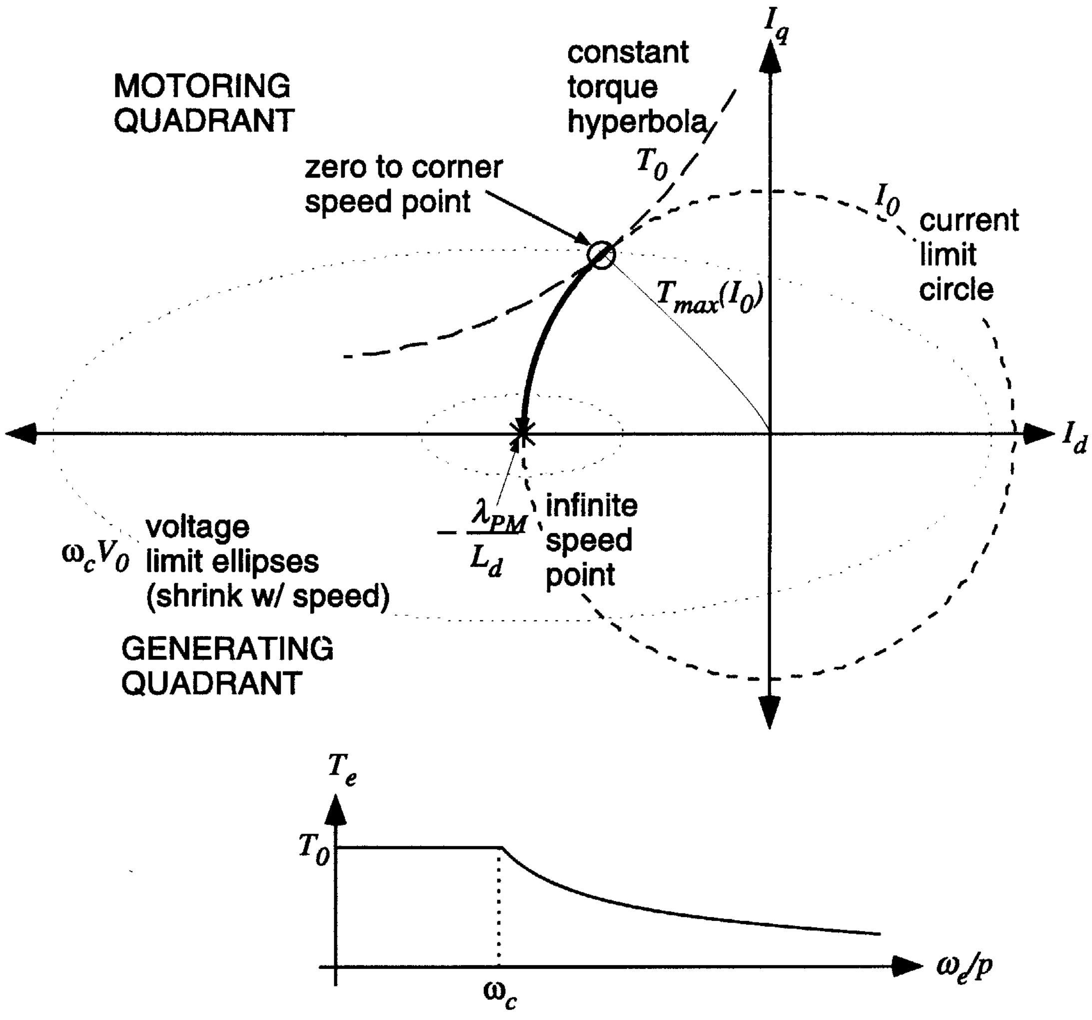

Figure 2.3: dq current plane analysis of an ideal infinite CPSR salient PM machine drive.

It has been shown [7, 15] that rated, variable-speed, ac synchronous machine drive operation can be classified into three modes, I, II, and III, based on the limiting terminal variable(s). Mode I is operation at rated torque when limited by rated current alone. With optimal torque control (maximum torque-per-Ampere) Mode I operation occurs at all speeds below the corner speed, ω_c, and is shown in each figure by a circular marker. As the operating speed increases above ω_c the machine drive becomes limited by the maximum available converter voltage in addition to the current limit and Mode II is entered. Mode II operation follows the current limit circle's intersection with the voltage limit, moving down towards the I_d axis at infinite speed in the case of the ideal optimal CPSR design noted above. Mode III operation exists if the center of the voltage ellipse is inside the current limit circle. Mode III is characterized by operation at a point on the voltage limit where torque is maximized as the speed increases further, the details of which are discussed further in [7].

Lines of constant torque are also shown as hyperbolas for the salient PM machine and horizontal lines for the non-salient PM machine. Because the SPM machine is not salient, the optimal torque operating point for Mode I operation is on the q-axis, while for the salient PM machine the Mode I point is shifted along the current limiting circle into the second quadrant.

This means to achieve rated torque parity the SPM machine will be designed for higher λ_{PM}, and also higher inductance so that (2.9) remains within the current limit circle for infinite CPSR design. The higher λ_{PM} requirement is evident from (2.5), and then from (2.9) and a given converter rating L_d must increase proportionally for the infinite speed point to remain within the current limit circle. It is difficult to increase the magnetizing portion of L_d as the magnets appear as an additional series airgap along the d-axis. The alternative is to add series leakage inductance that appears on both axes but this may produce a machine with excessively high reactance.

Conversely, the IPM machine has the opportunity to use lower strength ferrite-based magnets that are less expensive than the higher-strength rare earth magnet materials to achieve the desired λ_{PM}. What this also indicates, though, is that the SPM machine drive with the same number of stator turns will enter Mode II at a lower speed and therefore achieve a lower power rating than the salient PM machine drive of Figure 2.4. Since the SPM machine may require larger as well as stronger magnets, this will serve to lower the SPM inductances and mitigate the corner speed differences with the IPM machine. Again, there should be no differences in rated torque capability for well-designed SPM and IPM machines. But this all implies that ideal higher saliency machines could increase the corner point speed further, and the associated power rating for the CPSR above the corner speed. This is an important rationale behind seeking designs with higher saliency ratios.

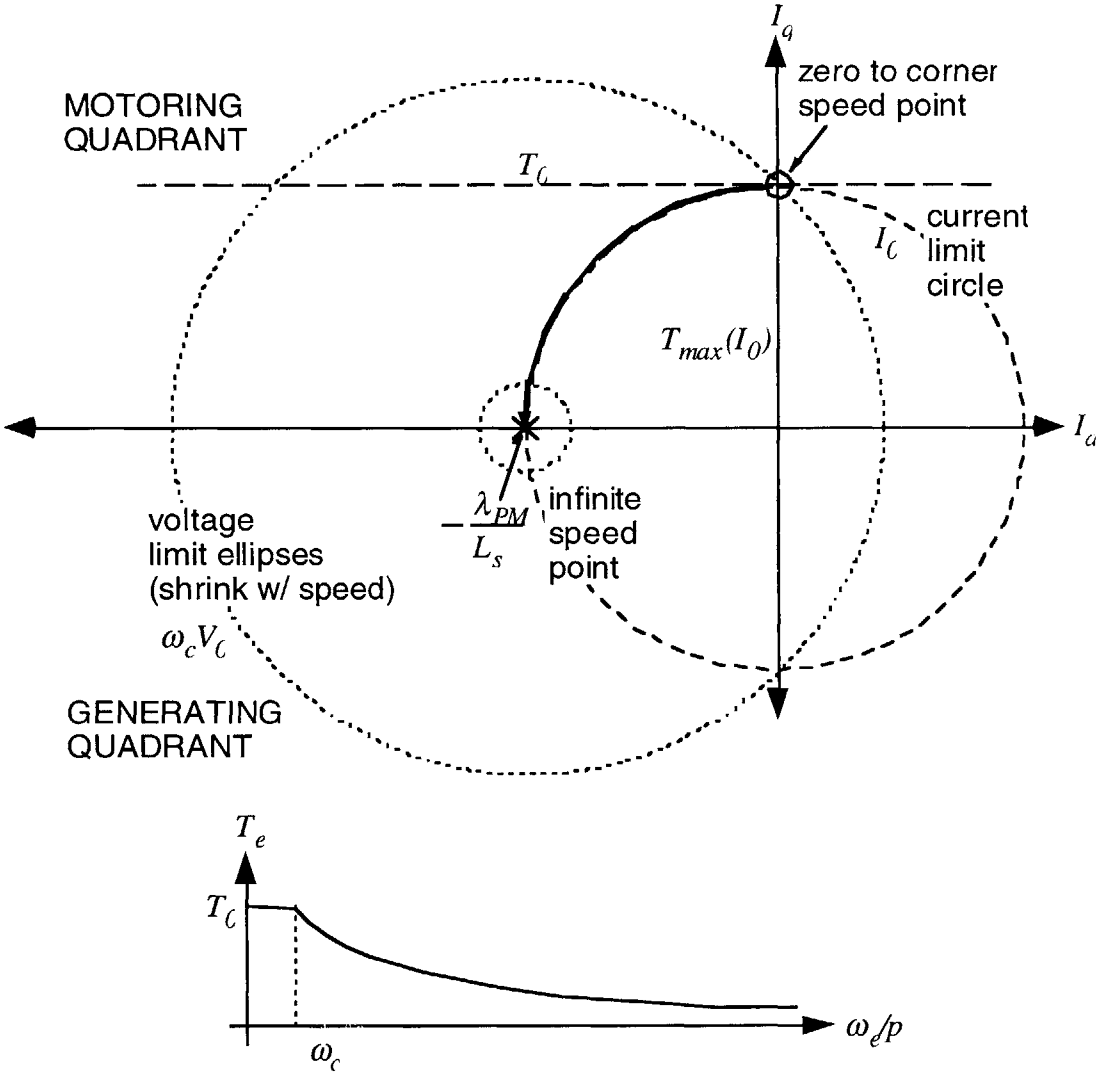

Figure 2.4: *dq* current plane analysis of an ideal infinite CPSR surface PM machine drive.

2.2.2 IPM Machine Saliency

Given the previous discussion, interior PM machines are attractive because of their potential for higher saliency ratios in contrast to the surface-mounted PM machines. Figure 2.5 depicts major sub-classes of PM synchronous machines in terms of their mechanical saliency. In Section 2.2.1 the general PM field, inductance, and torque characteristics due to PM field and saliency were discussed with respect to surface-mounted PM rotors. Rotors (a) and (b) shown in Figure 2.5 represent the extent of that discussion. Rotor (a), the surface PM machine has little-to-no saliency whereas rotor (b), the inset PM machine, has a minor degree of rotor saliency ($1 < S_r < 2$) in addition to the PM field.

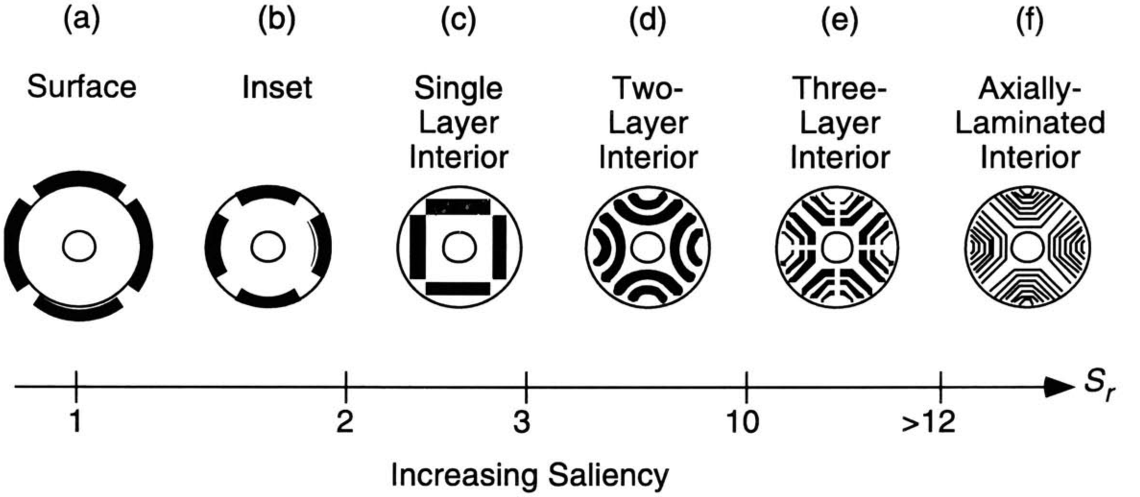

Figure 2.5: Major classes of PM synchronous machines in order of increasing saliency.

Rotors (c) through (f) in Figure 2.5 use magnets that are not mounted on the rotor surface but inside the rotor core, hence the name interior PM (IPM) machine. The single layer IPM, with typical $S_r < 3$, is the IPM topology that has been studied the longest [18-20]. A variant of the single-layer IPM that is not shown is a subclass in which the magnets are oriented radially as in wheel spokes. Conventionally laminated machines (with steel sheets in the $r\theta$ plane, also called radially- and transversely-laminated) with two and three layers of magnet inserted into curved or segmented arc cavities have chiefly been investigated by Fratta, Villata, Vagati, Honda, and Boldea [21-27]. Analytically predicted and experimentally demonstrated saliency ratios have been reported in the range $3 < S_r < 12$. Above three layers, IPM research and development has primarily focussed on axially-laminated rotor constructions [7] achieving experimental saliency ratios in excess of 12:1.

As described in Section 2.2.1, the saliency ratio has two chief effects: reducing the amount of required magnet material for the same torque production, and improving the opportunities for improved performance in constant-power operation. Figure 2.6 shows a plot of IPM machine drive characteristics in the motoring quadrant of the *dq* current frame as a function of saliency $S_r = 1.1$, 2.0, and 10. It should be noted that magnetic saturation has been neglected in the calculation of these curves. For each S_r the max torque-per-Ampere curve, *tmi*, and the associated one-per-unit constant torque line, *t1*, are shown. The intersection of each pair of curves is the Mode I operating point. The locus of Mode I points for varying saliency is also shown extended to $S_r = 1$ and $S_r = \infty$.

This further illustrates the point made in Section 2.2.1 that the unsaturated torque capability, or conversely now the current requirements for one-per-unit torque, is decreased with increasing saliency. But furthermore it clearly shows that the max torque-per-Ampere line approaches a 45-degree slope as saliency increases and that further saliency increases beyond $S_r = 10$ does not change the current vector characteristics substantially at rated current.

The operating characteristics, including modes and current vector control angles, will be revisited in later chapters to explore the contrast between these ideal analyses and analyses that incorporate the effects of magnetic saturation.

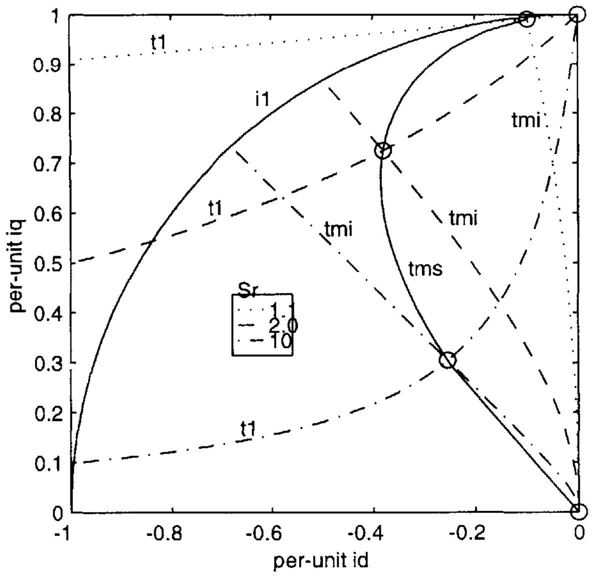

Figure 2.6: Mode I maximum torque per ampere, *tmi*, and constant torque curves, *t1*, as a function of saliency ratio, S_r, in the motoring quadrant of the *dq* current frame. *tms* is the locus of optimal rated torque points as a function of S_r.

2.2.3 Rotor Stack Construction

In Section 2.2.2 the principal IPM rotor construction styles, transversely- and axially-laminated, were introduced in the context of the orientation of the electrical steel laminations. Within each construction style there are of course many detailed variations possible regarding approaches for holding the lamination stack together, inserting the magnets, magnetizing the magnets, and retaining the magnets. This section summarizes the basic options and important characteristics that may be involved in the design decision for the rotor construction style.

The transverse lamination style is the most commonly used construction method in high-performance machine design [28]. It offers reduced core losses due to eddy currents compared to earlier construction techniques that employed cast blocks of iron. This is particularly important in AC synchronous machine stator construction where the fundamental flux components are alternating at the electrical excitation frequency. Electrically isolating the core material in the axial direction of the machine limits the magnitude of the eddy currents and the associated field fluctuations that appear as core losses in the electromechanical energy conversion process.

AC synchronous rotors are also typically constructed from laminated steel even though the eddy current losses are often lower per unit volume than in the stators. Eddy currents are a less significant loss mechanism in AC synchronous rotors because the rotor core is dominated by DC flux fields. This is particularly true for smooth airgap machines with little or no rotor saliency such as a PM synchronous machine with nearly closed stator slots, and surface inset rotor magnets. In machines with highly-salient rotors or open stator slots, though, harmonic flux components are introduced into the rotor core and efforts should be made to characterize the losses [29, 30].

Depending on the size of the machine, particularly the active length, and the geometric complexity of the rotor cross-section, it may be easier to cut and hold accurate tolerances with laminations over a solid rotor core. The cutting method may also affect the decision between solid or transversely-laminated rotor construction. For simpler rotor geometries stamp punching is often employed. In some IPM rotor geometries, though, there may be very narrow steel features in the rotor geometry between adjacent magnet cavities (as seen in the posts of Figure 2.5(e)) and between the tips of the magnet cavities and the rotor OD (see the bridges in Figure 2.5(c) through (e)). Punching these narrow bridges and posts can change the magnetic properties of the electrical steel significantly. In these cases, wire EDM cutting methods may be selected.

For higher volume applications, though, the wire EDM method is more expensive versus the cost of creating one punch die for a given design. If it is determined that core losses in the particular design are not significant, the rotor may be solid cast and then wire EDM cut to tolerance. Also for rotor designs and applications with particularly high tip speed, the structural integrity of an IPM rotor geometry with narrow bridges may be a limiting construction factor [21, 24, 31] in the decision between laminated conventional electrical steel and alternative higher-strength steels including solid iron [32-34].

In the case of either solid or transversely-laminated rotor construction, the rotor cross-section is a unitary piece. This means that further retention is typically not required. The only exception to this may be if rotor bridge dimensions are chosen that do not have sufficient mechanical strength to meet mechanical loading specifications. In this case, the worst-case rotor stress state must be reduced by other means such as a rotor OD wrap (often Kevlar or steel wire) or radial bolts that hold each pole piece. Of course, a non-magnetic wrap increases the machine's effective airgap.

The magnet material that is inserted into the rotor cavities poses both structural and magnetic challenges. The magnet material may be sintered blocks, flexible bonded sheets, or an injected matrix. The choice of material involves consideration of the required remanent flux density to meet the desired PM flux linkage, the operating temperature environment, the demagnetization withstand capability, and the shape and dimensions of the rotor cavities.

Any material type can be fit to cavities with straight segments as shown in Figure 2.5(c) and (e), however, sintered blocks are not practical to shape for smooth arc cavities as in Figure 2.5(d). Injected matrix and flexible bonded hard magnetic materials have lower remanent flux density levels than sintered magnets constructed from the same hard magnetic material base (25% to 50% lower). This limits them to roughly 0.7 T for Neodymium-Iron matrices or bonded sheets [35]. As noted, though, in Section 2.2.2 an IPM machine may likely only require the magnet strength that is available from ferrite-based materials. Operable temperature ranges for bonded and injected matrix PM materials is also widening with Nylon binding materials that can work without decomposing up to 180° C [35].

The other issue to keep in mind with operation over wide temperature ranges is that ferrite-based magnets exhibit a negative coercivity coefficient which is in direct contrast to rare-earth magnets. Therefore, the ferrite magnets may be less susceptible to demagnetization than rare-earth composites designed with similar nominal remanent flux density levels. Unless the cavities are regular rectangular shapes, only the injection-molded magnets can be reasonably designed to completely fill a cavity. Air spaces, mostly at the tips, will be filled with a binder of similar permeability (roughly that of air). Imperfect magnet fill of the cavities results in lower λ_{PM} due to the lower face area of the magnet and an effective increase in the airgap seen by the magnets.

The magnetization method must also be selected – either pre-magnetized or magnetized in-situo. Sheet magnets are usually pre-magnetized, injected magnet material is magnetized in-situo, and sintered blocks can be either. Higher-remanence magnets, though, will require a substantial applied magnetic field to become fully magnetized and this may be unreasonable to construct around the rotor geometry. Finally, the number of poles and number of cavities per pole will increase the manufacturing cost of any individual insertion technique making injection-molded magnet material more appealing. Injection-molded insertion, though, may also be challenging due to the pressures necessary to fill the cavity shapes and the associated clamping pressures on the lamination stack. For this reason, solid rotor construction may be appealing in conjunction with injection-molded magnet insertion.

The structural integrity of bridges is avoided when axially-laminated IPM rotor construction is used as shown in Figure 2.5(f). There is limited manufacturing experience with axial lamination assembly, and this among other reasons outlined below, makes this method a more expensive option. For higher-saliency design requirements where $S_r > 12$ is desired, axial lamination is often the only reasonable option. In this method, electrical steel laminations are stacked against a hub polygon section with the number of faces on the hub matching the number of machine poles. Each lamination spans only one machine pole and extends to the rotor OD at each pole end so the lamination takes on the shape of a rain gutter.

The rotor construction proceeds by alternately stacking PM sheets and steel sheets. Since the magnets are in sheet form, it is much easier to purchase and assemble them pre-magnetized. The remaining hole at mid-pole is usually filled with a solid iron pole piece. Then the whole pole structure is retained with a rotor OD wrap or a radial bolt through the center of the solid pole piece down to the hub polygon section. Each layer must be cut and bent to a different size to fit properly which adds considerably to the construction cost. In addition, unless a rotor OD wrap or some other retention mechanism is employed, the steel sheets are free to individually deflect into the airgap at high speeds, thus limiting the maximum allowable tip speed.

2.2.4 Selected IPM Machine Topology

Section 2.2 provided the foundations for IPM machine drive magnetic and operational characteristics. It showed how the specific IPM machine topology selected for investigation, and introduced in Chapter 1, fits into the broader class of IPM machines and, more generally, PM synchronous machines. The selected two-layer, transversely-laminated IPM machine subclass has the potential for moderate saliency ($3 < S_r < 8$) without the more expensive constructional features of three-layer, transversely-laminated, and axially-laminated IPM machines. In combination with the IPM machine's inherent suitability for flux-weakened operation, this makes the two-layer, transversely-laminated machine a good candidate for applications with the following characteristics:

- compatibility with motoring and generating operation;
- suitability for operation over a wide constant-power speed range;
- high performance in terms of power density and efficiency;
- good reliability over a range of environmental conditions;

- suitability for high-volume cost-optimized manufacturing.

The absence of any one of these factors may have made another machine drive class more appealing. Without motoring requirements, machine classes that do not require controlled-switch converters would be considered. Without the wide CPSR operation requirement with a given converter rating, surface PM machines may be more appealing. High performance over the wide speed range puts conventional induction machines at a disadvantage. The reliability and environmental issues make mechanically-commutated machines less attractive. Finally, the requirement for cost optimization makes the specific subclass of two-layer, transversely-laminated IPM machines more favorable than higher-saliency IPM machine designs.

2.3 Lumped Parameter Model (LPM) Design

The previous discussion of IPM machine drive characteristics was conducted using idealized models. For high-performance design, the implicit assumptions are certainly challenged and more realistic high-performance design methods are required. The chief assumption that can dramatically affect the accuracy of design predictions is that the ideal IPM machines are magnetically unsaturated. High-performance design means attempting to extract more power out of a smaller machine volume and this implies that the magnetic fields will be pushed into the saturation region of realistic ferromagnetic materials. As noted earlier, there is nothing fundamentally wrong with saturated designs and in fact an optimized machine drive's rated torque point will be likely be saturated in portions of the core even when losses, efficiency, and other realistic factors are considered. The following section outlines the previous work by other researchers that have investigated analysis and design methods for high-performance IPM machines. Their special contributions in relation to the analysis and design methods developed in this thesis are highlighted, particularly with regard to the key issue of bulk magnetic saturation in the machine's q-axis. Throughout this section and the thesis, the term linear model is used to refer to lumped parameter models where the materials' magnetic characteristics are linear models including constant, zero, and infinitely permeable materials.

2.3.1 Analytic Models

Fratta, Vagati, and Villata [23-25, 31] are the investigators that have most fully developed the lumped parameter analysis of IPM machines. Their early focus was on conventionally-laminated rotor designs using low numbers of barriers (two or three per pole). They developed analytical models based on linear magnetic circuits to calculate the

d-axis inductance and the required PM material within the cavities. The mechanical issues of bridge dimensions were also published. More recent work has focussed on three-layer IPM machines and issues of magnetic cross-coupling in synchronous reluctance machines [26, 27].

Fratta, et. al., proposed the three lumped parameters, λ_{PM}, L_d, and L_q could be simply calculated from linear magnetic circuit models. The major assumption is that the machine dimensions and loading are appropriately chosen to prevent magnetic saturation, and that therefore mmf drops in the core can be neglected. This meant that L_q could be represented by the synchronous inductance assuming a round rotor. It was further assumed that the rotor bridges in the transversely-laminated design class were fully saturated and could be represented by a constant flux magnetic sink.

Using the saturated-bridge assumption and the fact that the equivalent permeance of the magnets is approximately that of air, the magnet could be replaced by an equivalent air cavity that extended all the way to the rotor OD. The circuit formed by the magnet cavities, the airgap, the stator excitation, and the bridge sinks was solved for the magnetomotive forces (mmfs) across the airgap. Comparing this to the airgap mmfs of a perfectly-round rotor of high-permeability iron, a compact formula was established that calculated L_d as a linear function of L_q. Finally, a similar d-axis circuit was employed to calculate the required magnet remanent flux density for a target λ_{PM}, also with the assumption that the bridges are fully saturated.

The effects of q-axis saturation for high-performance design is recognized in some of their published work [26]. It has chiefly been accounted for by either of two methods:

- saturation factor constants in the inductance formulae, presumably arrived at from experimental experience;
- finite element calculation of inductance versus excitation.

This thesis directly uses the d-axis inductance formulae developed by Vagati, et. al.. The equivalent magnetic circuit they used to determine an optimal amount of magnetic material is modified for the different purpose of estimating the fundamental air-gap flux produced by a given PM geometry. For handling q-axis saturation, the thesis develops a new equivalent magnetic circuit that accounts for saturation in the core by representing it using nonlinear reluctance elements. This represents one of the major new contributions of this thesis. The nonlinear functions are determined directly from the machine geometry and the material's saturation characteristics. The advantage of this method is in developing a model that can accurately predict the saturation behavior over a wide IPM machine design space without adjustment.

2.3.2 IPM Parameter Plane

Soong and Miller's applicable contributions to this research fall into two major areas: characterization of IPM machine design by a second-order parameter plane [7, 17], and the analysis of magnetic saturation [7]. Though lumped parameter equivalent magnetic circuits that account for magnetic saturation are introduced in this work, there is limited explicit development of this approach for machine design and optimization that is the objective of this new work.

Section 2.2 made use of many of the observations and tools that Soong exploited in the development of a reduced-order parameter plane. Proceeding from the observations and analyses of [6, 15, 19], Soong presented a two-dimensional design plane using normalized magnet flux linkage and saliency ratio as the axes. On this plane Soong mapped the CPSR and inverter utilization capabilities of SPM, synchronous reluctance, and IPM machine drives in the absence of magnetic saturation. From these results, Soong determined the optimal CPSR design locus curve in this two-dimensional space, where optimal is defined as any machine design that can deliver infinite CPSR operation while simultaneously maximizing the inverter utilization. The analyses and results are also useful as an aid in the design of practical brushless AC synchronous machines that include non-ideal effects such as core losses, armature loss, and magnetic saturation.

Soong primarily investigated magnetic saturation from the standpoint of machine analysis rather than developing techniques for incorporating saturation effects into practical design tools. Using three numerical saturation models (constant, linear, and quadratic), Soong demonstrated their relative agreement with measurements on existing synchronous reluctance, SPM, and axially-laminated IPM machine designs.

Soong also developed a saturable magnetic circuit for analyzing axially-laminated machines that accounts for magnetic saturation. The accuracy of this method is highly dependent on the partitioning of the cross-section that is used to calculate the reluctance elements. This method does not employ elements to model saturation within the rotor core flux paths, and the use of an arbitrarily chosen polynomial function rather than a material characteristic makes the method more appropriate for analysis of existing machine designs.

Since there are no rotor reluctance elements for the axially-laminated design, there is also no discussion in Soong's work of how to appropriately chose dimensions for partitioning the elements. This is a reasonable approximation for axially-laminated designs that contain many layers. The electrical steel layers are generally of constant thickness along the main q-axis field path. The stator excitation would understandably be rated to prevent bulk saturation that would otherwise occur throughout this constant cross-section in the rotor core material. Transversely-laminated IPM machines are significantly different in this regard since the rotors in these machines typically contain high-permeance paths of varying widths and saturation susceptibility that have to be selected by the designer.

2.3.3 Other Models of Interest

Other researchers have published work on the effects of magnetic saturation in salient AC synchronous machines but they have also generally concentrated on addressing saturation from the standpoint of analysis rather than design, and primarily with synchronous reluctance machines as the target. Boldea, in particular, presents a generalized nonlinear equivalent circuit approach for a line-start, conventionally laminated, synchronous reluctance machine (i.e. without PM material) with multiple barriers [22]. The explicit circuit parameters are not discussed nor are the challenges in appropriately selecting the constants for the reluctance elements. The q-axis inductance as a function of excitation is presented and is compared to measured results on an existing machine design. In [36-38] the effects of magnetic saturation are analyzed with particular attention to the impact on low-speed torque capability.

Morimoto, Honda, et. al. have also analyzed and tested various rotor configurations for interior PM machines [15, 16, 21, 39-46]. These machines provide an interesting array of experimental results to demonstrate the effects of different design decisions such as the number and arrangement of magnet cavities, the impact of magnet volume and remanent flux density, and performance in the constant power speed region. Magnetic saturation again has been treated in terms of the analysis of existing machines and can be observed in the resulting q-axis inductances as a function of q-axis current.

Also of special note are the works that have been concerned with magnetic cross-coupling [36, 47, 48]. Magnetic cross-coupling occurs when the either of the dq inductances is influenced by excitation in the orthogonal axis as reflected in (2.2) and (2.3). The responsible orthogonal excitation can originate from either stator current or the magnets. In each case it has been concluded that cross-coupling is usually only significant in single-barrier and spoke interior PM machine designs. More recently models to predict cross-coupling in synchronous reluctance machines that are heavily overloaded or designed with skewed rotors have been proposed [27, 49]. Even if assumed negligible in modeling, the impact of any cross-coupling can be evaluated through comparative analysis of the design predictions for the torque-angle characteristics of a machine.

2.4 Summary

Whereas Chapter 1 motivated the study of optimal design of IPM machine drives, this chapter presented the technical characteristics of IPM machine and discussed the pertinent previous research upon which this thesis draws to develop new optimal design methods.

The general class of IPM machines was described and the characteristics were compared to other machines in the AC PM synchronous machine class. In particular, it was stressed that PM machines in general afford the opportunity for flux weakening to achieve operation over wide speed ranges at nearly constant output power. The IPM machine drive class is particularly well-suited to both high torque density and higher CPSR ratings than similarly-sized SPM machine drives with the same converter limits. The performance capabilities of major IPM subclasses were compared and the challenges associated with construction and operation of different types were presented. The implicit assumptions and examination of the IPM machine geometry highlighted the need for more practical design methods that model magnetic saturation to produce high-performance machine drives.

To summarize the previous work, there has been significant work published regarding the numerous IPM machine variations and the advantages of IPM machines for constant-power operation over wide speed ranges. To date, IPM machines have been primarily designed using either finite element analysis or linear lumped parameter circuit techniques. Past research on optimization of various features (maximizing torque, constant power speed range, or efficiency) has also been presented, again using the same techniques. Nonlinear lumped parameter techniques that model magnetic saturation have been proposed in different forms but have primarily been employed for analysis of existing designs. There has been very little development of effective techniques for determining appropriate reluctance element functions as part of an organized design process. The unique contribution of this new research has been to develop both a complete lumped parameter design optimization process for the IPM machine, and the explicit incorporation of magnetic saturation effects into the lumped parameter model. Of lesser academic significance, but also novel and demonstrative, is the application of the IPM machine to the requirements of the automotive ISG.

Chapter 3

LUMPED PARAMETER MODELS (LPM)

3.1 Introduction

This chapter presents two analytical models for the IPM machine. The models represent the electromagnetic behavior of the machine with equivalent magnetic circuits. These lumped parameter models (LPM) are created by appropriately partitioning the geometry and excitation under a specified set of assumptions. The first model is a simple linear airgap model. The second model is a more complex but more accurate nonlinear magnetically-saturable model. The comparison of the two models highlights the advantages of the saturable model for optimized IPM machine design.

3.2 Linear LPM (Infinitely Permeable Core, Saturated Bridges)

In this section, an equivalent magnetic circuit model for the IPM machine is developed from the machine geometry, windings, and excitation specifications. First the general synchronous and leakage inductance terms are developed. Then the lumped parameters for the equivalent magnetic circuit that are particular to IPM machines are presented. The electrical terminal and torque expressions are then derived from the model. Analytic estimates for machine losses and overall mechanical and electrical terminal power flow for motoring and generating operation are also derived from the model.

3.2.1 Round-Rotor Synchronous and Leakage Inductances

In this section, the synchronous and leakage inductances for an equivalent round-rotor synchronous machine are calculated. These inductances will be useful in determining the actual IPM machine inductance parameters in the following section. Figure 3.1 and

Figure 3.2 show the geometric parameters for the main IPM machine cross-section and the stator in detail. The active length, l, is assumed to be corrected by a stacking factor, typically greater than 95%. This section assembles the required parameters from the geometric and winding data to calculate the synchronous and leakage inductance parameters of the machine using well-established analytic methods [11, 28-30].

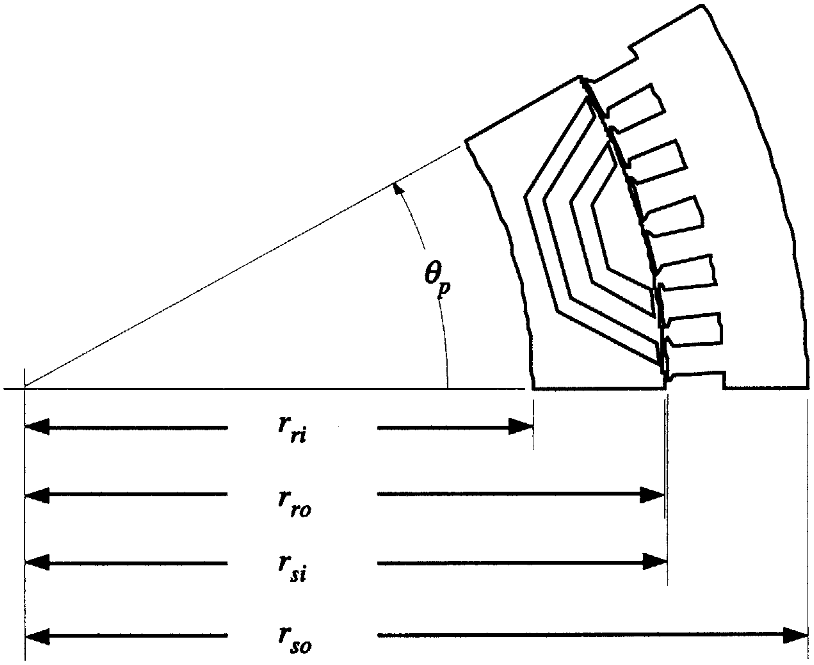

Figure 3.1: IPM machine pole cross-section with main radial dimensions.

The tooth and slot dimensions in Figure 3.2 are used to determine the equivalent series turns per phase. The windings are assumed to be double-layer symmetric windings with an integral number of slots per pole and constant turns per phase per slot. Because the windings are placed in slots, the series turns per phase are adjusted to estimate the effective series turns per phase as if the windings were sinusoidally distributed on the surface of the stator. An additional effect of winding in slots is that the induced mmf wave has harmonic components, the fifth and seventh being the most significant in magnitude. The coils from one phase are distributed in m_a slots per pole. For a machine with q phases and p pole pairs

$$n_{sp} = qm_a \tag{3.1}$$

$$\theta_t = \frac{\pi}{n_{sp}} \tag{3.2}$$

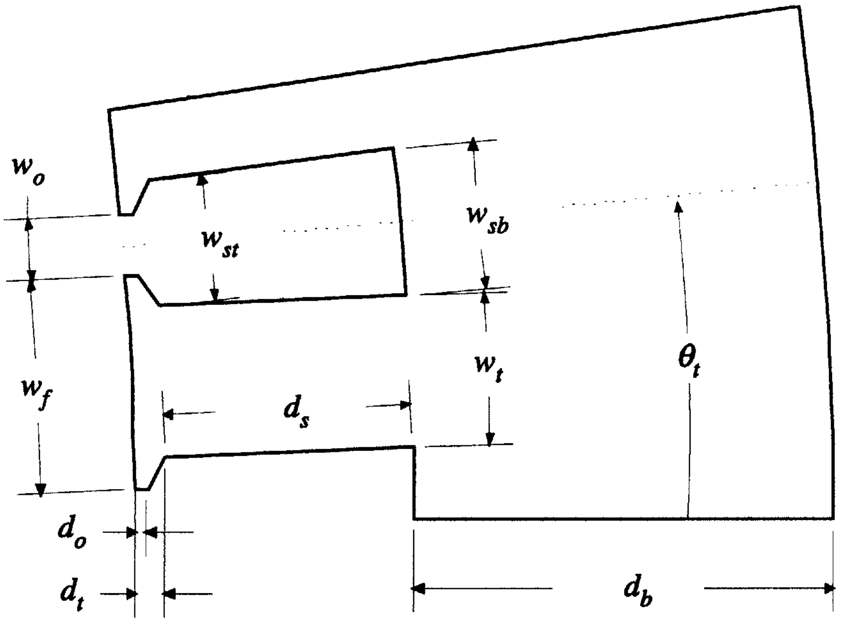

Figure 3.2: Stator tooth pitch cross-section with dimensions.

$$n_s = 2pn_{sp} \tag{3.3}$$

where n_{sp} is the number of slots per pole, θ_t is the tooth pitch, and the n_s is the total number of stator slots. Two useful short pitching quantities are the ratio of the actual coil pitch to the full pitch λ_{ssp}, and the actual coil throw angle θ_{ssp}

$$\lambda_{ssp} = \frac{n_{sp} - n_{ssp}}{n_{sp}} \tag{3.4}$$

$$\theta_{ssp} = \pi\lambda_{ssp} \tag{3.5}$$

where n_{ssp} is the number of slots short-pitched for each coil.

The breadth, pitch, skew, and overall winding factors are then, respectively

$$k_{bn} = \frac{\sin(m_a n\theta_t/2)}{m_a \sin(n\theta_t/2)} \tag{3.6}$$

$$k_{pn} = \sin(n\theta_{ssp}) \tag{3.7}$$

$$k_{sn} = \frac{\sin(n\theta_{sk}/2)}{n\theta_{sk}/2} \tag{3.8}$$

$$k_{an} = k_{bn}k_{pn}k_{sn} \tag{3.9}$$

where θ_{sk} is the skew angle and n is the harmonic order number. The most significant harmonic orders are $n = 1$, 5, and 7 for the fundamental, fifth, and seventh harmonic components of the stator winding mmf wave. For a machine wound with N_a series turns per phase, the effective turns per phase for the fundamental mmf wave are $N_a k_{a1}$.

Before stating the synchronous inductance, the airgap, $g = r_{si} - r_{ro}$, must also be adjusted for the effects of the stator slot openings. The equivalent smooth airgap is given by

$$g' = g\frac{w_o + w_f}{w_o + w_f - k_{cs}g} \tag{3.10}$$

where the stator slot Carter coefficient, k_{cs}, is

$$k_{cs} = \frac{w_o}{2g}\tan^{-1}\left(\frac{w_o}{2g}\right) - \log\left(\frac{\sqrt{w_o^2 + (2g)^2}}{2g}\right) \tag{3.11}$$

If the IPM rotor features are ignored for the time being, the synchronous magnetizing inductance can then be given directly as

$$L_{ag} = \frac{q}{2}\left(\frac{4}{\pi}\right)\frac{\mu_0 N_a^2 k_{a1}^2 lr}{p^2 g'} \tag{3.12}$$

where μ_0 is the permeability of free space, $r = r_{si}$ is the stator inner radius, and p is the number of pole pairs in the machine.

Since the fifth, seventh, and higher-order harmonics of the mmf wave do not normally contribute to torque production, they appear as leakage inductance terms and are written directly as

$$L_{nbelt} = L_{ag}\left(\frac{k_{an}}{nk_{a1}}\right)^2 \qquad n = 5, 7, \ldots \tag{3.13}$$

The stator slots introduce two sources of flux leakage that are accounted for in this model: 'zig-zag' tooth face leakage and slot leakage. The 'zig-zag' leakage inductance is flux that crosses the airgap back and forth when phase coils are not concentrated in a single slot, i.e., $m_a > 1$. It is comprised of traveling waves in the forward and backward directions with frequencies indicated by the following harmonic orders

$$n_{fz} = \frac{n_s}{p+1} \tag{3.14}$$

$$n_{bz} = \frac{n_s}{p-1} \tag{3.15}$$

respectively. The associated winding factors are calculated in a manner similar to the fundamental mmf wave terms

$$k_{bfz} = \frac{\sin(m_a n_{fz} \theta_t / 2)}{m_a \sin(n_{fz} \theta_t / 2)} \tag{3.16}$$

$$k_{bbz} = \frac{\sin(m_a n_{bz} \theta_t / 2)}{m_a \sin(n_{bz} \theta_t / 2)} \tag{3.17}$$

$$k_{pfz} = \sin(n_{fz} \theta_{ssp}) \tag{3.18}$$

$$k_{pbz} = \sin(n_{bz} \theta_{ssp}) \tag{3.19}$$

$$k_{sfz} = \frac{\sin(n_{fz} \theta_{sk} / 2)}{n_{fz} \theta_{sk} / 2} \tag{3.20}$$

$$k_{sbz} = \frac{\sin(n_{bz} \theta_{sk} / 2)}{n_{bz} \theta_{sk} / 2} \tag{3.21}$$

$$k_{afz} = k_{bfz} k_{pfz} k_{sfz} \tag{3.22}$$

$$k_{abz} = k_{bbz} k_{pbz} k_{sbz} \tag{3.23}$$

where the subscripts *b, p, s*, and *a*, identify, respectively, the breadth, pitch, skew, and overall winding factors for the forward and backward zig-zag waves. The forward- and backward-wave zig-zag leakage inductances for $m_a > 1$ are then, respectively

$$L_{fzig} = L_{ag}\left(\frac{k_{afz}}{n_{fz}k_{a1}}\right)^2 \tag{3.24}$$

$$L_{bzag} = L_{ag}\left(\frac{k_{abz}}{n_{bz}k_{a1}}\right)^2 \tag{3.25}$$

To account for leakage flux across the stator slots, the model presented by Lipo [29] was selected, and providing a reasonable approximation for semi-closed slots. First, a short-pitching factor k_{ssp} based on the degree of short pitching is defined

$$k_{ssp} = \begin{cases} \dfrac{3\lambda_{ssp}}{2} - \dfrac{1}{2}, & 1 > \lambda_{ssp} > \dfrac{2}{3} \\ \dfrac{3\lambda_{ssp}}{2} - 1, & \dfrac{2}{3} > \lambda_{ssp} > \dfrac{1}{3} \\ 3\lambda_{ssp} - \dfrac{3}{2}, & \dfrac{1}{3} > \lambda_{ssp} > 0 \end{cases} \tag{3.26}$$

and the average slot width is determined as

$$w_{sa} = \frac{w_{st} + w_{sb}}{2} \tag{3.27}$$

Then the permeance $\mathcal{P}_s$ of the slot leakage path is calculated using the slot dimensions defined in Figure 3.2 as

$$\begin{aligned} \mathcal{P}_s = \mu_0 l & \left(\frac{2d_o}{w_o} + 2(d_o - w_o)\log\left(\frac{w_{sa}}{w_o}\right)\frac{1}{w_{sa} - w_o} + \frac{5d_s}{6w_{sa}}\right) \\ +k_{ssp} & \left(\frac{d_o}{w_o} + (d_o - w_o)\log\left(\frac{w_{sa}}{w_o}\right)\frac{1}{w_{sa} - w_o} + \frac{d_s}{4w_{sa}}\right) \end{aligned} \tag{3.28}$$

and, subsequently, the slot leakage inductance is expressed as

$$L_{slot} = \frac{N_a^{\,2}\mathcal{P}_s}{n_s} \tag{3.29}$$

The last leakage term of interest is the end-turn leakage inductance. The end-turn leakage is highly dependent on the mechanism used to wind and install the coils into a machine but a reasonable approximation is given here [29] as

$$L_{end} = \frac{1}{2}\left(\frac{140}{4\pi^2}\frac{q}{2}\frac{\mu_0 r N_a^2\left(\lambda_{ssp} - 0.3\right)}{p^2}\right) \tag{3.30}$$

Collecting all of the leakage terms together, the total leakage L_l is

$$L_l = L_{slot} + L_{end} + L_{5belt} + L_{7belt} + L_{fzig} + L_{bzag} \tag{3.31}$$

and the total synchronous inductance is

$$L_s = L_{ag} + L_l \tag{3.32}$$

3.2.2 Inductance Calculations

Figure 3.3 and Figure 3.4 show the detailed dimensions of the IPM rotor lamination including the magnet cavities. As introduced in the previous chapter, this rotor structure can have significant electromagnetic saliency due to the cavity shapes and is therefore conveniently modeled using dq-reference frame analysis [11, 28, 30]. In particular, the round-rotor synchronous inductance, L_s, that was calculated in the previous section is replaced by q-axis and d-axis synchronous inductances, L_d and L_q, that appropriately model the effect on linked flux for each axis, respectively.

Since the q-axis represents a path that is wholly through the steel portion of the rotor core, this parameter is initially estimated using an airgap reluctance model. By contrast the d-axis flux must pass directly through, or circulate around, the magnet flux barriers. Analytic models published by Fratta, Vagati, et. al., [23, 24, 31] are employed here for the initial linear LPM. The concepts were introduced in the previous chapter, and are presented here in detail.

The IPM machine synchronous inductances along the two orthogonal axes can be broken down into their magnetizing and leakage portions as

$$L_q = L_{qm} + L_l \tag{3.33}$$

and

$$L_d = L_{dm} + L_l \tag{3.34}$$

L_{qm} can be approximated using the synchronous machine calculation for round-rotor inductance since the associated magnetic flux primarily passes through rotor iron. Qualitatively, this is a reasonable first-order approximation since the magnetizing flux that crosses the airgap along the q-axis has the full rotor peripheral face through which to enter. Furthermore, a significant fraction of the total q-axis flux should pass through the rotor parallel to the magnet cavities. The cross-sectional area that is available for the main q-axis flux paths is certainly less than would otherwise be available in a solid round-rotor machine. This can be managed for the linear non-saturating model by appropriately resizing the rotor depth, $r_{ro} - r_{ri}$, and the stator q-axis excitation to prevent significant bulk magnetic saturation along the q-axis. These are the principal linear LPM assumptions that lead to assigning the round-rotor magnetizing inductance determined in the previous section to the q-axis inductance for the IPM machine. In this case,

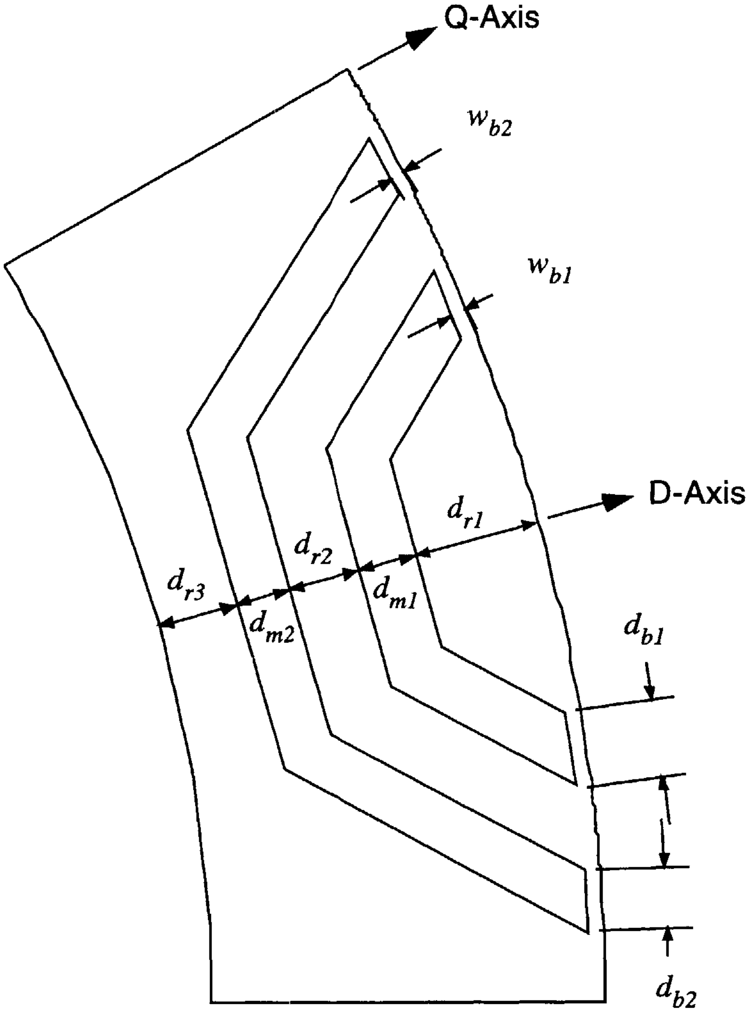

Figure 3.3: Rotor pole cross-section with dimensions.

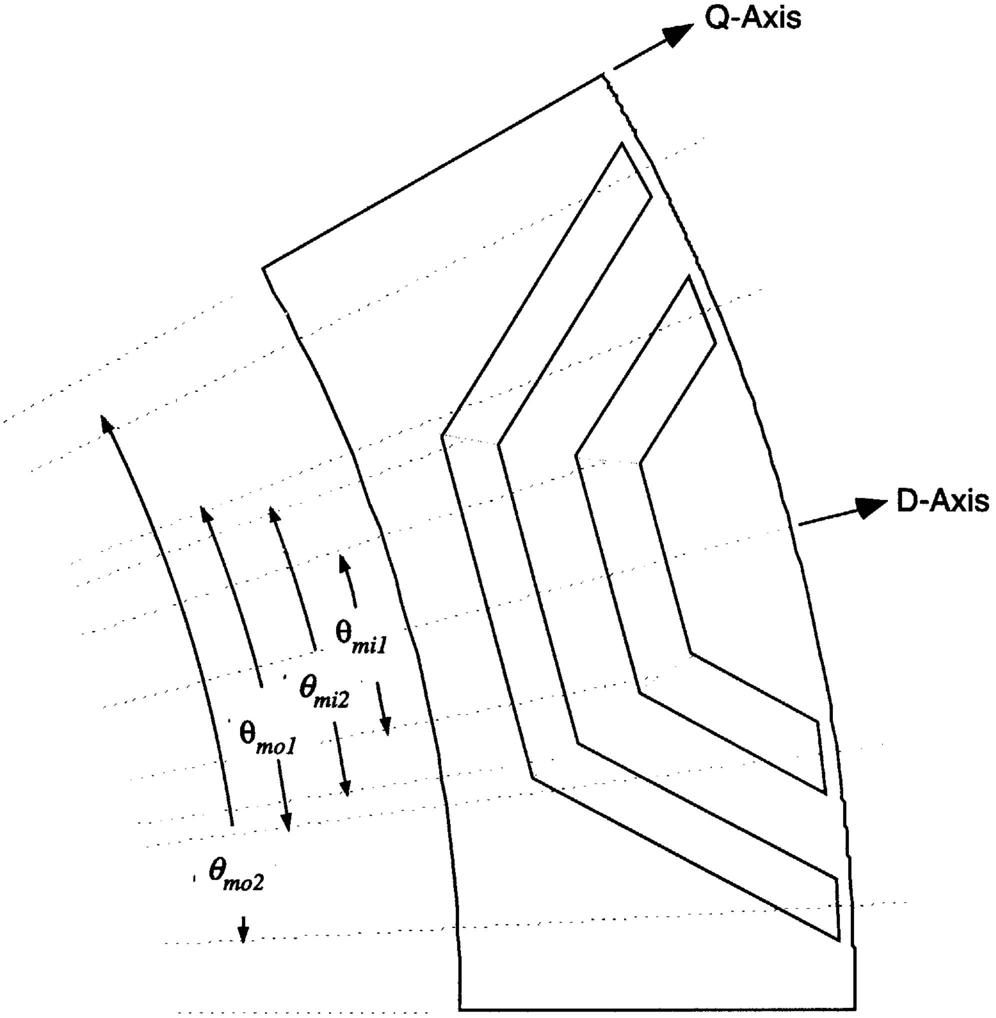

Figure 3.4: Rotor cross-section with angular magnet dimensions.

$$L_{qm} = L_{ag} \tag{3.35}$$

By definition, therefore, L_{qm} implies that the rotor core is infinitely permeable and that it can be thought of, equivalently, as a linear, non-saturable machine parameter. The leakage terms depend solely on the stator and winding design since there are no features on the IPM rotor surface that would add significant additional leakage mechanisms. Therefore, the leakage inductance is assumed to be the same as developed in the previous section:

$$L_q = L_s \tag{3.36}$$

The d-axis magnetizing inductance is modeled by a combination of 'through' and 'circulating' components

$$L_{dm} = L_{dt} + L_{dc} \tag{3.37}$$

as described in [23]. L_{dt} and L_{dc} are estimated using magnetic circuit analysis based on formulas from [23]. These formulae assume constant magnetic potentials in the core iron (i.e. infinitely permeable), fixed magnet remanence, and fully-saturated iron bridges which carry a constant flux density at the periphery of the rotor.

Figure 3.5 shows the per-unit magnetic circuit for a machine with K magnet layers that is solved to determine these inductance components. Figure 3.6 shows this same circuit for $K = 2$ superimposed on the IPM rotor cross-section. Several geometric quantities based on Figure 3.5 need further definition. The angle, $\Delta\alpha_k$, is defined as the angular distance at the rotor surface between adjacent magnet flux paths such that

$$\Delta\alpha_k = \alpha_k - \alpha_{k-1} \tag{3.38}$$

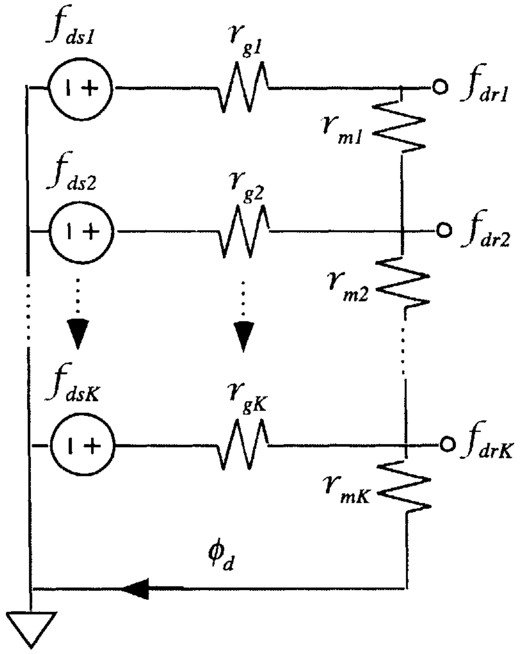

Figure 3.5: Equivalent d-axis inductance circuit for IPM rotor with K magnet layers.

The cross-sectional areas for the total stator airgap surface, A_r, for a stator tooth pitch, A_s, and for each magnet, A_{mk}, are defined as

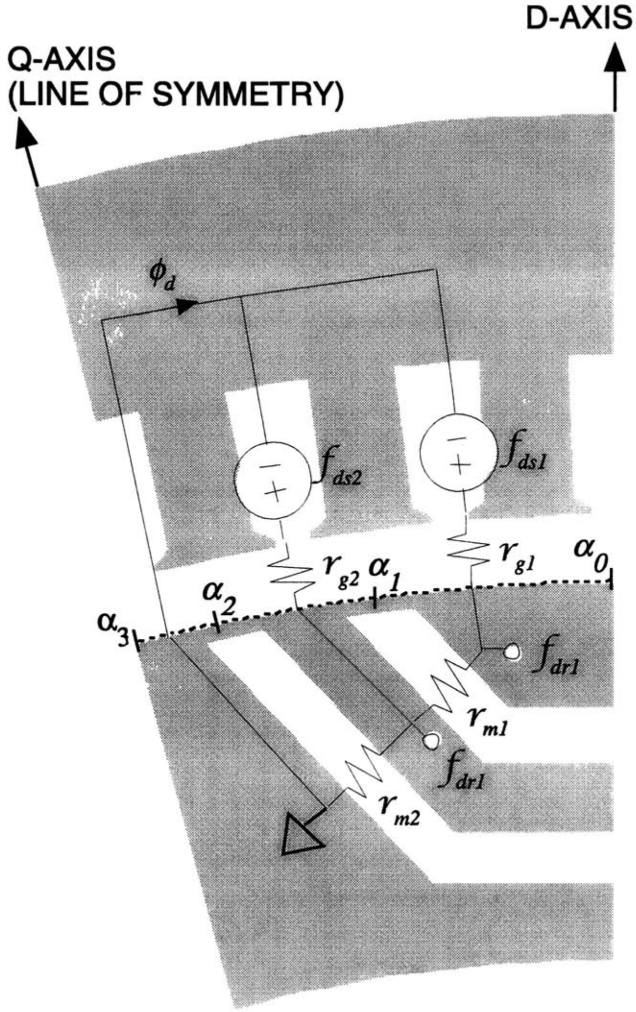

Figure 3.6: Equivalent *d*-axis inductance circuit for IPM rotor with two magnet layers.

$$A_r = 2\pi r l \tag{3.39}$$

$$A_s = \frac{A_r}{n_s} \tag{3.40}$$

$$A_{mk} = l_{mk} l \tag{3.41}$$

where k is the index used to sequentially identify each magnet, and l_{mk} is the average peripheral length of the k^{th} magnet cavity as determined from the radial and angular dimensions in Figure 3.3 and Figure 3.4. Then the per-unit circuit reluctances for the k^{th} magnet cavity and airgap segment can, respectively, be defined as

$$r_{mk} = \frac{2d_{mk}A_s}{g' A_{mk}} \tag{3.42}$$

$$r_{gk} = \frac{\Delta\alpha_s}{\Delta\alpha_k} \tag{3.43}$$

and the stator mmf source for the k^{th} peripheral segment is expressed as

$$f_{dsk} = \frac{\left(\cos(\alpha_{k-1}) - \cos(\alpha_k)\right)}{\Delta\alpha_k} \tag{3.44}$$

by applying Fourier analysis to the equivalent sinewave per-unit excitation.

Analyzing the magnetic circuit of Figure 3.5 yields the rotor surface mmf potentials f_{drk}. For the K-layer IPM machine design shown in this figure, the solution for the k^{th} layer is

$$f_{drk} = \left[(1/r)_{kj}\right]^{-1}\left[f_{dsj}/r_{gj}\right]_{j=1\ \text{to}\ K} \tag{3.45}$$

with the elements of the per-unit reluctance matrix given by

$$(1/r)_{kj} = \begin{cases} -\frac{1}{r_{mk-1}} & j = k-1 \\ \frac{1}{r_{gk}} + \frac{1}{r_{mk-1}} + \frac{1}{r_{mk}} & j = k \\ -\frac{1}{r_{mk}} & j = k+1 \\ 0 & else \end{cases} \tag{3.46}$$

Figure 3.7 shows a sketch of a typical distribution for a two-layer solution of the airgap mmf potentials.

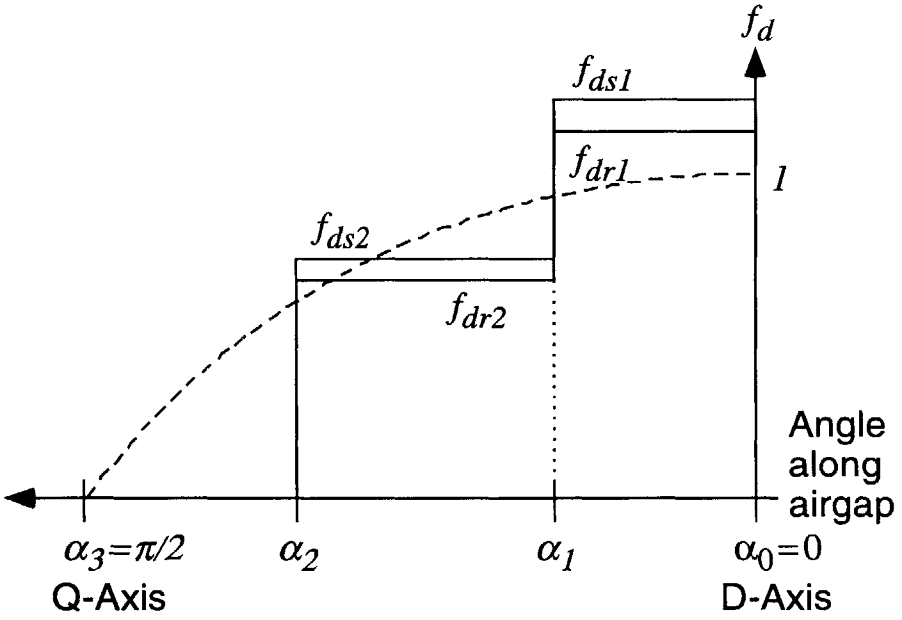

Figure 3.7: Sketch of per-unit *d*-axis mmf functions with a dashed line showing the fundamental per-unit stator excitation mmf.

The *d*-axis inductance is calculated using the following ratios [23]

$$\frac{L_{dc}}{L_{qm}} = 1 - \frac{4}{\pi}\sum_k \Delta\alpha_k f_{dsk}^{\ 2} \tag{3.47}$$

$$\frac{L_{dt}}{L_{qm}} = \frac{4}{\pi}\sum_k f_{dsk}\left(f_{dsk} - f_{drk}\right)\Delta\alpha_k \tag{3.48}$$

The *d*-axis total magnetizing inductance is then given by

$$L_{dm} = \left(\left(\frac{L_{dt}}{L_{qm}}\right) + \left(\frac{L_{dc}}{L_{qm}}\right)\right)L_{qm} \tag{3.49}$$

Finally, using the definitions of L_d and L_q established above, the saliency ratio is

$$S_r = \frac{L_q}{L_d} \tag{3.50}$$

3.2.3 PM Flux Linkage

The PM flux linked by the stator is calculated using a linear per-unit magnetic circuit similar to the d-axis inductance ratio circuit as shown in Figure 3.8 for K magnet layers. The circuit is shown again in Figure 3.9 overlaid on an IPM rotor cross-section with two layers. The same assumptions of constant potentials in the core iron (i.e. infinitely permeable), fixed magnet remanence, and saturated constant-flux-density iron bridges at the periphery of the rotor are adopted here again. Since the PM flux is oriented along the d-axis, the same basic circuit is analyzed with the stator mmf sources removed and the flux sources added. The per-unit PM source ϕ_{mk} is represented by a constant flux source proportional to the nominal remanent flux density, B_r, and the saturated bridges are modeled by constant flux sources ϕ_{bk} proportional to the estimated saturation flux density, B_s, and opposing ϕ_{mk}.

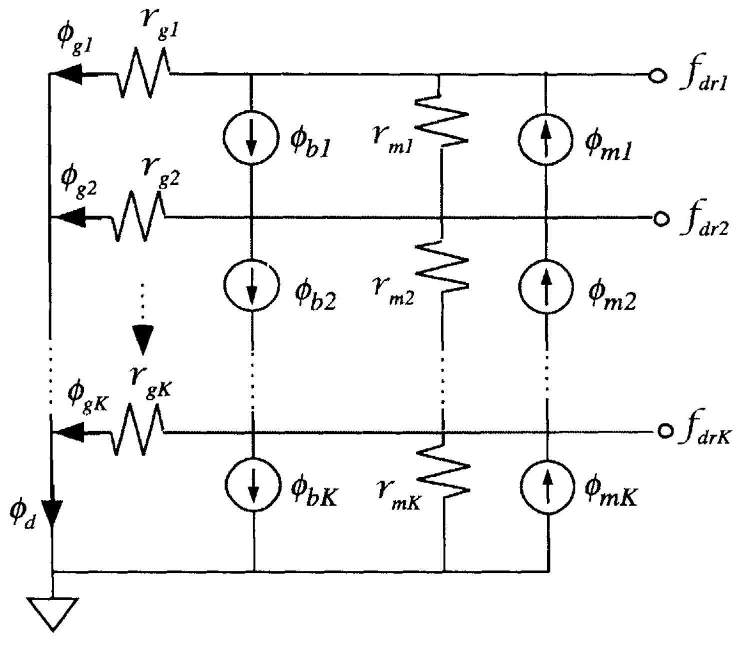

Figure 3.8: Equivalent d-axis PM circuit for IPM rotor with K magnet layers.

Some additional geometric quantities are now defined. The cross-sectional areas of the rotor bridges, A_{bk}, for the k^{th} magnet segment are given by

$$A_{bk} = w_{bk} l \tag{3.51}$$

The average airgap flux density crossing the k^{th} section of the airgap, B_{gk}, can now be written as an area-weighted function of the two sources

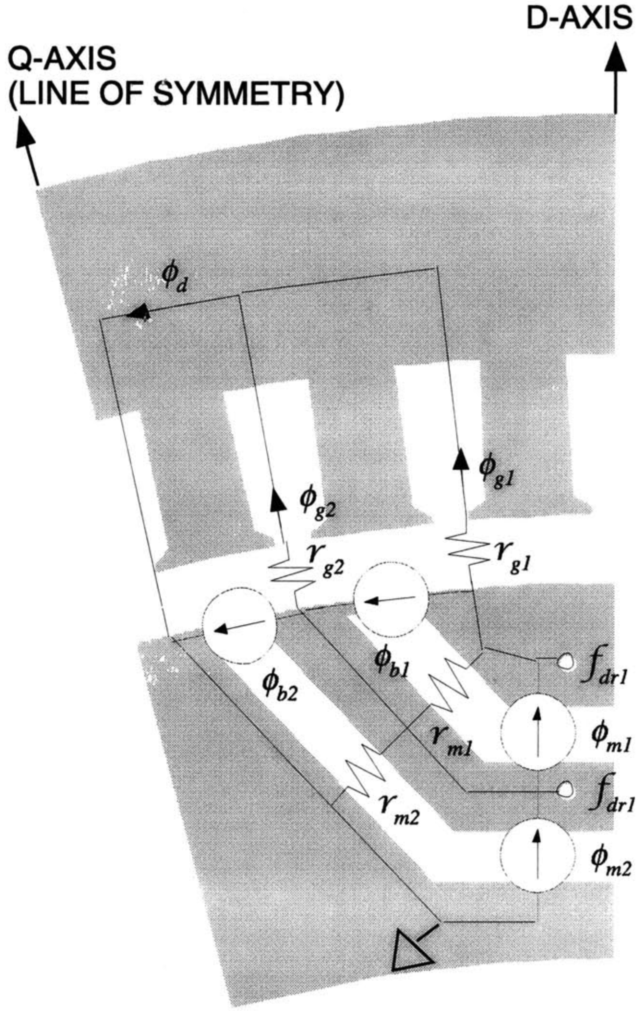

Figure 3.9: Equivalent *d*-axis PM circuit for IPM rotor with two magnet layers.

$$B_{gk} = \frac{1}{A_s}\left[(1/r)_{kj}\right]^{-1}\left[\frac{B_r A_{mj}}{2} - B_s A_{bj}\right]_{j=1 \text{ to } K} \tag{3.52}$$

The RMS fundamental airgap flux density, B_1, resulting from Fourier analysis of the staircase function, B_{gk}, is

$$\mathrm{B}_1 = \frac{4}{\pi}\sum_k B_{gk}\left(\sin(\alpha_{k-1}) - \sin(\alpha_k)\right) \tag{3.53}$$

Figure 3.10 sketches the form of the solution for the two-layer IPM rotor.

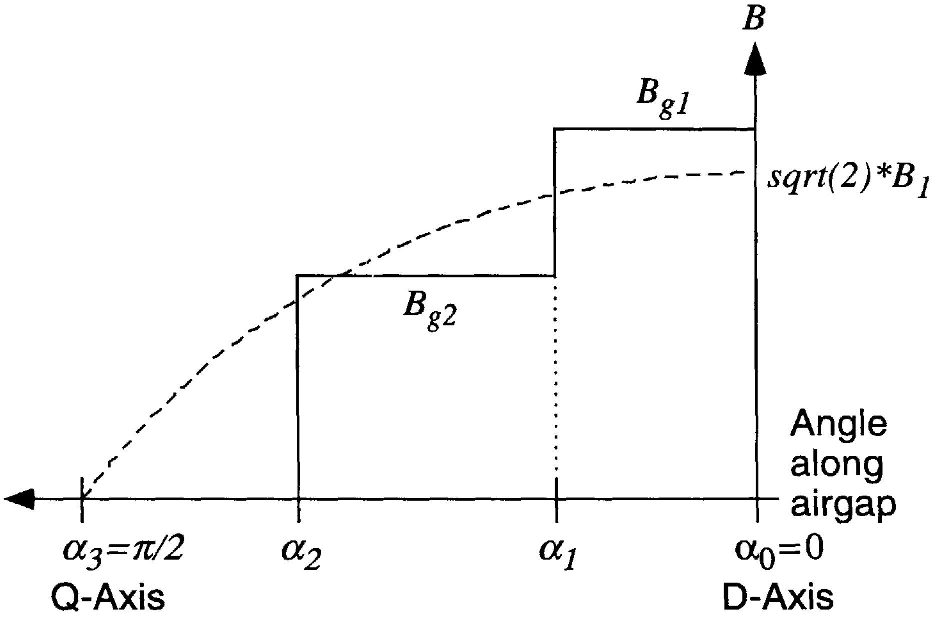

Figure 3.10: Sketch of per-unit *d*-axis flux densities with a dashed line showing the fundamental airgap flux density solution.

Using the winding factors developed earlier in this chapter, the PM flux linkage, λ_{PM}, will take the following form

$$\lambda_{PM} = \frac{\sqrt{2}RlB_1N_ak_a}{p} \tag{3.54}$$

3.2.4 Loss Calculations

Three sources of loss are considered for the IPM machine design: armature losses, stator core losses, and slot-induced harmonic losses. Mechanical losses such as windage and friction are readily quantifiable but are not heavily dependent on the particulars of the machine design and so are ignored in this development [28].

The armature losses are given by

$$P_a = qR_aI_a^2 \tag{3.55}$$

where I_a is the RMS phase current and R_a is the phase resistance. As in the previous sections, R_a is calculated from the basic machine dimensions and winding specifications. The axial height of the end turns must at least accommodate two coil sides crossing each other in a conventional double-layer lap winding, so as a reasonable estimate, the end turn axial height is estimated as three times the width of an average coil bundle

$$l_{e1} = 3w_a \tag{3.56}$$

For reference, the total machine length is then

$$l_{out} = l + 2l_{e1} \tag{3.57}$$

The average azimuthal coil length at one end, assuming that end turns follow the circumference of the stator, is

$$l_{e2} = \frac{\theta_{ssp}\left(r + d_o + d_s/2\right)}{p} \tag{3.58}$$

Assembling these lengths, the total conductor length for a single phase is

$$l_a = N_a\left(2l + 4l_{e1} + 2l_{e2}\right) \tag{3.59}$$

The conductor cross-sectional area, A_a, must match the specified wire gauge. If the wire size is selected for a given slot design and an estimated conductor fill factor, λ_a, the cross-sectional area will be

$$A_a = \frac{\lambda_a d_s w_a}{N_a/\left(pm_a\right)} \tag{3.60}$$

Assuming that appropriate stranding and wire diameters are employed, skin effects are neglected and the phase resistance is given as

$$R_a = \frac{l_a}{\sigma_a A_a} \tag{3.61}$$

The core loss model employed here combines both hysteresis and eddy-current components. These losses are primarily controlled by the particular choice of core material and lamination thickness. The exact magnetic characteristics can change from lot to lot for identically specified material. Punching and laser cutting change the nominal material properties further, so short of testing fully-processed laminations for a particular machine design, the core losses are difficult to quantify precisely. An electrical steel manufacturer reports typical properties as a function of magnetic induction and excitation frequency which can be fit to a double-exponential function for a reasonable core loss estimate [30] as shown here

$$P_{ci} = m_i p_B \left(\frac{\omega_e}{\omega_B} \right)^{\varepsilon_f} \left(\frac{B_i}{B_B} \right)^{\varepsilon_B} \tag{3.62}$$

where m_i is the mass of the i^{th} core section, B_i is the average flux density through that section, ω_e is the electrical excitation frequency, and the other base parameters are chosen to fit the core loss data sheet for the chosen material. The teeth and back iron are each treated as separate sections represented by an m_i and B_i value. US Steel M19 29-gauge electrical steel is represented by the values in Table 3.1 and one curve at 0.3 T is shown in Figure 3.11. This model is employed assuming that the magnetic material is linear, non-saturating; that the harmonic frequency loss components are insignificant; and that the air gap flux is sinusoidal.

Table 3.1: Core Loss Model Parameters for USS M19 29-gauge Electrical Steel [50]

Parameter	*Value*	*Units*
p_B	6.46e-005	W/kg
B_B	1	T
ω_B	1	rad/sec
ε_f	1.62	
ε_B	1.89	

These assumptions produce a simple, tractable model for estimating the core losses in the machine. The first assumption is generally conservative, but it is recognized that ignoring harmonics particularly near the airgap surface may not be conservative in some designs. At low excitation frequencies and rated operation, the average flux densities in portions of the core using this linear model may be unreasonably high compared to flux densities achievable with real materials, but the net effect on the calculated losses is insignificant at such frequencies.

At higher speeds, the decreasing flux densities in the flux-weakening operating region dominate the losses despite the increase in electrical excitation frequency, resulting in relatively low predicted core losses. Also note that the rotor, which may experience the highest degree of bulk saturation, is principally subjected to DC excitation and therefore will not contribute significantly to the core loss total.

The mass and average flux densities must be determined for the two main stator core sections: the teeth and the back iron. For a loaded machine the average airgap flux density, B_{ag}, is related to the airgap voltage, V_{ag}, by

$$B_{ag} = \frac{\sqrt{2}pV_{ag}}{\pi\omega_e rlN_a k_a} \tag{3.63}$$

From this result, the average tooth flux density is

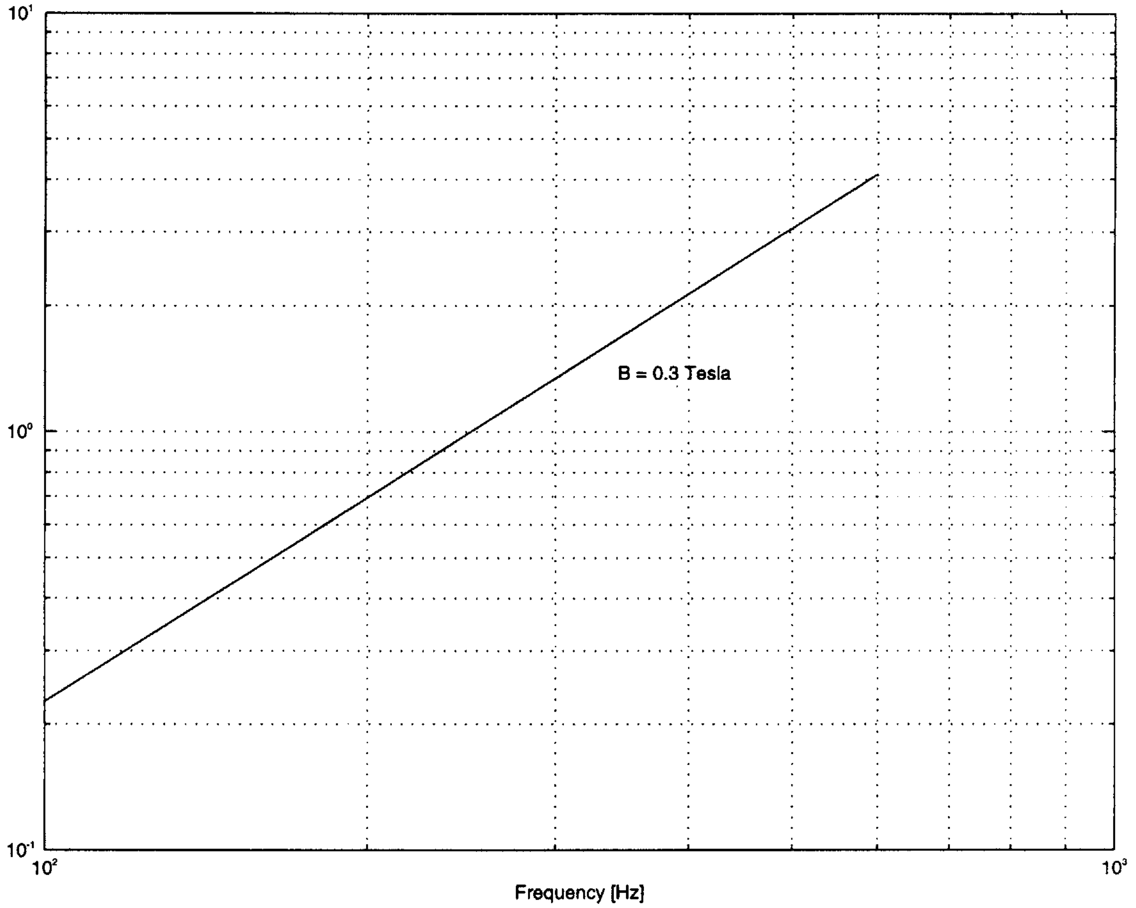

Figure 3.11: Core loss model for M19 29-gauge electrical steel.

$$B_t = (1 - \lambda_s)B_{ag} \tag{3.64}$$

assuming all the airgap flux is collected by the teeth. The average back-iron flux density is

$$B_{db} = \frac{\pi r}{2pd_b}B_{ag} \tag{3.65}$$

Using (2.1) and (2.2) as inputs to the core loss function (2.3) and the total tooth and back iron masses m_t and m_{db} the tooth and back iron core losses P_t and P_{db} are determined

$$P_t = m_t p_B \left(\frac{\omega_e}{\omega_B}\right)^{\varepsilon_f} \left(\frac{B_t}{B_B}\right)^{\varepsilon_B} \tag{3.66}$$

$$P_{db} = m_{db} p_B \left(\frac{\omega_e}{\omega_B}\right)^{\varepsilon_f} \left(\frac{B_{db}}{B_B}\right)^{\varepsilon_B} \tag{3.67}$$

The total machine core loss can then be calculated as

$$P_c = P_{db} + P_t \tag{3.68}$$

The final loss mechanism considered here is slot-induced harmonic core losses. These losses are present because the airgap flux harmonics induced by the stator teeth openings result in surface eddy currents and alternating fields in the rotor lamination surface. A model is employed here which estimates the harmonic magnitude from the slot opening dimensions, and then estimates their penetration into the rotor surface using approximations for the core surface conductivity, σ_c. The development here follows [30] directly.

First the slot opening angle is calculated

$$\theta_o = \frac{w_o n_s}{r} \tag{3.69}$$

The slot harmonic flux density magnitude and frequency are

$$B_h = B_{ag} \frac{2}{\pi} \sin\left(\frac{\theta_o}{2}\right) \tag{3.70}$$

$$\omega_h = \omega \frac{n_s}{p} \tag{3.71}$$

where ω is the mechanical rotation frequency. This sets up an electric potential and surface current on the rotor

$$E_z = \frac{r \omega_h B_h}{p} \tag{3.72}$$

$$|K_z| = \left|\frac{E_z}{Z_s}\right| \tag{3.73}$$

$$|Z_s| = \sqrt{R_s^2 + X_s^2} = \sqrt{R_s^2 + \left(\frac{R_s}{2}\right)^2} \cong 1.116R_s \tag{3.74}$$

where Z_s is the surface impedance of the rotor, and R_s is the associated surface resistance. R_s is defined as

$$R_s = \frac{16}{3\pi\sigma_c\delta_c} \tag{3.75}$$

where δ_c is the rotor skin depth and σ_c is the conductivity of the iron. The skin depth can be approximated by

$$\delta_c = \sqrt{\frac{2B_0}{\omega_h\sigma_c|K_z|}} \tag{3.76}$$

where B_0 is 75% of the core saturation flux density. Substituting the definition of R_s into the definition of $|Z_s|$ gives

$$\delta_c = \sqrt[3]{\frac{3.790B_0}{\sigma_c^2\omega_h E_z}} \tag{3.77}$$

The slot harmonic loss component can then be expressed as

$$P_{sh} = 2\pi rl\frac{|K_z|^2}{\sigma_c\delta_c} \cong 1.75rl\sigma_c\delta_c E_z^2 \tag{3.78}$$

3.2.5 Electrical and Mechanical Port Conditions

The power balance model for the IPM machine is given by

$$P_{elec} = P_{shaft} + P_a + P_c + P_{sh} \tag{3.79}$$

where electrical power, P_{elec}, is defined is defined as positive into the machine, and the shaft power, P_{shaft}, is positive for motoring operation. The term shaft power is used to refer to the actual power delivered to the physical shaft as shown graphically in Figure 3.12. During generating operation, therefore, $P_{elec} < 0$. P_{shaft} is defined as

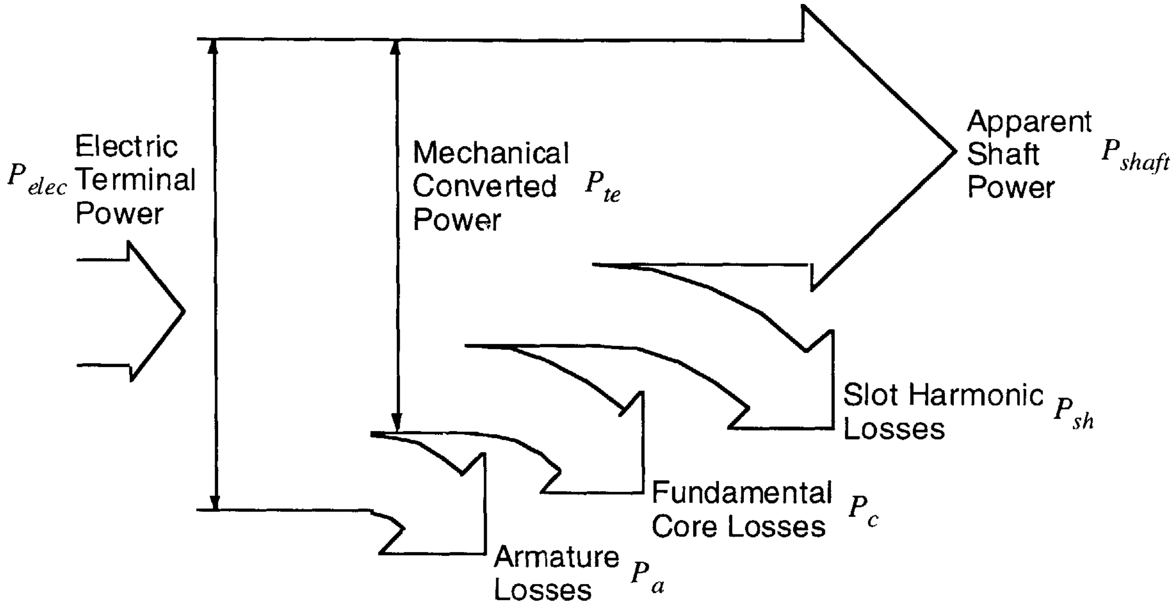

Figure 3.12: Rotating machine power flow (motoring reference direction).

$$P_{shaft} = T_{shaft}\omega \tag{3.80}$$

where T_{shaft} is the torque actually transferred through the rotating shaft. The other power reference of interest is the mechanical converted power, P_{te}, which results directly from the conversion of energy from the electrical terminals and is defined as

$$P_{te} = T_e\omega \tag{3.81}$$

The torque of electric origin, T_e, is a well-defined quantity in electric machine theory [11]. This concept was introduced in the previous chapter, but the general formula in the *dq*-frame is repeated here as

$$T_e = qp\left(\Psi_d I_q - \Psi_q I_d\right) \tag{3.82}$$

where the d and q axis flux linkages, Ψ_d and Ψ_q, are defined as

$$\Psi_d = \lambda_{PM} + L_d I_d \tag{3.83}$$

$$\Psi_q = L_q I_q \tag{3.84}$$

which include an implicit assumption that magnetic cross-coupling is negligible. Substituting back into the equation for torque, the convenient formulation for IPM machines is repeated here as

$$T_e = qp\left(\lambda_{PM} + \left(L_q - L_d\right)I_d\right)I_q \tag{3.85}$$

In general the inductances, L_d and L_q, can be functions of the electrical excitation, I_d and I_q, but for this linear, non-saturating, IPM machine model it is assumed that they are constants as defined in the previous sections. Another convenient form of the torque relationship is

$$T_e = qp\left(\lambda_{PM} + \left(S_r - 1\right)L_d I_d\right)I_q \tag{3.86}$$

Using the definition of λ_{PM} developed in the previous sections, the energy conversion of the IPM machine is fully specified as a function of the *dq*-frame electrical inputs.

As introduced in the previous chapter, the *dq*-excitation is synthesized by the machine controller which acts through the power electronic converter connecting the supply to each machine phase. For balanced excitation, the electric power input is

$$P_{elec} = qV_a I_a \cos(\phi) \tag{3.87}$$

where V_a is the RMS phase terminal voltage and $\cos(\phi)$ is the power factor. Using phasor notation with the motoring reference convention [11], the AC voltage terminal relation is then

$$\overline{V}_a = R_a \overline{I}_a + jX_d \overline{I}_d + jX_q \overline{I}_q + \overline{E}_a \tag{3.88}$$

where the *d* and *q* axis reactances are

$$X_d = \omega_e L_d \tag{3.89}$$

$$X_q = \omega_e L_q \tag{3.90}$$

and the back-emf is

$$E_a = \omega_e \lambda_{PM} \tag{3.91}$$

For reference, the airgap voltage is

$$\overline{V}_{ag} = \left(R_a + j\omega_e L_l\right)\overline{I}_a + \overline{E}_a \tag{3.92}$$

3.2.6 Machine Drive Operating Capability

With the IPM machine parameters established by a machine design (λ_{PM}, L_d, and either L_q or S_r) and with specified maximum converter ratings (V_0 and I_0), the drive system capabilities can be determined. Performance calculations are made for motoring operation using reasonable approximations for low-speed at rated torque. Then performance during generating operation is presented with particular attention paid to constant-power operation over an extended speed range. Throughout the development windage and friction are neglected as they are more a function of the machine installation and not germane to distinguishing the characteristics of different machine designs of similar geometry that are considered for the same application.

For motoring operation the metrics of interest are the maximum torque and the associated efficiency versus speed for a given IPM machine drive design. The efficiency is simply defined as

$$\eta_m = \frac{P_{shaft}}{P_{elec}} = 1 - \frac{P_a + P_c + P_{sh}}{P_{elec}} \tag{3.93}$$

At low speeds the core and slot harmonic losses are negligible since they are exponentially related to the excitation frequencies, so that

$$T_{shaft} \cong T_e \tag{3.94}$$

$$\eta_m \cong \frac{P_{te}}{P_{elec}} = 1 - \frac{P_a}{P_{elec}} \tag{3.95}$$

For torque calculations there are three operating modes as outlined in the previous chapter [7, 15]: Mode I (Constant Torque), Mode II (Constant Current and Voltage), and Mode III (Constant Voltage). That discussion was based on lossless machine analysis with no armature resistance or leakage. Though the leakage does not affect the torque production normally it does affect the voltage limit ellipse at a given speed. The predicted corner speed diverges somewhat from the ideal as the voltage limit is approached because the armature resistance effectively lowers the available voltage. Above the voltage-limited corner speed this is even truer because increasing leakage reactances further reduce the airgap voltage thus altering the power and speed range in the constant-power speed region.

Focussing again on the low speed rated torque operation, the Mode I maximum torque per ampere equations are presented as follows. For convenience, per-unit current and flux linkage base quantities are defined as [30]

$$I_B = I_0 \tag{3.96}$$

$$\lambda_B = \lambda_{PM} \tag{3.97}$$

and the base torque is given by

$$T_b = qp\lambda_B I_B \tag{3.98}$$

Using (2.9), (2.2), (2.5), and (3.98), the definitions of normalized variables for the *dq* inductances, currents, and torque are developed as follows

$$x_d = \frac{L_d I_B}{\lambda_B} \tag{3.99}$$

$$x_q = \frac{L_q I_B}{\lambda_B} \tag{3.100}$$

$$i_d = \frac{I_d}{I_B} \tag{3.101}$$

$$i_q = \frac{I_q}{I_B} \tag{3.102}$$

$$i_a = \sqrt{i_d^{\,2} + i_q^{\,2}} \tag{3.103}$$

$$t_e = \left(1 - \left(x_q - x_d\right) i_d\right) i_q \tag{3.104}$$

Expressions for the *dq* current components that maximize the per-unit torque, t_e, for a given per-unit current, i_a can be developed using (2.4), (3.100), (3.103), and (3.104) under the assumption of no magnetic saturation (i.e. the per-unit reactances are constant). The resulting current expressions are

$$i_d = -\sqrt{\frac{i_a^{\,2}}{2} + 2\left(\frac{1}{4\left(x_q - x_d\right)}\right)^2 - \frac{1}{2\left(x_q - x_d\right)}\sqrt{\left(\frac{1}{4\left(x_q - x_d\right)}\right)^2 + \frac{i_a^{\,2}}{2}}} \tag{3.105}$$

$$i_q = \sqrt{\frac{i_a^{\,2}}{2} - 2\left(\frac{1}{4\left(x_q - x_d\right)}\right)^2 + \frac{1}{2\left(x_q - x_d\right)}\sqrt{\left(\frac{1}{4\left(x_q - x_d\right)}\right)^2 + \frac{i_a^{\,2}}{2}}} \tag{3.106}$$

The electrical terminal conditions associated with the rated current vector can now be calculated. The unsaturated Mode I operating point is found by substituting $i_a = 1$ into (3.105) and (3.106), and then solving for the Mode I current vector $\left(I_{d0}, I_{q0}\right)$ using (3.101) and (2.4). The terminal voltage components are found from the derivatives of (2.5) and (2.2) at a given electrical operating frequency ω_e, and the resistive drop as

$$V_q = \omega_e\left(\lambda_{PM} + L_d I_d\right) + R_a I_q \tag{3.107}$$

$$V_d = -\omega_e L_q I_q + R_a I_d \tag{3.108}$$

The terminal voltage is then

$$V_a = \sqrt{V_d^2 + V_q^2} \tag{3.109}$$

Figure 3.13 graphically shows the definition of the torque angle,

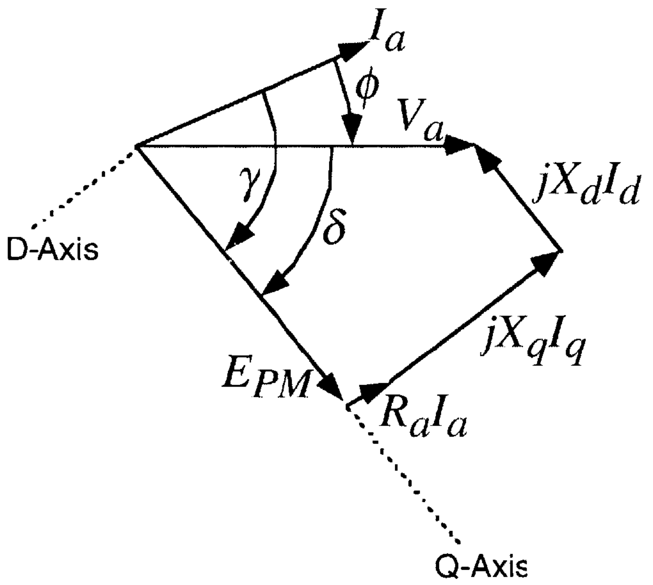

Figure 3.13: Phasor diagram during motoring.

$$\delta = \tan^{-1}\left(\frac{V_d}{V_q}\right) \tag{3.110}$$

the current control angle,

$$\gamma = \tan^{-1}\left(\frac{I_d}{I_q}\right) \tag{3.111}$$

and the power factor angle

$$\phi = \gamma - \delta \tag{3.112}$$

ϕ is defined positive counterclockwise from I_a to V_a while δ is defined positive counterclockwise from V_a to E_a. The motoring reference direction is used throughout so that

$$\mathrm{mod}(\phi) \equiv \begin{cases} -\frac{\pi}{2} < \mathrm{mod}(\phi) < \frac{\pi}{2} & \textit{motoring} \\ \frac{\pi}{2} < \mathrm{mod}(\phi) < \pi; -\pi < \mathrm{mod}(\phi) < -\frac{\pi}{2} & \textit{generating} \end{cases} \tag{3.113}$$

where $\mathrm{mod}(\;)$ is the modulo operator defined for the range specified.

The electrical frequency at the corner speed, ω_0, is calculated by setting $V_a = V_0$, substituting back into (3.107), (3.108), and (3.109), and solving for the frequency. The solutions are used in (3.107) through (3.112) to define the remaining electrical terminal variables at the corner speed using the subscript '0' as V_{d0}, V_{q0}, δ_0, and ϕ_0. Of course at the Mode I operating point $\gamma = \gamma_0$ for all $\omega_e \le \omega_0$.

Unlike motoring, the generating capability is an iterative solution. For motoring, maximizing torque simultaneously maximizes the efficiency, whereas for generating, there is no closed-form solution and so maximizing the real power delivered requires searching the current space (I_a, ϕ) for achievable solutions and then selecting the one that minimizes the required T_e input. The generating efficiency is defined as

$$\eta_g = \frac{P_{elec}}{P_{shaft}} = 1 - \frac{P_a + P_c + P_{sh}}{P_{shaft}} \tag{3.114}$$

In this case P_c and P_{sh} are not negligible assuming that generating operation occurs at relatively high speeds. Figure 3.14 shows a typical phasor diagram during generation. Note that the motoring convention is retained.

As noted above, determining the electrical terminal conditions and power capability at a given speed is an iterative solution. It is a constrained optimization problem in three variables. The selection of variables is somewhat arbitrary but it is reasonable to choose variables with a well-defined generating solution range such as γ, δ, and I_a. The appropriate ranges are

$$\begin{aligned}&0 < \delta \le \frac{\pi}{2}\\&-\pi \le \gamma < -\frac{\pi}{2} - \delta\\&0 < I_a \le I_0\end{aligned} \tag{3.115}$$

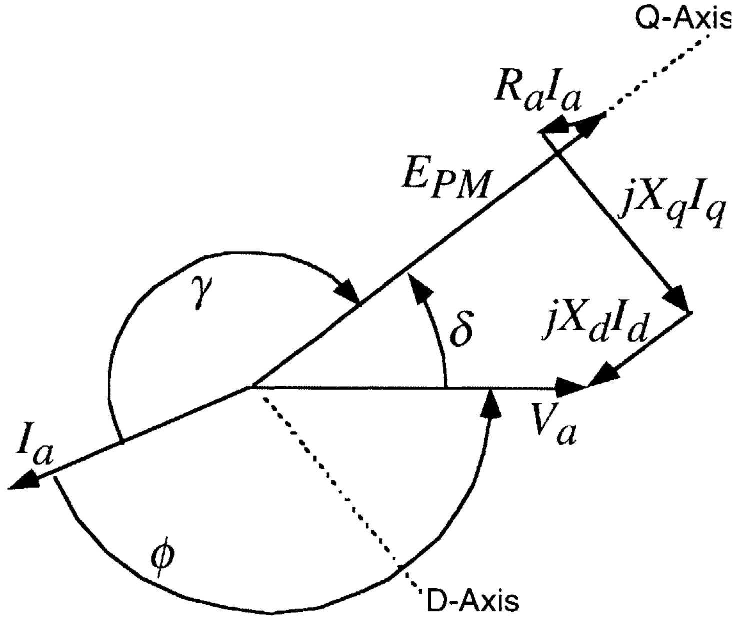

Figure 3.14: Phasor diagram during generation.

At a given speed and excitation frequency, ω_e, the constrained problem of maximizing the generated power to determine generating capability at a given speed can be addressed by solving (2.4), where E_a, X_d, X_q, and R_a are known and I_d, I_q, and $\angle E_a$ are functions of γ, δ, and I_a. The solution, V_a, is constrained by

$$0 < V_a \le V_0 \tag{3.116}$$

where the voltage vector has been selected for convenience as the reference, aligned with the positive horizontal axis $\angle V_a = 0$.

The problem becomes two-dimensional if, instead of power maximization, the objective is to deliver a specific output power with maximum efficiency. But of course, there will now be no guarantee of a solution for a given P_{elec} requirement. The subject of finding an electrical terminal solution in generation is revisited during the discussion of design optimization in Chapter 7.

3.3 Saturable LPM (Nonlinear Core, Saturated Bridges)

Section 3.2 presented a complete analytical model for an IPM machine drive using the assumption of linear materials. In the linear LPM, the rotor steel bridges were modeled with constant saturation (constant flux sources) and the remainder of the core as infinitely permeable (i.e. unsaturated). This section seeks to extend the linear LPM by incorporating the effects of magnetic saturation using a nonlinear permeability model for the bulk of the core. This provides a more accurate prediction of the lumped parameters and performance for high-performance machine design.

Nonlinear saturation effects will only be modeled for calculation of the q-axis inductance. This has been demonstrated as the chief source of modeling and performance prediction errors by the experimental results from other researchers outlined in Chapter 2 [9, 25, 36, 45, 51]. The assumption of constant saturation in the bridges is still employed in this saturable model which will be referred to as the saturable LPM.

3.3.1 Saturable Q-Axis Inductance

For high-performance applications the exciting mmf is likely to drive the q-axis into the saturation region of the core material. To accurately predict L_q under rated magnetic load, a saturating model of the magnetizing component is proposed here. As introduced in the previous chapter, an appropriate model for multiple-barrier IPM machines uses I_q as the driving mmf source for saturation. Previous research also concluded that cross-coupling from the d-axis magnets and stator excitation is less significant in multiple-barrier machines except under heavy overload conditions or with skewed rotor designs [27, 36, 47-49].

The d-axis does not bulk saturate because each of the cavity layers contribute an additional flux barrier that prevents rated excitation from bulk saturation along the d-axis of the core. Since the permeability of each barrier is roughly that of air, the effective airgap seen by the d-axis is orders of magnitude higher than that seen by the q-axis. Therefore the excitation required for the onset of saturation in the d-axis would also be orders of magnitude higher. Therefore it does not naturally occur except under extreme overload conditions. As noted in the development of the linear LPM, though, the bridges around the tips of the magnet cavities are expected to saturate heavily and that local saturation is reflected in the models.

Cross-coupling, as noted above, is assumed negligible. The mechanisms of cross-coupling are varied and depend on the particular geometry being considered. The relative impact is influenced by the number of layers, overloading, and rotor skew and is treated in-depth in [27, 36, 47-49]. It is assumed to be insignificant for the IPM rotor geometries investigated in this thesis because they are multiple-barrier rotors without skewing. Significant overload current along the q-axis could saturate the bulk regions of the core with the effect of reducing the d-axis flux linked by the stator; both the λ_{PM} and $L_d I_d$ components. This would occur because the heavily saturated core would appear as an additional flux barrier along the d-axis. The excitation levels required are beyond what optimized designs should experience since there would be limited performance improvement for the incremental excitation increases at heavily saturated flux levels.

First, the linear equivalent circuit corresponding to the development in Section 3.2.2 is reviewed in the context of developing more complex nonlinear circuits. Then an equivalent magnetic circuit comprising nonlinear core reluctance elements, linear airgap reluctance elements, and linear mmf sources is presented. Finally the general iterative solution and benchmarking techniques are presented.

In Section 3.2.2 the q-axis magnetizing inductance L_{qm} is calculated from the round-rotor synchronous inductance L_{ag} and given by (2.5) and (2.2). Equation (2.5) shows that L_{ag} is inversely proportional to a linear model of the airgap reluctance $\mathcal{R}_{ag}$ that can be expressed as

$$\mathcal{R}_{ag} = \frac{g'}{\mu_0 l r} \tag{3.117}$$

Figure 3.15 shows the q-axis equivalent magnetic circuit of this linear LPM where $\mathcal{F}_{qs}$ is the fundamental rms mmf stator excitation applied along the q-axis and Φ_q is the corresponding q-axis flux. Given the rms phase current I_a, the mmf source $\mathcal{F}_{qs}$ is calculated using the equivalent sinewave series turns $N_a k_{a1}$ according to

$$\mathcal{F}_{qs} = \frac{q}{2}\left(\frac{4}{\pi}\right)\frac{N_a k_{a1}}{p^2} I_q \tag{3.118}$$

The magnetic circuit in this figure can be solved for the q-axis magnetic flux Φ_q to give

$$\Phi_q = \frac{\mathcal{F}_{qs}}{\mathcal{R}_{ag}} = \frac{q}{2}\left(\frac{4}{\pi}\right)\frac{\mu_0 N_a k_{a1} l r}{p^2 g'} I_q \tag{3.119}$$

Multiplying by $N_a k_{a1}$ leads to an expression for the q-axis magnetizing flux linkage λ_{qm} expressed as

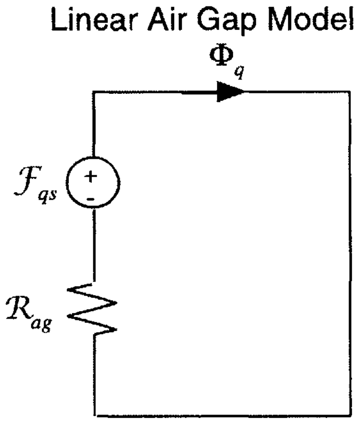

Figure 3.15: Linear q-axis equivalent magnetic circuit (linear LPM).

$$\lambda_{qm} = N_a k_{a1} \Phi_q = \frac{q}{2}\left(\frac{4}{\pi}\right)\frac{\mu_0 N_a{}^2 k_{a1}{}^2 lr}{p^2 g'} I_q \tag{3.120}$$

and to an expression for the q-axis magnetizing inductance

$$L_{qm} = \frac{\lambda_{qm}}{I_q} = \frac{q}{2}\left(\frac{4}{\pi}\right)\frac{\mu_0 N_a{}^2 k_{a1}{}^2 lr}{p^2 g'} \tag{3.121}$$

which is identical to (2.9). This alternative derivation demonstrates the equivalent magnetic circuit methods that are now used for the nonlinear q-axis inductance model.

The implied assumptions for the linear LPM are that the full rotor periphery links q-axis flux and that the mmf drops in the iron are insignificant. This section improves on this model by accounting for changes in the mmf potential in the core material. This is particularly important in the rotor where the flux must be concentrated to flow along the narrow sections of rotor steel separated by the magnet cavities. By contrast, the main flux along the d-axis is not generally concentrated and flows across the whole pole face and must cross each magnet cavity after saturating the rotor steel bridges.

At high levels of q-axis stator excitation, therefore, it is reasonable to assume the rotor steel segments become saturated where the flux paths are most constricted as shown in Figure 3.16. Using a double-layer IPM machine to illustrate, areas with some degree of magnetic saturation are shaded, and the main q-axis flux is sketched using dashed lines. Bulk saturation is likely to occur in Sections 1 and 2 as shown, but is less likely in Section 3 where the pole piece cross-sectional area is large and the coincident q-axis mmf source across the airgap is nearly zero.

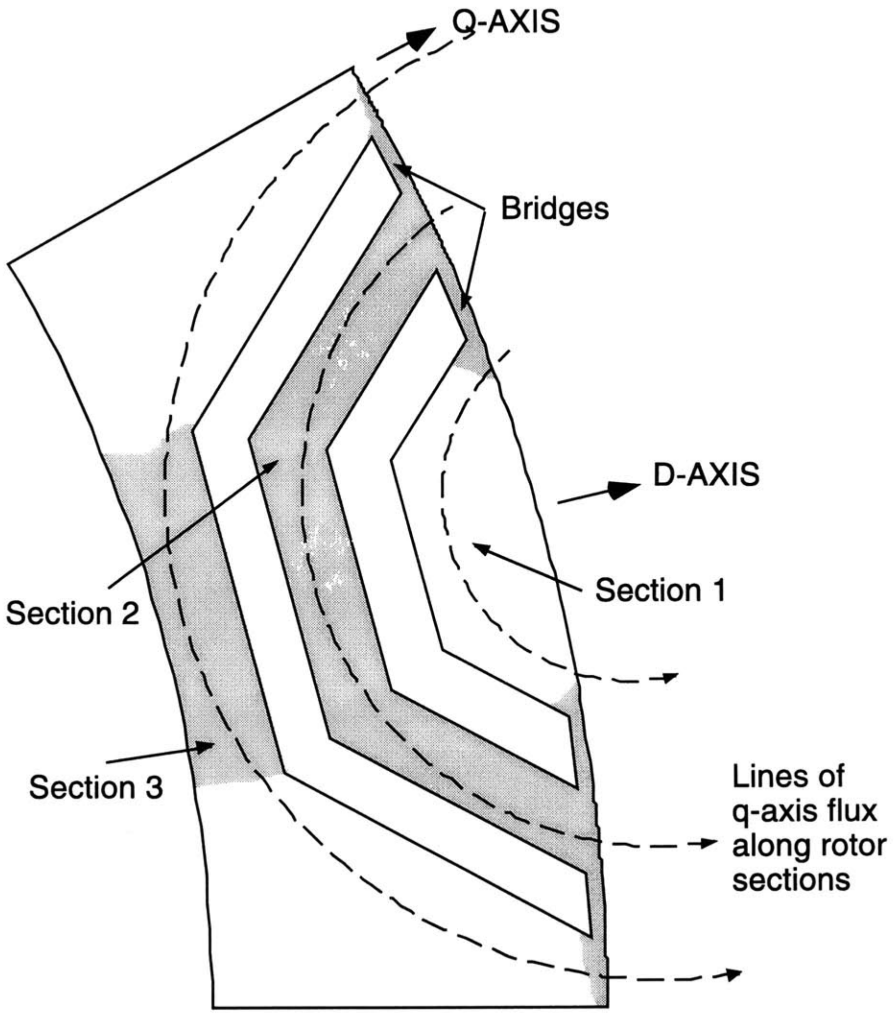

Figure 3.16: Sketch of magnetically-saturated regions in the rotor (shaded) under rated q-axis excitation.

Along the direction of q-axis flux, the reluctance of the partially-saturated rotor surface is insignificant compared to the long and narrow sections behind each magnet cavity and centered on the d-axis. In particular, assuming parallel cavities, the inter-cavity sections should saturate to some degree along their full length. Saturation in the innermost section, between the rotor ID and the innermost cavity, depends highly on the geometry of the section. As shown, Section 3 becomes significantly wider near the q-axis symmetry boundary while carrying the same flux. As a result, this region would not be expected to saturate to the same degree as the portion of Section 3 directly behind the cavity-centered on the d-axis.

Cavity designs that are nearly parallel to the q-axis line of symmetry, as the cavity approaches the rotor OD, will be more likely to saturate along the full length of the rotor section. As was the case with the linear model, it is assumed that flux enters along the full periphery of the rotor despite saturation around the tips of the magnet. The particular geometry of the bridge design and the level of d-axis excitation will affect the accuracy of this assumption.

A q-axis equivalent magnetic circuit that models the principal areas of magnetic saturation is now described. The paths of q-axis flux are modeled using lumped reluctance elements, similar to the approach used with the linear LPM. However, now the reluctances are nonlinear to represent the variable degree of saturation in each modeled core section.

The nonlinear functions for the saturable q-axis reluctances are based on the core material's nonlinear magnetic characteristics. Figure 3.17 shows the DC magnetization curve for 29-gage M19 electrical steel, a typical high-performance machine laminated core material. By contrast, Figure 3.18 depicts a number of analytic models for the core material. The simplest model, the infinitely permeable model, implies that the electromagnetic behavior of the machine is dominated by the airgap, and the equivalent airgaps introduced by any magnets in the flux path, and so can be represented simply by a reduced order constant reluctance network. If there are no magnets in the main flux paths, the equivalent circuit model is reduced to a single airgap reluctance element. The linear model is a slight variation on this, but requires that each of the main core paths is represented by a constant reluctance. Textbook models often start from this point and build complexity for the effects such as non-smooth airgaps, non-sinusoidally distributed windings.

But as Figure 3.17 shows, at higher excitation levels the permeability is reduced dramatically, approaching that of air, as the material enters into magnetic saturation. This implies, that higher performance machine designs, those with higher exciting current densities and torque capabilities are going to drive the core material into some degree of saturation. Saturation onsets locally, usually the stator teeth, and as excitation is increased further more of the core cross-section goes into bulk saturation. So for higher performance machine design, some of the alternative analytic models are often employed. The limited flux model can be coupled with either the infinite or linear model. This results in a conservative model that prevents the designer from overestimating capability at higher excitation levels. The piecewise constant model is a slight variation on this that sets the incremental permeability to that of air above the saturation flux density. This of course requires two models for each reluctance element of the equivalent magnetic circuit and a decision for which model to use.

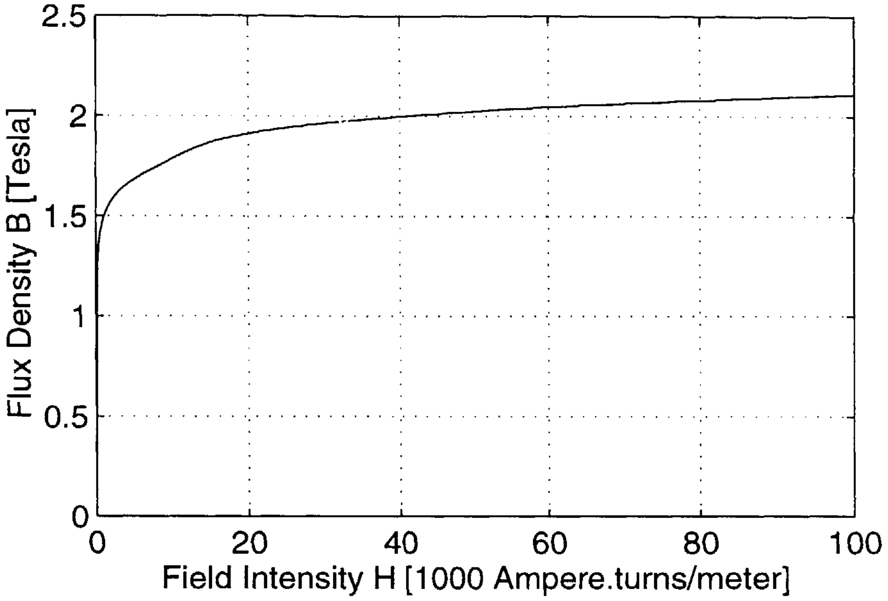

Figure 3.17: DC magnetization, or BH, curve for 29-gage M19 electrical steel.

For this reason, the nonlinear core magnetic characteristic is modeled by a nonlinear curve fit to the steel's BH data. The curve is represented in the saturable LPM by the core's total permeability at a particular point (H,B) on the magnetization curve

$$\mu = \mu(B) \equiv \frac{B}{H} \tag{3.122}$$

The saturable reluctance in the i^{th} section of the core is then

$$\mathcal{R}_i = \frac{l_i}{\mu(B_i)A_i} \tag{3.123}$$

where l_i, B_i, and A_i are the average length in the magnetic field line direction, the average flux density, and the average cross-sectional area normal to the field.

The particular choice of nonlinear equivalent circuit presents many more opportunities for trading off complexity and accuracy in modeling L_q. Figure 3.19 shows perhaps the simplest magnetically-saturable LPM in which the stator teeth, stator yoke, and the rotor yoke are each modeled by a single nonlinear reluctance. The rotor yoke is defined as the main flux-carrying segments in the rotor core (i.e. the rotor steel minus the magnet cavities and the bridges). As was the case with the linear LPM, the magnetizing q-axis inductance is found using the general method demonstrated in (3.117) through

(3.121), now using the nonlinear reluctance definition (3.123) for the core elements. Since B_i is initially unknown for each nonlinear reluctance, the solution process is iterative and converges as the mmf drops around the loop approach the source mmf $\mathcal{F}_{qs}$.

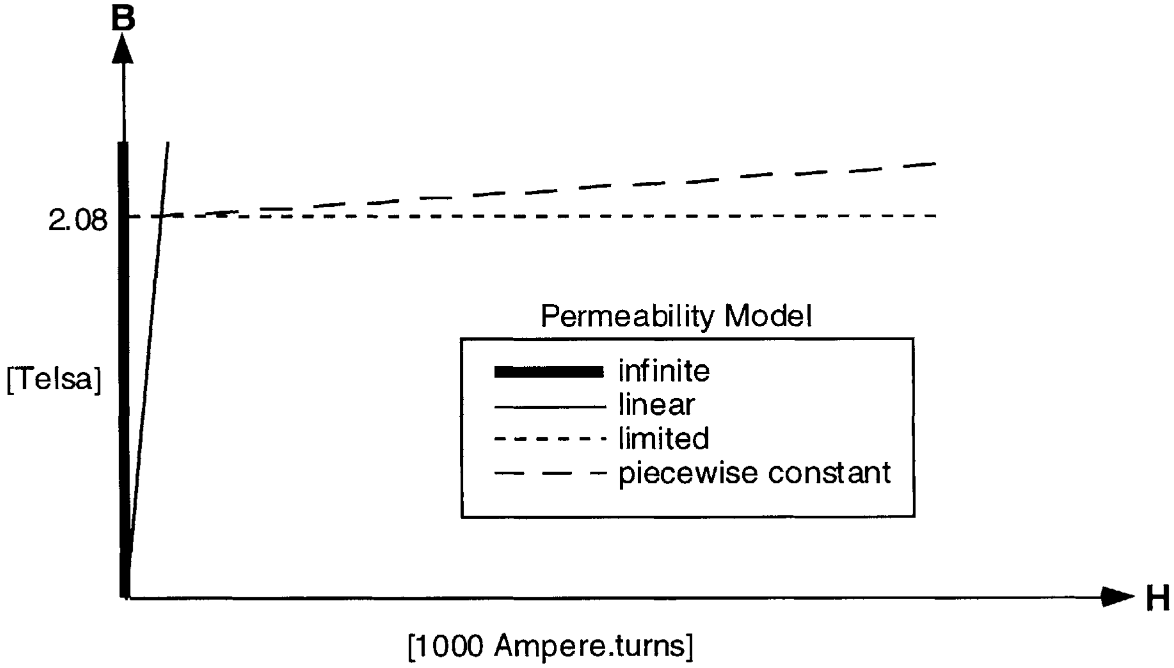

Figure 3.18: Analytic BH core models differentiated by their slopes (permeability).

The next step in this model development takes into account the irregular geometry of the rotor as shown in Figure 3.20. Compared to the magnetically-salient rotor geometry, the stator teeth are all uniform and can therefore be reasonably modeled by their average flux-carrying capabilities. More specifically, the slot fraction λ_s is constant for all teeth of the stator but the rotor core path width d_{rk} behind each magnet may be different. Note in this model, that rotor bridge reluctances have been shown. It is reasonable, though, to neglect the bridge reluctance as little flux would be expected in the θ direction along the bridges since the q-axis fields should be primarily orthogonal to those paths.

With this model, some assumptions must be made regarding the magnetic potential on the rotor side of the airgap. Since an average potential is required for each rotor reluctance terminal, an appropriate method is to integrate the sinewave excitation function along the airgap to obtain the k^{th} average rotor potential as follows

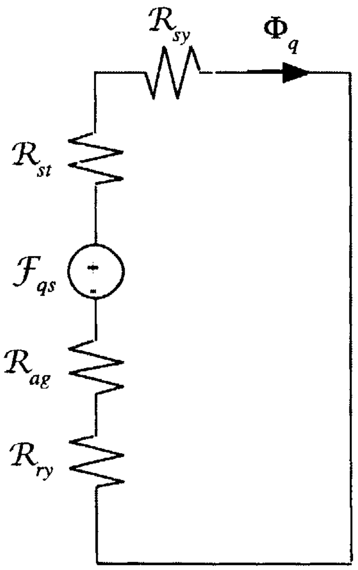

Figure 3.19: Average nonlinear q-axis equivalent magnetic circuit.

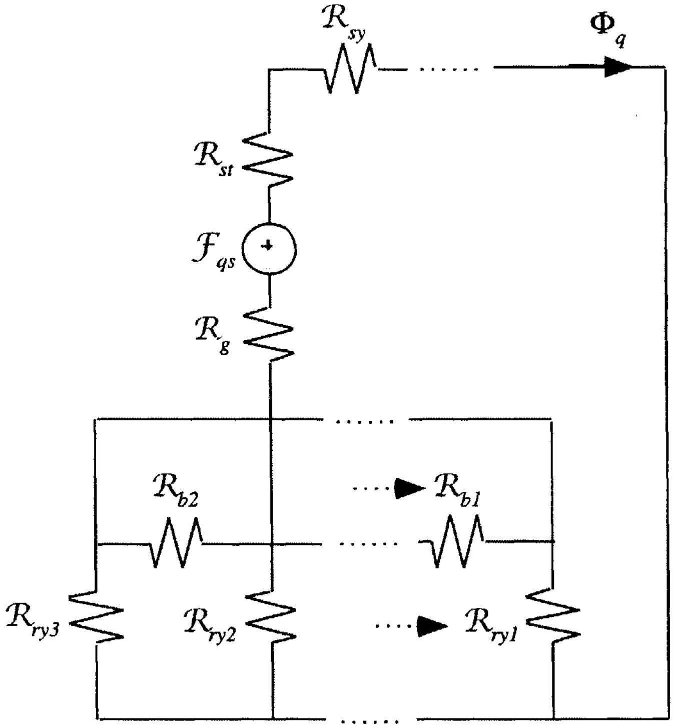

Figure 3.20: Stator-averaged nonlinear q-axis equivalent magnetic circuit.

$$\mathcal{F}_{ryk} = \frac{1}{\alpha_k - \alpha_{k-1}} \int_{\alpha_{k-1}}^{\alpha_k} \left(\left(\mathcal{F}_{qs} - \mathcal{R}_g \Phi_q \right) \sin\alpha \right) d\alpha \tag{3.124}$$

Again, the analysis of this nonlinear network is iterative following the same general procedure.

Figure 3.21 shows a more complex reluctance model of the stator. In this model, the stator is partitioned in a manner similar to the rotor. It is assumed that the magnetic flux is carried in a single flux tube from each rotor segment through the teeth to the stator back iron. Each section of the back iron collects flux from a sum of the rotor flux tubes with the back iron segment positioned on the d-axis line of symmetry carrying all of the q-axis flux. This model is particularly appropriate for heavily-saturated designs because it models the situation when the design of one segment saturates at a lower rms excitation level than the other segments. This effectively chokes that flux tube and results in redistribution of the total q-axis flux to the other tubes thus affecting their respective levels of saturation.

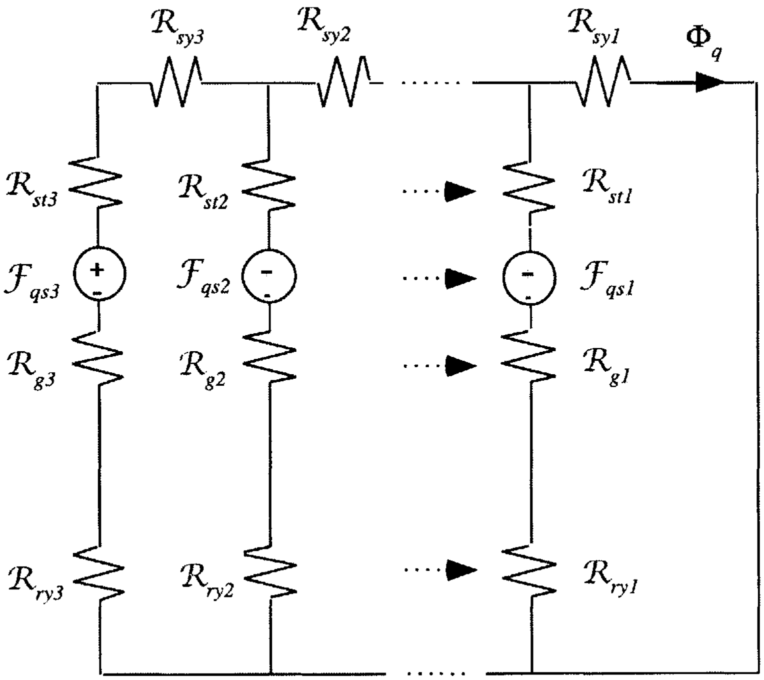

Figure 3.21: Parallel nonlinear q-axis equivalent magnetic circuit.

Figure 3.22 shows the magnetic circuit of Figure 3.21 as it appears for a double-layer IPM machine. Like the previous nonlinear models, this LPM is also solved iteratively for the flux along each branch using the same general procedure. The relative computational time for solution convergence of this model is only incrementally longer than for the other proposed nonlinear models in Figure 3.19 and Figure 3.20. This is in direct contrast to the significant solution time difference between the simplest nonlinear model and the linear q-axis model of Section 3.2.2.

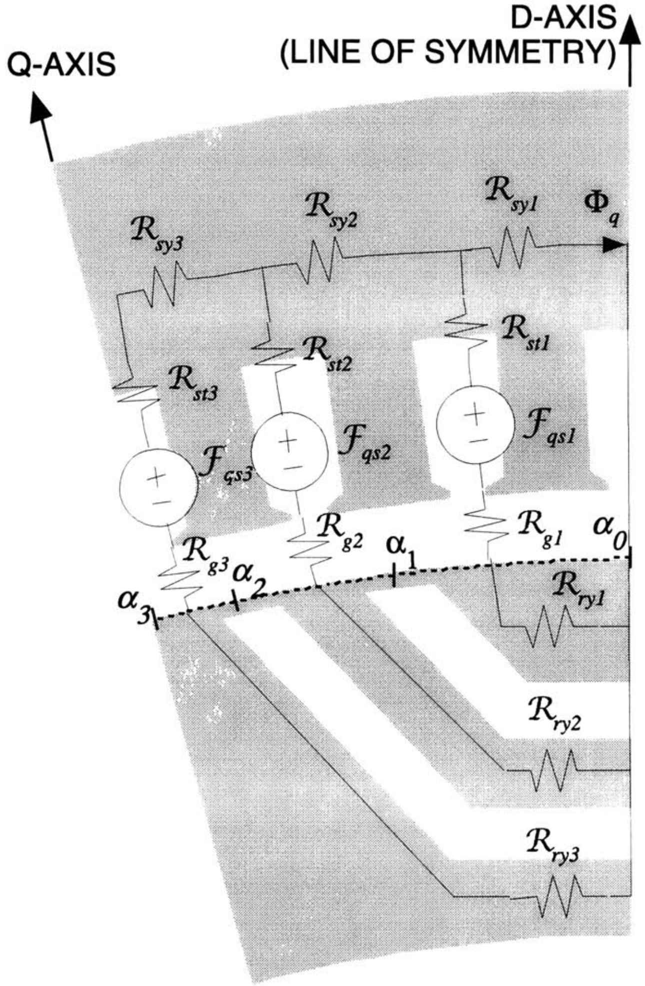

Figure 3.22: Parallel nonlinear q-axis equivalent magnetic circuit for double-layer IPM machine.

The nonlinear reluctances for this model are calculated using (3.123). The element lengths are defined as the average length through each segment and are shown in Figure 3.23. The k^{th} tooth area is

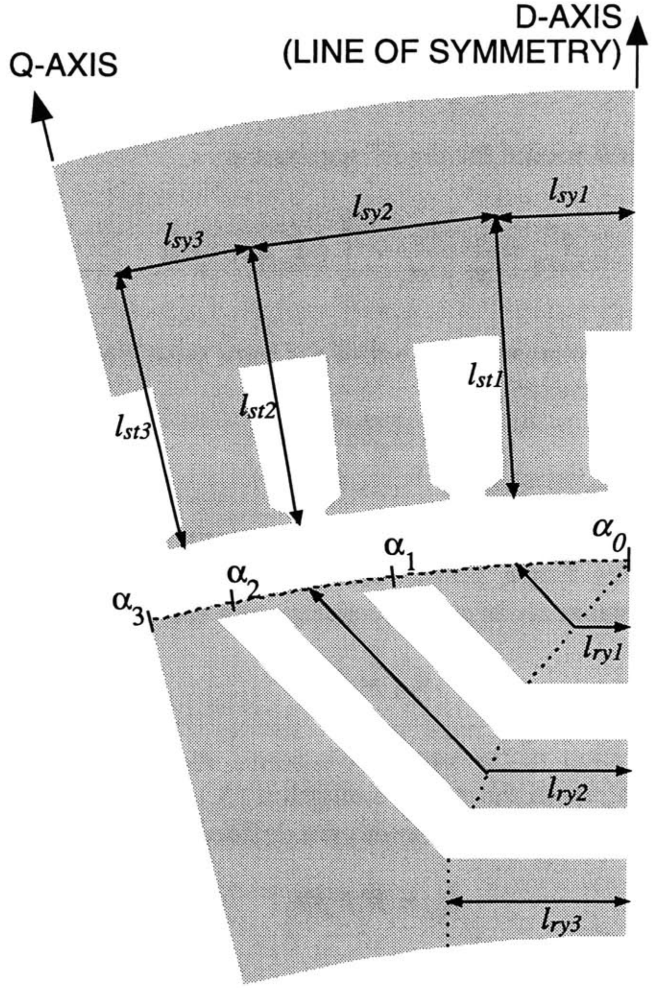

Figure 3.23: Segment length definitions for nonlinear core reluctance elements.

$$A_{stk} = \lambda_t \Delta\alpha_k \left(r + \frac{d_t + d_s + d_b/2}{2} \right) l \tag{3.125}$$

where use of the tooth fraction λ_t implies that all the airgap flux between angles α_{k-1} and α_k is collected uniformly and compressed to the tooth average width. The average tooth width is taken as the width at average of the stator airgap and mid-back iron radii. The stator yoke average area is

$$A_{syk} = A_{sy} = d_b l \tag{3.126}$$

The k^{th} segment airgap reluctance is

$$\mathcal{R}_{gk} = \frac{g'}{\mu_0(\alpha_k - \alpha_{k-1})rl} \tag{3.127}$$

The stator mmf excitation source for the k^{th} segment is

$$\mathcal{F}_{qsk} = \frac{1}{\alpha_k - \alpha_{k-1}} \int_{\alpha_{k-1}}^{\alpha_k} (\mathcal{F}_{qs} \sin\alpha) d\alpha \tag{3.128}$$

The average cross-sectional area of the outermost rotor yoke element on the rotor OD is

$$A_{ry1} = \left(\frac{\Delta\alpha_1 R + d_{r1}}{2} \right) l \tag{3.129}$$

The inter-cavity cross-sectional areas are constant along the full segment length assuming parallel cavities. For $r_{ri} >> l_{ryk}$, the width of the innermost segment at the rotor ID is approximately constant so its cross-sectional area can be approximated as

$$A_{ryk} = d_{rk} l \tag{3.130}$$

After constructing each of the circuit elements, the parallel nonlinear network is solved iteratively for Φ_q from the given excitation (3.118). For this saturable LPM, the saturable q-axis flux linkage and inductances are defined according to

$$\lambda_{qs} = N_a k_{a1} \Phi_q \tag{3.131}$$

$$L_{qms} = \frac{\lambda_{qs}}{I_q} \tag{3.132}$$

and the total q-axis inductance is

$$L_q = L_{qms} + L_l. \tag{3.133}$$

which replaces (3.33) from the linear LPM.

3.3.2 Differences with First-Order LPM

Section 3.3.1 above calculates L_q from a magnetically-saturable equivalent magnetic circuit for use as part of a complete LPM. The equations for calculating L_d, the losses, and the mechanical shaft conditions from Section 3.2 are employed again to complete the model.

The electrical terminal conditions under maximum torque-per-Amp control are different for the saturable LPM because (3.105) and (3.106) are only valid when the *dq* reactances are assumed constant. If the derivative of the torque expression (3.104) is taken with respect to i_a, there will now be additional terms for the variation of x_q with respect to i_q as shown below

$$\left.\frac{dt_e}{di_q}\right|_{i_a} = \left(1-\left(x_q - x_d\right)\sqrt{i_a^{\,2} - i_q^{\,2}}\right) + \left(\frac{i_q\left(x_q - x_d\right)}{\sqrt{i_a^{\,2} - i_q^{\,2}}}\right) i_q - \left(\frac{\partial x_q}{\partial i_q}\sqrt{i_a^{\,2} - i_q^{\,2}}\right) i_q = 0 \qquad (3.134)$$

The last term with the partial derivative does not exist in the linear LPM, and is due to the saturable magnetizing inductance L_{qms} that is now implicit in the definition of x_q. This means that the electrical terminal conditions for maximum motoring torque operation will require an iterative solution if saturation is to be accounted for using the models developed in this section. Furthermore, this adds another dimension of iteration in the solution of the generating mode electrical terminal conditions.

3.4 Effects of the Cavity Shape

The IPM rotor sketches shown to this point have only shown one cavity shape, but many possibilities exist and others may be more practical for structural and manufacturing reasons. The configuration for a single cavity layer depicted thus far comprises three straight segments with the middle segment symmetrically placed across the *d*-axis and the two side segments angled towards the rotor OD with reflected symmetry across the *d*-axis. This is a reasonable general model because it allows relatively simple calculation of the magnet geometry parameters, A_{mk} and l_{mk}. The three-segment cavity model also approximates a semi-circular cavity well. This is important because a semi-circular cavity is an easily manufacturable shape that is often employed [39, 40, 42]. If the included angle between the side and mid segments is varied this three-segment model can be used to analyze designs with any two magnets oriented in a V-shape or cavities where the side segments are parallel to the *q*-axis as shown in Figure 3.24 and Figure 3.25.

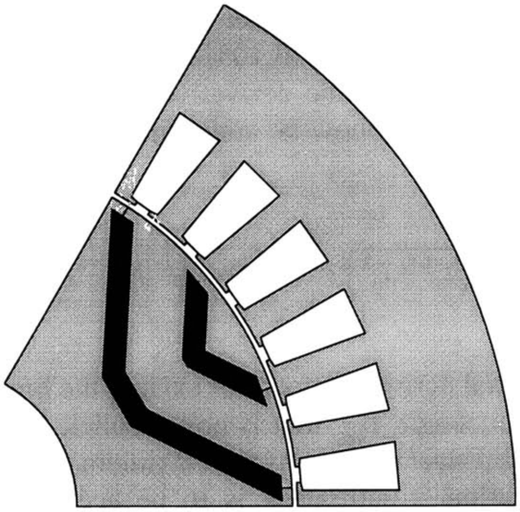

Figure 3.24: IPM machine with nearly V-shaped cavities.

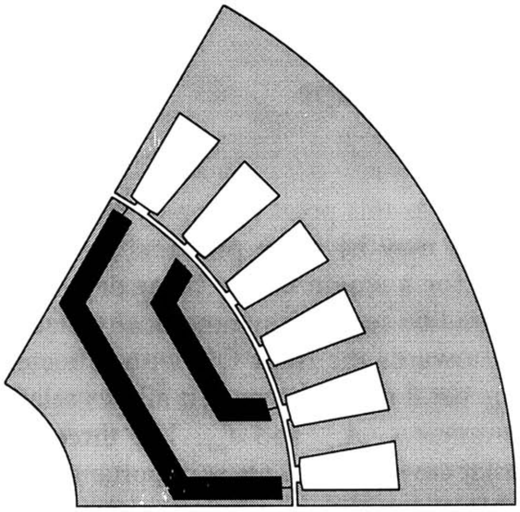

Figure 3.25: IPM machine with cavity side segments parallel to the q-axis.

Cavities that are not parallel to each other as shown in Figure 3.26 would make accurately modeling the saturable rotor reluctances more challenging because the cross-sectional area would vary along the full length of each rotor core section. This is not a typical cavity configuration and there is no apriori reason to expect desirable machine performance with such a design.

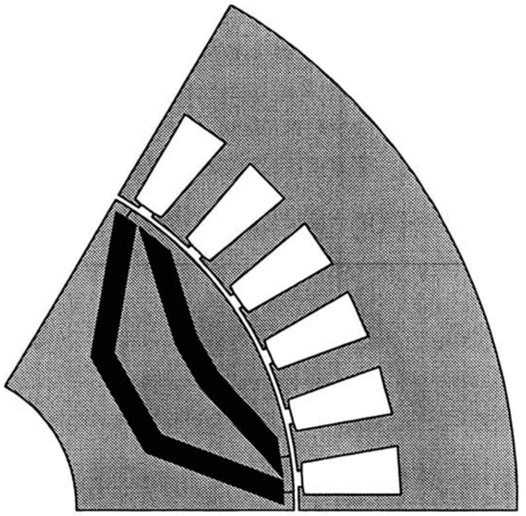

Figure 3.26: IPM machine with non-parallel cavities.

The shape of the cavity tips is often dictated by manufacturing and structural needs. A rounded cavity tip as shown in Figure 3.27 is a convenient design to laser cut that is considerably more stiff than the straight edge cavity tips. The shape of the cavity tip is important in both the linear and saturable LPMs as it affects the appropriate division between the main modeled flux paths designated by the angles α_i. An appropriate division is the point on the rotor periphery where the bridge width is smallest as shown in Figure 3.28. Compared to the straight-edged bridges, the α_i associated with rounded bridges are all shifted towards the *d*-axis. With all other machine dimensions held constant, this one change affects the calculation of L_d and λ_{PM} in the linear LPM by changing the calculations of per-unit mmfs f_{dsk} and the airgap cross-sectional areas A_{gk}. Changing the shape of the bridges also changes the calculation of L_q using the saturable LPM again primarily due to changes in the calculation of the A_{gk} areas.

Another impact, albeit a less significant one, is that the effective length of the bridge path for calculating L_d and λ_{PM} is no longer similar to the cavity depth. This impacts (3.46) where r_{mk} should be substituted with $r_{mk} \| r_{bk}$ for a more accurate calculation of L_d. r_{bk} is the per-unit reluctance of the bridges given by

$$r_{bk} = \frac{w_{bk} A_s}{g' A_{bk}} \tag{3.135}$$

where the effective length of the bridge l_{bk} must be estimated. For circular rounded bridges, $l_{bk} = w_{bk}$ is a reasonable estimate.

For IPM rotors that are designed for applications with even higher structural loading one or more posts are added across the larger cavity layers. With respect to the LPMs the posts represent additional flux paths that the magnets will saturate and so can be treated as together with the bridges. If a single central post on the k^{th} cavity is employed as shown in Figure 3.29 with width w_{ck}, the effective bridge width for the LPMs is

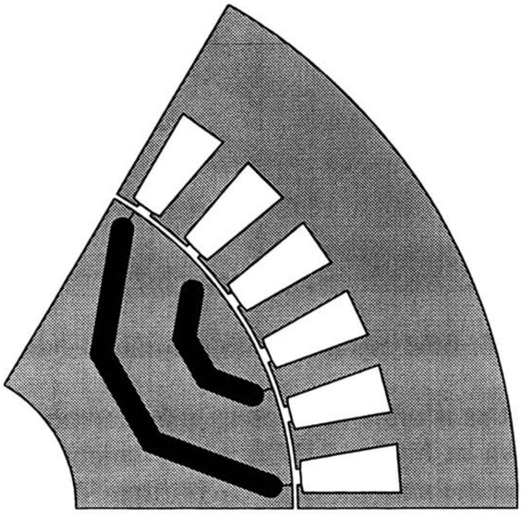

Figure 3.27: IPM machine with rounded cavity tips and therefore rounded bridges.

$$w_{bk} + \frac{w_{ck}}{2} \tag{3.136}$$

3.5 Summary

This chapter presented analytical design models for a transversely-laminated multiple-layer IPM machine drive. The models are all based on representing the machine drive through lumped parameter techniques. The lumped parameters are calculated from machine cross-section dimensions, material characteristics, the winding arrangement, and the drive ratings. The dq frame inductances are calculated using equivalent magnetic circuit techniques.

The linear LPM assumes that the rotor bridges are fully saturated and that mmf potential drops in the core are insignificant resulting in dq inductances that are linear functions of the corrected airgap g'. The saturable LPM accounts for bulk magnetic saturation in the q-axis through the solution of a nonlinear reluctance network using the core material's BH characteristics. This provides a much more accurate prediction of the electrical and torque-production capabilities of IPM machines that is critical to developing high-performance designs.

The following chapter examines some specific design examples that are verified using finite element analysis (FEA), and compares design predictions from the nonlinear saturable LPM to existing machine designs.

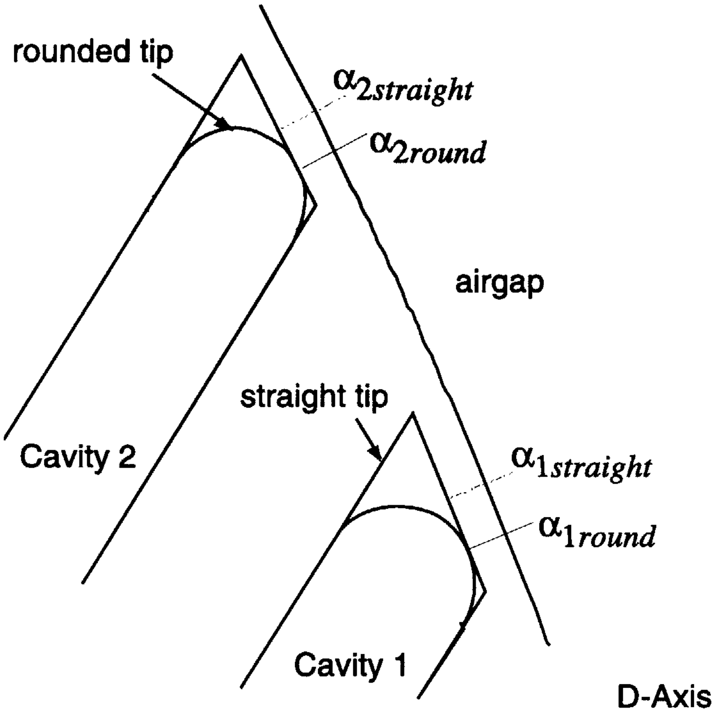

Figure 3.28: Close up view showing the cavity tip details with rounded tip design superimposed over a straight tip design showing the effect on α_k.

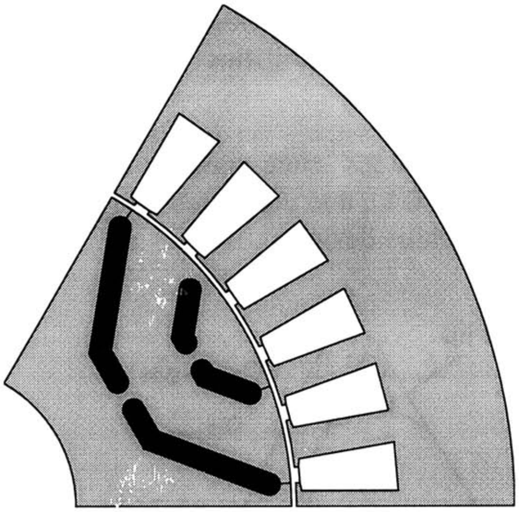

Figure 3.29: IPM machine with rounded cavities and central posts.

Chapter 4

DESIGN VERIFICATION

4.1 Introduction

This chapter applies the lumped parameter models from the previous chapter to the analysis of machines. A design example is explored, fully calculating motoring performance both in the constant-torque and in constant-power regions to demonstrate the capabilities of the LPMs. Finite element analysis (FEA) is employed to explore the relative accuracy of the saturable LPM. Finally, existing prototype machines are analyzed to provide direct comparisons between experimentally gathered data and both LPM and FEA predictions.

4.2 Design Example

In this section, an example IPM machine drive is specified and modeled using the LPMs. Then, the lumped parameters and performance predictions are compared to FEA calculations. Both the linear (infinitely-permeable core) and saturable (nonlinear, saturable core) LPMs are employed for comparison.

Table 4.1 gives the specifications, and Figure 4.1 shows the design, of a 4-pole, 14.9 Nm, IPM machine with a drive rated at 9.8 kW. This machine requires magnet material with nominal remanent flux density 0.56 T that corresponds to bonded Neodymium Iron material. 29-gage M19 steel is used for the laminations. Table 4.1 includes the principal dimensions and design parameters for the machine and converter. The rated speed is determined in the course of the LPM calculations. The winding factor k_{a1} is calculated using the formulae from the previous chapter, and all the other machine parameters are directly specified for the geometry.

Table 4.1: 9.8kW double-layer IPM machine specifications.

Parameter	*Value*	*Units*
I_0	12.4	Arms
V_0	265	Vrms
k_{a1}	0.9261	
N_a	84	turns
n_s	18	slots
p	2	pole pairs
B_r	0.56	T
l	0.1615	m
r	0.0272	m
g'	4.0898e-04	m
g	3.5560e-04	m
d_{m1}	0.0014	m
d_{m2}	0.0038	m
d_{r1}	0.0024	m
θ_{m2o}	141.6	elect. deg.
d_{r2}	0.0036	m
d_{r3}	0.0031	m
w_{b1}, w_{b2}	0.0010	m

Using the MATLAB computing environment [52] and the LPMs, λ_{PM}, L_d, and L_q are calculated for the 9.8 kW IPM machine drive. The inductance curves are shown in Figure 4.2 and $\lambda_{PM} = 0.103$ Wb.turns. The saturable model is shown with a solid line, and the linear model is shown with a dash-dot line. This convention is used for all figures which follow in this design discussion. The MATLAB design scripts and functions developed to make these calculations are given in Appendix A.

The saturable L_q curve shows the characteristic decrease in inductance with increasing excitation. The minor positive inflection at low excitation corresponds to the permeability inflection of electrical steel at low induction. This can be seen at the beginning of the BH curve of M19 and common electrical steels. Also note that at low excitation, prior to the onset of saturation, the saturable and linear models for L_q are nearly equal which is as expected. They would be precisely equal if the permeability of

M19 at very low excitation was infinite. The small inflection in the L_q curve at low excitation is due to the real drop in total permeability for M19 steel near the BH curve origin.

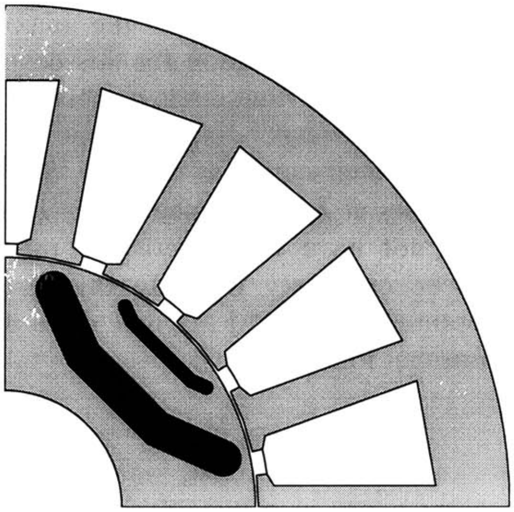

Figure 4.1: Cross-section of a 9.8kW double-layer IPM machine.

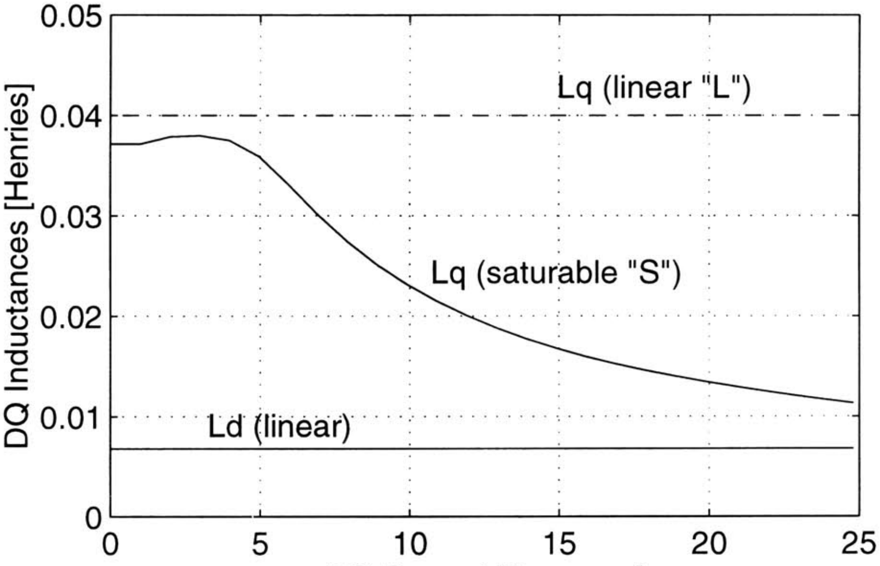

Figure 4.2: Lumped parameter calculations for the 9.8 kW IPM machine using LPMs.

The specifications of the power converter are now taken into account to calculate the performance and operating limits of the machine drive system. The motoring quadrant of the *dq* current frame is shown in Figure 4.3. Refer to Chapter 2 for a detailed explanation of the maximum torque-per-Ampere, constant torque, and current limit curves. The curves emanating from the origin represents the maximum torque-per-Ampere trajectories during Mode I motoring operation for this design. The intersection of the linear model trajectory with the current limit circle is labeled 'L', and the saturable model intersection is labeled 'S'. The corresponding constant torque loci for the linear and saturable LPM are also shown intersecting at 'L' and 'S'. 'I' marks the center of the voltage limit ellipse that occurs at λ_{PM}/L_d. Since point 'I' is outside the current limit circle, this machine does not have a theoretically infinite CPSR. Only modest overcurrent, 21%, would be necessary to make the system design meet Soong's conditions for a lossless optimal CPSR IPM machine drive design [7, 8]. The definition of CPSR for the calculations that follow is

$$CPSR = \frac{\omega_{\max}}{\omega_0} \tag{4.1}$$

where $\omega_{\max}$ is the maximum speed at which the output power (P_{shaft} for a motor) is equal to the output power at the corner speed ω_0.

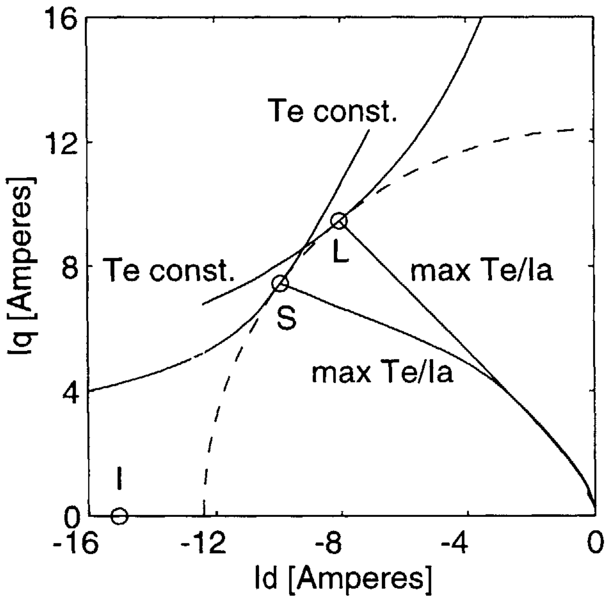

Figure 4.3: Maximum torque-per-Ampere trajectories and associated constant torque lines for linear and saturable LPMs.

Table 4.2 shows the predicted performance of this system design using both LPMs. The effects of q-axis saturation are evident in almost every performance characteristic. In Mode I operation at rated current, the saturated saliency ratio is 28% lower than the unsaturated value. This reduces the rated torque by 32% and shifts $\gamma < -45^\circ$, again at the corner speed point. This effect is also viewed in the motoring region of the torque versus control angle plot shown in Figure 4.4 (starting at $\gamma > -90^\circ$). The existence of four torque peaks, two motoring and two generating over the 360° (though only $-180^\circ < \gamma < 0^\circ$is used) also illustrates that this system is dominated by the saliency torque component even in the presence of magnetic saturation.

Table 4.2: 9.8kW double-layer IPM machine performance.

Parameter	*Value*		*Units*
	Linear Model	*Saturable Model*	
S_r	5.9	4.2	
T_0	20.9	14.3	Nm
γ_0	-40.4	-53.1	elect. deg.
I_{d0}	-8.03	-9.92	Arms
I_{q0}	9.44	7.44	Arms
ω_0	3255	5700	mech. RPM
$\cos(\phi_0)$	0.74	0.88	
CPSR	14.9	6.4	

On the other hand, the corner speed prediction using the saturable model increases by 75% resulting in a predicted constant power rating increase of 20%. At this higher power level, the saturable model constant-power speed ratio (CPSR) value is 57% smaller than with the linear model. Figure 4.5 and Figure 4.6 show the shaft torque and power versus speed for this IPM machine drive. The shaft torque and power in the constant-power region using either model is roughly equal, so the apparently large difference in the constant-power level (indicated by horizontal lines in Figure 4.6) and the CPSR value is actually caused by only a shift of the corner-point speed at which the system becomes voltage-limited.

It can also be seen that converter utilization (i.e. power factor) in the constant power region increases up to about 15 krpm for both models where the peak power output is reached as shown in Figure 4.6. This, however, is not the peak efficiency point as is made evident by examining the saturable model losses and machine efficiency in Figure 4.7 and Figure 4.8. Because flux is weakened in the constant power region, the core and harmonic loss components have a decreasing trend. The peak machine efficiency, 96.7%, occurs near 18 krpm.

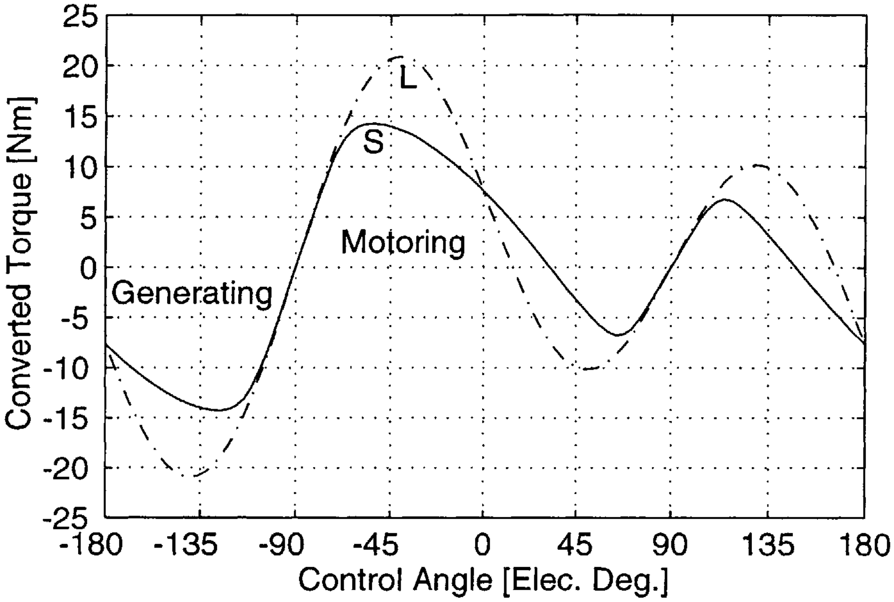

Figure 4.4: Torque T_e versus control angle γ for the 9.8kW IPM machine drive.

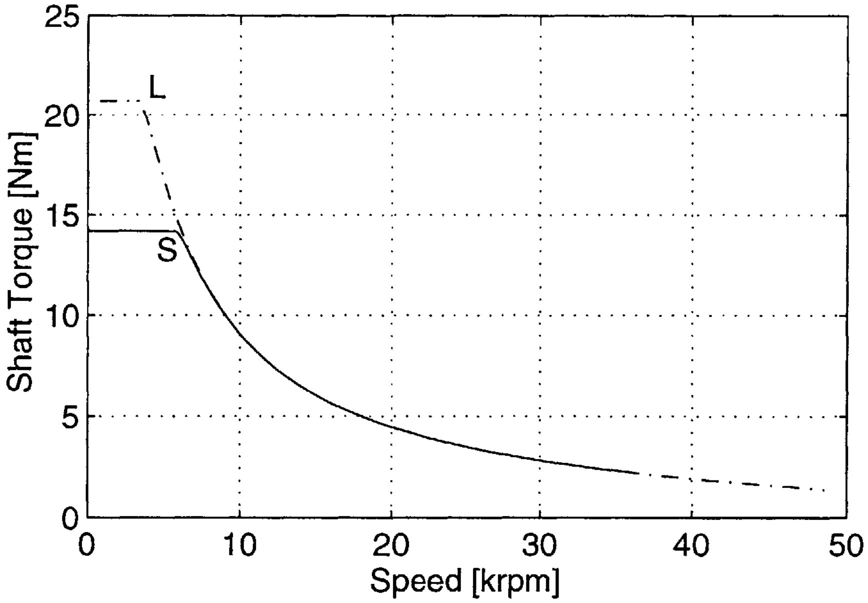

Figure 4.5: Shaft torque versus speed for the 9.8 kW IPM machine drive.

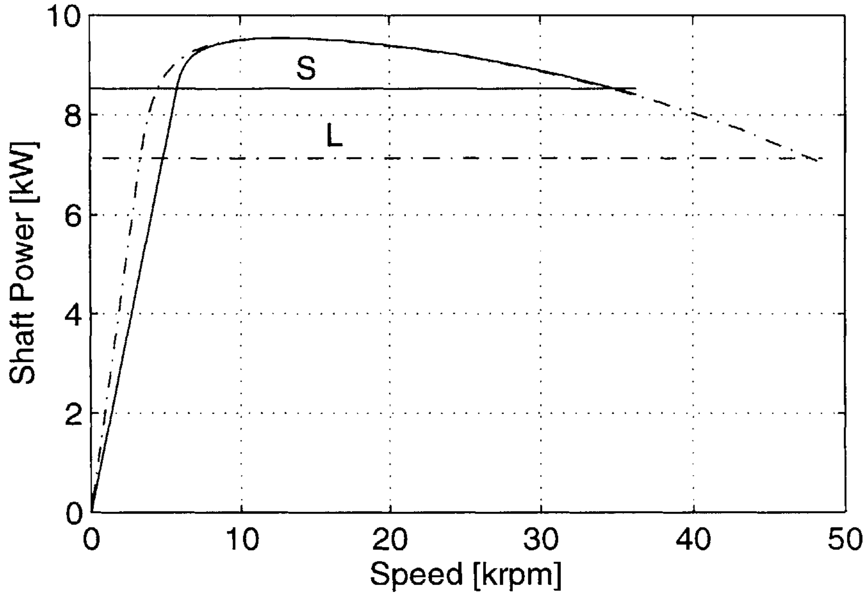

Figure 4.6: Shaft power versus speed for the 9.8 kW IPM machine drive.

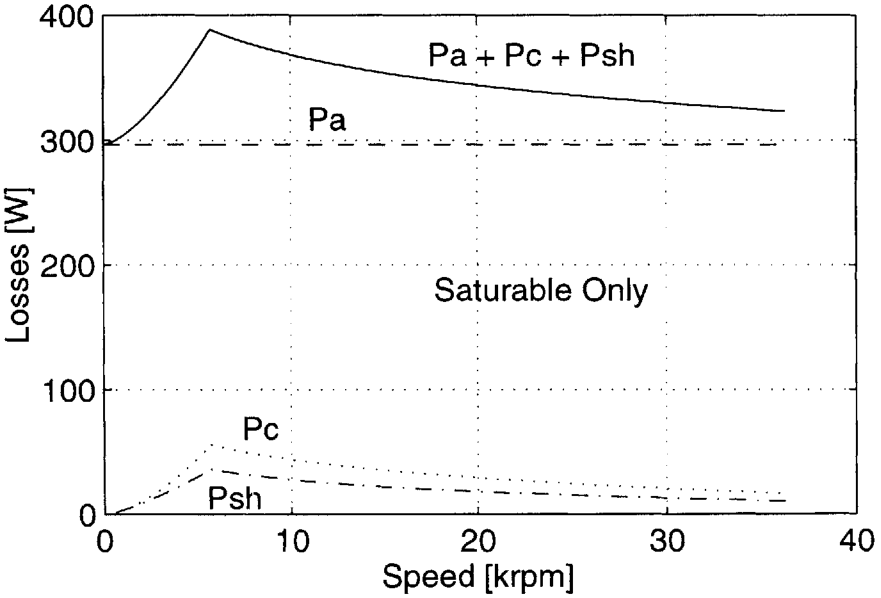

Figure 4.7: Armature, core, and slot harmonic losses (P_a, P_c, and P_{sh} respectively) versus speed for the 9.8 kW IPM machine drive.

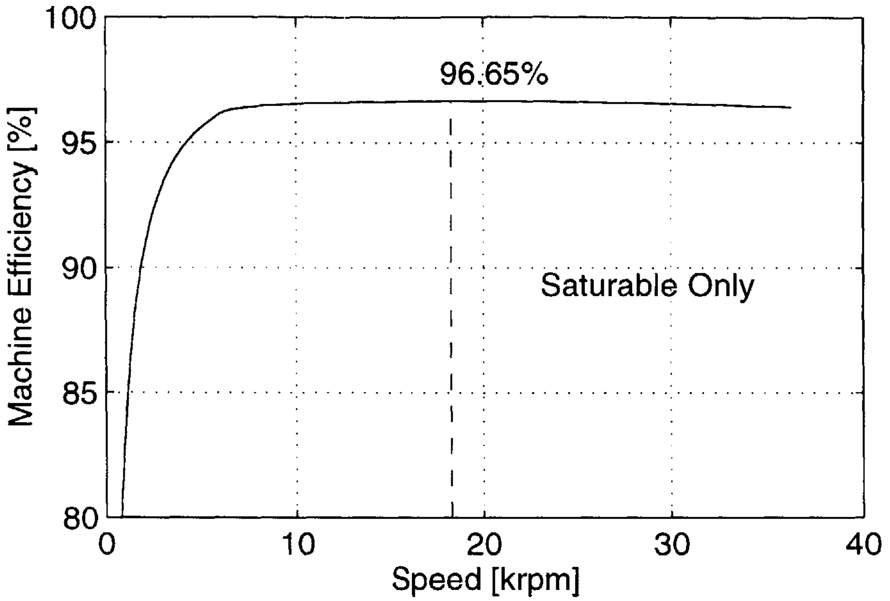

Figure 4.8: Machine efficiency at rated current for the 9.8 kW IPM machine drive.

The actual peak speed of this IPM machine will likely be limited for mechanical reasons before reaching the high end of the constant power region. Mechanical losses that are not present in these models include windage and friction. Furthermore, bearing and structural limitations may prevent operation at high speed. Except for structural limits, though, these concerns are common to other synchronous and induction machines and are therefore not a distinguishing feature for comparisons. The peculiar structural limitations of the IPM rotor are revisited in a later chapter.

4.3 Comparison to Finite Element Analysis (FEA)

Finite element analysis (FEA) is employed for a fundamental accuracy check of the LPMs that were developed in the previous chapter and applied to the candidate machine in Section 4.2. FEA is useful for verifying the lumped parameter calculations of L_d, L_q, and λ_{PM}, and the converted torque T_e. The field plots are also examined to ascertain to what degree the principal modeling assumptions are justified. The FEA is not employed to verify losses or performance at higher speeds, including the constant-power region.

The 9.8 kW IPM machine drive introduced in Section 4.2 is analyzed using MagNet 2D FEA software .[53]. A two-pole model is generated since there are a non-integral number of slots per pole (i.e., 4.5), and hence the machine is only geometrically symmetric over two poles. Figure 4.10 shows the solution mesh for this FE model. The mesh includes 9000 elements and it is used in all the results that follow. The stator excitation is modeled as a constant evenly-distributed current density across each coil that fills half a slot. The instantaneous current magnitudes are constructed from sinusoidal current waveforms displaced 120° in time (i.e. balanced three-phase AC excitation).

The magnets are modeled by three segments in each cavity with the magnetization direction normal to the appropriate cavity boundary. In this particular design, the magnet material is assumed to be linear with the designed B_r value and the permeability of air. It is noted that this neglects the effects of having less than 100% fill factor within the cavities as would be experienced with an experimental IPM machine. Also, if a flexible bonded material were employed, the magnetization direction at the bends within the cavity would be locally different that the chosen FE model.

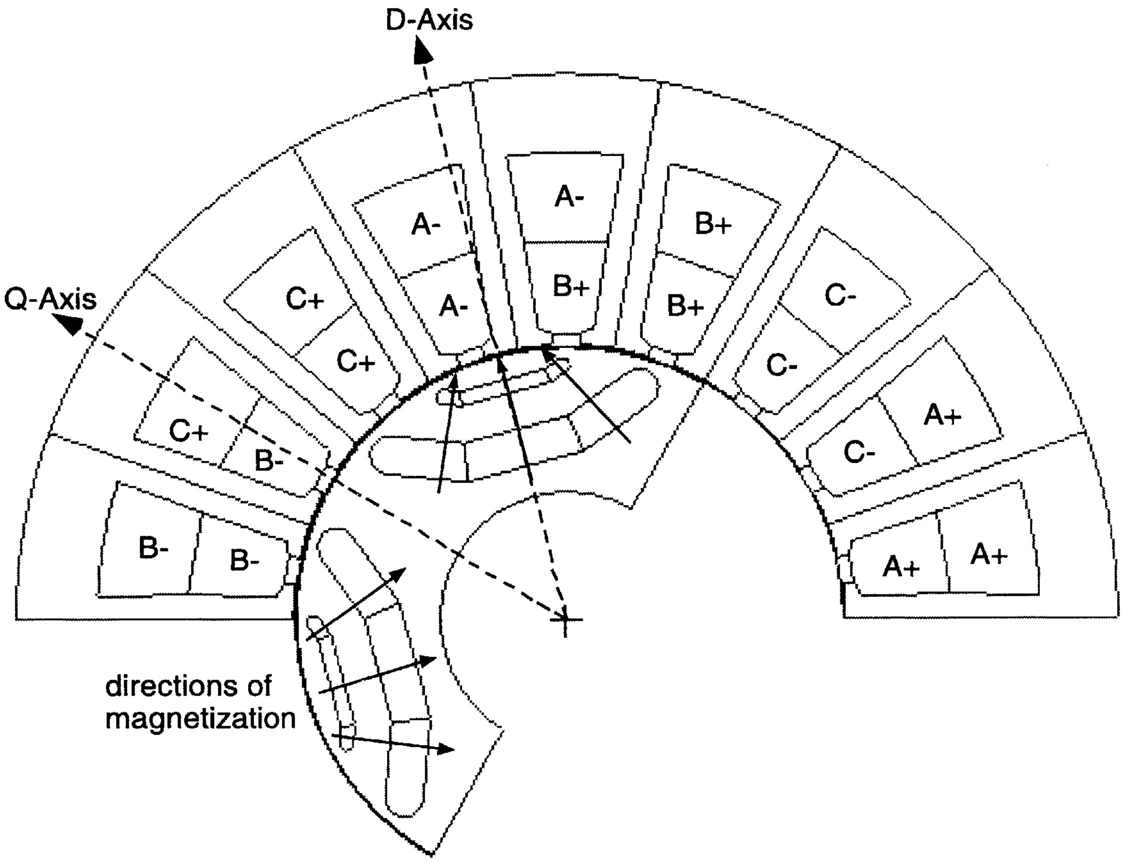

Figure 4.9: Solid model employed for FEA of the 9.8 kW IPM machine.

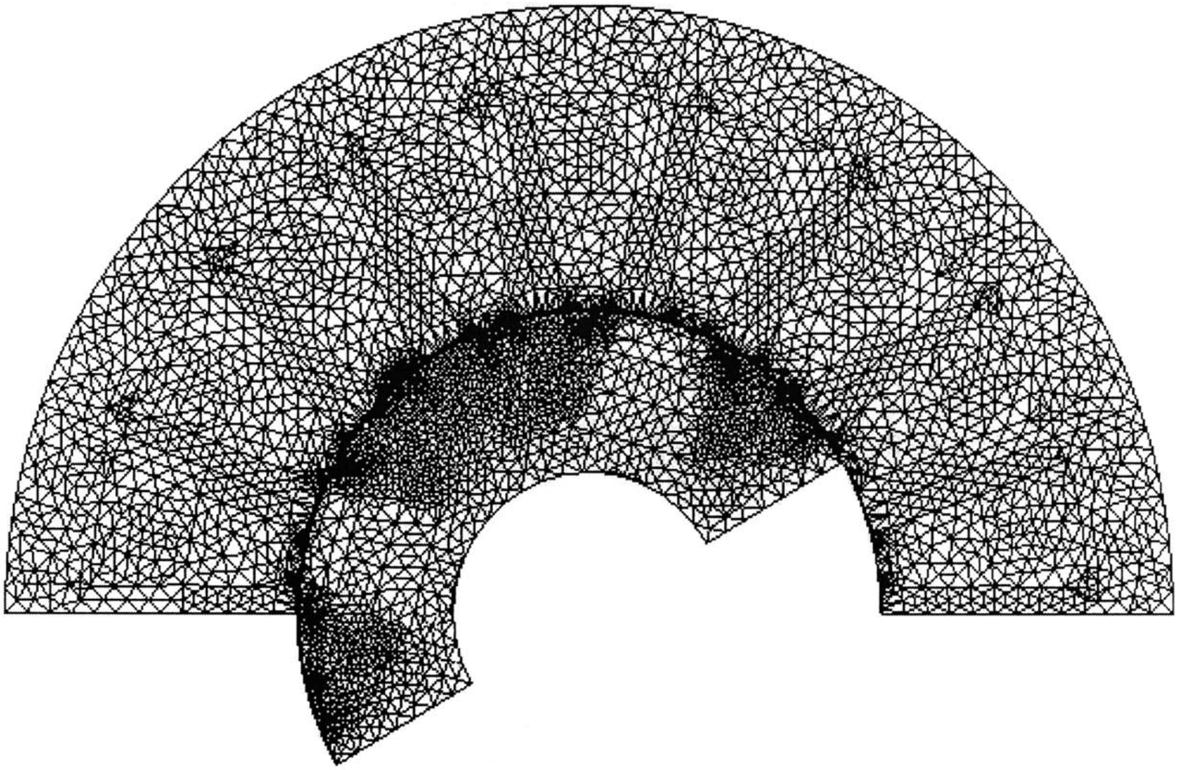

Figure 4.10: FE mesh for the 9.8 kW IPM machine.

The lumped parameters are derived from the MagNet flux linkage calculations. The resulting inductances are shown in Figure 4.11 in comparison to the saturable LPM inductances. The PM flux linkage calculated via FEA is 0.103 Wb.turns which is equal to the LPM calculation. The L_d versus I_d calculations agree very well, particularly in the high current region. The curvature in the FEA result indicates that the PM alone is not fully saturating the bridges and that some initial *d*-axis flux is being preferentially directed through the bridges. As the excitation increases, the bridges become fully saturated and L_d approaches a constant. This corresponds well with the LPM assumption that the bridges are heavily saturated and suggests that the constant-L_d model becomes increasingly valid as the rated operating point is approached.

There is a 7.5% worst-case difference, though, in the L_q versus I_q predictions. This is reflected in a comparison of the T_e predictions as seen in Figure 4.12. As expected after making the inductance comparison, the torque prediction difference between FEA and MATLAB is 7% at the peak-torque control angle.

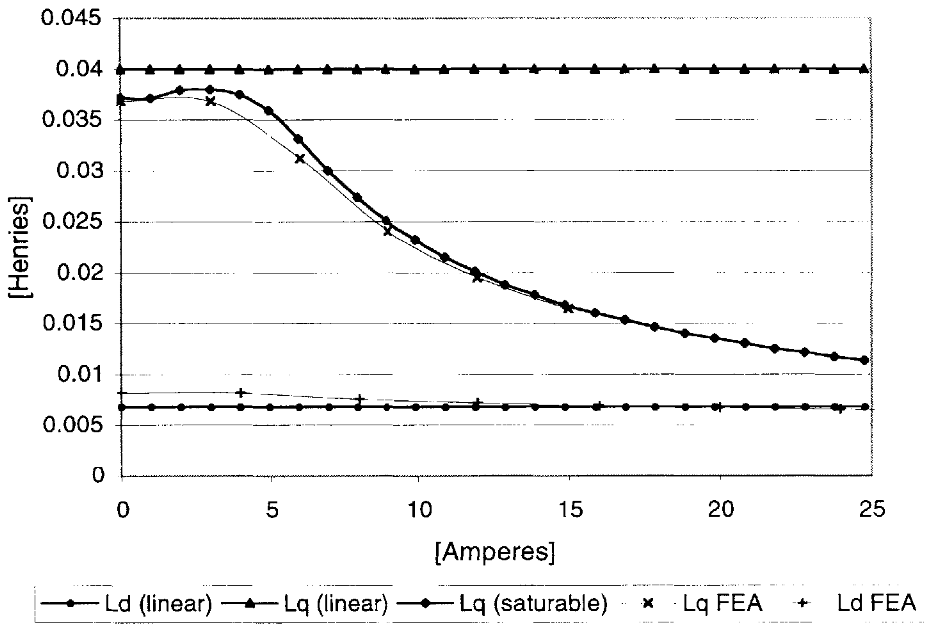

Figure 4.11: *DQ* inductances versus current for FEA and MATLAB LPM calculations.

The FEA torque was obtained using two methods. The torque curve labeled 'FEA Force' averages MagNet's direct computation of force on the stator from the Lorentz force on the conductors, and Magnet's torque calculation derived from virtual work on the rotor. Both the rotor and stator force computations are essentially equal except at very low energy states. The other FEA torque curve labeled 'FEA Lumped Parameters' is calculated from the FEA lumped parameter predictions discussed above and (3.85). The two FEA-based calculations should be the same, and do show the same peak but with some differences in shape. The visible differences between the two FEA torque solutions result from the precision of the FEA solution, the effects of precise alignment of the stator slots with the rotor features, the precision of the FEA lumped parameter curve fit, and the neglected cross-coupling effects.

The vertical error bar at the peak torque condition indicates the torque variation with stator slot position. This torque ripple is actually reduced in the prototype machine by the stator skew that is not present in the 2D FE model.

Figure 4.13 is a plot of the field lines and $|B|$ at rated current near the peak torque control angle. This plot confirms qualitatively the major modeling assumptions established in the previous chapter. The highest magnetic saturation, $|B| > 2$ T, is seen through the rotor bridges, particularly at the tips of the larger cavity. At that saturation level, the incremental permeability of electrical steel is nearly that of air which supports the L_d calculation assumption that the magnet cavities extend to the airgap.

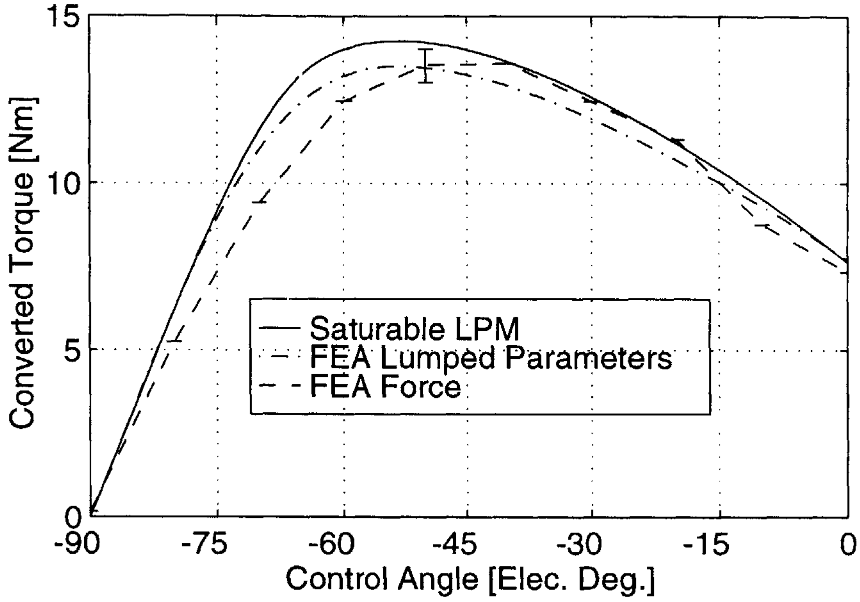

Figure 4.12: Torque versus control angle for FEA and MATLAB LPM.

One area of particular concern in accurately modeling IPM machines is the assumption that there is no magnetic cross-coupling from the d-axis to the q-axis. The q-axis inductance calculations in Figure 4.11 were made from q-axis flux linkage measurements with the PM material simultaneously exciting the orthogonal d-axis. The excellent agreement between LPM and FEA calculations of L_q indicates that the PM material alone does not introduce significant cross-coupling on the q-axis. In Figure 4.12 the good agreement between LPM and FEA torque calculations with combined d and q axis excitation indicates that any cross-coupling effects due to stator excitation are small. These results substantiates the assumption of negligible cross-coupling for this machine and reinforces the conclusions of the previous research noted in Chapter 2.

FEA results are used to examine the underlying field solution to further appreciate why there is no significant cross-coupling observed in the results of Figure 4.11 and Figure 4.12. Figure 4.14 shows field lines and $|B|$ with only the magnet excitation and no stator current. The magnetic flux density is only saturated across the bridges but the distribution of field lines crossing the airgap indicates this is not sufficient to effectively block flux from entering the parts of the rotor surface at the bridges. With the addition of negative d-axis current the areas of the rotor surface that are at least moderately saturated increase in size. The only observable effect is minor distortion of the direction of the field lines that enter the rotor from the portions of stator teeth that are across from rotor bridges as shown in Figure 4.13.

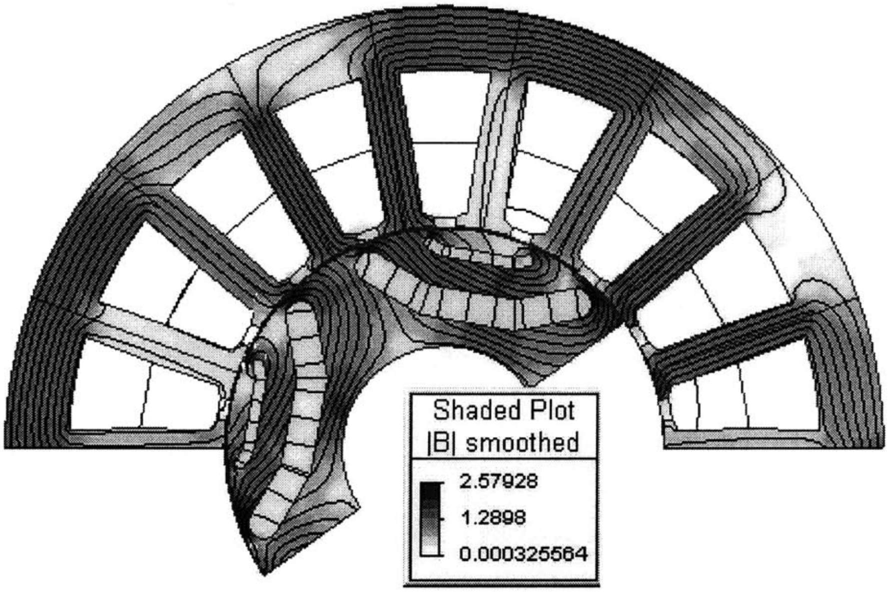

Figure 4.13: Field lines and $|B|$ at rated stator current and maximum-torque control angle.

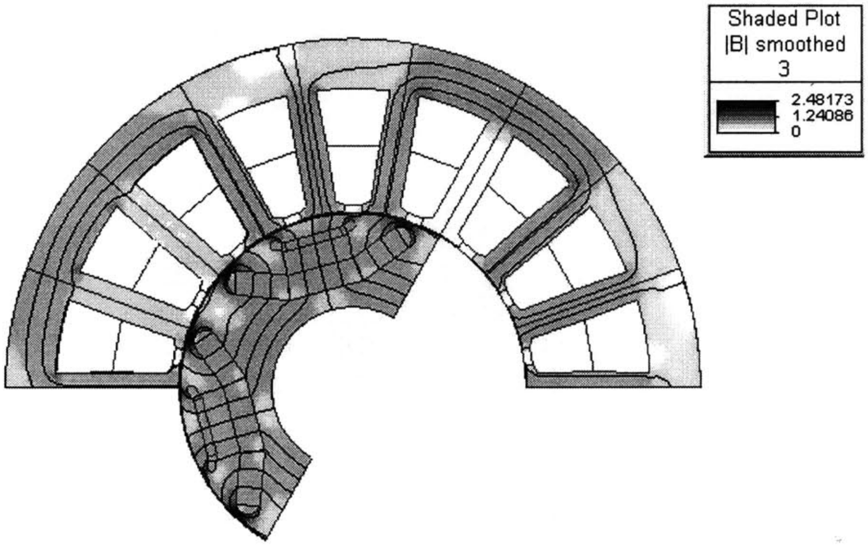

Figure 4.14: Field lines and $|B|$ with no stator current excitation, only magnet excitation.

4.4 Comparison to Experimental Machines

In this section the LPMs are used to analyze existing experimental IPM machine drives. Design and test data for three-layer and four-layer transversely-laminated IPM machines from Soong have been evaluated [54]. From the machine geometry and drive system ratings the necessary design parameters are determined and then lumped parameter models are calculated. The measured lumped parameter values are then compared to calculations derived from the linear and saturable LPMs. In particular, the comparison provides experimental verification of the saturable LPM's ability to accurately predict the saliency ratio as a function of excitation.

4.4.1 Experimental IPM Machine Designs

Figure 4.15 and Figure 4.16 are sketches of the three-layer and four-layer IPM machine prototypes designed, built, and tested by Soong [54]. Both machines are constructed with the same inverter drive, stator, windings, airgap, rotor outline, materials, and cavity thicknesses. Table 4.3 and Table 4.4 list the pertinent machine design and drive specifications. The magnet cavities were designed with semi-circular shapes for ease of inserting flexible bonded magnet material and also to approximate the ideal flux barrier shape reported by Miller for synchronous reluctance machines [55]. The peripheral span of the largest magnet in the four-layer design is somewhat larger than the span of the largest magnet in the three-layer machine to accommodate the additional magnet layer. Likewise the inter-cavity core depths, d_{rk}, are smaller for the four-layer machine to remain within the same rotor volume.

The shown rotors both divide the larger magnet cavities into two sections by utilizing a center post formed in the core lamination. The center post is not used on the smallest cavity in both cases. The minimum thickness' of the center post are given in Table 4.3 and Table 4.4 as w_{ck} for the k^{th} center post.

4.4.2 Lumped Parameter IPM Machine Models

To simplify the modeling comparison, certain approximations of the experimental IPM machine design have been made to fit the structure of the LPMs presented in Chapter 3. Figure 4.17 and Figure 4.18 show LPM model representation of the three- and four-layer experimental IPM machines, respectively. The principal difference is that the LPMs assume that each rotor cavity is approximated as three straight sections with angles that are symmetric with respect to the *d*-axis, as opposed to their actual semi-circular shapes. As a reasonable approximation, the dimensions radially along the *d*-axis exactly match the machine drawing specifications. Furthermore, the angular span along the airgap from tip to tip of each layer, θ_{mok}, matches the experimental machine. As discussed in Chapter 3, the semi-circular magnets are modeled using three segments for each layer. The angular span at the 'joint' between of each segment of a single layer is specified as

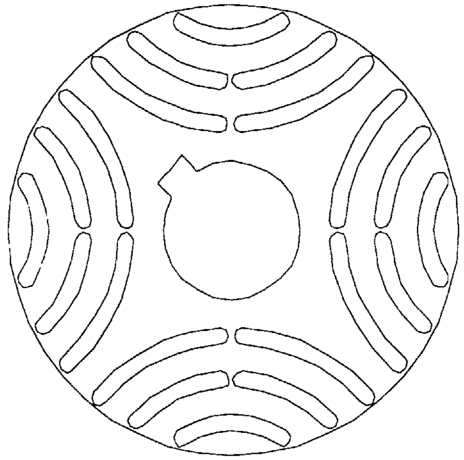

Figure 4.15: Rotor drawing for three-layer experimental IPM machine.

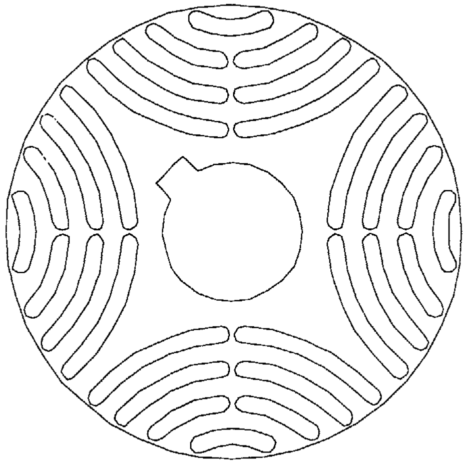

Figure 4.16: Rotor drawing for four-layer experimental IPM machine.

Table 4.3: Three-layer experimental IPM machine specifications.

Parameter	*Value*	*Units*
I_0	2.4	Arms
V_0	231	Vrms
k_{a1}	0.9549	
N_a	282	turns
n_s	36	slots
p	2	pole pairs
B_r	0.21	T
l	0.095	m
r	0.046	m
g'	3.9e-04	m
g	4.5230e-04	m
d_{mk}	0.0035	m
θ_{m3o}	141.6	elect. deg.
d_{rk}	0.0048	m
	0.0053	
	0.0053	
	0.0044	
w_{bk}	0.0006	m
w_{ck}	0.0000	m
	0.0006	
	0.0008	

Table 4.4: Four-layer experimental IPM machine specifications.

Parameter	*Value*	*Units*
I_0	2.4	Arms
V_0	231	Vrms
k_{a1}	0.9549	
N_a	282	turns
n_s	36	slots
p	2	pole pairs
B_r	0.21	T
l	0.095	m
r	0.046	m
g'	3.9e-04	m
g	4.5230e-04	m
d_{mk}	0.0035	m
θ_{m3o}	159.678	elect. deg.
d_{rk}	0.0026	m
	0.0034	
	0.0034	
	0.0034	
	0.0035	
w_{bk}	0.0006	m
w_{ck}	0.0	m
	0.0006	
	0.0007	
	0.0008	

$$\theta_{mik} = \frac{\theta_{mok}}{2} \tag{4.2}$$

These angular design parameters are defined in Figure 3.4.

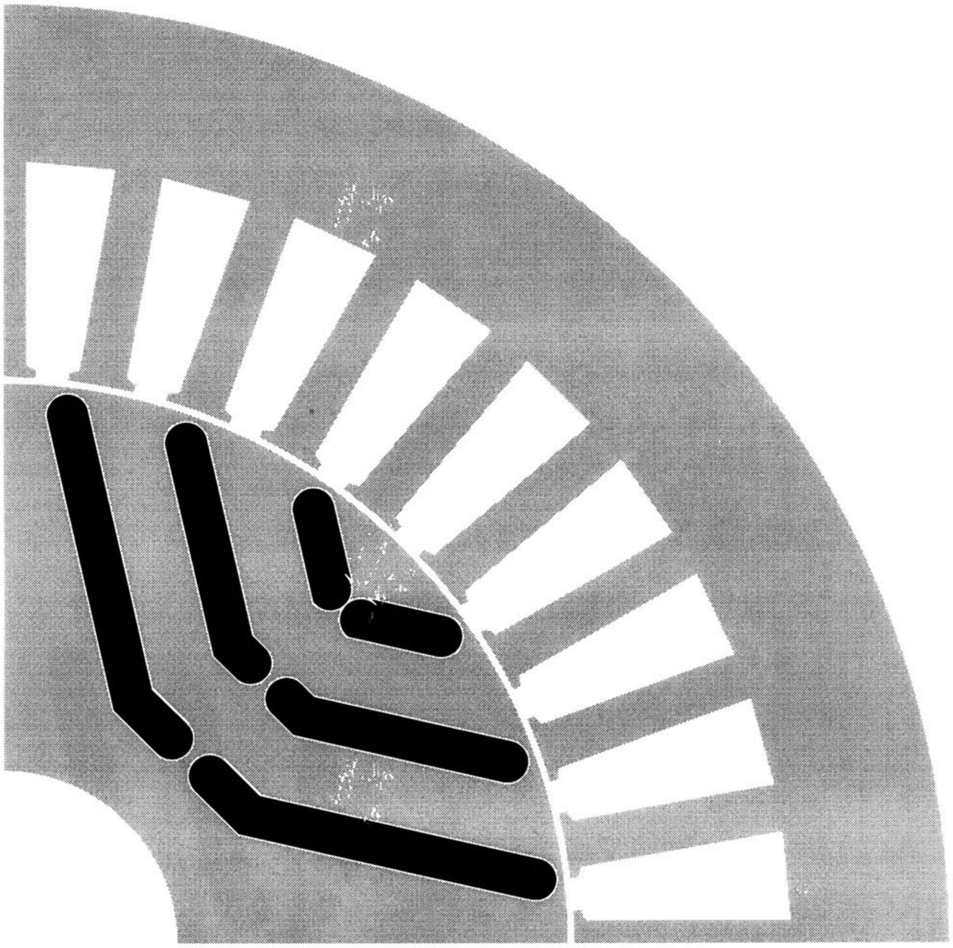

Figure 4.17: Three-layer experimental IPM machine LPM representation.

Another difference is that the center posts are not all modeled precisely. Center posts are not an explicit part of the models developed in the Chapter 3. The magnetic function is precisely the same, though, as the bridges at the rotor periphery. Like the bridges, the posts act magnetically to increase the cross-sectional area of steel that provides a shorting path for flux around the cavities. This has the effect of increasing L_d and decreasing λ_{PM} just as the bridges do. Therefore, the minimum width of the center posts is simply added to the bridge thickness when calculating L_d and λ_{PM} with the same assumption of full saturation at B_s that was used for the bridges.

There is also a noticeable distortion of the smallest magnet cavity in both Figure 4.17 and Figure 4.18. This is only an effect of the MATLAB drawing code which assumes that all layers in a given design either have center posts or do not. In both of these figures, the absences of a center post in the smallest layer is modeled by a center post with zero thickness. This is equivalent, with respect to the lumped parameter calculations, to an assumption that there is no center post at all in the smallest magnet cavity of each design.

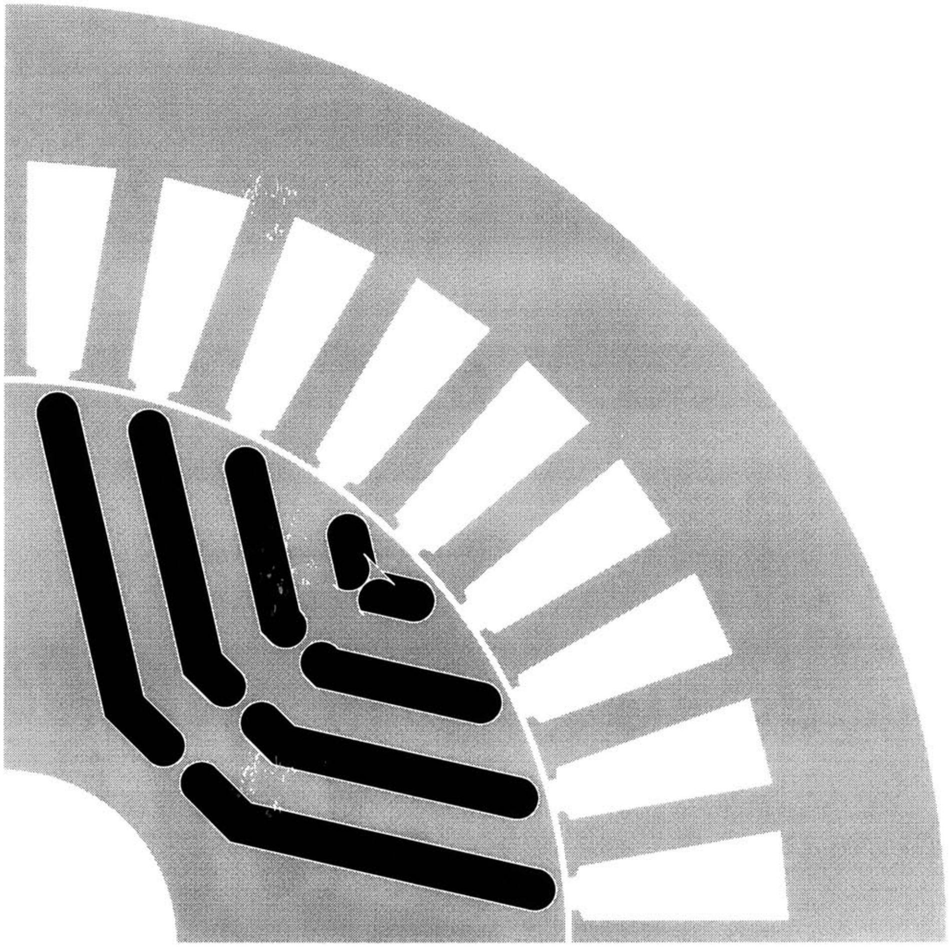

Figure 4.18: Four-layer experimental IPM machine LPM representation.

These differences and additional minor ones are summarized below in Table 4.5. Also there are some experimental machine details that are not known: the specific steel BH curve, an accurate measure of the magnet remanent flux density (though rough measurements indicated a value of 0.21 T), the magnet fill factor across the thickness of each cavity, and the actual measured airgap of each experimental machine assembly.

4.4.3 Measured and Calculated Lumped Parameters

The *dq* lumped parameters are calculated using both the LPMs and FEA and compared to measured results. Both the linear LPM for L_d, L_q, and λ_{PM}, and the saturable LPM for

L_q are applied to both experimental machine models. A 2D FEA model is generated using the same cross-sectional approximations as the LPMs and employed to calculate the same results. FEA inductances are calculated from the specified instantaneous currents and resulting flux linkage calculations produced by the FEA application. Since the FEA is two-dimensional, it does not include end effects in the resulting flux linkage calculations. The same steel curve, 29-gage M19, which is used for LPM calculations is used in the FEA model. Likewise, the same magnet remanent flux density is specified for both FE and LPM analyses. However, the relative permeability of magnets in the FEA is specified as 1.05 which is more representative of the experimental material. The effect of the small change in relative permeability, though, is quite negligible when compared to the permeability of the surrounding core material even under saturated conditions.

Table 4.5: Summary of known differences between LPMs and experimental machines.

Item	*Lumped Parameter Model*	*Experimental Machine*
Cavity shape	3 straight sections	semicircular
Smallest cavity center post	zero thickness center post	no center post
Stator slot shape	trapezoid	teardrop slot bottom edge
Relative magnet permeability	1.0	1.04 to 1.08

A series of FE solution plots for the three-layer IPM machine are now presented to provide an overview of the FE model used to verify the LPM predictions. Insight is also gained into the underlying field conditions and how well or poorly they relate to the chosen saturable LPM structure. Figure 4.19 shows the stator current excitation aligned with the q-axis. Note that with the magnets contributing to the d-axis field, the resultant field lines are not symmetric along the q-axis. For reference, the plot also shows that this stator is a concentrically-wound single-layer winding distributed in three slots per phase per pole. Figure 4.20 shows a solution mesh that is reasonable to achieve good accuracy for the results. There is good element density across each magnet, within the bridges and posts, and at the rotor periphery where the field gradients are large.

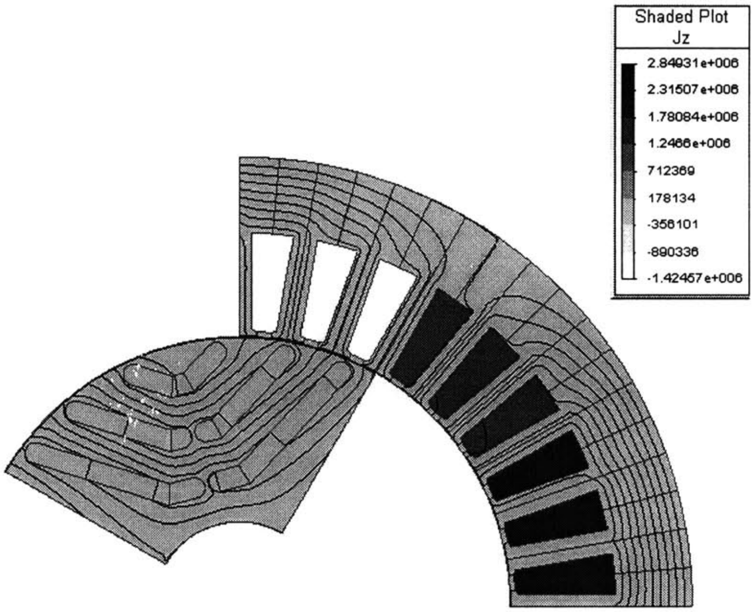

Figure 4.19: FE plot of current density and field lines for the three-layer experimental IPM machine with $(I_d, I_q) = (0,4)$ Arms.

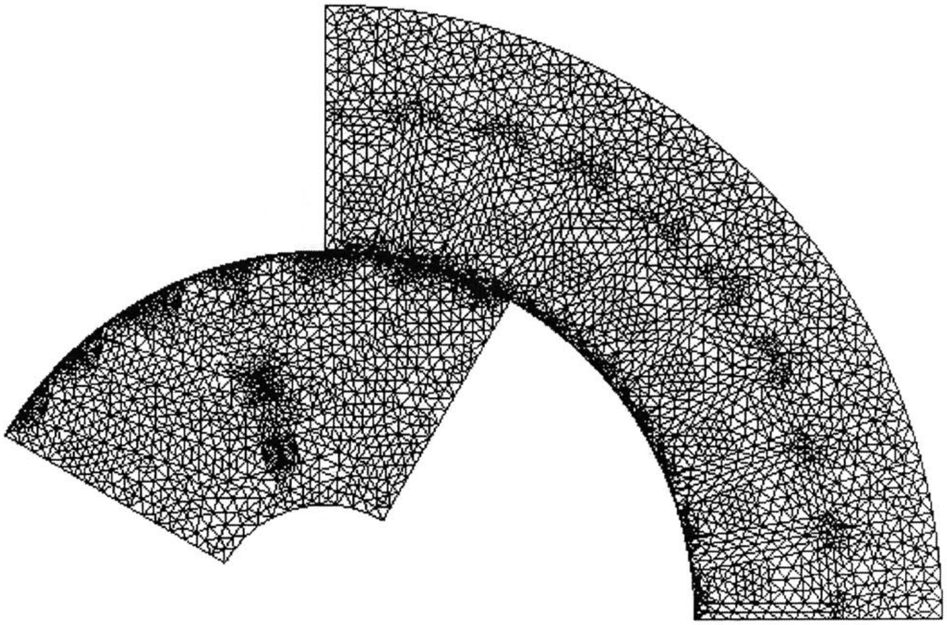

Figure 4.20: FE plot of solution mesh for the three-layer IPM machine.

Figure 4.21 and Figure 4.22 show the PM field alone and with stator excitation along the *d*-axis only. These show that the magnets are indeed saturating the bridges but only along a short length. The addition of negative *d*-axis current extends the saturated region of the bridges to a length roughly equal to the cavity thickness. This is important because this is the assumed state in the LPM model for L_d and λ_{PM}.

Figure 4.23 shows rated excitation in both axes which represents the conditions for overall worst-case bulk saturation in the core. Notice that the saturation level is roughly uniform in the inter-cavity rotor sections. This corresponds well with the decision to represent each inter-cavity section by a single reluctance in the saturable LPM. Likewise, the back iron of the stator shows roughly four separate sections at different saturation levels which also corresponds well with the division of elements in the stator portion of the saturable LPM.

The core path between the largest magnet cavity and the rotor ID, however, indicates an uneven distribution of flux density throughout this section. It was noted in Chapter 3 that this section is problematic to model accurately as a single saturable reluctance and is likely to be a source of some error.

The field characteristics are generally similar for the four-layer machine and only Figure 4.24, which shows rated excitation on both axes, is included for reference.

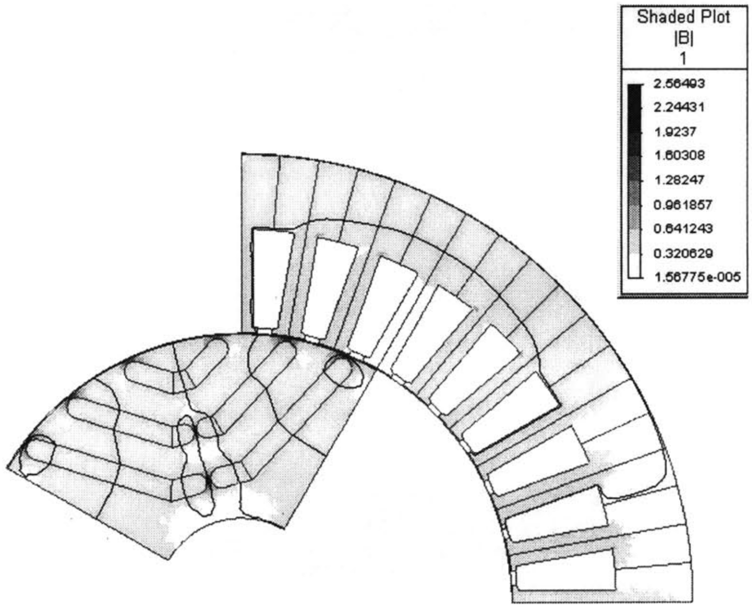

Figure 4.21: FE plot of $|B|$ with PM excitation only for the three-layer experimental IPM machine.

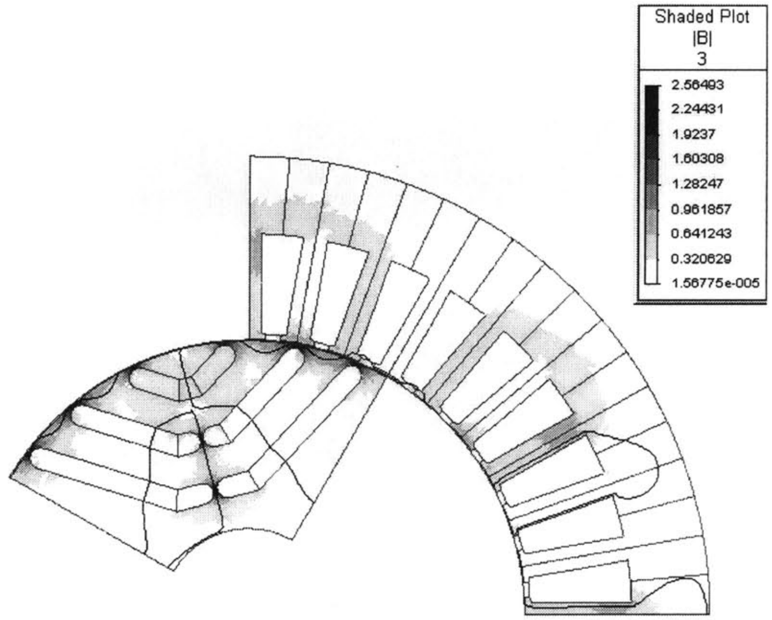

Figure 4.22: FE plot of |B| with $(I_d, I_q) = (-4,0)$ Arms for the three-layer experimental IPM machine.

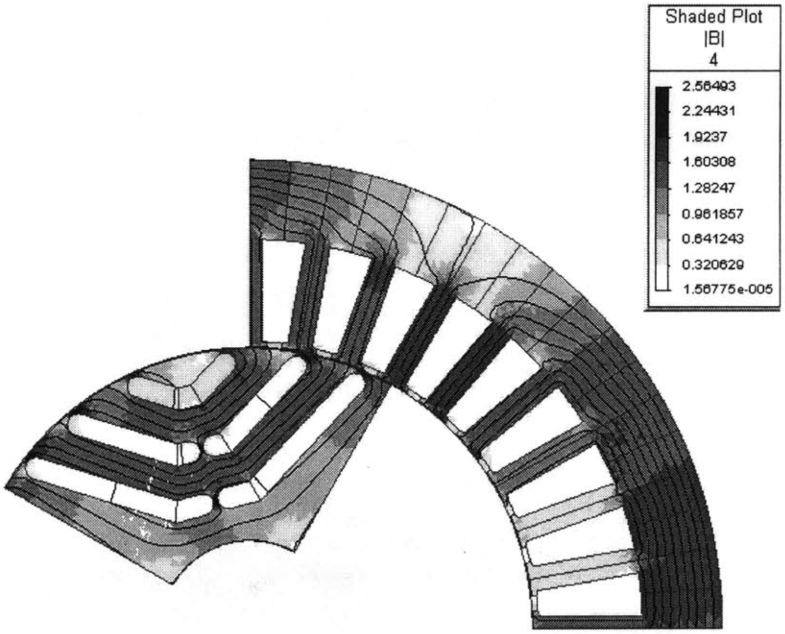

Figure 4.23: FE plot of |B| with $(I_d, I_q) = (-4,4)$ Arms for the three-layer experimental IPM machine.

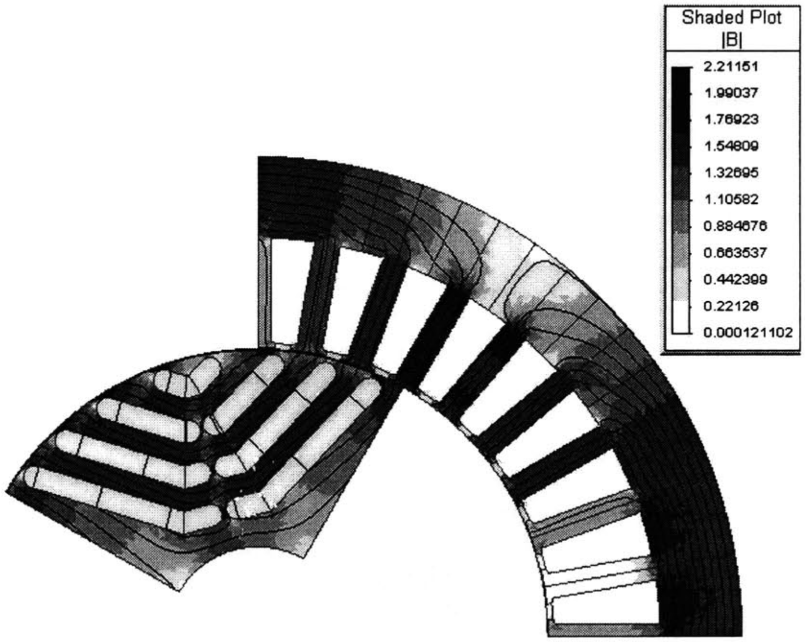

Figure 4.24: FE plot of $|B|$ with $(I_d, I_q) = (-4,4)$ Arms for the four-layer experimental IPM machine.

The experimental data was measured by Soong and checked using two methods. The principal method was to record phase voltage and current waveform transients following injection of a DC voltage step into a machine phase with a locked rotor. From the phase voltage and natural frequency response the flux linkage was calculated. The fundamental RMS components were then obtained from both flux linkage calculations and current measurements. Both AC and DC current injection methods were employed to locate the q-axis of the machine to insure waveform injection and measurements on the d- and q-axes.

It was determined that the DC step tests on the q-axis of three-layer IPM machine were not taken accurately, so data from an identical synchronous reluctance rotor (i.e. the same rotor but without magnets in the cavities) was substituted. This substitution is not expected to introduce any significant inaccuracy since the permeability of the magnets is so close to that of air. Furthermore, AC sinewave excitation tests that showed good correlation to the DC step tests on all machines were made on both the three-layer synchronous reluctance and the IPM rotors to verify that their L_q characteristics were similar.

Figure 4.25 and Figure 4.26 show L_d and L_q for the three-layer and four-layer IPM machines respectively using LPMs, FEA, and experimental measurements. In general, the results show excellent agreement between all methods. As noted, the experimental L_q data in Figure 4.25 is actually for the identical three-layer synchronous reluctance rotor. The three-layer IPM rotor was tested using alternate means to verify the L_q curve results would be the same but that data was not recorded.

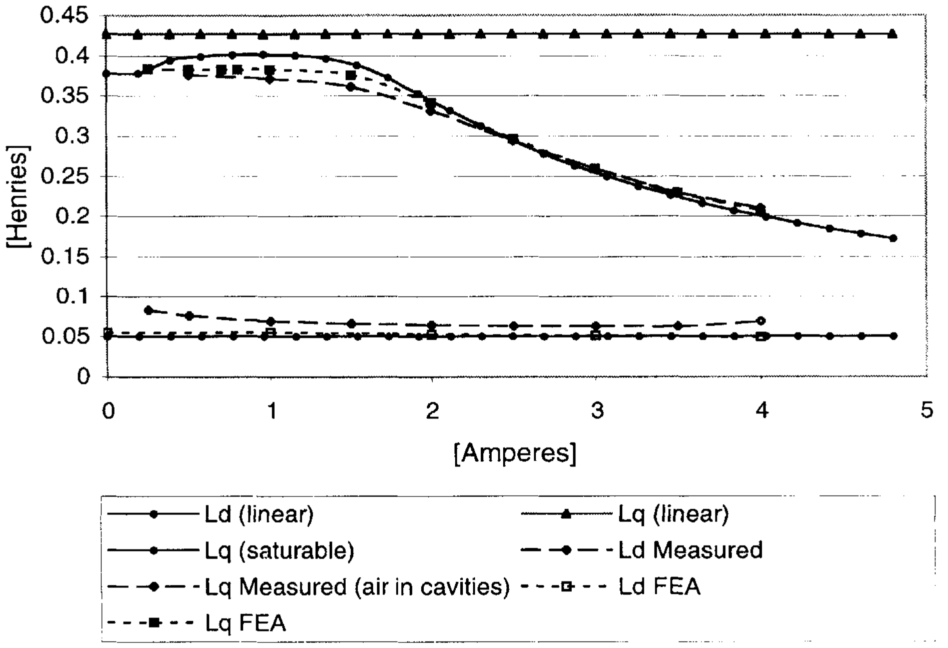

Figure 4.25: Comparison of the *dq* inductances between LPMs, FEA, and measured data on the three-layer experimental IPM machine.

The only significant difference between the lumped parameter curves is that in Figure 4.26 the measured L_q inductance curve for the four-layer rotor starts at a lower inductance level at low current values. If the measured L_q of both Figure 4.25 and Figure 4.26 is extended to zero current, the values are approximately 380 mH and 350 mH respectively. For an IPM machine with this general cross-section, L_q is expected to approach the inductance of a solid round rotor as current goes to zero. For the same rotor outline dimensions, stator, and airgap, therefore one would expect both these machines to approach the identical value.

One possible explanation of the L_q difference is that the final dimensions of the four-layer laminations resulted in a larger airgap. This is a particularly plausible explanation because an airgap difference only affects L_q at low current where the overall reluctance along the q-axis is dominated by the airgap. As the machine goes into bulk saturation under increasing q-axis magnetic loading, L_q becomes dominated by the core cross-section reluctances instead of the airgap reluctance. Since the LPM calculations with the nominal airgap match the experimental data in the saturated excitation region, it is less likely that there are other dimensional, rotor positioning, or measurement errors.

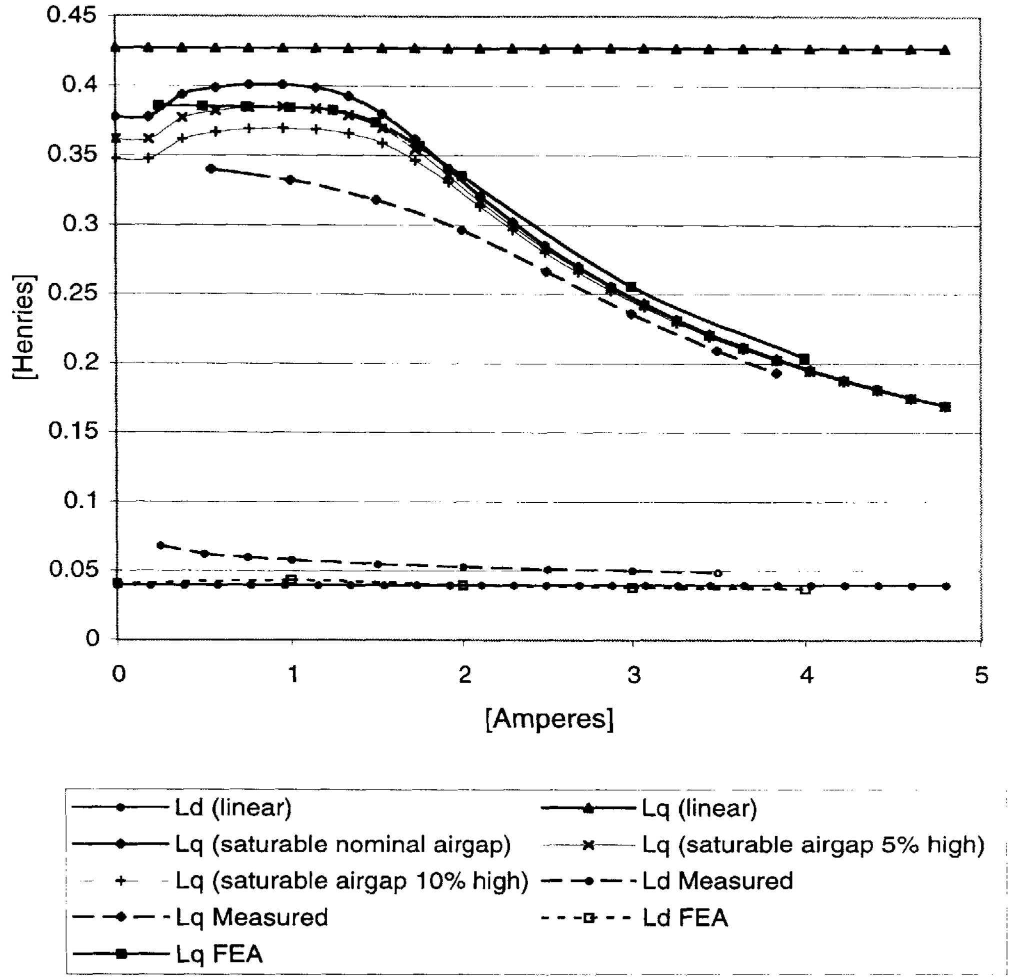

Figure 4.26: Comparison of the *dq* inductances between LPMs (with 3 airgap values), FEA, and measured data for the four-layer experimental IPM machine.

In Figure 4.26, two additional saturable LPM curves for L_q with a 5% and a 10% larger airgap are shown. The measured L_q data for the four-layer machine matches the LPM curve with the 10% larger airgap in a manner very similar to the agreement between the LPM with nominal airgap and experimental results for the three-layer machine suggesting a likely explanation for the initial difference.

The small differences in the L_d calculations and measured data are likely attributable to differences in leakage inductance. In both cases, at high current the FEA calculates the lowest L_d of the three curves. This is reasonable since end-turn leakage, which is 2.1 mH as calculated by LPM, is not modeled in the FEA. As mentioned previously, the constant-L_d assumption is not expected to be accurate at low levels of excitation, but the LPM prediction matches the FEA value well at higher currents. The measured L_d data in both machines is higher than the LPM and FEA calculations, but well within reasonable expectations of leakage calculation errors.

The PM flux linkage calculations and measurements are given in Table 4.6. The FEA estimate is calculated from the flux linked along the d-axis with no stator excitation. The experimental estimate for λ_{PM} is calculated from the measured RMS line-to-line open-circuit voltage V_{l-l} for each machine at $\Omega = 1500$ rpm mechanical speed. The actual measured values for these test conditions were 70 Vrms and 68 Vrms for the three- and four-layer IPM machines, respectively. With the phases wye-connected, the PM flux linkage (in RMS Wb.turns) can be calculated as

$$\lambda_{PM} = \frac{V_{l-l}}{\sqrt{3}\Omega(\pi/30)p} \tag{4.3}$$

Table 4.6: Comparison of the PM flux linkage between LPMs, FEA, and measured data for the three- and four-layer experimental IPM machines.

PM Flux Linkage	*Three-Layer IPM* [Weber.turns rms]	*Four-Layer IPM* [Weber.turns rms]
Lumped Parameter Model	0.153	0.157
FEA	0.149	0.153
Experimental Machine	0.129	0.125

The LPM and FEA λ_{PM} calculations agree very well but are 15-20% higher than the λ_{PM} value calculated from the measured data. Since the FEA and LPM calculations are consistent, this difference with the measured data is most likely attributable to lower-than-expected remanent flux density in the actual PM material which would cause a nearly linearly-proportional error in the magnet flux linkage.

In addition, any magnet fill factor across the thickness of each cavity that is less than unity will shift the load line down on each magnet. For the LPM magnet flux linkage calculation, this effectively shifts some of the magnet reluctance to the airgap reluctance, thereby reducing the flux at the airgap. However, this factor alone would require an unreasonably low fill factor to produce the difference shown in Table 4.6. On the other hand, incomplete filling of the cavity at the tips would cause a nearly proportional reduction in λ_{PM}.

No experimental data was available with excitation on both axes so the relative degree of magnetic cross-coupling is evaluated using FEA. Figure 4.27 and Figure 4.28 show families of curves from FEA calculations of L_q versus I_q with varying amounts of I_d, and likewise, L_d versus I_d with varying amounts of I_q. The family of curves for the four-layer IPM machine in Figure 4.28 show no distribution, and therefore, do not indicate any magnetic cross-coupling. For the three-layer IPM machine in Figure 4.27 there is a minor degree of distribution of the L_q curves at low excitation levels. This effect is not likely to be due to cross-coupling. The distribution at low current is more likely due to the precision of the FEA drawing, the specific location of the stator slots with respect to the rotor cavities, the precision of the magnetization directions, and the precision of the solutions at the low energy levels associated with minimal excitation. Also the region of greatest concern is at rated I_q and I_q where there is no distribution within the curve families for both L_q and L_d in both machines.

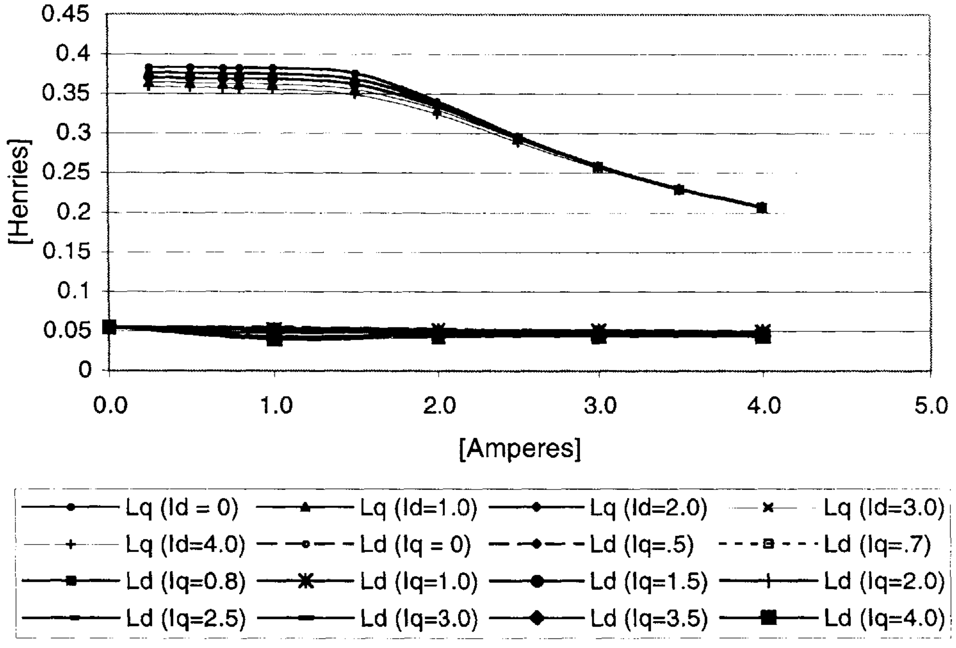

Figure 4.27: Inductance calculations with cross-current excitation for the three-layer experimental IPM machine.

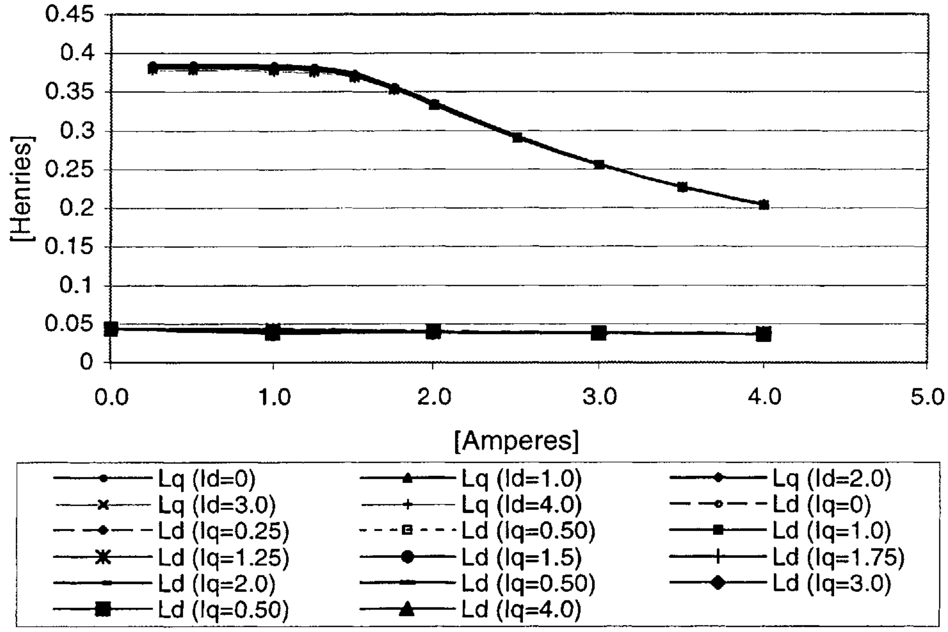

Figure 4.28: Inductance calculations with cross-current excitation for the four-layer experimental IPM machine.

4.5 Summary

The first half of this chapter demonstrates the accuracy of the saturable LPM using an example machine. The calculated lumped parameters are used to predict the performance of the design over a wide speed range. The performance of the design is predicted using both the linear and saturable LPMs and the predictions of the two LPMs are compared. As expected, the linear model cannot provide accurate predictions without appropriate limitations on the drive ratings to prevent operation under conditions of significant magnetic saturation. The machine performance is also described in relation to the ideal, lossless, constant-power design point. Including major loss mechanisms yields more realistic performance predictions. FEA shows good corroboration of the LPM calculations for the *dq* inductances and the converted torque.

The second half of this chapter provides direct verification of the accuracy of the saturable LPM applying it to two existing transversely-laminated IPM machines including a three-layer and a four-layer rotor design. FEA is employed as a verification method as well as a means to illuminate possible sources of error and the reasonableness of the nonlinear equivalent magnetic structure chosen in the saturable LPM. The comparisons show excellent agreement at both high and low q-axis excitation and at rated d-axis excitation, as expected. In particular, the saturable LPM demonstrated itself to be well-suited to analyzing possible deviations from the nominal print dimensions for one of the experimental machines.

The accuracy of the saturable LPM in calculating the key inductance and PM flux linkage parameters has been demonstrated. The accuracy of the saturable LPM for calculating L_q is within 5% for FEA comparison, and within 5-7% at high excitation levels where rated operation is expected for two experimental machines. The likely sources of error are off-nominal machine dimensions for the experimental machines and inaccuracies in the leakage inductance calculations. Cross-coupling was shown to be minor through agreement of L_q calculations by LPM and FEA, through torque-angle calculations, and using cross-current FEA results. PM flux linkage agreement was nearly exact for FEA comparison to the LPM, and within 15-20% for comparison to the experimental machine data. Off-nominal remanent flux density, and imperfect fill factors for the magnets in the cavities should account for most of the PM flux linkage calculation errors.

With confidence in the lumped parameters established, the model can then be used to rapidly predict the remainder of the machine behavior including losses over the full operating speed range. This further demonstrates the usefulness of the LPM tools for the design and optimization of new IPM machine drives. Optimized design of IPM machine drives is the subject for the remainder of the thesis.

Chapter 5

COST OPTIMIZATION OF AN AUTOMOTIVE ISG MACHINE DRIVE

5.1 Introduction

This chapter develops a cost-optimizing design methodology for an automotive integrated starter-generator (ISG) machine drive using an IPM synchronous machine. The optimization method makes use of the lumped parameter models (LPMs) developed in Chapter 3 with the addition of constraining application specifications and optimization design goals. The chosen cost function and the background behind the choice are presented, and the target application requirements are fully described. The use of Monte Carlo synthesis for optimization to a target cost function is outlined and the specific implementation is described. Lastly, local gradient optimization as a means of fine tuning the design is described.

5.2 ISG Requirements

Chapter 1 outlined the general torque and power requirements as functions of crankshaft speed for a high-power automotive ISG application. This section describes the requirements more fully including mechanical, environmental, and cost constraints in addition to the performance and electrical interface requirements.

The system for the ISG application, shown in Figure 5.1, is defined as the IPM electrical machine and the associated converter. Since the system is to be connected to a vehicle battery bus, the electrical system terminals are specified as a DC voltage V_{DC}. For the next-generation automotive electrical system, this system is being investigated for $V_{DC} = 42$ VDC as introduced in Chapter 1. As defined in Chapter 3, the motoring reference direction is used throughout this thesis so that electrical power is defined positive into the system as P_{DC} and shaft power P_{shaft} is defined positive out to the crankshaft. The total machine losses P_l were calculated in Chapter 3, but the ISG system also includes the losses of the converter P_d, which are derived below.

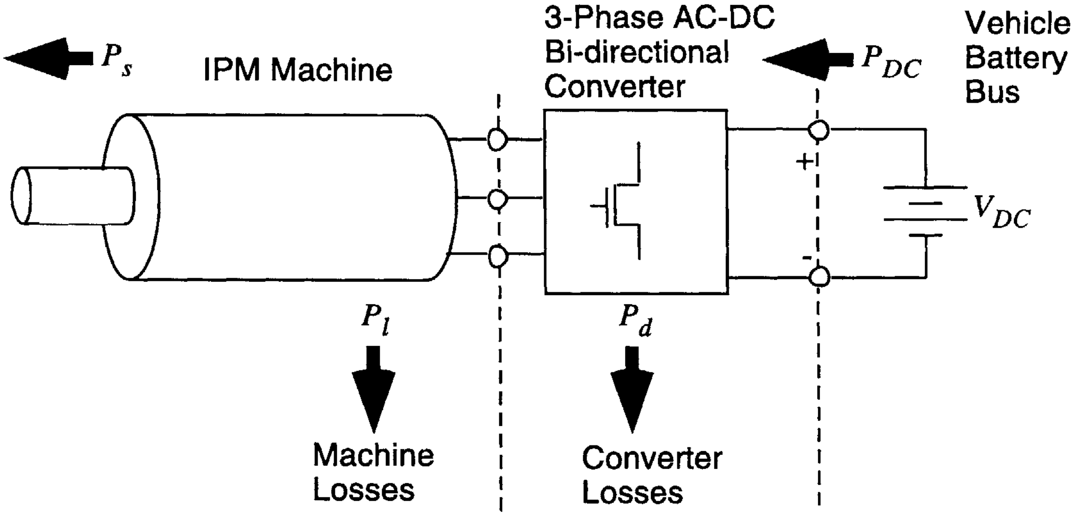

Figure 5.1: Sketch of the ISG IPM machine drive system.

The motoring torque and generating electrical power requirements were given in Figure 1.1 and Figure 1.2. The motoring torque is specified as the shaft torque previously defined as T_{shaft} and the power P_{DC} is specified at the battery bus terminals before the AC-DC converter. Because the motoring region occurs at low speed, the machine losses can be approximated as consisting of only stator winding losses as discussed in Chapter 3. Thus

$$P_l \approx P_a \tag{5.1}$$

which implies that the machine's shaft power and torque can be approximated by converted torque in the absence of significant friction and windage losses in this speed regime as

$$\begin{aligned} P_{te} &\approx P_{shaft} \\ T_e &\approx T_{shaft} \end{aligned} \tag{5.2}$$

Figure 5.2 shows the combined starting and generation requirements referenced to T_{shaft}. The exact shaft requirements during generation will not be known without calculating the system losses for a particular IPM machine drive design, but they are noted as overhead beyond the P_{DC} requirements.

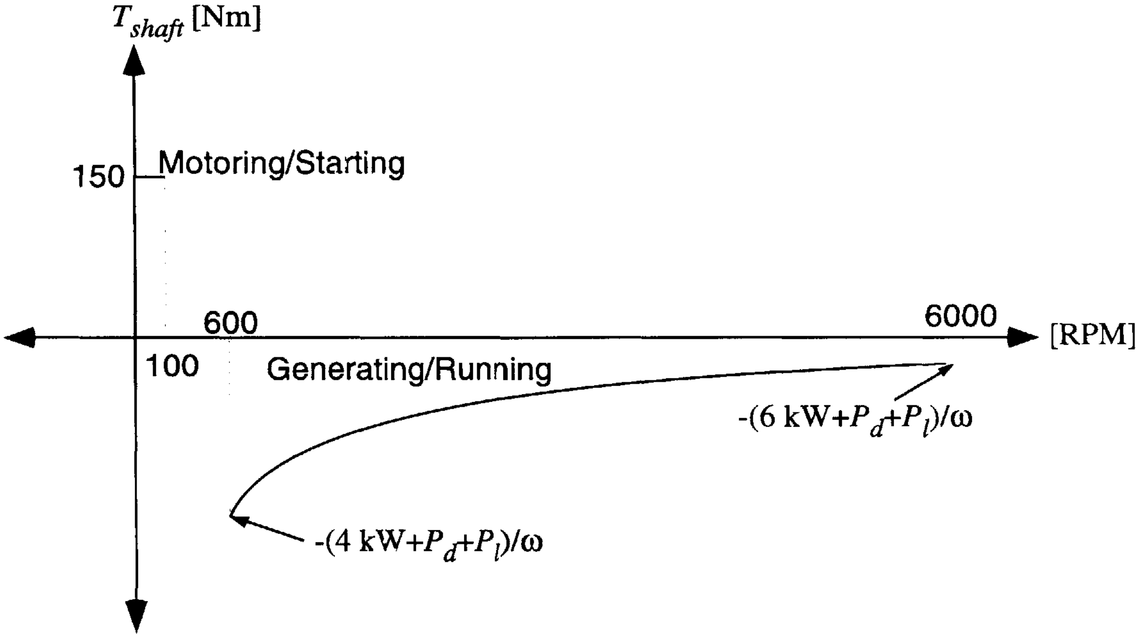

Figure 5.2: Shaft torque versus speed for the ISG application.

The ISG must draw electrical power from the DC bus for starting and deliver electrical power back when the vehicle is at idle speed or above, so the converter must be a bi-directional AC-DC converter capable of three-phase inversion and rectification. As introduced in Chapter 1, the flux weakening capability of the IPM machine drive results in a system with generally lower voltage requirements than non-salient PM machines, so the converter semiconductor switches can be MOSFETs rather than IGBTs.

Figure 5.3 shows a sketch of the baseline converter topology, a conventional three-phase full-bridge converter topology that is based on these assumptions. Since the objective of this research is not power electronic converter design, no attempt has been made to consider novel techniques or topology details. Instead, it is assumed that reasonable full-load converter losses during generation are dominated by the voltage drops across the two MOSFET body diodes in series for each conducting path through the machine. Assuming the drop across the body diode is $V_d = 1.5$ VDC at rated conditions, then the total drop through the converter is 3 VDC. Switching losses in the converter switches are not included in the model, based on the assumption that the converter losses will be dominated by the conduction loss component for fast MOSFET switches operating from such a low bus voltage. Given the generating power requirements versus speed, the converter loss is then approximated as

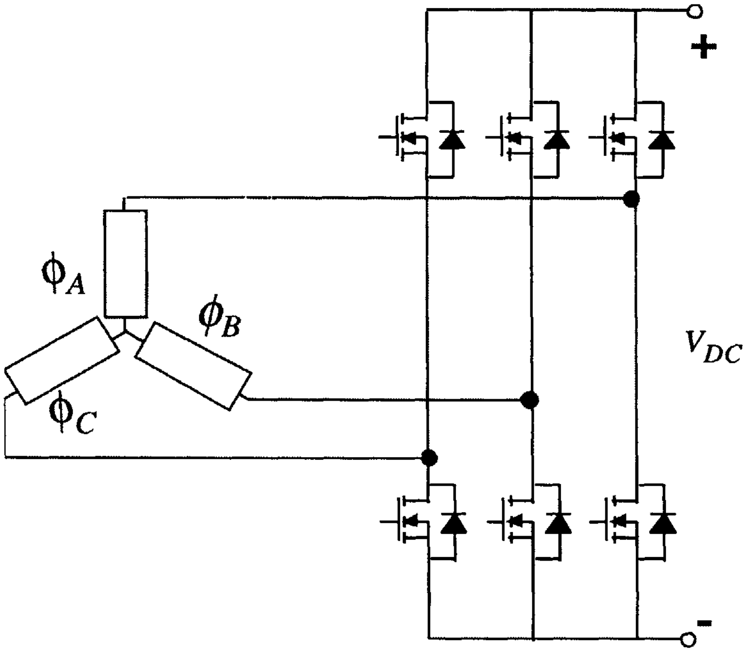

Figure 5.3: Sketch of the IPM drive, a three-phase bi-directional AC-DC converter.

$$\begin{aligned} P_d &= 2V_d \frac{P_{DC}}{V_{DC}} = \frac{3}{42}\left(4000 + \left(\frac{2000}{6000-600}\right)(\Omega - 600)\right) \\ &= \frac{(\Omega - 600)}{37.8} + 286 \text{ Watts} \end{aligned} \tag{5.3}$$

where Ω is the engine speed in rpm.

In addition to delivering the required torque and power, the new ISG system must be more efficient than conventional automotive alternators in order to avoid excessive heating at the elevated output power levels associated with this new system. Since the bulk of typical drive-cycle operation will be at partial load, a single-point efficiency target at a cruise engine speed of 1500 rpm was chosen with a required minimum system efficiency (machine plus converter) of 75%. At 1500 rpm, (2.1) results in a converter efficiency of 93.3% so that the minimum required machine efficiency is 80.6% at the efficiency design point. By comparison, conventional Lundell alternators including their integral rectifiers have efficiencies in the range of 40-60% [2]. Note that low Lundell efficiencies at high speed are dominated by poor fan efficiencies. Such low efficiencies resulting from alternator cost reductions are tolerable in today's vehicles because the average output power is less than 1 kW.

To minimize the need for separate thermal analyses, stator winding current density limits compatible with liquid cooling using engine coolant were established based on automotive industry experience [3]. This coolant can reach temperatures up to 100°C steady-state and up to roughly 120°C on a transient basis, depending on the specific vehicle and environment. The current density limits chosen with this rationale are 20 A/mm^2 steady-state and up to 50 A/mm^2 for periods less than 15 seconds during starting.

The other electrical system concern is protecting the 42 V automotive electrical system from failures in the machine, controller, or converter hardware. One of the major concerns is bus overvoltage caused by the ISG following a failure at high engine speeds. Such overvoltages can come about because the spinning IPM machine can act as an uncontrolled generator feeding power back to the DC bus through the converter diodes even if the MOSFET switches are all deactivated [56]. Based on current preliminary specifications for the 42 V system, it is expected that power devices in the electrical system will be rated between 60 and 100 VDC. For this study, a maximum steady-state post-fault voltage of 55 VDC was selected for the ISG system when operating in this uncontrolled generator mode. This choice results in a machine back-emf voltage limit of 25 Vrms per phase at maximum speed, 6000 rpm, when calculated to include the effects of the converter switch voltages V_d and the conversion coefficient of a standard six-pulse converter [57].[28]

Along with these major electrical constraints and performance specifications, a cost objective function was developed. The system cost is

$$\text{System Cost [\$]} = \text{Machine Cost} + \text{Converter Cost} \tag{5.4}$$

For mass manufacturing scenarios, a simple machine cost model was proposed

$$\sum_{materials} \left((Overhead)(UnitCost\ [\$/\text{kg}])(MaterialMass\ [\text{kg}]) \right) \tag{5.5}$$

The principal materials in terms of mass for the IPM machine are the steel, copper, and magnets. These materials have been assigned the mass-based unit costs and overhead factors shown in Table 5.1. It is assumed that the magnets used in the ISG machine will be made of a bonded-ferrite material rather than more expensive rare-earth magnet materials (e.g., Neodymium-Iron). This assumption is consistent with the maximum limits on the remanent flux density that were set during the optimization exercises. Also from a perspective of achieving a high CPSR, the discussion in Chapter 2 explained that limited λ_{PM} magnitude is desirable which also supports the assumption of ferrite-based magnets.

Since the specific cost of the bonded-ferrite magnets is much higher than that of the copper and steel, an adjustment was made to the magnet overhead factor to prevent the magnets from incurring unjustified cost penalties. After consultation with engineering colleagues in the automotive industry, the magnet overhead factor for bonded ferrite was set such that the magnet overhead cost per unit mass matches that of steel – approximately $1/kg.

Table 5.1: Cost factors for IPM machine materials.

Material	*Unit Cost*	*Overhead Factor*
Copper	$5/kg	2
Steel	$1/kg	2
Bonded Ferrite PM	$11/kg	1.1

As described in Chapter 1, it is apparent that the converter will dominate the cost of the machine drive system at the 4-6 kW power level with the required controlled converter topology. A cost function was developed with the assistance of an automotive OEM based on their experience in building and costing converters [58]. The OEM's cost model was based on a full accounting of the materials, components, processes, and overhead to build three-phase full bridge MOSFET-based converters with current ratings that are consistent with the ISG application. The detailed cost inventory is proprietary to the automobile manufacturer. It was found that the converter cost is roughly linear with respect to the rated RMS current through the power devices. The following formula was arrived at through a curve fit to sampled converter cost calculations with similar ratings

$$\text{Converter Cost} = \$423 + (0.341\ [\$/\text{Arms}])I_b \tag{5.6}$$

where I_b is the converter rated RMS current, and the converter cost is in $US. Equation (2.1) represents the manufacturing cost, not selling price, of the converter assuming a volume of 100,000 units per year. Present day technology was assumed for the manufacturing costs. From this it can be calculated that the base cost of the converter rated for 6 kW with unity power factor and rated voltage is $461. For the rough ISG machine volumes that are being considered this will result in a converter-to-machine cost ratio ranging between 5:1 up to 10:1. Though the total converter cost may seem like a large number, this corresponds to less than 10 cents per Watt which is competitive with other high volume switching power supply applications [59]. Note that the system optimization couples the machine design to the converter cost through the rated current required by the machine which is observed in the results presented in the following chapter.

Mechanical specifications were also set for the ISG application and are summarized in Table 5.2. The stator OD limit is specified to keep the vertical outline of the ISG roughly the same as a conventional flywheel. The rotor ID limit is set to allow space for a torque converter inside the ISG machine. This also keeps the overall length of the engine drivetrain from becoming too long by forcing the necessary rotor surface area out to a larger diameter and therefore lower length than might otherwise be found during optimization. Finally, the overspeed design specification is the top machine speed required without mechanical rotor damage. This is an estimate of the maximum speed that may be reached during abnormal operation of an automobile equipped with a manual transmission.

Table 5.2: Mechanical specifications for ISG machine.

Item	*Specification*
Maximum Stator OD	300 mm
Minimum Rotor ID	160 mm
Minimum Speed without Rotor Damage	10 krpm

5.3 Optimization Methodology

A Monte Carlo optimization method was selected in order to investigate a wide system design space while avoiding erroneous biases about optimal machine geometries [60]. The major core, winding, and magnet parameters are introduced as variables into the LPMs to determine whether a particular candidate design will meet performance specifications and to calculate the total cost of the machine drive system. Figure 1.8 outlined this general procedure but it is repeated here as Figure 5.4 for clarity. The lowest-cost designs are then further refined using a local gradient optimizer.

The two-stage optimization method involving a broad optimization followed by a local gradient refinement requires the generation of millions of designs to cover the desired design space with sufficient resolution. The availability of the LPM detailed in Chapter 3 makes it possible to conveniently carry out such large numbers of design iterations using modern computers with a fraction of a second of computing time for each design. This methodology can also easily be adapted to any objective function such as torque or CPSR maximization.

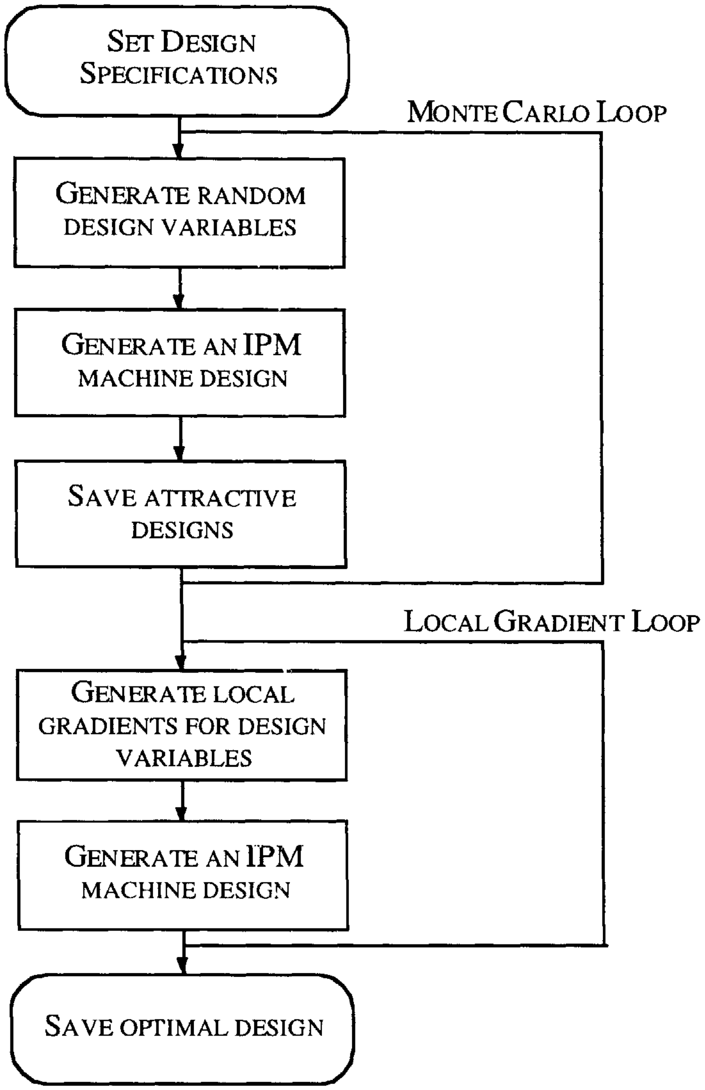

Figure 5.4: Optimization process for the IPM machine ISG application.

To improve the efficiency of the optimization and widen its applicability to different IPM machine configurations (ratings, main dimensions, number of cavities), an effort was made to both minimize the number of variables and to define the variables non-dimensionally whenever possible. Table 5.3 lists the parameters that are randomly varied for optimization, and Table 5.4 lists the parameters that are typically held constant for a single optimization exercise. Each parameter held constant was chosen either because the parameter has only a minor effect on performance or because it reflects a fundamental design decision made before entering into the optimization process.

The radial dimensions are defined as non-dimensional quantities except for one reference dimension, selected as either the stator inside or outside radius (r_{co} or r). In the case of the ISG the machine is built from the outside inwards since there is a stator OD limit. The stator back-iron depth d_b is retained as a dimensional quantity because the lower limits are often selected in conjunction with the main radii (r_{co} or r) to maintain the necessary mechanical stiffness of the stator yoke.

Table 5.3: Random design variables for optimization.

Description	*Variable*	*Units*
Stator OD	d_{out}	m
Stator back iron depth	d_b	m
Ratio of slot height to width	λ_{hs}	
Ratio of slot opening to slot-tooth pitch	λ_{us}	
Ratio of slot width to slot-tooth pitch	λ_s	
Ratio of rotor OD to ID	λ_{rd}	
Ratio of total cavity to total rotor depth	λ_m	
Percentage of total cavity depth for each cavity	λ_h	
Percentage of total rotor core depth for each rotor section	λ_{md}	
Ratio of angular span of largest magnet from tip to tip versus the span of a pole	λ_{mo}	
Number of slots distributed	m_a	
Number of slots short pitched	n_{ssp}	
Number of turns per slot	$N_a/(2m_a p)$	
Number of pole pairs	p	
Active length	l	m
Magnet remanent flux density	B_r	T

The non-dimensional stator ratios are defined from the geometrical parameters in Chapter 3 according to

Table 5.4: Constant parameters for optimization.

Description	*Constant*	*Units*
Number of phases	q	
Number of cavity layers	K	
Slot opening depth	d_o	m
Slot fill factor	λ_a	m
Rotor bridge thickness	w_b	m
Rotor center post thickness	w_c	m
Airgap	g	m
Base (not necessarily rated) RMS current	I_b	Arms
Base (rated) RMS voltage	V_b	Vrms
Relative length of middle cavity segment (explained in the text)	λ_{ia}	
Relative angle between side segments of cavities (explained in the text)	λ_{4a}	

$$\lambda_{hs} = \frac{d_s}{w_{st}} \tag{5.7}$$

$$\lambda_s = \frac{w_{st}}{w_{st} + w_t} \tag{5.8}$$

$$\lambda_{us} = \frac{w_o}{w_o + w_f} \tag{5.9}$$

From r_{co}, d_b, and (2.2) through (2.3) the stator inside radius is derived as

$$r = \frac{r_{co} - d_b}{1 + \frac{2\pi\lambda_{hs}\lambda_s}{n_s}\left(1 + \frac{\pi(\lambda_s - \lambda_{us})}{n_s}\right)} \tag{5.10}$$

where n_s is calculated using (3.1) and (3.3). Calculating r_{co} from r is accomplished by solving (2.5) for r_{co}. From these quantities and the input parameters in Table 5.3 and Table 5.4, k_{an}, R_a, L_{qm}, L_l, and l_{out} are calculated as specified in Section 3.2. The rotor outside radius is calculated from r and g, and the inside radius is specified by the variable λ_{rd} as

$$r_{ri} = \lambda_{rd} r_{ro} \tag{5.11}$$

The shapes of the magnet cavities could result in many parameters if arbitrary non-parallel shapes are permitted. With the magnet cavities restricted to three straight sections per layer, the location of the cavities can be fully specified by four points as shown for the second layer labeled A, B, C, and D in Figure 5.5. By exploiting the symmetry across the d-axis, the specification can be reduced to finding the radius at point E, r_{rmk}, for the k^{th} cavity, and the outer and inner angular spans θ_{mok} and θ_{mik}.

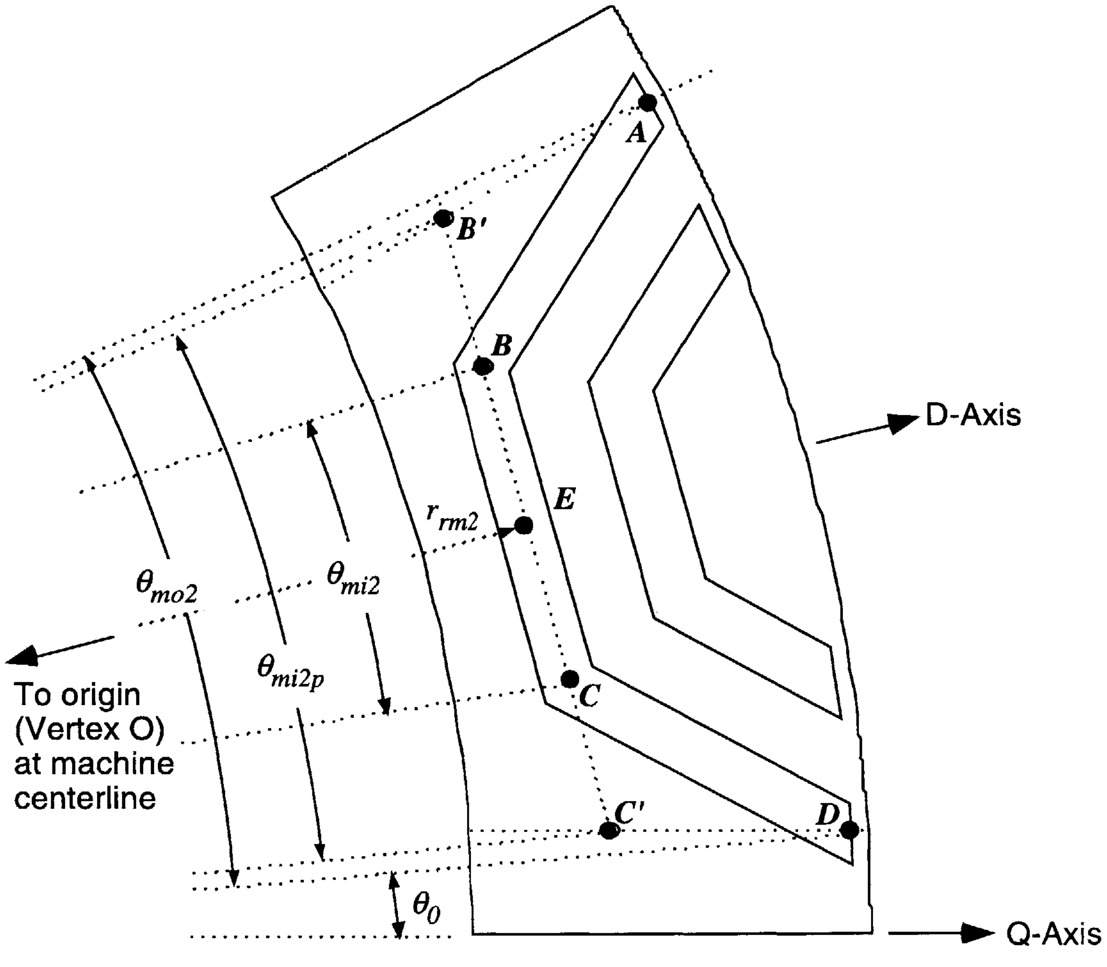

Figure 5.5: Definition of end and corner points for a magnet cavity.

To specify the magnet parameters non-dimensionally, the radial depths of each core section and cavity must be assembled first. Using the ratios λ_m, λ_h, and λ_{md}, the depths shown in Figure 1.3 are

$$d_{mk} = \lambda_{hk}\lambda_m\left(r_{ro} - r_{ri}\right) \tag{5.12}$$

$$d_{rk} = \lambda_{mdk}\left(1 - \lambda_m\right)\left(r_{ro} - r_{ri}\right) \tag{5.13}$$

Then, r_{rmk} is calculated as

$$r_{rmk} = r_{ro} - \sum_{i=1}^{k} d_{ri} - \frac{d_{mk}}{2} - \sum_{i=0}^{k-1} d_{mi} \tag{5.14}$$

Compared to other geometric factors, the relative difference between θ_{mok} and θ_{mik} has a minor effect on the LPM predictions. The two possible specifications

$$\theta_{mik} = \begin{cases} \theta_{mok}/2, \text{ or} \\ \lambda_{ia}\theta_{mikp} \end{cases} \tag{5.15}$$

have been tested where λ_{ia} is a constant scale factor between 0 and 1 and θ_{mikp} is the maximum allowable inside angular span that would make segments $\overline{AB}$ and $\overline{CD}$ parallel to the q-axis. Figure 5.5 illustrates this limit where $\overline{AB'}$ and $\overline{CD'}$ are parallel to the q-axis. θ_{mok} is also specified non-dimensionally as a fraction of the full pole pitch

$$\theta_{mok} = \lambda_{mo}\frac{\pi}{p} \tag{5.16}$$

Using trigonometry, the maximum inner angular span is

$$\theta_{mikp} = \tan^{-1}\left(\tan\left(\frac{\pi}{2p}\right) - \frac{\left(r_{ro} - w_{bk}\right)\sin(\theta_0)}{r_{rmk}\sin\left(\frac{\pi(p-1)}{2p}\right)}\right) \tag{5.17}$$

where the angle from the q-axis to $\overline{OD}$ is

$$\theta_0 = \frac{\pi/p - \theta_{mok}}{2} \tag{5.18}$$

as shown in Figure 5.5.

By specifying the largest cavity first, the rest of the cavities can be specified with only one additional parameter and the single assumption that the middle segment of each cavity is parallel to the middle segment of the largest cavity. Figure 5.6 demonstrates the necessary geometric parameters for the double-layer IPM machine. Using all of the r_{rmk} values from (2.4), the location of E'' is defined. Then it is recognized that for the steel path between the magnets to have the same depth, the corner point B'' must intersect the line formed by half the included angle $\angle ABE$ which is defined as θ_{4k}. In Figure 5.6 the largest cavity is associated with $k=2$. This same construction is then made on the $(k-1)^{\text{th}}$ cavity, where the included angle is now defined as $\angle A''B''E'' = \theta_{42}+\theta_{41}$ for the double-layer case. If, in addition to the center segment of each cavity, the side segments are also parallel, then $\theta_{41}=\theta_{42}$. In general, though, another non-dimensional scalar is defined for side segments at arbitrary angles so that

$$\theta_{4k} = \lambda_{4a}\theta_{4K} \tag{5.19}$$

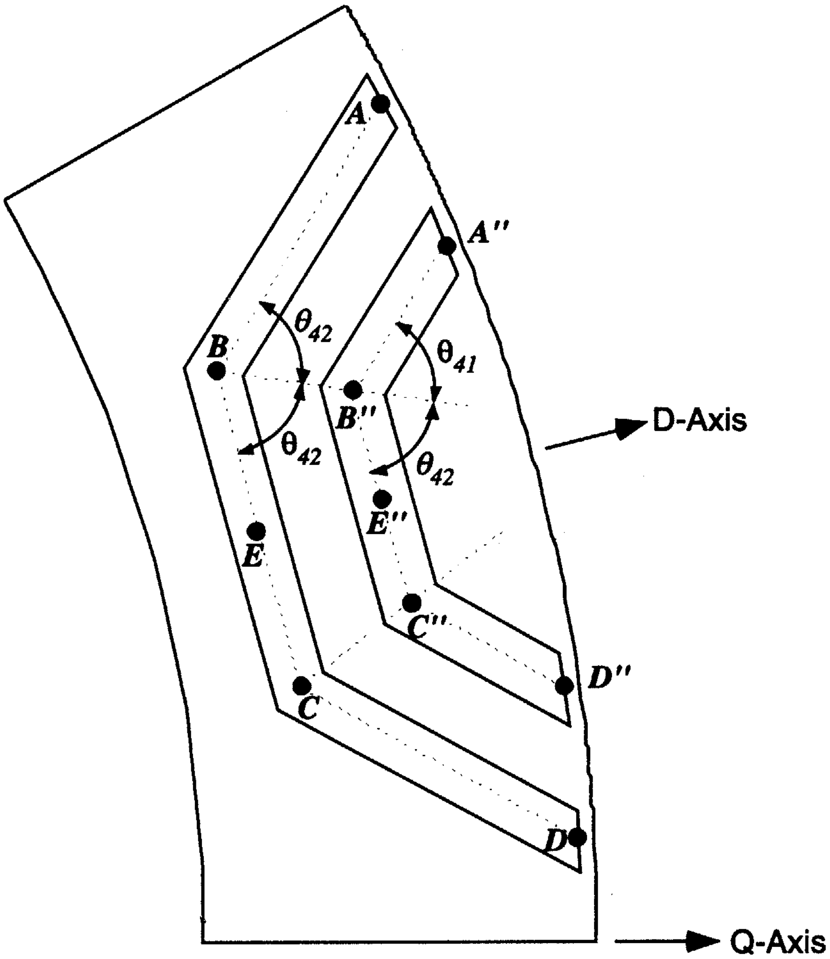

Figure 5.6: Definition of smaller cavities referenced to the largest cavity.

where θ_{4K} is the angle of the K^{th}, or largest, cavity.

The remaining parameters (both constant and variable) from Table 5.3 and Table 5.4 that have not been discussed are not synthesized as non-dimensional quantities and are directly defined in the LPMs of Chapter 3.

With specified input system parameters, the random numbers for each of the 16 variables in Table 5.3 are generated. The static calculations to fully specify the machine geometry and winding patterns are then completed so that the inductances, fluxes, and phase resistance can be determined. The random variable limits are chosen where possible to prevent unrealizable geometries but for remainder of the geometry is checked at this point to see that it does not violate any basic physical constraints, and rejected if it does. Then the optimizer checks desired operating characteristics at specified speeds where reactances, losses, and both the electrical and mechanical terminal characteristics are calculated. The design calculations repeat millions of times with a new set of random numbers for each design, and the designs that meet the criteria set forth in Section 5.2 are saved.

Attractive designs are then locally optimized using a gradient optimizer- routine with a subset of the variables. The attractive designs are those that have the best objective function value (system cost in the case of the ISG optimization) and which have cross-sections that are realistic (e.g. no zero length magnet segments). The local gradient optimization uses the built-in MATLAB function, CONSTR.M, which conducts a gradient search for a given list of variables and the machine design script [52]. A small range must be provided for each variable to achieve convergent results because the IPM machine calculations leading to cost are highly nonlinear. If a variable limit is approached within a tolerance the limits are adjusted and the local optimization process begins again until a specified solution tolerance is reached. Finally, the best design is post-processed to calculate additional parameters of interest including weight, inertia, cost breakdowns by material, and additional performance parameters such as shear stress. The Monte Carlo and local gradient optimization codes for the ISG application are implemented in MATLAB and found in Appendix B. Additional Monte Carlo software contained in Appendix C is designed to optimize torque and constant-power speed range capabilities (instead of the ISG cost function (2.5)) while using the same underlying LPMs.

5.4 Summary

This chapter has specified the details of the automotive ISG application requirements. The specifications have been described in the context of how they constrain the design of an IPM machine drive system, and in particular, the calculations of the LPMs. The requirements include performance, electrical, thermal, and mechanical constraints that together make it challenging to find a single system that simultaneously meets all of them. This high complexity level motivated the adoption of Monte Carlo optimization techniques to rapidly identify the best machine designs that meet all of the application constraints. The cost objective function used as the basis for selecting the "best" designs has also been presented.

The details of the variable and constant parameters that are introduced for a single machine design iteration were then presented. Up to sixteen variables are considered in the design of the IPM machine drive for this application, again supporting the advantages of Monte Carlo optimization techniques.

As described in this chapter, many of the input parameters can be defined as non-dimensional quantities to simplify the scaling of the optimization solution for different applications. The chapter closed by summarizing the optimization process executed by the software.

In the next chapter, additional issues are presented that require attention for the ISG application, but which fall outside of the formal optimization process.

Chapter 6

ANCILLARY ISG DESIGN CONSIDERATIONS

6.1 Introduction

The ISG application requirements detailed in the Chapter 5 raise system design issues that are not directly related to electrical performance but are nonetheless critical to the ultimate success of the system. This chapter discusses two additional major issues that arise in the design of an IPM machine drive for an automotive ISG application: structural integrity and demagnetization.

Structural integrity is discussed in light of the geometric constraints and the application's mechanical design point. Special attention is given to the impact that the particular rotor structure of an IPM machine has on appropriate mechanical design.

Concern regarding demagnetization is significant because the dual goals of high performance and low cost typically drive the design to conditions that may cause the magnets to be more susceptible to this damaging condition. Both issues are discussed in the context of how proper design will affect the design and optimization of the IPM machine-based ISG.

6.2 Structural Integrity

The major structural integrity design issue is to prevent the machine from exceeding the yield strength of the rotor core. Chapter 5 set forth mechanical constraints for the ISG application that make it challenging for the rotor core material to meet the yield strength requirements. This section examines the forces on the rotor of an ISG with the given constraints and the localized stress concentrations that are particular to a transversely-laminated IPM rotor cross-section. This is followed by a discussion of methods to mitigate the peak stresses observed in the rotor using FEA. The ultimate objective is to determine a rotor geometry that will experience peak mechanical stresses that are below the material yield strength at the mechanical design point.

6.2.1 Qualitative Analysis of Resultant Forces and Stress State

For the purpose of this discussion, the mechanical design point corresponds to the application specification that produces the worst-case mechanical stress in the IPM rotor. The assumptions employed in this development are as follows:

- steady-state speed conditions only;
- temperature effects are neglected;
- baseline core material is M19 29-gage electrical steel;
- mechanical specifications apply as provided in Chapter 5;
- yield is indicated by planar Von Mises stress.

With these assumptions, the forces on the rotor are dominated by the steady-state centrifugal forces at constant speed. Therefore, the mechanical design point corresponds to steady-state operation at the maximum overspeed value, 10 krpm.

The analytical calculation of the peak stresses due to centrifugal forces on a transversely-laminated IPM machine is a challenging task that is not attempted in this thesis since it is not a central theme of the research. However, these peak stresses affect the boundaries of the optimization variables that determine the optimal system design, so a qualitative discussion of the resultant forces due to inertial loading is appropriate. The discussion is conducted employing well-known principles of the behavior of materials under static loading [61, 62].

Figure 6.1 shows a solid rotor cross-section with annotations to indicate the major forces on the core due to centrifugal loading. At the simplest level, neglecting the magnet cavities, the rotor resembles a hoop with constant centrifugal loading. Under these conditions, an elemental member of the rotor is under tangential tension and radial compression. Thin-walled hoop approximations can be justified for modeling the rotor because of the narrow depth of the ISG rotor in comparison to the rotor ID . As a result, the rotor segments mainly experience tangential tension forces. Using this assumption, the major factors affecting the peak stress are the average radius of the 'hoop' and the rotational speed. Each of these factors has a nominally squared effect on the Von Mises stress.

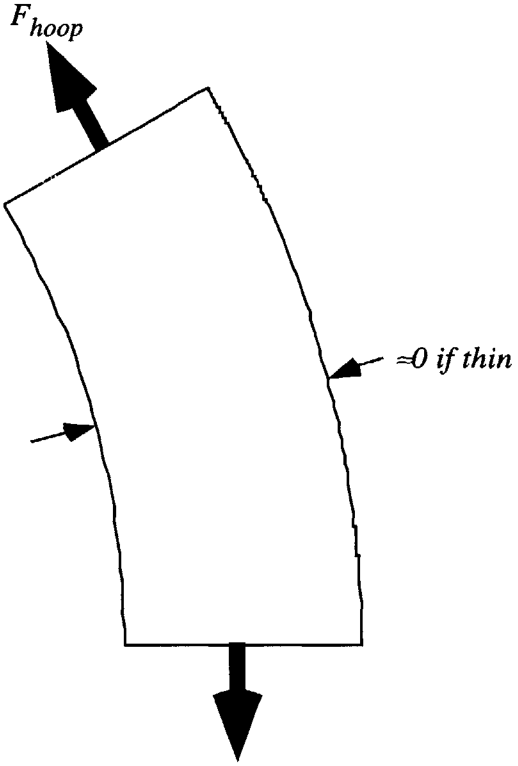

Figure 6.1: Sketch of resultant forces on a solid rotor.

If the rotor cavities are now considered as in Figure 6.2 which only contains one cavity layer, the pole piece centered on the *d*-axis is now only attached to the rest of the core by the thin bridges at each end. Therefore, the centrifugal loading on the pole piece is not evenly distributed around the rotor 'hoop' and is substantially a radially-directed inertial load on the two retaining bridges.

It should be noted that the bonded PM material in the cavity will also contribute to this loading because it is generally less stiff than the steel and will therefore contribute additional loading against the inside edge of the pole piece. Therefore, the equivalent mass, m_1 in Figure 6.2, must be the sum of both the pole piece and the magnet (the shaded portion of Figure 6.2).

The challenge then reduces to modeling the bridges, and this is largely dependent on the specific bridge shape. If the bridges are substantially straight, then beam bending approximations are appropriate. As multiple layers are considered as in Figure 6.3, each layer can be considered as independently loaded if the inter-cavity steel sections are wide enough to distribute any stress concentrations between adjacent bridges. The load on each bridge is then the end load in the radial direction due to the inertial loading on the remaining section of the pole-piece between the bridge under consideration and the *d*-axis.

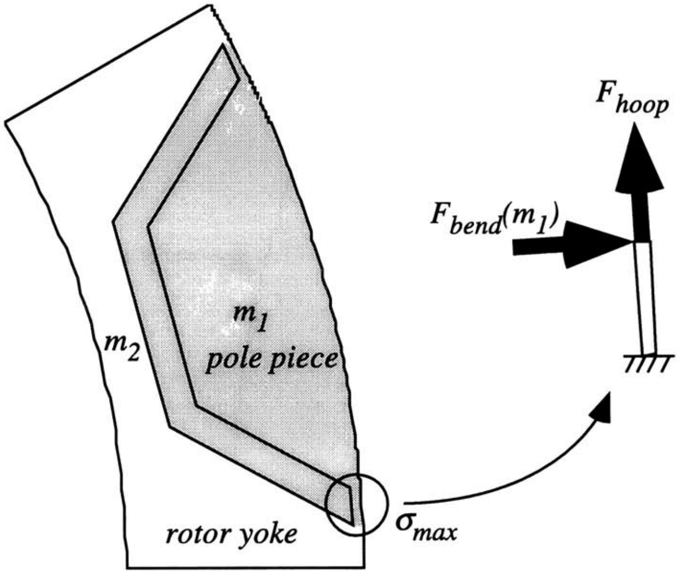

Figure 6.2: Sketch of resultant forces on an IPM rotor with one magnet-filled cavity.

If the bridges on each layer have the same dimensions, the bridge at the end of the longest cavity will be under the highest stress. If the steel bridges are rounded, then the effective length of the 'beam' is reduced, and the approximations are no longer reasonable. The rounded bridge now resembles a round notch stress concentration element under side loading as shown in Figure 6.4.

The precise location of the peak stress within each bridge configuration would require significant analysis. In particular, the equivalent mounting (fixed or simple) at the ends of each 'beam' for the straight bridge model is not clearly defined. If the ends of the bridge have minimal bending compared to the rest of bridge, it is reasonable to assume that the peak stress will be found at the ends. In contrast, the peak stress in the rounded cavity structural model would be expected at the root of the stress concentration which is the midpoint of the bridge.

At this stage, some general observations can be made about IPM rotor design decisions that would worsen or improve the mechanical stress conditions.

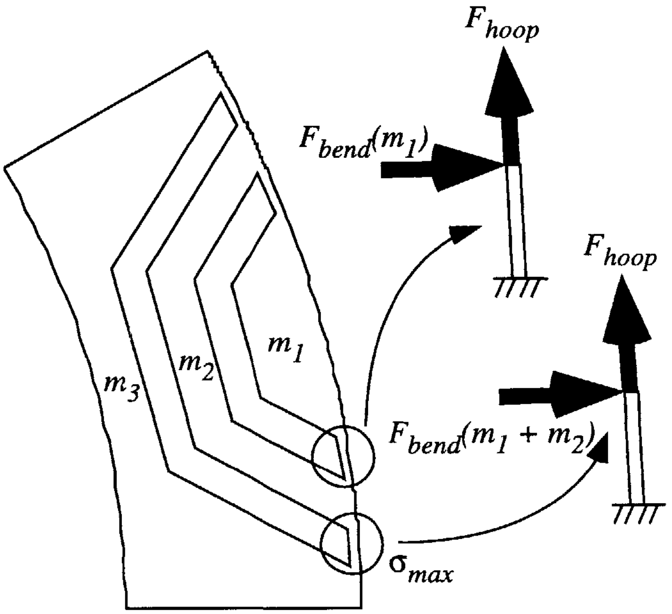

Figure 6.3: Sketch of resultant forces on an IPM rotor with multiple layers.

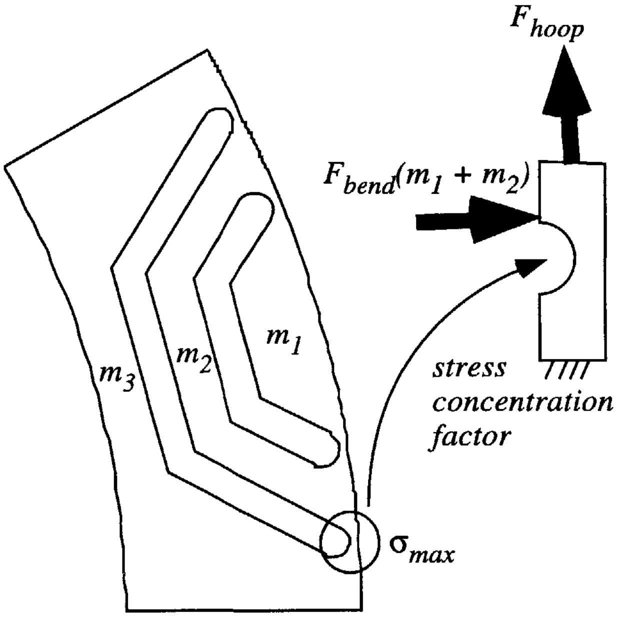

Figure 6.4: Sketch of resultant forces on an IPM rotor with multiple cavity layers with rounded tips.

- Maximum rotor speed – A 10% reduction in the mechanical design point speed would reduce the peak Von Mises stress by almost 20%.

- Rotor OD – Similarly, a 10% reduction in the radius at the rotor surface, where the bridges are located, would also reduce the stress by a 20% factor.

- Rounded bridges – The 'beam' stresses are reduced as the 'beam' gets shorter with all other dimensions equal. Based on the characteristics of the notch stress concentration model, a circularly-rounded bridge shape should nearly minimize the peak stress.

- Smaller pole pieces – A 10% reduction of the deflecting pole piece mass per unit axial length will reduce the stress almost linearly. This can be achieved by reducing the fraction of the pole pitch that the cavities span, or the same effect can produced by increasing the number of machine poles. Alternatively, adding a center post across the d-axis of each cavity will divide the deflecting mass approximately in half.

Another factor in the resultant forces caused by the inertial loading is the effect that the radial deflection of the entire rotor has on the magnitude of the tensile component of hoop stress. The hoop tension in the bridge is due to stretching as the rotor expands into the airgap at higher speeds. The implicit boundary conditions in hoop stress calculations are that the rotor ID and OD boundaries are unconstrained. As a result, reduction of the deflection at either boundary will reduce the expansion of the rotor at the bridge radius and therefore the hoop stress component of loading. Constraining the rotor OD is problematic since it would require a material substantially stiffer than steel to decrease the radial bending under inertial load. Furthermore, adding any material in the airgap that adversely affects the electromagnetic saliency of the original rotor would degrade the performance of the machine.

Constraining the rotor ID is a more feasible solution for improving the structural integrity of the rotor. Since there is already a hub that must attach the rotor to the crankshaft, there is an opportunity to specially design the hub to retain the rotor radially. Typically a hub is only designed to transmit the torque in the circumferential direction as would occur with a hub that is press fit inside the rotor. A press fit, though, does nothing to constrain the rotor ID and so would not mitigate the maximum stress at the mechanical design point.

If there are no space constraints inside the rotor ID, a variety of different hub fixtures might be considered. A welded hub may work but could alter the magnetic properties of the core. One alternative is an axial cylinder that mates with the rotor ID using dovetailed surfaces as shown in Figure 6.5. Another alternative is to construct an end plate with studs distributed around the circumference of the end plate (one per pole) as shown in Figure 6.6. The laminations would be cut with a hole on the q-axis where the core is widest (i.e. there no cavities on the q-axis), and then assembled onto the studs. This system is only practical if sufficient bolt tension can be developed and maintained so that the radial load is taken up by the end plate. If adequate bolt tension is not developed, there will be significant side-loading on the studs that would likely result in shearing off the studs at the surface of the end plate.

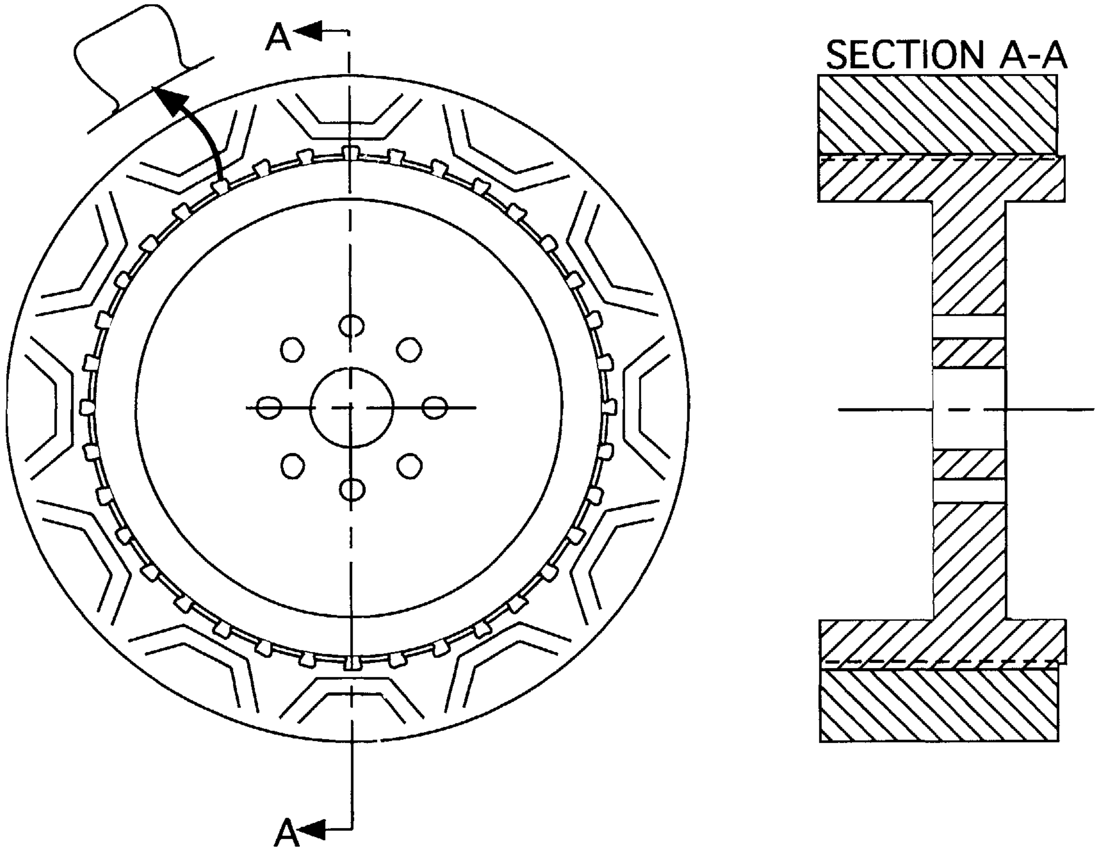

Figure 6.5: Rotor hub design using dovetailed joints between the hub and rotor ID.

The advantage of the dovetail fixture or any fixture along the rotor ID surface is that it is structurally robust and nearly symmetric if the radial plate portion of the hub is located axially near the midpoint of the rotor stack. It chief disadvantage is that the hub cylinder has a finite thickness that may make it necessary to reduce the available space for the rotor laminations. The advantage of an endplate structure is that the radial plate is at the end of the stack and does not use any internal real estate that might otherwise be allocated for a clutch or torque converter. As a result, this approach may yield the most compact ISG configuration. Furthermore, the absence of the internal hub allows the rotor to be designed with the smallest possible ID and OD which will reduce the peak stress (squared impact on stress). However, any endplate approach must solve the practical installation problems associated with heavily-loaded studs and compressed laminations.

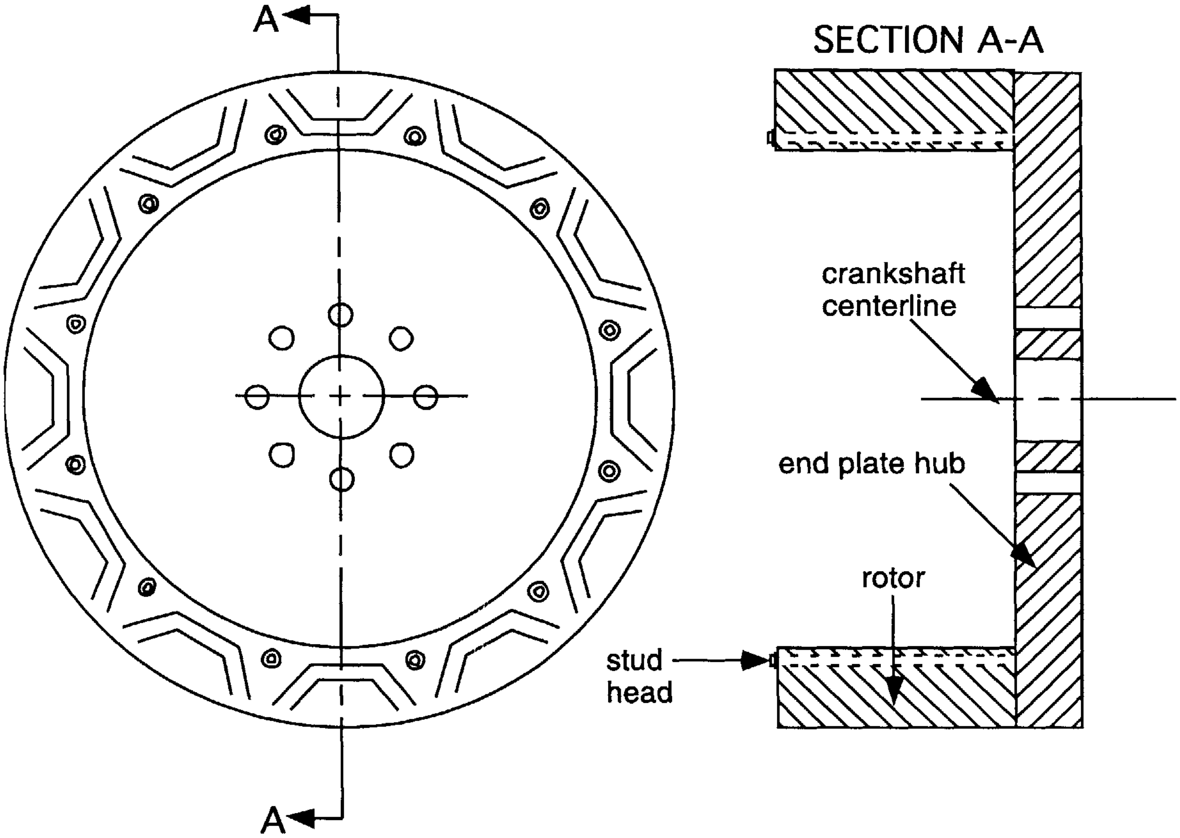

Figure 6.6: Rotor hub design using axial bolts through the stack to an end plate.

In the following section the endplate hub structure is analyzed in concert with proposed rotor cross-section modifications to demonstrate a plausible solution for the mechanical design of an IPM machine for the ISG application. The endplate design is chosen for analysis because it allows the smallest rotor diameters with the given ISG constraint to provide space inside the rotor for a torque converter.

6.2.2 Structural FEA

Structural FEA was conducted to confirm the qualitative understandings presented above. Since it is impractical to carry out a separate mechanical FEA for each new design, these results are also used as a baseline for scaling to other IPM machine designs, provided that the dimensional differences with the baseline are sufficiently small. The FEA was carried out using the ANSYS 2D software package [63].

Figure 6.7 shows the predicted radial displacement of a double-layer IPM machine at 10 krpm without considering any rotor ID deflection constraint due to an attached hub (i.e. a free rotor ID boundary). This cross-section is from an ISG with 12 poles and a rotor OD of 122 mm having straight-edged bridges. The plot indicates a maximum deflection on the *d*-axis outer surface of 0.42 mm which is 64% of the nominal specified ISG airgap. The plot confirms that the bulk of the deflection gradients are in the bridges since the rotor yoke and main pole piece are both uniformly deflected. This is reasonable because the yoke and pole piece are much thicker than the bridges and so should not bend very much by comparison.

It should also be noted that the bonded magnet material is in roughly continuous contact with the inner boundaries of the two *d*-axis pole pieces. The associated tangential stress plot shown in Figure 6.8 predicts a peak stress of 2.6 GPa at the end of the bridge on the largest cavity. Qualitatively, these results match the expected trends quite well. Unfortunately, the peak stress is more than seven times the yield stress of typical electrical steel.

To mitigate the predicted stress, the end plate hub design was analyzed as a means of reducing the radial loading. Furthermore, the machine was sized so that the rotor ID is at the minimum specified limit, the bridges were rounded, and posts were added to the midpoint of the cavities. Figure 6.9 shows the deflection of the combined hub-rotor structure in the R-Z plane (with the crankshaft centerline shown on the left. Physically, this FE model is half of the structure shown in Section A-A of Figure 6.6. The underlying axisymmetric model leads to this deflection plot that can be revolved around the crankshaft centerline. The maximum deflection at 10 krpm is 0.039 mm at the far end of the rotor stack from the endplate. This is about 70% less deflection at the rotor ID than predicted for the previous configuration with an unconstrained rotor ID in Figure 6.7.

After applying this calculated boundary condition to the rotor ID of an $R-\theta$ plane rotor model, the Von Mises stress was calculated and the results are shown in Figure 6.10. Note that in this particular model, the center post of the smaller cavity is not semi-circular. This study was conducted at a point when the necessary center shape had not been finalized. The shape of the center post on the smaller cavity, though, is not significant as the preceding discussion suggests because this is not the point of maximum stress in the rotor. The stress at the straight-edged center post should actually be worse than if it had been rounded making the analysis marginally more conservative. With these design and boundary condition changes, the peak stress at the 10 krpm mechanical design point has reduced by a factor of five, so that the maximum stress is only 20% higher than the yield stress of M19 steel. Though not shown here, analyses were also conducted with a specified deflection of zero on the rotor ID surface, and the resulting Von Mises stress in this case was about 25% lower than the M19 steel yield strength.

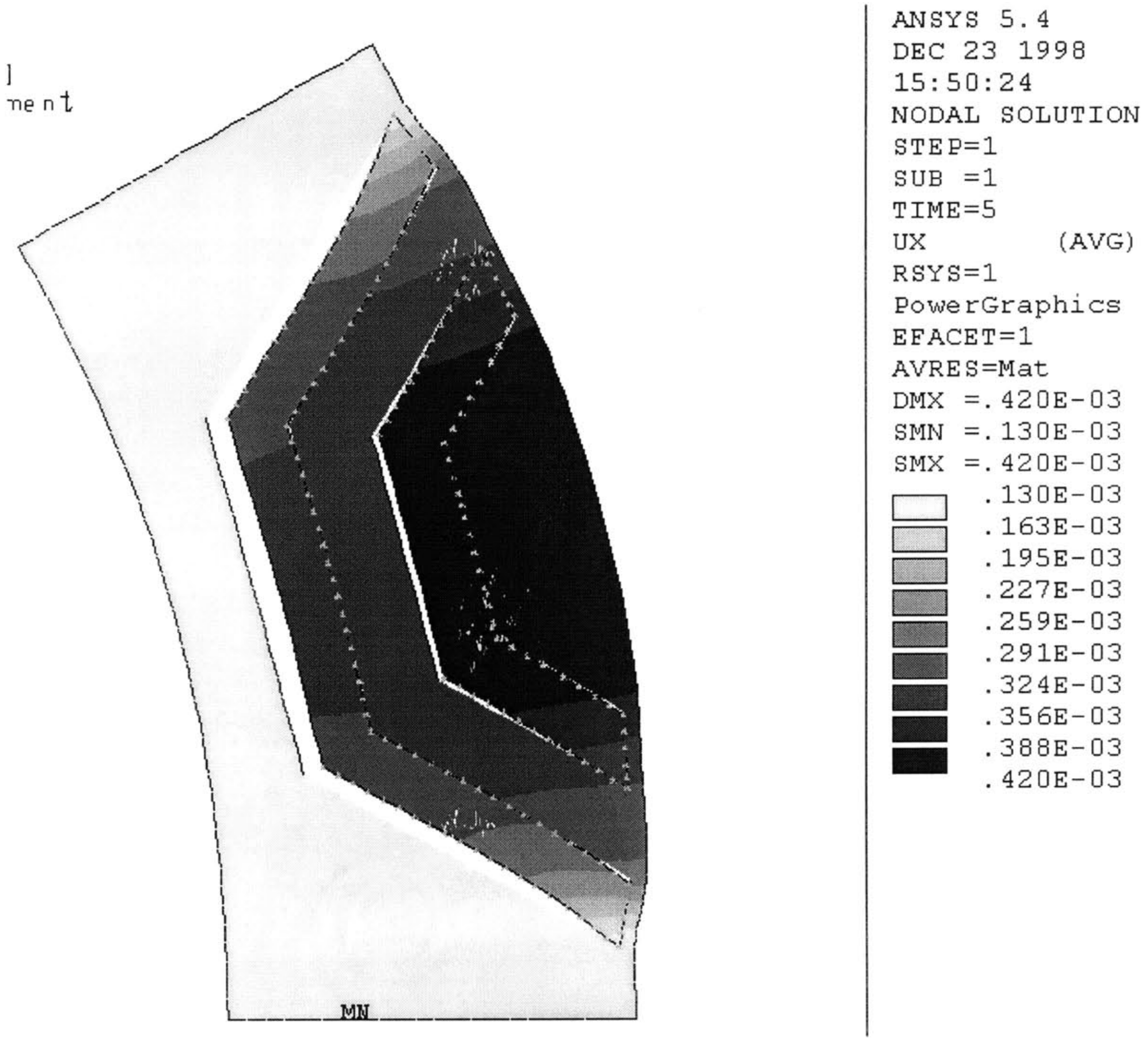

Figure 6.7: Radial displacement with straight-edge bridges at 10 krpm.

All of these results support the conclusion that the IPM machine for the ISG application should be designed with rounded bridges, a minimized diameter, and center posts. Furthermore, the results indicate that additional steps may be required to further reduce the peak stresses within the limits of M19 steel. For example, a modest reduction in the mechanical design point speed would provide one effective means of meeting the mechanical strength limit if the automotive application constraints could be modified. For the rotor used in this analysis the required change in the mechanical design point can be estimated using

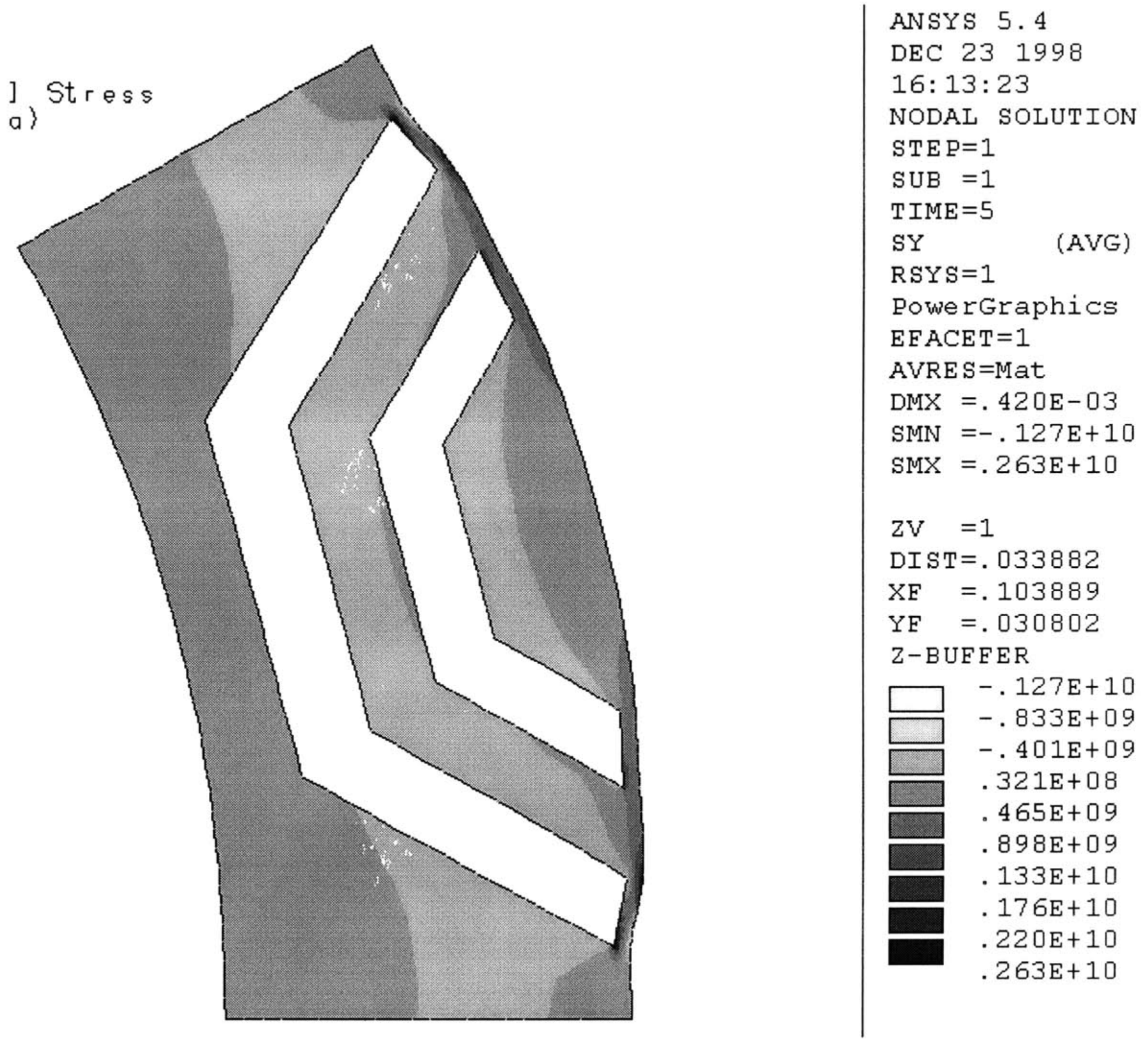

Figure 6.8: Tangential stress [Pa] with straight-edged bridges at 10 krpm.

$$10000\ \text{RPM}\sqrt{\frac{350\ \text{MPa}}{420\ \text{MPa}}} = 9130\ \text{RPM} \tag{6.1}$$

which is less than a 10% reduction in the maximum speed requirement. Also alternative materials with greater yield strength may be considered. These stress-mitigating solutions are discussed further in the next chapter in the context of the particular ISG solution.

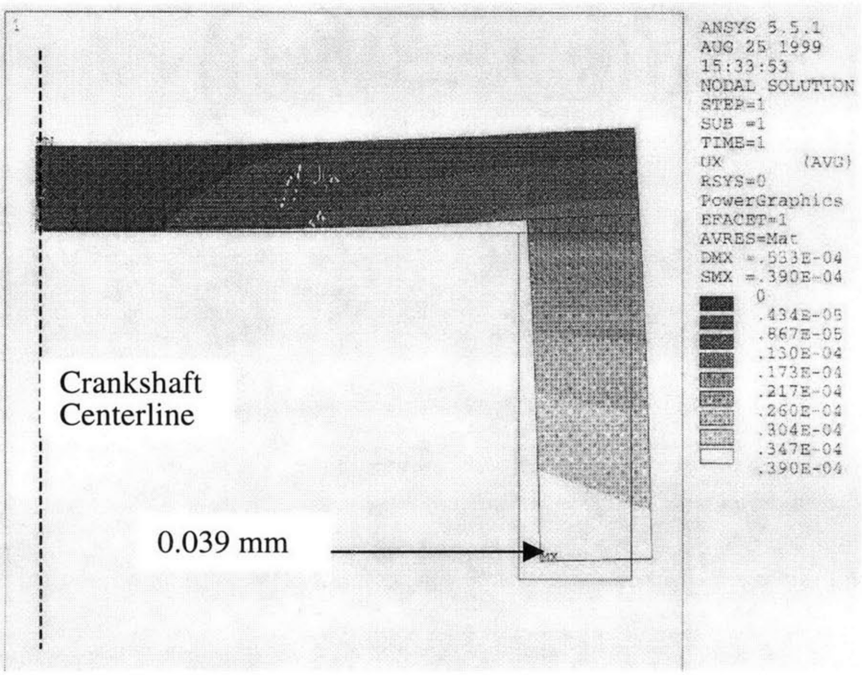

Figure 6.9: Deflection of the rotor with endplate hub design in R-Z plane (axisymmetric).

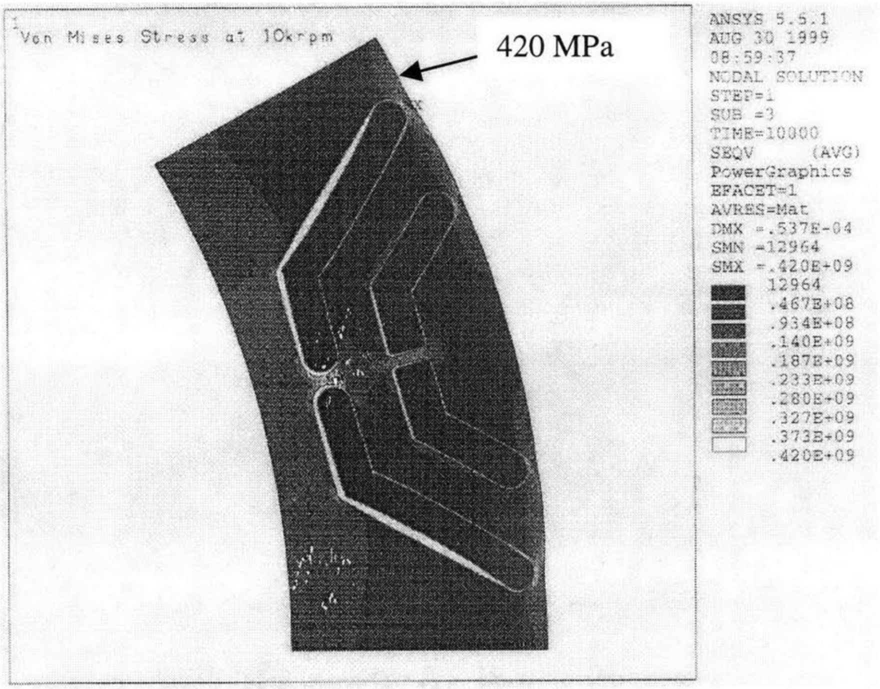

Figure 6.10: Von Mises stress at 10 krpm with rotor ID deflection constrained by hub.

6.3 Demagnetization

Although small regions of localized demagnetization are not unusual during normal operation for permanent magnets used in rotating machines, large regions of irreversible demagnetization must be avoided to maintain repeatable performance. In this section the process of demagnetization is briefly discussed using well-known hard magnetic material theory [64], and the issues particular to demagnetization in IPM machines are presented.

Normally, PM synchronous machines function with the magnets operating on a fully reversible recoil line when subjected to the negative external magnetic field resulting from stator winding excitation. To be fully reversible, the excitation must not exceed the intrinsic coercivity H_{ci} of the material. Figure 6.11 shows the second quadrant of the BH curve for a typical ferrite-based permanent-magnet material. The original fully-reversible recoil line extends from the remanent flux density B_r point down to the intersection of the recoil line with H_{ci}.

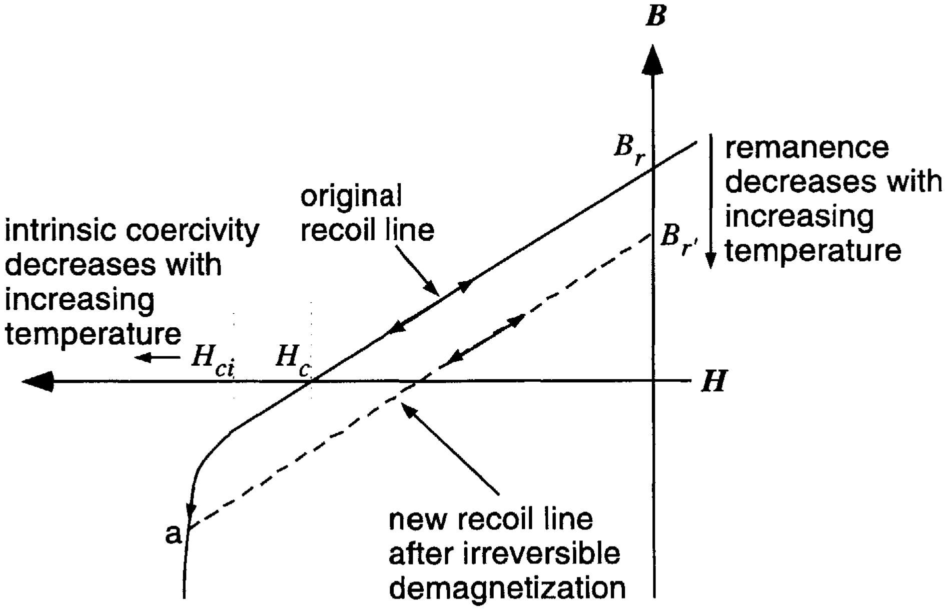

Figure 6.11: Recoil lines of a typical ferrite-based permanent magnet.

Beyond this point, the internal magnetization $\vec{M}$ is permanently altered, thus changing the recoil line of the material. For instance, if the field excitation drives the material to point (a) and then the excitation is removed, the magnet will recoil along the dashed line back to a new lower remanent flux density $B_{r'}$. Only remagnetizing the magnet can restore the original behavior. This requires a special magnetizing fixture capable of delivering dramatically greater positive mmf excitation than is normally available from the machine windings. The implication is that the rotor will have to be removed from the assembly for replacement or remagnetization.

Temperature also affects the magnetic characteristics of a permanent-magnet, but within normal automotive operating temperature ranges, these changes are typically fully reversible. Both H_{ci} and B_r change as a function of temperature which changes both the PM flux linkage that will be produced in a machine and, to a minor extent, the slope of the recoil line. Ferrite-based permanent magnets, in particular, have the general characteristics shown in Figure 6.11 where, with increasing temperature, H_{ci} becomes more negative and B_r increases. For rare-earth magnets, both H_{ci} and B_r generally decrease in amplitude with increasing temperature. Thus, the resistance of ferrite magnets to demagnetization generally increases with temperature, opposite to the trends with rare-earth magnets. But the details will depend on the exact nature of the magnetic circuit that governs the flux density and mmf operating point in the permanent magnet. This is not analyzed in detail in this thesis.

For the ISG application, a worst-case condition with respect to irreversible demagnetization must be hypothesized to ensure a robust design. There are a number of failure scenarios that could be evaluated. For this application, the most serious failure that is considered is a complete loss of vector control, allowing the current vector to be oriented in any direction in the *dq* plane. Consequently, the worst-case condition for demagnetization can be assumed to correspond to rated current along the negative *d*-axis. It is also worthwhile to estimate the magnitude of overcurrent in this direction that would produce irreversible demagnetization.

The major impact that irreversible demagnetization has on the IPM machine is a reduction in torque capability. It is possible to estimate the impact for a given design simply by examining the torque equation. Since λ_{PM} is proportional to B_r, a change in the remanent flux density ΔB_r would affect the torque capability as follows

$$T_e - \Delta T_e = qp\left(\left(\frac{B_r - \Delta B_r}{B_r}\right)\lambda_{PM} - \left(L_q - L_d\right)I_d\right)I_q \tag{6.2}$$

$$\Delta\lambda_{PM} = \frac{\Delta B_r}{B_r}\lambda_{PM} \tag{6.3}$$

$$\Delta T_e = qp\Delta\lambda_{PM} I_q \tag{6.4}$$

If the magnet is completely demagnetized with $B_r = 0$ the machine will perform as a synchronous reluctance machine. For multiple-layer IPM machines constructed using ferrite magnets the saliency-only torque should be in the range of 50 to 80% of the original rated torque since these machines are dominantly reluctance-torque machines (see the discussion in Chapter 2). Though the saliency has not been affected, there will also be an impact on the CPSR for the IPM machine drive design since the center of the voltage ellipse moves by $\Delta\lambda_{PM}/L_d$.

One question that this discussion raises is whether the LPMs can be used to predict threshold excitation conditions for demagnetization. A simple estimate might look at the second quadrant of magnet operation at nominal temperature and approximate the threshold condition for irreversible demagnetization as the extrinsic coercivity H_c. This is the point where $B(H_c) \equiv 0$. This is a conservative estimate since the actual coercivity corresponding to the knee of the B-H curve is larger in amplitude (more negative) than H_c.

In terms of the LPM, the net flux density B through the permanent magnet is most closely related to Ψ_d. Therefore, the simplest assumption might be that the magnet flux density $B = 0$ when $\Psi_d = 0$. But Ψ_d includes leakage components of L_d that are certainly not linked through the magnets, so a more reasonable approximation of the current necessary to irreversibly demagnetize a PM machine can be expressed using the mutual component of the d-axis inductance L_{dm}, as follows

$$I_{d\,\mathrm{lim}} = \frac{\lambda_{PM}}{L_{dm}} \tag{6.5}$$

This may serve as a useful starting point, but for some IPM machine designs L_{dm} may only be marginally smaller than L_d. This suggests that some portions of normal Mode II and Mode III flux-weakening operation pass through current excitation conditions that should demagnetize the permanent magnets.

One reason that even this estimate might not be adequate is that all the magnetic flux that links the IPM rotor on the d-axis does not go through the magnets. Instead, some of the flux gets diverted through the bridges and center posts if they are used. λ_{PM} also does not account for all the flux sourced by the magnets since some of this flux also gets shunted through the bridges and post. An expression would need to be developed that includes additional factors to account for the leakage through the bridges in order to better estimate the total flux passing through the magnets and the stator mmf excitation that is imposed on them. Equation (6.5) is likely to be a better demagnetization threshold estimate for surface PM machines that do not have the same issues with significant leakage paths around the magnets within the rotor.

Furthermore due to the non-uniform reluctance through the rotor on the d-axis, demagnetization is not likely to onset at the same degree over the full face of each magnet. Because there is a high concentration of flux through the bridges, and center posts if used, it would be reasonable to expect irreversible demagnetization to onset at the tips of the magnets first, and then propagate through the bulk of the magnet with increasing applied demagnetizing field strength.

As this discussion suggests, the LPMs developed in this thesis cannot predict demagnetization conditions over a wide variety of IPM machine designs. A new expression must be developed to capture the net flux at the magnet surface and the localized demagnetization phenomena at the magnet tips. In the next chapter where the results of the ISG design optimization are presented, electromagnetic FEA has been employed to check the actual field characteristics to determine under what conditions bulk irreversible demagnetization occurs.

6.4 Summary

This chapter discussed the issues of structural integrity and demagnetization as they affect the design and operation of IPM machine drives, with a particular focus on the automotive ISG application. The mechanisms that produce the worst-case planar stress state in the IPM rotor have been discussed, and then design techniques to mitigate these stresses were proposed and verified using structural FEA.

The structural FEA of an IPM rotor was analyzed with an unconstrained rotor ID boundary. The results shows that for the 10 krpm mechanical design point for the ISG the example IPM design would fail by exceeding the material yield strength by a factor of seven. An endplate hub fixture is proposed as a part of a plausible solution for meeting the mechanical design requirements of the ISG. FEA of the hub-rotor assembly with modified rotor geometry showed dramatic improvement in the stress state being only 20% above the core yield strength. Reducing the mechanical design speed, reducing the rotor OD, or using alternate materials are suggested as means to bring the stress state within the yield strength of the chosen core material. The results are scalable by rotor diameters to the particular optimized ISG design that is presented in the following chapter.

The distinction between reversible and irreversible demagnetization of permanent magnets was presented in the second half of the chapter. Particular attention has been paid to the magnetization characteristics of ferrite-based magnets that are the preferred candidates for use in the ISG application. The impact of irreversible demagnetization on machine performance was qualitative explored. Finally, the limitations of LPMs for accurately predicting the demagnetization characteristics of IPM machines were discussed.

Irreversible demagnetization reduces the remanent flux density of the magnets, which affects the IPM machine performance. The magnet-torque portion of the overall torque capability of the machine is reduced proportionally. Since multiple-layer ferrite-based IPM machines are generally reluctance-dominated, the impact in the worst case of complete loss of magnet torque should be less than 50%. The CPSR performance must also be affected because the infinite speed point will shift due to the change in λ_{PM} with irreversible demagnetization. Prediction of the onset of irreversible demagnetization cannot be accomplished solely with the LPMs as developed in this thesis. A model that accounts for the demagnetization appearing initially at the tips and propagating through the rotor would have to be developed. In the following chapter where the optimal ISG design is presented, demagnetization is evaluated using FEA to determine when irreversible demagnetization will occur and what the impact is on the ISG performance.

Chapter 7

ISG OPTIMIZATION RESULTS

7.1 Introduction

A cost-optimized IPM machine for the ISG application is designed in this chapter. The design optimization is performed using the constraints and goals specified in Chapter 5 and the considerations for structural integrity and demagnetization in Chapter 6. The physical characteristics and predicted performance of the optimal ISG design are presented. FEA is used to corroborate the calculations from the saturable LPM. Then structural integrity and demagnetization characteristics for the optimized ISG design are determined. The prediction accuracies of the linear and saturable LPMs are investigated as they affect the constant-power operation of the IPM machine. Finally, the sensitivity of the machine optimization result is explored by considering the impact of including the converter cost in the objective function, and by considering the effect on the resulting optimized designs when using either the linear or saturable LPM.

7.2 Optimized IPM Machine Drive Design

The Monte Carlo and local gradient optimization were performed using the cost function (5.4), together with the constants and variables that were constrained within the specified ranges shown in Table 7.1 and Table 7.2.

The principal design constants in Table 7.1, such as the airgap and slot fill factor, were dictated by information on practically achievable values for mass manufactured automotive machinery [3]. A rotor configuration with two cavity layers was selected to limit the rotor manufacturing complexity while still achieving the benefits of IPM rotor saliency with regard to constant power operation and reduced magnet requirements compared to surface PM machines.

The base voltage is the maximum rms phase voltage that can be extracted from a 42 VDC battery bus, assuming a wye-connected three-phase machine and 3 Volts of conduction drop in the inverter. The base current listed in the table represents a convenient upper limit value for the machine phase current. However, the minimum current needed to achieve the required torque at each specified speed point determines the actual rated current for an optimized design.

Based on the structural integrity investigations presented in Chapter 6, it was clear that both bridges and center posts would be necessary in the optimized ISG design. Bridge and post thicknesses were set at 1.0 mm since the structural FEA with rounded cavity tips showed minimal stress reductions for any values larger than 1.0 mm for IPM rotors with the overall machine dimensions of the ISG application. The angles in the last two rows in Table 7.1 were chosen to produce cavities that are approximately semicircular arcs and parallel, based on experience with preliminary designs that suggested that these would be good choices with limited sensitivity to changes.

Table 7.1: ISG constant parameters for optimization.

Description	*Constant*	*Units*
Number of phases	3	
Number of cavity layers	2	
Slot opening depth	$\frac{w_{st} - w_o}{2} + d_o$ (= 45° camber)	mm
Slot fill factor	0.35	
Rotor bridge thickness	1.0	mm
Rotor center post thickness	1.0	mm
Airgap	0.66	mm
Base (rated) RMS current	500	Arms
Base (rated) RMS voltage	19.3	Vrms
Relative length of middle cavity segment	0.5	
Relative angle between side segments of cavities (1 = parallel)	1	

It was practical to make a few of the parameters dependent on others. In Table 7.1, the slot depth was made dependent on the slot opening and slot fraction to make the slot depth equal to the area of the tooth face overhanging the slot. This produces a reasonable path for the magnetic flux to turn in the tooth tips and enter the main shaft of the tooth. The slot opening ratio cannot be larger than the slot ratio, so the upper limit was made a dependent variable. The allowable number of slots for distributing a phase winding was limited to prevent stator designs with more than 72 slots. For the range of airgap diameters associated with the ISG application, the minimum slot/tooth pitch is approximately 5 mm which approaches the practical manufacturing limits for automotive electrical machines. Likewise, the number of short-pitched slots was limited to produce a minimum stator coil pitch of 120 electrical degrees.

Table 7.2: ISG design variables for optimization.

Description	*Minimum*	*Maximum*	*Units*
Stator OD	230	300	mm
Stator back iron depth	10	20	mm
Ratio of slot height to width	0.75	3.0	
Ratio of slot opening to slot-tooth pitch	0.35	λ_s	
Ratio of slot width to slot-tooth pitch, λ_s	0.35	0.65	
Ratio of rotor OD to ID	0.5	0.82	
Ratio of total cavity to total rotor depth	0.1	0.8	
Percentage of total cavity depth for each cavity (1 inner cavity)	0.25	0.75	
Percentage of total rotor core depth for each rotor section (2 inner sections)	0.15	0.40	
Ratio of angular span of largest magnet from tip to tip versus the span of a pole	0.50	0.80	
Number of slots distributed, m_a	2	$36/p$	
Number of slots short pitched	0	m_a	
Number of turns per slot, $N_a/(2m_a p)$	1	3	
Number of pole pairs, p	2	6	
Active length	40	100	mm
Magnet remanent flux density	0.01	0.45	T

With these input parameters, over a million Monte Carlo design iterations were executed, and the resulting low-cost designs were locally optimized. For each iteration, the design is checked to determine whether it meets the performance criteria. The torque versus speed and efficiency requirements from Figure 1.2 were reduced to tests at four operating points to minimize the computation time.

Table 7.3 lists the specific tests performed for each design iteration to determine if the design is acceptable. First, initial static calculations are made. Because of the complexity and number of design variables, it was not possible to completely prevent unreasonable geometries from occasionally being generated. Therefore, the geometry is automatically checked for invalid conditions such as adjacent cavity layers that intersect. The back-emf limit is also checked during the static calculations because the maximum back-emf solution can be made without iteration. By contrast, the solution for the electrical terminal conditions (ϕ, δ, γ) requires iterations at each speed point using the saturable LPM. To improve the efficiency of the Monte Carlo process, only those calculations that are frequency-dependent and iterative are performed for each speed point.

During post-processing, the system cost for the new design is checked against the lowest recorded system cost from previous iterations. The best few designs in terms of system cost are saved and passed to the local gradient optimizer. High cost designs are discarded.

During local gradient optimization, only the non-integer variables from Table 7.2 are exercised, since the integer variables such as number of poles would produce unacceptably large gradients for the local optimizer. Furthermore, the minimum and maximum specified values are expanded for the local optimization. Experience with the ISG optimization has shown, though, that changes to the variable values of more than a few percent did not occur during local optimization.

The percentage of Monte Carlo designs that passed the tests for the initial static and speed point conditions was less than 0.1%. Detailed analyses of the variable value combinations that passed these initial screens was not conducted. However, it was observed that particular combinations of the integer variables never produced a successful design that passed the tests. If the list of variable parameters had been further refined to eliminate such combinations, the success ratio certainly would have increased by orders of magnitude.

Figure 7.1 and Figure 7.2 show cross-sections of the final cost-optimized ISG IPM machine drive design. The optimized parameter values are shown in Table 7.4. Operating conditions at the tested speed points are shown in Table 7.5.

Table 7.3: Tested conditions for ISG optimization.

Test Points	*Pass/Fail Tests*
Initial static calculations	back-emf limit, 55 VDC rational geometry
10 rpm	motoring torque, 150 Nm transient current density limit, 50 A/mm^2
600 rpm	generating power, 4000kW steady-state current density limit, 20 A/mm^2
1500 rpm	generating power, 3250 kW steady-state current density limit, 20 A/mm^2 minimum machine efficiency, 80.3%
6000 rpm	generating power, 6000 kW steady-state current density limit, 20 A/mm^2
Post-processing calculations	minimum system cost

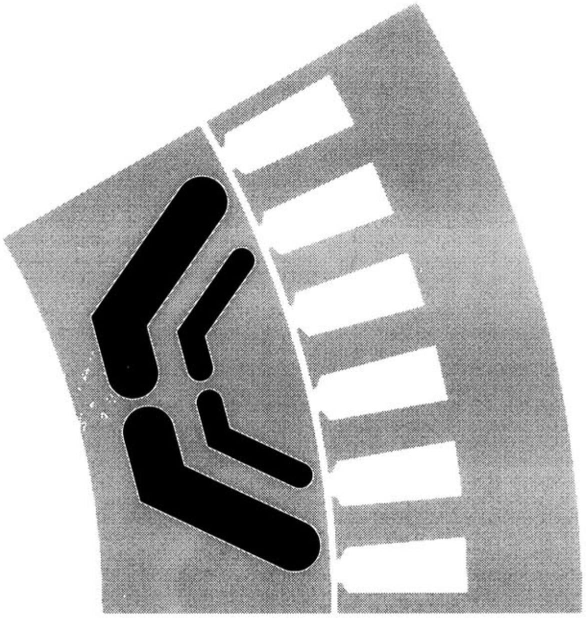

Figure 7.1: Pole cross-section of the optimal design for the ISG IPM machine drive.

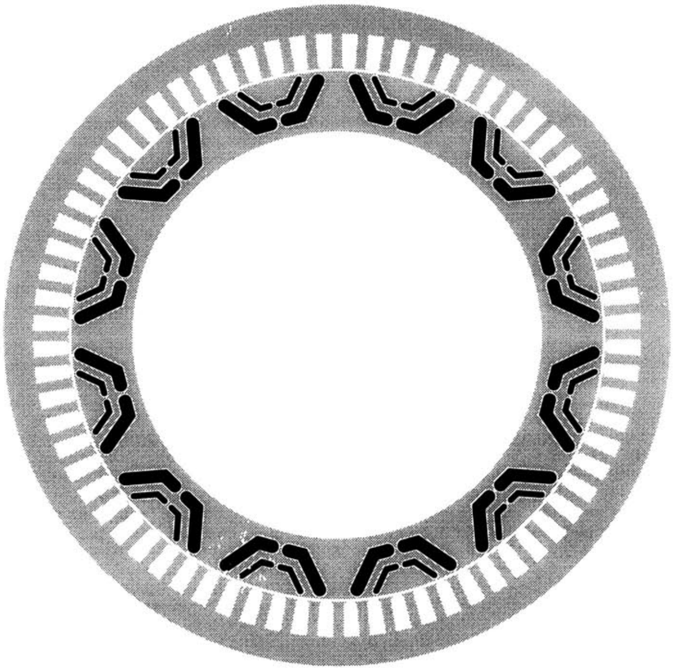

Figure 7.2: Machine cross-section of the optimal design for the ISG IPM machine drive.

As required by the optimization process, the predicted performance of the final ISG machine at the four test points meets the required ISG specifications. It is expected that one or more of the machine variables may approach either their minimum or maximum allowable values as a result of the optimization process. In this case for the ISG application, the maximum back-emf limit was approached very closely. Referring to Table 7.5, $E_a = 24$ Vrms at 6000 rpm. When this is reflected back through the converter, the resulting open-circuit DC bus voltage will be almost 55 VDC which is the specified maximum limit.

Another limit that is approached within 10% is the maximum allowable steady-state current density, set at 20 A/mm^2 . At the 600 rpm idle speed, the optimized current density value is 18 A/mm^2. Though the ISG requirements are not strictly speaking constant torque/constant power requirements it is not surprising that one of the constrained conditions is near where the corner point (voltage limited) speed would be expected. It is worth noting that during other optimization exercises with different variable selections and restrictions, the idle density limit was approached even more closely. However, in this case additional iterations of the optimization routine revealed no further change in the maximum current density.

Table 7.4: Optimal ISG IPM machine drive parameter values.

Parameter	*Value*	*Units*
I_0	327	Arms
V_0	19.3	Vrms
k_{a1}	0.9224	
N_a	24	turns
n_s	72	slots
p	6	pole pairs
B_r	0.28	T
l	0.060	m
r	0.109	m
g'	6.96e-4	m
g	6.35e-4	m
d_{m1}	0.0029	m
d_{m2}	0.0057	m
d_{r1}	0.0092	m
θ_{m2o}	140.8	elect. deg.
d_{r2}	0.0030	m
d_{r3}	0.0044	m
w_{b1}, w_{b2}	0.0010	m
w_{c1}, w_{c2}	0.0010	m

The reported machine efficiency at the ISG test point speed of 1500 rpm is 13% than the minimum requirement for the machine 80.3%. Machine efficiencies under rated load at the other speed points is respectable and up to twice that of a typical Lundell alternator (40% – 60%) [2]. Since the optimization process finds the maximum torque-per-Ampere operating points, the reported currents are precisely the minimum necessary to produce the required torque or power. The 10 rpm operating point requires the highest stator current because it has the highest torque requirement of all the speed points by a significant margin.

Table 7.6 shows more system-level calculations completed during post-processing, including the mass, volume, and cost calculations. Of particular interest is the maximum shear stress level of 4.9 psi that is developed in the airgap when the machine is developing 150 Nm at low speeds. This is higher than might be expected from most high-performance servo systems and matches that of some aerospace machine drive systems [11] where weight and volume are higher design priorities. The cost proportions for the converter and machine are 89% and 11% of the total system cost, respectively. Since the converter cost model is a strong function of the required current, this cost split indicates that the system optimization effectively minimizes the machine's rated current.

Table 7.5: Optimal ISG IPM machine drive performance at test points.

Parameter	*10 rpm*	*600 rpm*	*1500 rpm*	*6000 rpm*	*Units*
Operating Mode	Motoring	Generating	Generating	Generating	
T_{shaft}	150	N/A	N/A	N/A	Nm
P_{DC}	N/A	4000	3250	6000	Watts
I_d	-279	-171	-53	-126	Arms
I_q	172	-144	-68	-17	Arms
γ	-58	-130	-142	-98	elect. deg.
$\cos(\phi)$	1.0	-0.55	-0.75	-0.87	
E_a	0.04	2.4	6.0	24	Vrms
V_a	3.5	11.6	19.3	19.3	Vrms
P_a	3304	1539	229	501	Watts
P_c	11.7	16	25	24	Watts
P_h	46	42	56	48	Watts
η (machine only)	0.05	0.73	0.93	0.92	
converter efficiency	0.93	0.93	0.93	0.93	
total efficiency	0.05	0.68	0.86	0.86	
Current Density	26	18	6.9	10	A/mm^2

The details of the inductance calculations are shown in Table 7.7, Table 7.8, and Figure 7.3. These results show that the total leakage inductance L_l is 3% of L_q, while it is 14% of L_d, highlighting the conclusion that leakage estimates comprise a larger fraction of uncertainty in L_d calculations. At the I_q levels quoted at the speed points in Table 7.5, Figure 7.3 shows that there is a significant difference between actual saturated saliency and the unsaturated, linear predictions. An expanded discussion of both optimized cost and saliency in a more general context is provided in Sections 7.4 and 7.5.

Table 7.6: Optimal ISG IPM machine drive system calculations.

Parameter	*Value*	*Units*
Phase Resistance	10.3	milliOhms
Maximum Back EMF	23.9	Vrms
PM Flux Linkage	6.3	mWb.turns
Stator OD	272	mm
Total Length	90	mm
Active Rotor Volume	2215	cm^3
Shear Stress	4.9	psi
Copper Mass	1.92	kg
Magnet Mass	2.25	kg
Core Mass	11.41	kg
Total Mass	15.59	kg
Moment of Inertia	63.3	$kg.m^2$
Maximum RMS Switch Current	231	Arms
Converter Cost	534.80	$
Machine Cost	69.13	$
Total Cost	603.93	$

Also shown in Figure 7.3 are the electromagnetic FEA inductance and PM flux linkage results that have been performed as verification of the accuracy of the saturable LPM calculations. The FEA procedures and models are similar to those presented in Chapter 3. As with the other FEA comparisons, the saturable LPM shows excellent agreement with the FEA lumped parameter and torque calculations. The agreement between the saturable LPM and FEA calculations for L_q are within 5% over the I_q range required in the results of Table 7.5 ($I_q \leq 172$ Arms). This is consistent with the results discussed in Chapter 4. The λ_{PM} LPM calculation are also within 5% of the FEA result. The L_d linear model agrees well with FEA at high excitation levels as expected for the L_d model assumptions.

Figure 7.4 shows the converted torque as a function of control angle γ with the constant current $I_a = 327$ Armswhich is the starting (i.e. transient current density limited) rated current value. At each γ value the position of the stator slots with respect to the rotor cavities is varied in the FEA model to determine the torque ripple due to stator slot. Since this is a 2D model and the stator is assumed skewed by one slot pitch, the expected torque at each control angle is approximated by the average of the torque values produced by each stator slot orientation at a given γ. The average torque after accounting for the stator skew is plotted with the dashed line. Note that the peak torque capability is right at 150 Nm demonstrating excellent corroboration of the saturable LPM design calculations.

Table 7.7: Optimal ISG inductance component calculations.

Parameter	*Value [Henries]*
forward zig-zag space harmonic inductance, L_{fzig}	1.08e-8
backward zig-zag harmonic inductance, L_{bzig}	2.10e-8
5th space harmonic (belt leakage) inductance, L_{5belt}	3.53e-8
7th space harmonic (belt leakage) inductance, L_{7belt}	9.19e-8
stator slot leakage inductance, L_{slot}	6.38e-6
armature end turn leakage inductance, L_{end}	3.11e-6
leakage inductance, L_l	9.56e-6
airgap magnetizing inductance, L_{ag}	3.07e-4
q-axis magnetizing inductance, non-saturable, L_{qm}	3.07e-4
q-axis synchronous inductance, L_q	3.17e-4
d-axis circulating inductance, L_{dc}	1.32e-5
d-axis through inductance, L_{dt}	4.22e-5
d-axis magnetizing inductance, L_{dm}	5.54e-5
d-axis synchronous inductance, L_d	6.50e-5

Table 7.8: Saturable q-axis inductance versus current.

Iq [Amperes]	*Lq [Henries]*
0	0.000295
1	0.000295
22	0.000309
43	0.000310
63	0.000310
84	0.000302
105	0.000278
126	0.000254
147	0.000235
167	0.000219
188	0.000206
209	0.000193
230	0.000182
251	0.000172
271	0.000163
292	0.000155
313	0.000147
334	0.000141
354	0.000135
375	0.000129
396	0.000124
417	0.000119
438	0.000114
458	0.000110
479	0.000106
500	0.000103
688	0.000103

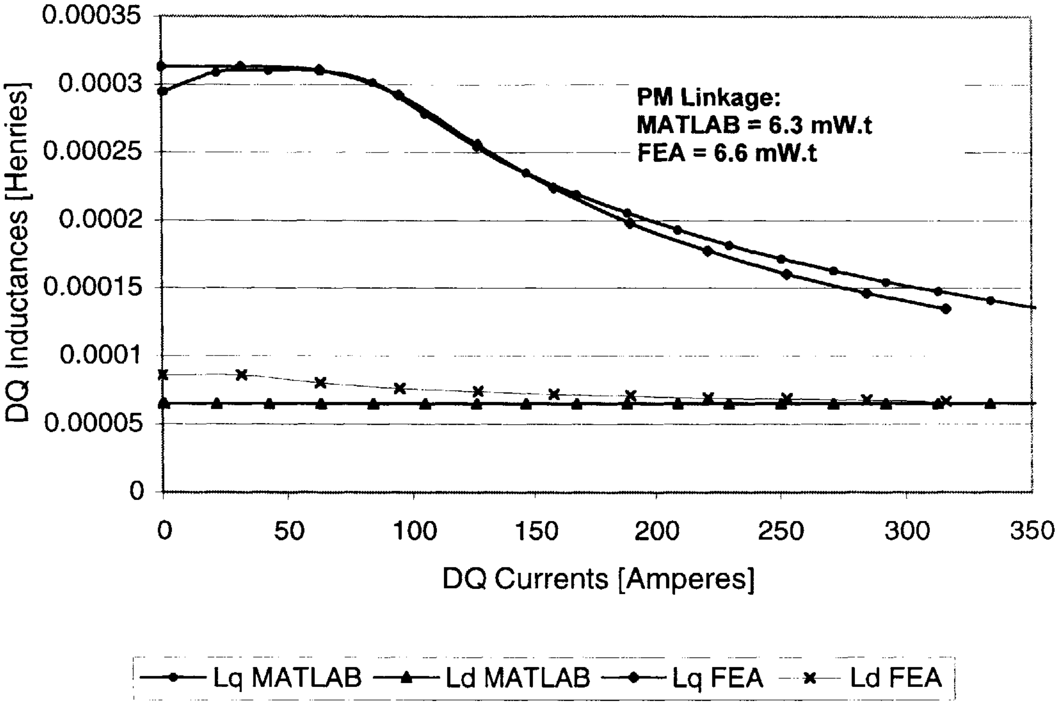

Figure 7.3: L_q versus I_q, L_d versus I_d, and λ_{PM} .for the optimal ISG design in the *dq* frame, comparing predictions of the saturable LPM and FEA models.

7.3 Ancillary Considerations

In Chapter 6 the bases for evaluating the structural integrity and demagnetization characteristics of the optimal ISG were developed. This section applies the qualitative analyses and estimations to the optimal ISG design presented above.

The structural integrity predictions for the optimal ISG at the mechanical design point are considered to be directly scalable from the results developed in Chapter 6 for a very similar geometry. Both the optimal ISG and the IPM rotor cross-section that was analyzed in Chapter 6 have the following identical physical characteristics: 12 poles, two cavity layers, 1.0 mm bridges, and cavity center posts. The rotor radii are different, but since the maximum Von Mises planar stress is largely a squared function of the outer radius, the results from Chapter 6 can be conveniently scaled to the radius of the optimal design. Using the structural FEA results with the endplate hub design to estimate the rotor ID boundary condition, the maximum stress for the optimal ISG is calculated to be

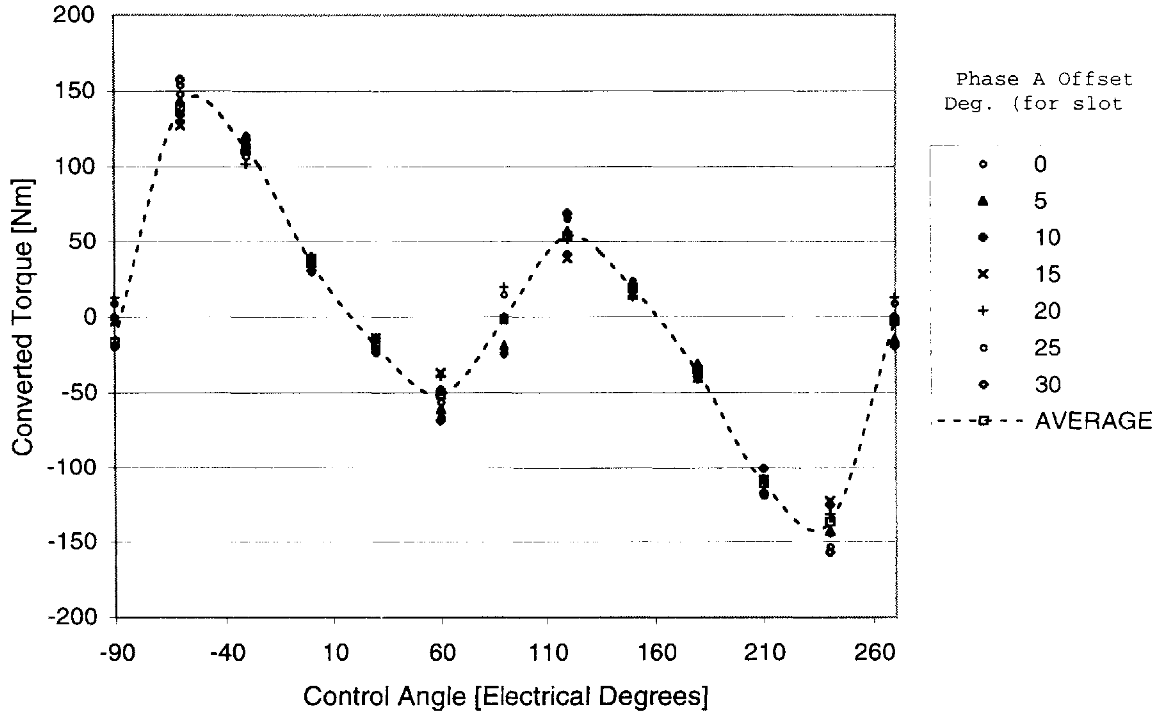

Figure 7.4: FEA predictions of torque versus current control angle for the optimal ISG design, showing torque variation with stator slot position at each control angle value.

$$\left(\frac{108}{102}\right)^2 420 = 470 \text{ MPa} \tag{7.1}$$

This is 34% above the yield strength of the baseline core material, M19 29-gage electrical steel, leaving two options for consideration: reduce the mechanical design speed to 8500 rpm, or select an alternative core material with higher yield strength. It is not the intention of this research to fully explore the mechanical aspects of this solution. The first alternative to reduce the speed is straightforward, but it directly burdens the automotive system with requirements for additional safeguards to restrict the engine system to lower overspeed limits. This is a system tradeoff that exceeds the scope of this research.

There is evidence to support the engineering feasibility of the second suggestion involving use an alternative rotor core material. First, since the structural integrity issue is particular to the rotor and the rotor experiences a substantially DC field, a soft magnetic material with higher core losses may be tolerable in the rotor assembly. Figure 7.5 shows a qualitative comparison of different classes of steels [32, 61, 65]. Conventional machine lamination steel is made with 0.5 to 4% Silicon (Si Alloys), and M19 is in this class with a silicon content of roughly 3.5%. High-performance aerospace machines are sometimes constructed of Cobalt or Vanadium alloys (Co or V Alloys) that have excellent loss characteristics as well as higher mechanical strengths, but this group of steels is far too expensive for automotive applications.

Both aluminum and nickel alloys (Al or Ni alloys) exist with a spectrum of cost. An Armco Steel aluminum alloy has a yield strength of 465 MPa and a specific cost only 17% higher than M19 steel [65]. A second alternative manufactured by Carpenter Steel is a nickel alloy with a yield strength of approximately 650 Mpa. However, the cost of this non-production alloy is uncertain [32] but likely at least twice the cost of M19 because of the high cost of Nickel.

Kliman recently presented research showing that conventional Si steel could be custom-processed at different temperatures and rates to produce a fully-processed electrical steel with a tailored compromise between loss density and mechanical strength with yield strengths in the range of 600 MPa [34]. Since there is nothing inherently more expensive with the associated processes, this is an excellent solution for high-volume automotive manufacturing that could likely justify a new cost-effective steel line for high-strength laminations.

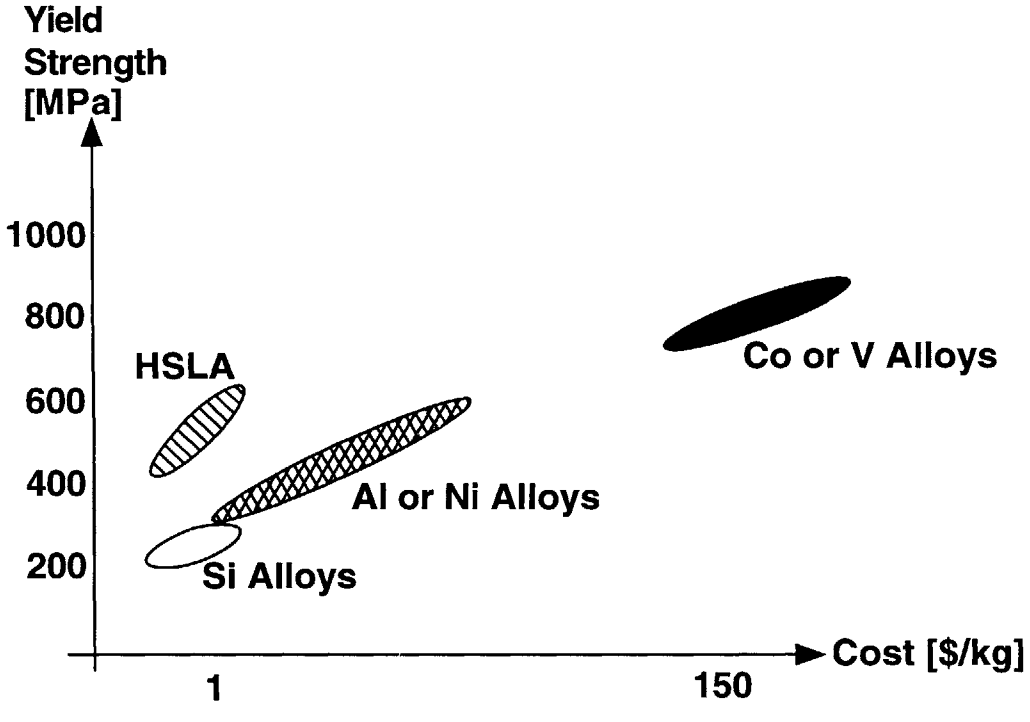

Figure 7.5: Comparison of relative costs and mechanical strengths of steel alloys [32, 61, 65].

The second topic, demagnetization, must be explored for the specific optimal ISG design since the fields are highly dependent on the specific machine cross-section and excitation. As outlined in Chapter 6, the goal is to prevent irreversible demagnetization with rated current at any control angle and operating temperature. Figure 7.6 shows the magnetization characteristics of a candidate bonded-ferrite magnet material [35] whose remanent flux density range includes the value (0.28T) determined for the optimal ISG design. The chief points to note are the following

- Ferrite materials have both a positive temperature coefficient for both the coercive force and the remanent flux density, so, in contrast to NdFe magnets, the demagnetization situation will be worst at the minimum temperature condition
- This sample ferrite material is linear in the second quadrant and well into the third quadrant (down to roughly -0.1T at all temperatures), providing an extended margin in the coercive force threshold for demagnetization

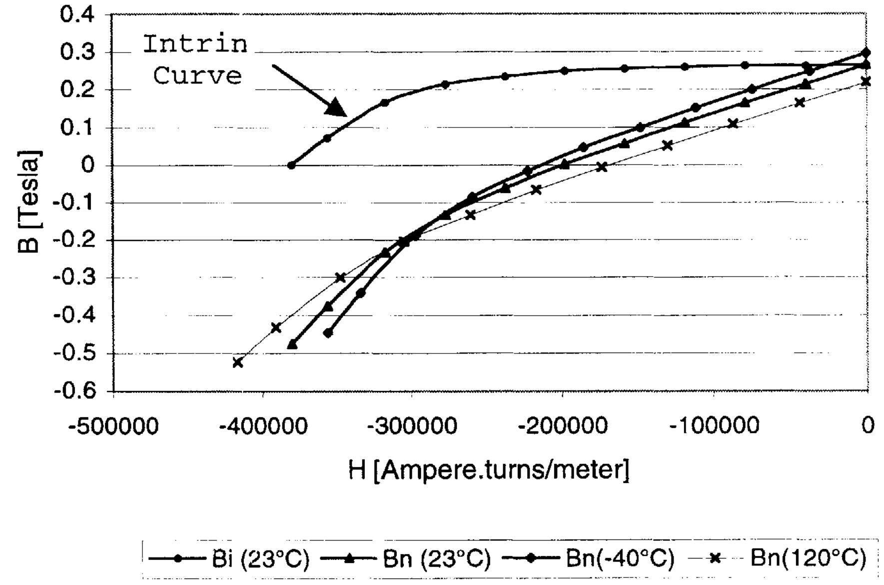

Figure 7.6: Typical bonded ferrite magnetization characteristics versus temperature [35].

Figure 7.7, Figure 7.8, and Figure 7.9 present an overview of the demagnetization characteristics of the optimized ISG machine design by displaying the magnitude and direction of the flux density within the magnets as predicted by FEA. At rated current, the FEA shows that a small portion of the magnet tips operate in the third quadrant of the B-H plane. Furthermore, the vector directions are skewed by less than 90 degrees, where 0 degrees is normal magnetization and 180 degrees is fully reversed. The only exception is on the boundary elements bordering the core material, and it is reasonably assumed that the FEA cannot accurately predict behavior at these points.

The conclusion is that this design will safely withstand rated current in the demagnetizing direction. To better understand the potential penalties associated with demagnetization, the resultant machine torque was also calculated for the case where the magnetization of the magnet tips is fully reversed (i.e. at -0.28T). The net effect on the electromagnetic torque is a reduction of 14%, meaning that the ISG continues to operate (exclusive of other possible effects such as converter damage) but at reduced starting capability. It is important to note that this severe case of tip demagnetization did not propagate the reversed flux density vector field into the bulk of the magnet material.

FEA was also conducted at overcurrent conditions to determine the level required for bulk demagnetization with the materials chosen. It was found that the magnets do not enter irreversible demagnetization until roughly 2 per-unit current, or 654 Arms, using the starting current rating. It is likely the converter semiconductor switches would fail if this high overcurrent condition was reached. With the converter cost predicted at over $535 and the IPM machine cost at $69, the automotive system designer may be more concerned about preventing damage to the converter and thus would design to prevent such current levels. On the other hand removal of the crankshaft assembly to replace a demagnetized rotor may also be quite expensive. This type of system-integrated failure and cost analysis, though, is necessarily dependent on the specific vehicle installation and is not treated further in this thesis.

7.4 Comparison of LPMs for Constant Power Operation

Further comparison of the predicted capabilities from both the linear and saturable LPMs in constant power operation is provided in Table 7.9, Figure 7.10, Figure 7.11, and Figure 7.12. It must be reaffirmed that the dramatic differences between the linear and saturable LPM results highlight the fact that the linear LPM predicts machine performance characteristics that are simply not achievable. In these comparisons, the linear model develops design predictions that do not limit the allowable magnetic flux within the core even though core loss predictions were made with unreasonably high flux densities. These linear LPM predictions would certainly not be achievable in a physical ISG prototype built using the parameters of the optimal ISG design. Section 7.5 later in this chapter explores the impact when the problem is turned around and the linear LPM is actually employed in the optimization process rather than just being used to post-calculate the linear LPM performance predictions for the optimal ISG design that was determined using the saturable LPM.

For the purpose of the discussion, the system is assumed to operate only as a motor for these calculations. But since the interest is in the constant power region performance, the steady-state rated current $I_a = 223$ Arms is employed instead of the higher transient starting current. Table 7.9, which shows the performance at the Mode I corner speed point, exhibits a 20% reduction in predicted saliency for the saturable LPM compared to the linear model. With a calculated PM flux linkage of 6.3 mWb.turns, the predicted fraction of torque due to the magnets rises from 14% with the linear LPM compared to 16% with the saturable LPM. The effect of saturation on the machine's peak torque capability is 29% lower predicted torque with the saturable LPM than with the linear LPM.

Figure 7.10 plots the Mode I current vector trajectories in the *dq* current plane. These current locus lines demonstrate the same trends seen in the example designs discussed in Chapter 3, with the saturable maximum torque-per-Ampere curve bent over into the lower half of the second quadrant.

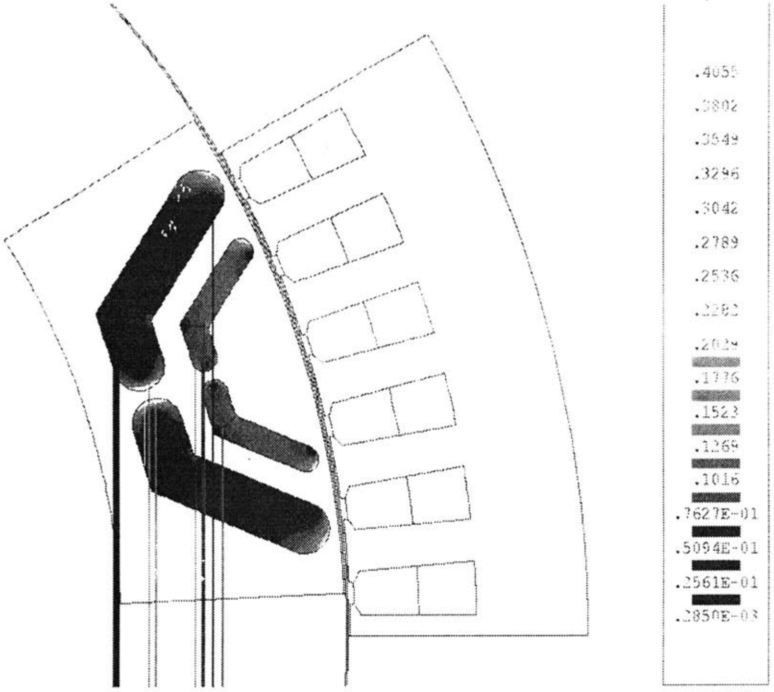

Figure 7.7: Predicted flux density in the magnets with rated current oriented along the negative *d*-axis. (ignore vertical streaks which are graphical output flaws of the FEA)

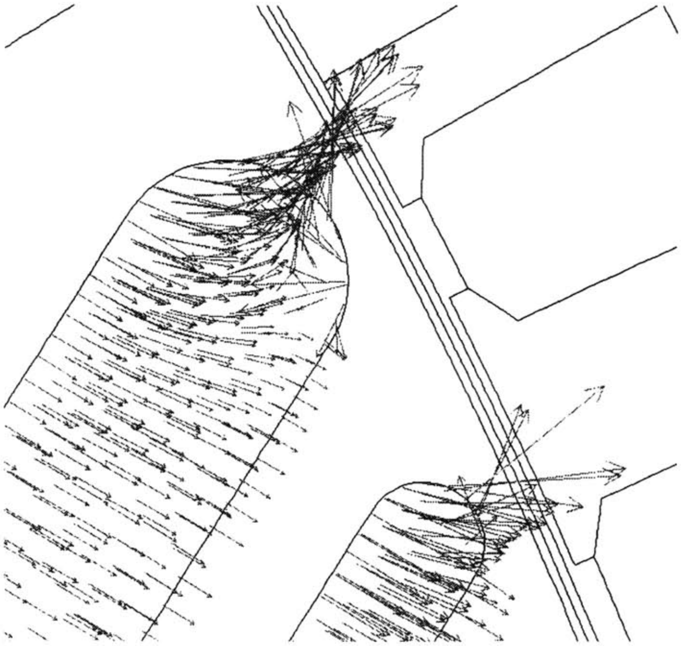

Figure 7.8: Flux density vectors with - I_d set at rated current for max. demagnetization.

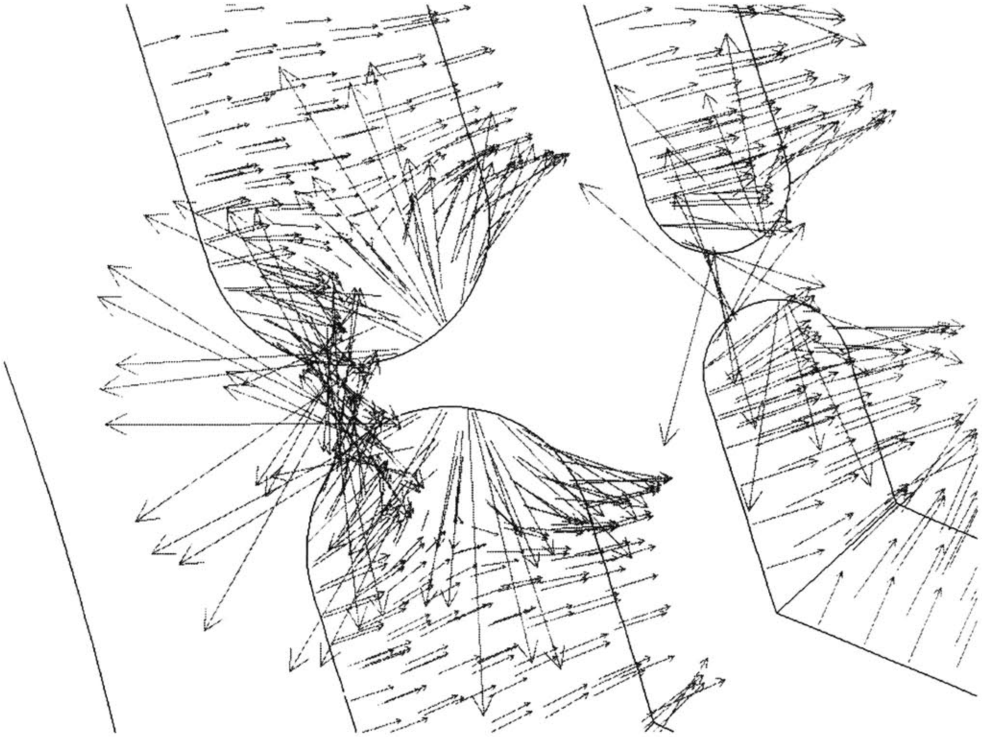

Figure 7.9: Center magnet flux density vectors with - I_d set at rated current.

A surprising feature of this optimized design is the location of the center of the voltage ellipse, marked with an 'I'. This center point is roughly 45% of the rated current limit and would be expected to yield poorer performance during generating operation compared to a design with the voltage ellipse center located much closer to the current limit value on the negative *d*-axis. However, the location of the voltage ellipse center is not as surprising when all of the ISG specifications are taken into consideration. In particular, the maximum back-emf constraint limits the value of λ_{PM} to lower values, preventing the ellipse center from reaching the current limit value.

Table 7.9: Mode I corner speed performance comparisons between the linear and saturable LPMs for the optimal IPM design (motoring reference only at $I_0 = 223$ Arms).

Parameter	*Value*		*Units*
	Linear Model	*Saturable Model*	
$V_a = V_0$	19.3	19.3	Vrms
$I_a = I_0$	223	233	Arms
S_r	4.9	3.9	
T_0	131	93	Nm
γ_0	-43	-55	elect. deg.
I_{d0}	-152	-183	Arms
I_{q0}	164	128	Arms
ω_0	544	856	mech. RPM
$\cos(\phi_0)$	0.70	0.77	
CPSR	4.6	2.4	

Figure 7.11 and Figure 7.12 show the shaft torque and power in the constant-power speed range, assuming here again that the machine is operated only as a motor. The saturable LPM predicts a corner speed that is 57% higher than the predicted value for the linear model. The peak shaft power for motoring operation in the constant-power region is approximately 9 kW at 1200 rpm for the saturable model, suggesting that the optimal ISG is sized well to meet the 6 kW DC bus generating requirement. If the losses, which are dominated by the armature component, are simply reversed to estimate the generator output power at the same current, the result is a peak of 7.5 kW generating in the constant-power speed region. The CPSR value calculated via the saturable LPM is only half that of the linear LPM calculation which means that the maximum operating speed of the ISG is not within the constant-power region of the machine as shown in Figure 7.12. With only two magnet layers it would be unreasonable to expect a full 10:1 CPSR in

saturated operation, but the machine is capable of delivering roughly 85% of its constant-power rating at 6000 rpm. Operation above the end of the constant-power region at roughly 2000 rpm will be conducted in Mode III for vehicle acceleration and climb.

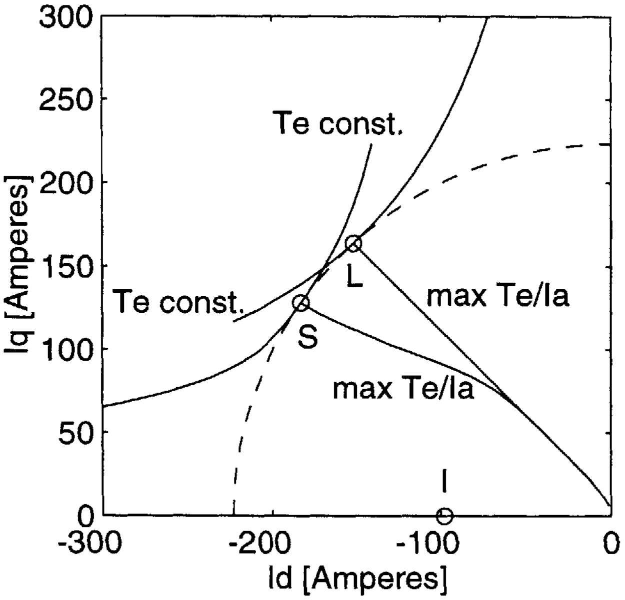

Figure 7.10: Maximum torque-per-Ampere and constant-torque loci lines in the motoring quadrant of the *dq* plane for the optimal ISG design using the linear and saturable LPMs.

7.5 Effects of Saturation and Converter Cost on Optimization

Two of the interesting optimization results from the optimal ISG design presented in the previous section are the relative cost of the machine and converter, and the impact of magnetic saturation on the optimized design and its associated performance. This section discusses cost-optimized IPM machine drive designs and the impact that magnetic saturation and converter cost have on their performance and design optimization.

Cost-optimized designs for IPM machines and combined machine-converter systems are compared for the ISG application. The optimization is performed twice, once with the linear LPM, and again using the nonlinear saturable LPM. The saturating model produces cost-optimized IPM machines that have lower saliency ratios, larger volumes, and more magnet material than the linear non-saturating designs, but the saturating model designs are electromagnetically realizable unlike the linear model designs. The inclusion of converter cost in the drive cost optimization has a significant impact on the machine design, exchanging a larger and more expensive machine for lower power electronics costs made possible by reduced converter current.

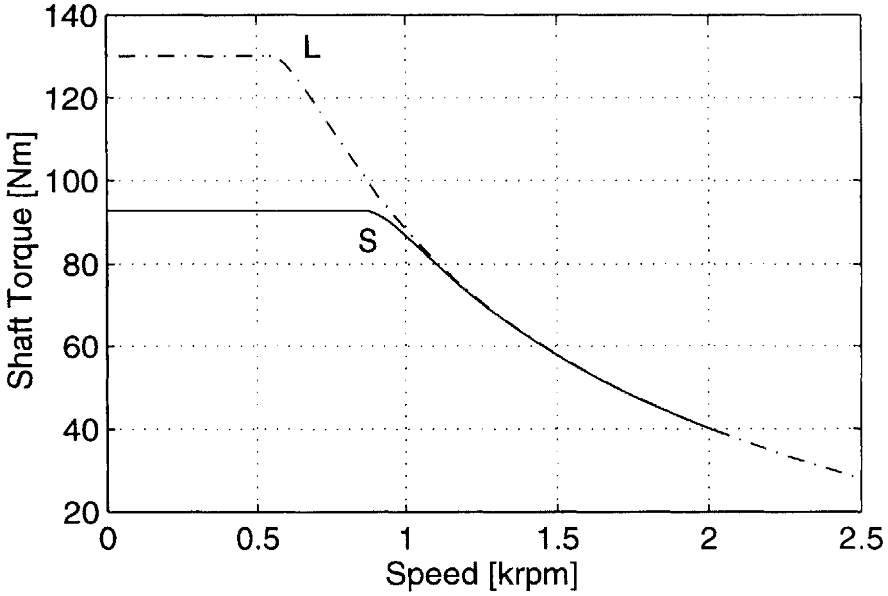

Figure 7.11: Motoring shaft torque versus speed for the optimal ISG design at the lower end of the constant-power region, using the linear and saturable LPMs

These optimizations are carried out using an earlier revision of the ISG optimization software and design specifications. The design parameters are largely the same as presented in the previous section, but those details are not explored in the same depth as before because the details are not germane to the discussion. However, the optimizations in this section are made using consistent sets of parameters and methodology to produce meaningful comparative results.

A direct examination of the impact that magnetic saturation has on the cost of an IPM machine and the optimization of this cost is performed using the saturable LPM. For comparison, design optimizations are also performed using the linear LPM that assumes the mmf drops in the iron are negligible (i.e. the iron is infinitely permeable). The resulting comparisons illuminate the trends in optimized design and operation that are introduced by employing the saturable LPM. The minimized-current torque curves produced by the linear and nonlinear models in the *dq* plane are explicitly compared, illustrating the recognized effects that magnetic saturation has on the current vector locus for maximum torque-per-Ampere operation.

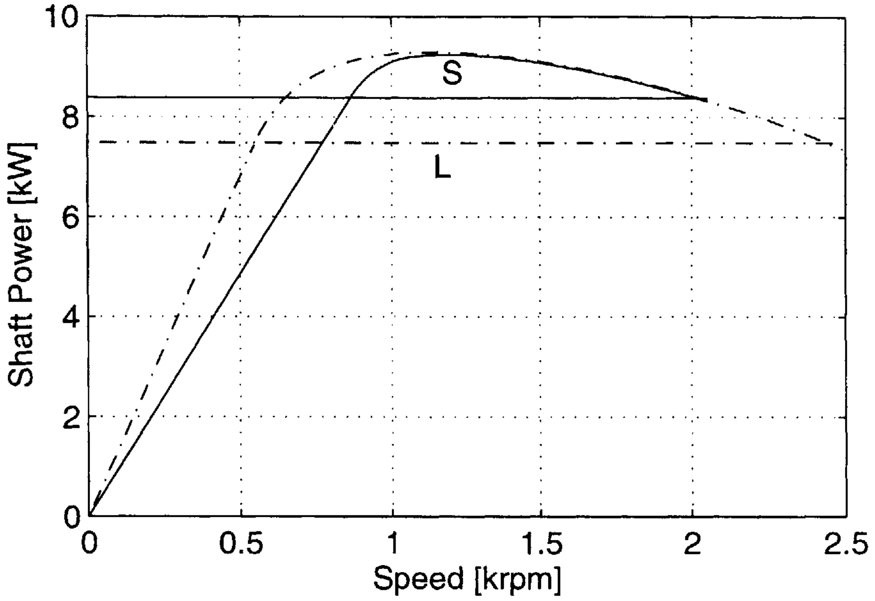

Figure 7.12: Motoring shaft power versus speed for the optimal ISG design at the lower end of the constant-power region for the linear and saturable LPMs.

The optimizations also explore changes in the IPM machine design when converter costs are included in the system cost optimization exercise. A common limitation of many previous machine drive studies has been the decision to optimize the cost of the machine alone without taking the associated power electronics into consideration. Since converter costs typically dominate the total drive system cost, there is no reason to expect that minimizing the cost of the machine alone will result in minimized cost of the combined drive system. This key point is clearly illustrated by comparing the optimized machine designs that result from optimization runs with and without the inclusion of converter costs. The ISG case provides an interesting example of how the converter costs can drive the optimum system design in the direction of larger and more expensive machines in order to minimize the required power electronics.

Both the linear and saturable LPMs (i.e. with and without magnetic saturation) were exercised separately using the general ISG optimization procedure to determine cost-optimized machine designs. For these optimization experiments, the stator OD was fixed at 300 mm, while it was an optimization variable for the optimal ISG presented in the previous section. All the other major machine cross-sectional dimensions, the winding characteristics, and the magnet strength were optimization variables as in Section 7.2.

In addition to exploring the impact of saturation, the effects of including the converter cost in the cost function were investigated separately. The lowest-cost designs that resulted from these optimization exercises are presented in Table 7.10. A total of four designs are included in the table, corresponding to the four possible combinations of the saturation and converter cost assumptions. Designs A and B compare the resulting machine designs with and without saturation when the combined machine-converter cost is optimized. Designs C and D provide a companion set of optimized designs with and without saturation when only the machine cost is included in the optimization.

7.5.1 Physical Characteristics

It is important to recognize at the outset that the linear model leads to optimal designs in Table 7.10 (Designs A and C) that are not realizable because the q-axis current required for rated starting torque will heavily saturate the q-axis inductance when real iron magnetization characteristics are considered. Nevertheless, the Design A and C results are valuable as bases for comparison with Designs B and D in order to quantitatively evaluate the impact of magnetic saturation.

Table 7.10 shows that introducing magnetic saturation into the model affects the minimum-cost design in three important areas: 1) the saliency ratio x_q/x_d under starting torque conditions is reduced significantly; 2) the active machine length increases; and 3) the magnet material increases. These trends can be observed comparing Design A to Design B, and Design C to Design D.

The net effect is that the projected cost of the machine increases significantly when the effects of saturation are included, and the impact is larger (20%) when the combined motor-converter system costs are optimized. On the other hand, the impact of saturation on the combined system cost is noticeably less on a percentage basis when the converter cost is included in the optimization (6% increase) compared to the machine-only optimization results (18% increase). It should also be noted that the required current increases by only 32% with the introduction of saturation when the combined converter-machine cost is minimized (compare Design A to Design B). In contrast, the introduction of saturation more than doubles the machine current when only the machine cost is being optimized (compare Design C to D). These trends appear because the system cost is dominated by the converter cost function (see the cost function development in Chapter 6), coupled with the basic fact that high current imposes a significant machine saliency penalty when saturation effects are included. The net result is that increases in current rating impose a higher system cost penalty than those imposed by increases in machine dimensions and magnet material. Thus, the cost function that includes the converter costs tends to drive the optimizer toward designs that minimize the required stator current in saturated operation at the expense of larger machines.

Table 7.10: Optimal ISG IPM machine drive performance at test points.

Characteristic	*Design A*	*Design B*	*Design C*	*Design D*	*Units*
Optimization Design Model	linear LPM	saturable LPM	linear LPM	saturable LPM	
Optimization Cost Function	machine + converter	machine + converter	machine only	machine only	
Rotor Radius	124	123	124	124	mm
Active Length	49	58	25	31	mm
Pole Pairs	4	6	4	6	
Shear Stress	4.7	4.0	8.9	7.1	psi
Magnet Mass	1.6	1.9	0.5	1.0	kg
Total Mass	12.5	17.4	7.9	8.9	kg
Saturated Saliency Ratio	N/A	4.5	N/A	3.3	
Unsaturated (linear) Saliency Ratio	7.3	5.9	5.3	6.0	
Magnet Remanent Flux Density	0.25	0.21	0.32	0.24	T
Slot Fraction	55	46	53	60	%
Phase Current	207	273	280	567	Arms
Q-Axis Current	151	158	203	196	Arms
Current Density	23	30	22	37	A/mm^2
Machine Cost	54	65	39	44	$
Inverter Cost	494	516	519	617	$
Total Cost	548	581	558	661	$

The nonlinear case, Design B, shifts the optimal current vector to a higher proportion of d-axis current, as described in more detail below. Furthermore, the machine size and slot fraction both increase in order to compensate for the reduced saliency during saturated operation.

The situation is different for Designs C and D where the IPM machine cost alone is optimized. As in Design B for the saturable LPM, Design D produces a machine that requires higher d-axis current than the corresponding unsaturated design (Design C). However, in this case the converter cost increases more dramatically (19%) than the machine cost (13%), driving the cost of the combined system up by a large percentage (18%).

The importance of explicitly including converter cost in the optimizer cost function is emphasized by comparing the results of Designs B and D. Although the cost of the machine (including saturation effects) is 33% less when the machine cost alone is optimized, the combined machine-converter cost for this design (Design D) is 14% *higher* than the corresponding system cost for Design B when converter costs are included in the optimization. The cost optimization trends using the linear model are similar. The Design C machine cost is 28% lower than for Design A, but the system cost is 18% higher.

7.5.2 Performance Characteristics

The impact of magnetic saturation on machine performance is observed more clearly by examining the effect in the dq current plane. Figure 7.13 displays the motoring quadrant of the dq current plane for Design A, which was optimized using the linear model. The figure shows the point where the rated torque locus and the rated current curves meet the maximum torque-per-Ampere current trajectory curve calculated using the linear model (i.e., excluding saturation effects).

The starred points in Figure 7.13 show the corresponding maximum torque-per-Ampere current vector trajectory calculated for the *same* Design A machine parameters except that the magnetic saturation characteristics for M-19 iron are taken into account using the nonlinear model. The two maximum torque-per-Ampere curves are labeled to mark the percentage of rated torque achieved at major increments. Note that the inclusion of realistic saturation characteristics causes a torque drop of approximately 75% under rated current conditions (278 A rms). This comparison demonstrates how poorly the linear model performs in accurately predicting the IPM machine's torque capabilities for high-performance designs.

The position of the new maximum torque-per-Ampere trajectory including current saturation effects should also be noted in Figure 7.13. As noted previously, saturation is responsible for bending this trajectory beyond the 45° line in this i_d-i_q quadrant, resulting in significantly higher total current requirements for a given torque compared to the linear non-saturated case.

Design B, optimized using the nonlinear model, is examined in Figure 7.14. Just as in Figure 7.13, two maximum torque-per-Ampere trajectories are plotted. The starred points mark this trajectory for the Design B machine as designed using the nonlinear model, while the companion solid line plots the corresponding trajectory for the same machine parameters when saturation is ignored ($\mu=\infty$). The observation that these two curves do not diverge as widely in Fig. 4 as in Fig. 3 reflects the higher level of saturation experienced in the Fig. 3 design. The rated current curve for Design B is also shown.

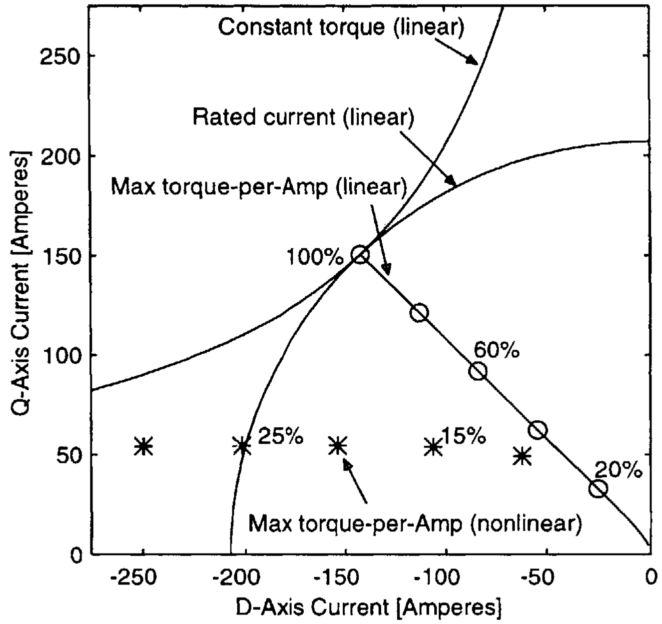

Figure 7.13: Design A, optimized using linear model, showing constant rated current and torque curves and the maximum torque-per-Ampere trajectory, all for the linear model. Maximum torque-per-Ampere trajectory for the same machine including saturation effects shown by starred curve. Percentages represent percent of rated torque at points along each trajectory.

The point labeled 100% on the nonlinear data in Figure 7.14 marks the optimal (i.e., maximum torque-per-Amp) current vector position for rated torque operation calculated using the nonlinear model. The point labeled 100% on the linear data curve identifies the corresponding minimum-current vector position for developing the same rated torque with this machine if the iron did not saturate. Also shown is the constant-torque locus predicted using the linear model for rated (100%) torque, intersecting the associated maximum torque-per-Ampere trajectory at the 100% linear data point.

Comparison of Figure 7.13 and Figure 7.14 highlights the importance of including saturation effects in the machine optimization exercise. When properly optimized, the IPM machine design in Figure 7.14 (Design B) is capable of delivering the same rated torque with only a 32% increase in stator current, thereby incurring a modest penalty in converter cost compared to the Design A machine in Figure 7.13 that ignores saturation. On the other hand, the Design B machine is admittedly larger and more expensive than the Design A machine, reflecting a nearly unavoidable effect of saturation.

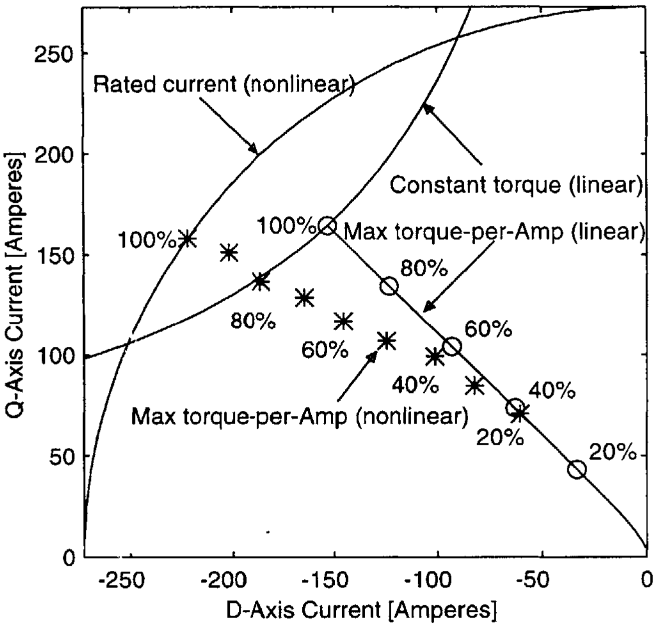

Figure 7.14: Design B, optimized using nonlinear model, showing rated current curve and the maximum torque-per-Ampere trajectory labeled with stars for the nonlinear model. The corresponding maximum torque-per-Ampere trajectory for the same machine without saturation (labeled 'linear') is plotted by a solid line, together with its corresponding constant torque locus line for rated (100%) torque.

Figure 7.15 displays predicted values for the q-axis inductance L_q for Design B as a function of q-axis current i_q using the linear and nonlinear models. As expected, the curve for the linear model predicts a constant value of L_q while the nonlinear curve predicts a drop in L_q by approximately 23% when the q-axis current reaches its rated value of 158 Arms. The L_q/L_d saliency ratio drops by a similar percentage since the d-axis inductance is almost immune to bulk saturation effects.

The small decrease in L_q observed in the non-linear L_q curve at low values of i_q approaching zero is caused by the characteristic drop in permeability exhibited by the iron core material (M-19 grade) at low flux density levels.

7.5.3 Overall Observations

The four optimized IPM machine designs developed using the ISG application specifications illuminate the impact of magnetic saturation and converter cost, separately and together, on the optimal machine designs. Comparison of these alternative optimized machine designs developed for the same set of ISG performance specifications yields the following key observations.

- As expected, inclusion of magnetic saturation leads to optimal machine designs that suffer penalties in their L_q/L_d saliency ratios, leading to increases in machine size and cost.
- Inclusion of converter cost in the optimizer cost function can have a major impact on the resulting machine designs, causing the machine size and cost to increase in order to minimize the resulting system cost.

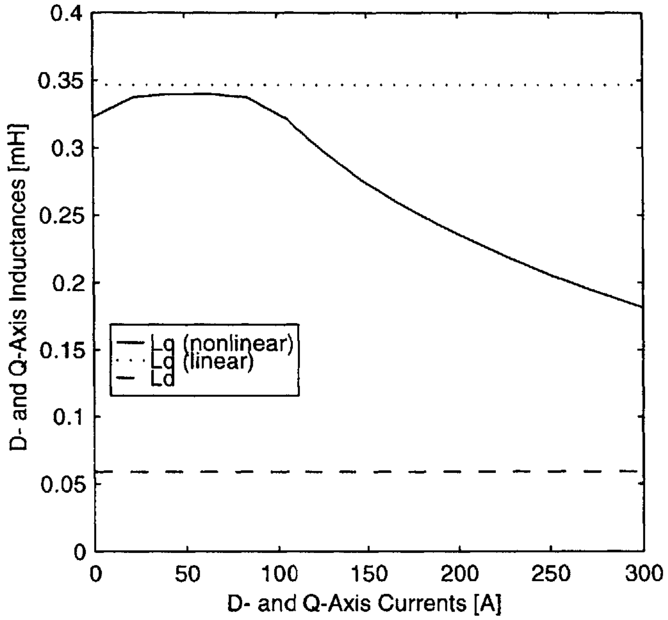

Figure 7.15: Design B, comparison of the q-axis (nonlinear), q-axis (linear), and d-axis inductances.

Regarding the second observation, a critically-important corollary conclusion is that efforts to optimize a machine based on the cost of the machine alone can lead to a combined machine-converter cost that is substantially higher than the minimum attainable system cost.

Of course, the extent of the impact of magnetic saturation and converter cost on the resulting optimal machine design depends on the details of each particular application. For example, high-performance applications that demand high machine torque density are likely to be the most sensitive to saturation effects because of their higher flux density levels. Similarly, the machine designs are more likely to be affected by including converter costs in the optimizer cost function when the cost of the power electronics is high relative to the machine.

The preferred approach for accommodating the negative effects of magnetic saturation depends on the driving factors in each application. In this chapter, it has been assumed that the combined machine-converter cost is the overriding concern. Although this is true in many cases such as the automotive application considered in this chapter, there are other applications where machine volume and weight may be more critical. Under these conditions, the optimizer cost function can be reformulated to minimize the machine volume or mass, driving the optimal machine designs back in the direction of smaller sizes.

The availability of these alternative cost functions should not mislead the IPM machine designer from the reality that magnetic saturation will almost inevitably impose a penalty on the system that must be taken into account. However, the clever designer will exercise the available degrees of design freedom to choose the system attribute/feature that can best absorb the resulting penalty while protecting the most important performance advantages made available by the selection of an IPM machine.

7.6 Summary

This chapter presented the results of the optimized design of a direct-drive automotive starter generator (ISG). The variable and constant machine parameters for the Monte Carlo and local gradient optimization were outlined. Then the optimal ISG design was analyzed including the details of the lumped parameter and system-level calculations. Performance at specified torque-speed operating points was addressed as well as the machine drive's capabilities in the constant-power region. The impact of the varied and challenging ISG requirements was discussed in the context of the IPM machine optimization. FEA verification of the chief results was provided.

The optimal double-layer IPM machine drive for the 150 Nm/6 kW ISG application as determined using the saturable LPM and the two-stage optimization process is a 12-pole machine with current ratings 327 Arms starting and 223 Arms generating. The optimization was chiefly limited by the restriction on back-emf at the maximum operating speed of 6000 rpm. FEA analysis similar those presented in Chapter 4 indicate good accuracy for the saturable LPM with the agreement between the FEA and saturable LPM calculations within 5% for L_q versus I_q. Agreement between FEA and the saturable LPM is within 5% for λ_{PM} and less than 1% for L_d and rated T_e.

The capabilities of the optimal ISG design with respect to the ancillary issues of structural integrity and demagnetization were also presented. Although final conclusions are not possible within the scope of this research program, candidate materials for the core and permanent magnets were proposed that support the feasibility of the machine design for the automotive ISG application. Using structural FEA with the rotor ID boundary condition assumptions associated with an endplate hub, the maximum stress in the rotor bridge is estimated at 34% above the yield strength of M19 steel at the nominal mechanical design speed. It is therefore suggested to use alternative higher strength materials and/or reduce the maximum required design speed. According to FEA, the magnets will not experience irreversible demagnetization even with rated starting current along the negative *d*-axis of the machine. In the worst case scenario where the magnet remanent flux density is fully reversed the reduction in rated torque is 14%. Also the magnets will not bulk demagnetize unless roughly twice rated starting current (654 Arms) is applied.

Then the behavior of the ISG IPM machine is explored contrasting the predictions of the linear and saturable LPMs in the constant-power operating region. It is demonstrated again that there is a significant difference between the predictions of linear and saturated analysis of high-performance IPM machine designs. It is found that the IPM machine drive delivers 85% of it's constant power level up to the maximum operating speed of 6000 rpm.

The final section more generally explored the effects of magnetic saturation and converter costs on the optimization of an IPM machine drive system. The optimization procedure was repeated with four variations: linear LPM, machine cost optimized; linear LPM, system cost optimized; saturable LPM, machine cost optimized; and saturable LPM, system cost optimized. This exercise provided useful insights into the performance shortcomings when linear LPM design techniques are used, and the cost benefits of optimizing a combined machine-converter system over optimization of machine cost alone.

Chapter 8

SUMMARY, CONCLUSIONS, AND RECOMMENDATIONS

8.1 Introduction

This thesis examined the design of transversely-laminated interior PM synchronous machine drives. A thorough analysis and design method based on equivalent magnetic circuit models of the machine was developed to calculate the principal machine lumped parameters and performance, including the effects of magnetic saturation. The accuracy of a magnetically-saturable lumped parameter model (LPM) has been verified by means of comparisons with finite element analysis results and experimental data from existing IPM machines. The value of the analysis method has been demonstrated by using it to develop the cost-optimized design of an automotive integrated starter/generator.

The major accomplishments of this thesis are the development of a saturable lumped parameter model for transversely-laminated interior PM machines, and the development of a cost-optimized IPM machine drive for a high-power automotive integrated starter/generator application that accounts for magnetic saturation.

IPM machine drive systems are attractive because of their capabilities for constant-power operation over wide speed ranges and their potential for higher power density and efficiency than alternatives such as induction machines. Additionally, IPM machines generally require lower-strength magnets than conventional surface permanent magnet (SPM) machines, resulting in lower magnet costs. Furthermore, lower magnet flux linkages in IPM machines generate lower back-emf voltages at top speed compared to SPM machines, reducing the need for more expensive high-voltage converter switches to protect against overvoltages following high-speed faults.

Soong investigated the theoretical limits of IPM machines compared to other machine types and designed an axially-laminated machine that demonstrated several of these desirable features [7-9, 17, 51, 66]. Candidate applications that might benefit from the special characteristics of IPM machine drives and have been investigated include appliances, aerospace actuators, electric propulsion drives, and automotive starter/generator systems [21, 40, 46].

Lumped parameter machine models are attractive for machine analysis and design because they are calculated directly from the machine geometry, winding pattern, material parameters, and excitation variables. It is generally rather intuitive to relate machine behavior characteristics back to the geometry using lumped parameter techniques. Furthermore, it is typically a far simpler task to investigate the effects of design variations using LPMs than by using other techniques such as FEA or hardware prototypes. Fratta, Vagati, et. al. developed and reported on lumped parameter models for IPM machines that successfully modeled the d-axis inductance, and they proposed similar methods to calculate the appropriate amount of magnet material to meet specific design targets [24, 25, 67, 68].

Magnetic saturation must be considered for high-performance IPM machine drives, making their equivalent magnetic circuit analysis more complex. High-performance operation implies excitation levels that force portions of the core material into magnetic saturation in order to extract the maximum amount of electromechanical energy conversion from a given machine volume, cooling system, and choice of magnetic materials. Because of the severe nonlinearity in the core material's electromagnetic properties following the onset of magnetic saturation, accurate modeling of the steel's magnetic saturation characteristics is critical for achieving accurate predictions of machine behavior. Researchers have reported on the effects of saturation and analyzed the departure of existing machines from linear, non-saturating, behavior [7, 22, 27, 31, 36, 38, 45, 49, 67]. No thorough and explicit models for saturation in transversely-laminated IPM machines for the purpose of design have been offered prior to this thesis. That makes the development of the saturable LPM in this thesis one of its' major accomplishments.

8.2 Saturable Lumped Parameter Model

A major contribution of this thesis has been the development of an approach for modeling magnetic saturation in IPM machines that is flexible, accurate, and computationally fast. The saturable LPM that has been presented retains the benefits of lumped parameter analysis while affording the ability to design IPM machine drives specifically for high-performance applications as described above.

The saturable LPM consists of equivalent magnetic circuit analyses for the *dq* frame inductances and PM flux linkage. With these three parameters, the electrical and mechanical terminal conditions can be calculated. Employing existing loss models [28-30], a realistic electromagnetic and electromechanical characterization of an IPM machine can be conveniently completed. The *d*-axis inductance that is generally not affected by saturation is calculated using the techniques of Fratta, Vagati, et. al. [24]. The PM flux linkage is calculated using a similar linear magnetic circuit model with specific accounting for the leakage flux that does not contribute to the PM flux linkage with the stator winding. This magnet leakage flux circulates in the rotor around the tips of the magnets through magnetically-conducting steel paths referred to as bridges at the rotor OD and center posts along the *d*-axis.

The major new contribution of this thesis lies with the saturable model of *q*-axis inductance. As shown by other researchers, the core flux paths along the *q*-axis are highly susceptible to bulk magnetic saturation in IPM machines, particularly in the rotor. The *q*-axis flux generally enters the full periphery of the rotor surface but is squeezed into narrower steel paths in the rotor due to the existence of the parallel magnet cavities. In this thesis, both the rotor and stator are modeled using reluctance magnetic circuit elements, where the individual element permeability is a nonlinear spline-interpolated representation of the electrical steel's DC magnetic induction, or BH, curve. The model is designed as a network to be completely scalable to any number of magnet cavity layers and to accommodate various cavity and cavity tip shapes. Furthermore, effects of individual stator teeth and slots are ignored to make the stator portion of the model easily compatible with different slotting and winding arrangements.

The accuracy of the complete saturable LPM has been verified through analysis of designs that yield matches to FEA results and to experimentally-obtained data for the same machine design within 5% on the inductance calculations. The utility of this analysis and design method has been demonstrated for a machine design with attractive flux-weakening capabilities by means of performance analyses over the complete speed range. The flexibility of this LPM approach has also been demonstrated through analysis of IPM machine designs with two, three, and four layers, as well as different configurations of bridges and posts.

8.3 Optimal Automotive Starter/Generator Design

The attractiveness and power of the saturable LPM has been thoroughly exercised by applying the method to the optimization of an automotive integrated starter/generator

(ISG) that is directly mounted on the end of the crankshaft of a conventional internal combustion engine. Challenging ISG performance requirements have been presented that create a daunting design task due to the divergent machine design trends that the individual requirements produce. Since the performance changes produced by varying the different machine design parameters is highly non-linear, the full design space is likely to result in many locally-optimized designs. Therefore, a two-step optimization process consisting of Monte Carlo design followed by local gradient optimization has been introduced. The Monte Carlo method avoids the built-in bias of designers when presented with a wide variable design space, and it takes advantage of the speed with which a single machine design can be calculated using LPM techniques [60]. Randomly-selected sets of design parameters are generated more than a million times during typical runs, and the most promising designs with respect to an established objective function are saved. These designs are then further optimized using local gradient solvers.

Using this optimization method, an optimal IPM machine design for the ISG application has been developed. The saturable LPM calculations and FEA have been used to explore serveral aspects of the performance of the cost-optimized design. The impact of saturation on designs using both linear and saturable models have been presented. The deficiencies of the linear LPM in predicting the performance characteristics of the optimal ISG machine have been clearly demonstrated.

Furthermore, the differences between optimizing the cost of the IPM machine versus optimizing the cost of the combined machine-converter have been highlighted. The results of the ISG design exercise demonstrate that there are clear financial benefits to optimizing the combined system cost. Since the converter cost dominates the combined system cost, the cost optimization exercise drives the machine design to the lowest RMS current requirements in order to minimize the converter cost. Addition analyses of ancillary issues including structural integrity and demagnetization vulnerability are required to achieve a final machine design that is both manufacturable and robust in the automotive environment.

The optimal IPM machine design was found to be a 12-pole machine, and was restricted to two magnet layers minimizing the complexity of the rotor to keep manufacturing costs down. The optimization appears to be constrained mainly by the maximum limit on the back-emf of the machine to protect the power devices on the remainder of the automotive electrical bus. The calculated lumped parameter inductances, PM flux linkage, and torque were calculated and compared to FEA with the inductances and PM flux linkage calculated by the saturable LPM agreeing with the FEA results within 5%. Peak torque predictions from the saturable LPM and FEA were identical.

The starting requirement which requires almost two times the equivalent machine sizing of the generation requirements was met using a transient current density limit. During generation a lower steady-state current limit was employed in the optimization process. Though the machine did not achieve a 10:1 constant power speed region, the machine is capable of delivering 85% of the constant power level at the maximum operating speed 6 kW.

In addition to the electromechanical performance, the structural and demagnetization design issues were also examined. The optimized ISG can meet the mechanical design point by constructing the rotor from materials with approximately 34% higher yield strength which is obtainable from alternative steel alloys. Rounded bridges with center posts across the middle of each cavity were also required to mitigate the stress. Demagnetization was also analyzed and it was found that rated current directed in the negative d-axis did not irreversibly demagnetize the magnets. At higher currents, the demagnetization was found to start and the tips and propagate into the bulk of the magnets at roughly 2 per-unit current.

8.4 Suggested Future Work

The optimal ISG machine drive design is currently being constructed for prototype testing. Additional confidence in the design and the optimization methods developed in this thesis will be gained from the experimental verification tests. Machine characterization tests will be made to calculate the machine's lumped parameters. Performance testing throughout the application's speed range will be carried out to determine torque capability, losses, and efficiency as well as steady-state and dynamic behavior with vector control. The predictions made regarding structural integrity and demagnetization will also be tested during the final segments of the planned experimental program.

Further interesting work would be to develop a means for providing accurate demagnetization predictions based on the lumped parameter models. The preliminary analysis presented in this thesis suggests that simple application of the machine's lumped parameter model is inadequate for determining the demagnetization threshold currents. Results in this thesis suggest that the key to accurate demagnetization predictions lies in properly accounting for the flux that is circulated through the narrow steel rotor bridges and posts both by the magnets and by the stator mmf excitation source.

The three-section magnet cavity model should be explored further to investigate optimal cavity shape characteristics over a wide variety of IPM designs. Research has been conducted that examines the optimal ratios of total magnet-to-steel depth as measured in the radial direction of an IPM rotor [31, 40, 55, 66, 67, 69]. However, few results have been presented examining the optimal overall shapes of cavities. The lumped parameter analysis method affords a unique opportunity to quickly explore a wide design space with varied cavity geometries to optimize them for different design requirements. Although one such design comparison was conducted in this thesis [54], the limitations of the three-section magnet model for approximating other rotor magnet geometries such as semicircular should be explored as part of an expanded investigation.

Finally, the most significant issue that calls for further investigation is the development of appropriate high-volume manufacturing techniques for IPM machines, both transversely-laminated and axially-laminated. The optimal ISG machine design presented in this thesis is a 12-pole machine with four separate cavity sections in each pole. This adds up to 48 separate irregularly-shaped magnets that must be inserted to fully populate the rotor. If a cost-effective method for injecting plastic ferrite-based PM materials can be successfully developed, one of the chief constructional impediments for this building this machine configuration would be eliminated.

Another major issue is the rotor's mechanical strength. Although this particular ISG machine configuration has the advantage of compact system design with the torque converter or clutch mounted inside the rotor, it has introduced high mechanical stress in the rotor bridges and posts. Several opportunities exist to explore alternative high-strength core materials to conventional electrical steel [32-34, 50, 61, 65]. Such a replacement would benefit any high-tip-speed machine application that also has severe cost constraints.

Both the prediction of demagnetization withstand and the structural analysis should be developed as part of a cohesive lumped parameter model for combined optimization of IPM machine drives to meet performance, structural, and demagnetization withstand goals at once.

Chapter 9 Appendix A

MATLAB LUMPED PARAMETER MODEL

The MATLAB lumped parameter model is the set of scripts and functions written in the MATLAB computing language to analyze and design multpitle layer transverse-laminated IPM machines. The top level scripts are:

srpmgvars – sets up the global variables

load <filename> - built-in MATLAB function to load variable values into the workspace

svars <filename> - likewise to save the list of machine variables to a file for later retrieval

srpmlinear – calculates all the linear and static portions of the IPM machine model

srpmsaturable – calculates the saturable q-axis inductance

srpmfeflexnew – draws the IPM machine or just one pole

srpmmg – calculates machine performance as a motor maximizing torque

srpm – calculates machine performance as a motor or generator to specified torque and power requirements

There are many lower level functions that are also included to accomplish tasks such as converting between polar and cartesian coordinates, and specifying arcs and lines for drawing objects.

```
% srpmgvars.m
% Global SRPM variables

global SRPMGVAR;

% deleted Bag and us
% added last line of variables
SRPMGVAR=[' dout l g p na ma ds hs lams
lamh lamh2 ratm ratm2 lama db',...
' Br pb bb epb omb epf nst Prat siga rhom
rhos rhofe', ...
' lamus lamrd raths lammd1 lammd2
lammd3', ...
' dratio mratio nac Trat ucmagnet Bs brw
tcsyst', ...
' geff crw1 crw2 crw3 brw1 brw2 brw3',
...
' nc mac Ib Vb ds os r lammd rata crw
ratia rat4a roundb'];

eval(['global',SRPMGVAR(1:229)]);
eval(['global',SRPMGVAR(230:length(SRPMGV
AR))]);

% svars(name)
% Saves SRPM variables in a file called
name.mat

function svars(name)
srpmgvars;
global SRPMGVAR;
```

```
if (abs(version)*abs(version)'==92928)
    if (size(SRPMGVAR>229)),
    eval(['save
',name,'A',SRPMGVAR(1:229)]);
    eval(['save
',name,'B',SRPMGVAR(230:length(SRPMGVAR))
]);
    else
    eval(['save ',name,SRPMGVAR]);
    end
else
    if (size(SRPMGVAR>229)),
    eval(['save -v4
',name,'A',SRPMGVAR(1:229)]);
    eval(['save -v4
',name,'B',SRPMGVAR(230:length(SRPMGVAR))
]);
    else
    eval(['save -v4 ',name,SRPMGVAR]);
    end
end

% Linear portion of the IPM static design

global ia Ib Lambda xd xq id te mflag;

% Here are a few constants
muzero=pi*4e-7;      % free-space
permeability
tol=1e-6;            % error tolerance in
power loop
cpair = 1005.7;      % mass heat capacity
of air
rhoair = 1.1774;     % density of air
nuair = 1.56e-5;     % kinematic viscosity
of air
psistep = pi/10;
% Defaults for mechanical losses
dtt = 100;
etf = 1;
Va = Vb;

% Stator Geometry
% Number of stator slots
% mac = [2 1];
% ma = mean(mac);
% ns = round(6*ma*p);
% mac is the number of full slots a coil
group requires divided by the actual
number of slots used
% nc is the of coils in each group
represented by mac
% nst is the number of slots short
pitched from one pole pitch for each coil
group

ma = sum(mac);
ns = round(6*ma*p);

% Slot opening
us = lamus*2*pi*r/ns;

% Coil depression
% Given by ABB design 3/5/00
% ds = pi*r*lams/ns - us/2;
% Number of total armature turns
na = sum(nc)*p;
nat = na*nac;
% Turns per coil
% ABB 2-layer definition 3/5/00
% nc = na/(2*ma*p);
% nct = nat/(2*ma*p);
% Tooth fraction
lamt = 1 - lams;
% slot top width
wst = 2*pi*(r+ds)*lams/ns;
% Slot height
hs = raths*wst;
% tooth width
wt = 2*pi*(r+ds)*lamt/ns;
% slot bottom width
% Old Formula
% wsb = wst*(r+ds+hs)/(r+ds);
% Corrected Formula
wsb = 2*pi*(r+ds+hs)/ns - wt;
% average
wsa = 0.5*(wsb+wst);
% Stator Core Inside Radius
rci = r+ds+hs;
% Stator Core Outside Radius
rco = rci + db;
% full-pitched coil throw
nsfp = ns/(2*p);
% actual coil throw
% ABB 2-layer definition 3/5/00
nsct = nsfp - nst;
% estimate of end cone length
% coil angle
thetae = acos(lams);
% azimuthal travel (half end)
laz = pi*(r+ds+.5*hs)*nsct/ns;
% end length (axial)
% ABB 2-layer definition 3/5/00
le1 = mean(laz)/tan(thetae);
% Overall machine length
lout = l+2*le1;
% end length (half coil)
le2 = laz/sin(thetae);
% Armature Conductor Length
% ABB 2-layer definition 3/5/00
Lac = 2*na*(l+2*mean(le2));
% Armature Conductor Area
% ABB 2-layer definition 3/5/00
% Aac = hs*wsa*lama/(2*nc);
Aac = hs*wsa*lama/(sum(nc)/ma);
% Armature Resistance
Ra = Lac/(siga*Aac);

% Rotor Geometry
% Average air gap radius
```

```
rag = r - g/2;
% Rotor Outer Radius
rro = r - g;
% Rotor Inner Radius
rri = lamrd*rro;
% Rotor Yoke and Magnet Heights
hm = [1-sum(lamh) lamh]*ratm*(rro-rri);
global nl;
nl = length(lammd);
hry = [1-sum(lammd) lammd]*(1-ratm)*(rro-
rri);

% Radius at the half magnet height on the
line of symmetry
rrm = rro - cumsum(hry(1:nl)) - 0.5*hm -
cumsum([0 hm(1:(nl-1))]);

% Rotor Vertices for Drawing

% Start with wider magnet
% Magnet pole span [elect. rad]
rata =
min(rata*pi/(2*p),acos(rrm(nl)/(rro-
brw(nl)))*.9)*(2*p/pi);
alphm = rata*pi;
% Angular distance from Q-Axis to End of
Magnet [elect. rad]
alpm = (1-rata)*pi/2;

% Mechanical Angles
% Angular delta from zero ref to
beginning of the magnet
ang0 = alpm/p;
% Inner angular span of the magnet
ang1i = ratia*atan((rrm(nl)*tan(pi/2/p)-
(rro-brw(nl))*sin(ang0)/sin(pi/2-
pi/2/p))/rrm(nl));

% len5 = locside(pi/(2*p)-
ang0,rrm(nl),rro-brw(nl)),
% ang5 = locangle(rrm(nl),len5,rro-
brw(nl))-ang0,
% ang6 = locangle(rro-
brw(nl),len5,rrm(nl))-pi/2,
% len6 = losside(len5,pi-ang6-ang5,ang5),
% ang1i=atan(len6/rrm(nl)),

% Outer angular span
ang1o = alphm/(2*p)-ang1i;
% Radius to end of middle section
rrem = rrm(nl)/cos(ang1i);
% Length of the side magnet piece
len1 = locside(ang1o,(rro-brw(nl)),rrem);
% Angle included between the outer radius
of the magnet and the side magnet length
ang2 = locangle(rrem,(rro-brw(nl)),len1);
% Angle included between the side magnet
length and the inner radius of the magnet
ang3 = pi - ang2 - ang1o;
% Half the angle between the side and
center magnet lengths
ang4 = 0.5*(pi/2 + ang2 + ang1i + ang1o);
% Length of the outer radius edge
len2 = hm(nl)/cos(ang2)/2;
% Length from the inner corner to the
outer corner
len3 = hm(nl)/sin(ang4)/2;
% alpm is angle at rro-brw and minimum
bridge width 'pinch point' 9/19/99
alpm = angle(pol2comp((rro-
brw(nl)),ang0)-
pol2comp(hm(nl)/(2*cos(ang2)),ang0-
ang2))*p;

% Repeat for all magnets fixed to
parallel
% ang1i and ang4 defined by parallel
constraint
ang1i = atan((rrm(nl)*tan(ang1i)-(rrm-
rrm(nl))./tan(ang4))./rrm);
ang4 = [rat4a 1]*ang4;
rrem = rrm./cos(ang1i);
ang3 = 2*pi-2*ang4-(pi/2-ang1i);
ang2 = losangle(rro-brw,ang3,rrem);
ang1o = (pi - ang3 - ang2);
alphm = 2*p*(ang1o+ang1i);
len1 = locside(ang1o,(rro-brw),rrem);
ratam = alphm/pi;
ang0 = (1-ratam)*pi/(2*p);
len2 = hm./cos(ang2)/2;
len3 = hm./sin(ang4)/2;

% Bridge Geometry
% Straight tips
alpms = (1-ratam)*pi/2;
% Rounded tips
alpmr = angle(pol2comp((rro-brw),ang0)-
pol2comp(hm./(2*cos(ang2)),ang0-ang2))*p;
if(roundb)
   alpm = alpmr;
else
   alpm = alpms;
end

% Continue with all
% Angular distance from End of Magnet #1
to D-Axis and between each magnet [elect.
rad]
dalpm = [pi/2 alpm(1:(length(alpm)-1))] -
alpm;

% Nonlinear Magnetic Circuit Areas and
Lengths
% Length of magnet assuming three
straight segments
% and middle portion is half the magnets
angular span
lm = 2*(rrm.*tan(ang1i) - crw ...
```

```
     + sqrt(rrem.^2 + (rro - brw).^2 -
2*rrem.*(rro - brw).*cos(anglo)));

% All half-pole lengths
% Rotor Yoke Length
lry = 0.5*mean([0
(lm+2*(brw+crw));(lm+2*(brw+crw))
2*rri*tan(alphm(nl)/(2*p))+2*(rro-
rri/cos(alphm(nl)/(2*p)))]);
% Tooth path length to middle back iron
depth
lst = hs+ds+db/2;
% Average length of stator yoke sections
from midpoint to midpoint of each section
% lsy =
(r+ds+hs+0.5*db)*[alphm1,alphm2,pi-
alphm1]/(4*p);
lsy = (r+ds+hs+0.5*db)*([pi/2 mean([pi/2
alpm(1:(nl-1));alpm])] - mean([pi/2
alpm;alpm 0]));

% Cross-sectional areas
% Full pole
Asy = db*l;
% Account for bridge width separately
from the magnet
% Am = (lm+2*(crw+brw))*l;
Am = lm*l;
Aag = rro*l*pi/p;
Agd = rro*l*2*dalpm/p;
% Half pole
Ag = 0.5*[Agd rro*l*(pi-2*sum(dalpm))/p];
Ast = lamt*Ag;
Ary = l*hry;
Ary(nl+1) = l*mean([hry(nl+1) ((rro-
brw(nl))*sin(ang0(nl))-hm(nl)/2)]);

% Saturating bridge dimensions
% Half pole
Ab = (brw+crw)*l;
% Length of the bridge
if(roundb)
    lb=(brw+crw);
else
    lb = 2*len2;
end

% Area of one slot pitch
As = 2*pi*r*l/ns;
% Electrical angle spanned by one slot
pitch
dalps = 2*pi*p/ns;

% Masses
% Armature Conductor
massa = 3*Lac*Aac*rhos;
% Stator Mass
% Back Iron
mcore = rhofe*l*pi*(rco^2-rci^2);
% Teeth
```

```
mtooth = rhofe*l*(ns*wt*hs+2*pi*r*ds-
ns*ds*us);
% Tapered opening
mtooth = rhofe*l*ns*(wt*(hs+ds) +
(ds+os)*(2*pi*r/ns-wt-us));
% Rotor Magnet Mass
marea = 2*p*lm*hm';
mmagnet = l*marea*rhom;
% Rotor Core Mass
mcorer = rhofe*l*(pi*(rro^2-rri^2)-
marea);
% Iron Mass
miron = mcore+mtooth+mcorer;
% Rotational Inertia
Jm = (mcorer+mmagnet)*(rro^2+rri^2)/2;

% Carter Coefficient
% only using stator extension
% Extension of the air-gap because of
slot openings
% slot top is depression width
sts = us;
% str = hm/2;
% tooth width is the rest:
tws = 2*pi*r/ns - sts;
% twr = 2*pi*(r-g)/(8*p) - str;
alphas = atan(sts/(2*g));
% alphar = atan(str/(2*g));
ccs = g*(alphas*tan(alphas) - log
(1/cos(alphas)));
% Ignore rotor effects for now
% ccr = g*(alphar*tan(alphar) - log
(1/cos(alphar)));
% geff = g*(sts+tws)/(sts+tws-
ccs)*(str+twr)/(str+twr-ccr);
geff = g*(sts+tws)/(sts+tws-ccs);

% Calculation of d-axis inductance ratios
using
% per-unit circuit elements (Vagati, et
al)
% Corrected all pu reluctances by
inverting 4/12/98
% Corrected to include bridge width which
is assumed saturated 9/19/99
% Corrected to assume that bridges don't
saturate over the full depth of the
magnet with rounded cavities 10/20/99
rm = hm.*As./(geff*0.5*Am);
rg = dalps./dalpm;
rb = lb.*As./(geff*Ab);
% Correction with cos()
puf = (cos(alpm) - cos([pi/2 alpm(1:(nl-
1))])) ./dalpm;

% PM circuit magnetic elements
% Full pole
Rm = hm./(muzero*Am);
Rg = geff./(muzero*Agd);
Rb = lb./(muzero*2*Ab);
```

```
% Circuit solver only works for three
layers numbered 1,3,2 in order
if (1)
   daxissol;
elseif (nl==2)
   doublelayercircuit;
elseif (nl==3)
   triplelayercircuit;
else
   fprintf('Need to write circuit solver
for higher numbers of barriers\n');
   break;
end

% Stator winding factors
% Stator slot pitch (in electrical
radians)
gama = 2*pi*p/ns;
% Coil throw (in electrical radians)
nssp = nsct/nsfp;
alfa = pi*nssp;

% Breadth or distribution
% Effective distribution is one slot
3/5/00 two values now 4/12/00
if (round(ma)==ma)
   kb = sin (0.5 * mac * gama) ./ (mac *
sin ( 0.5 * gama));
   kb5 = sin (2.5 * mac * gama) ./ (mac
* sin (2.5 * gama));
   kb7 = sin (3.5 * mac * gama) ./ (mac
* sin (3.5 * gama));
elseif(round(2*ma)==2*ma)
   kb = sin (0.5 * ma * gama) ./ (2*ma *
sin ( 0.5 * gama/2));
   kb5 = sin (2.5 * ma * gama) ./ (2*ma
* sin (2.5 * gama/2));
   kb7 = sin (3.5 * ma * gama) ./ (2*ma
* sin (3.5 * gama/2));
else
   lerror = 1;
   fprintf('Fraction Slot Winding greater
than a pole-pair period\n');
   break;
end

% Pitch
% Two values now 4/12/00
kp = sin (alfa/2.0);
kp5 = sin (5.0 * alfa/2.0);
kp7 = sin (7.0 * alfa/2.0);

% Skew of one slot pitch
ks = sin (gama/2.0) / (gama/2.0);
ks5 = sin (5*gama/2.0) / (5*gama/2.0);
ks7 = sin (7*gama/2.0) / (7*gama/2.0);

% Total
% Two values 4/12/00
ka = kb .* kp .* ks;
ka5 = kb5 .* kp5 .* ks5;
ka7 = kb7 .* kp7 .* ks7;

% Zig-zag Factors
np = ns/p+1;
nm = ns/p-1;
% if ma>1 we need to compute a separate
zigzag component
% np and nm are the positive and negative
zigzag harmonic orders
if ma>1,
  kbp = sin (0.5 * ma * np * gama) / (ma
* sin ( 0.5 * np * gama));
  kbm = sin (0.5 * ma * nm * gama) / (ma
* sin ( 0.5 * nm * gama));
  kpp = sin (np * mean(alfa)/2.0);
  kpm = sin (nm * mean(alfa)/2.0);
    ksp = sin (gama * np/2.0)  / (gama *
np/2.0);
    ksm = sin (gama * nm/2.0)  / (gama *
nm/2.0);
  kap = kbp * kpp * ksp;
  kam = kbm * kpm * ksm;
end

% Calculation of internal voltage
% lambda = 2*rro*l*B1*na*ka/p;
% Add together the two coil groups 3/5/00
lambda = 2*rro*l*B1*sum((p*nc).*ka)/p;
% RMS Air-gap flux linkage
Lambda=lambda/sqrt(2);

% Calculation of reactances: only two
count here!
% Air-gap inductance: basic round rotor
% Lag =
(3/2)*(4/pi)*muzero*na^2*ka^2*l*r/(p^2*ge
ff);
% Add together the two coil groups 3/5/00
Lag =
(3/2)*(4/pi)*muzero*((sum((p*nc).*ka)).^2
)*l*r/(p^2*geff);

% Stator Leakage Inductance Calculation
% Slot leakage
% FIX
perm = muzero*l*(ds/us+(1/3)*hs/wst);
% Estimate using mean 3/5/00
% Lslot = 2*p*nc^2*perm*(4*ma-nst);
Lslot = 2*p*mean(nc)^2*perm*(4*ma-
mean(nst));
if (nssp > (2/3)),
    knssp = 1.5*nssp - 0.5;
elseif (nssp < (1/3)),
    knssp = 1.5*nssp - 1;
else,
    knssp = 3*nssp - 1.5;
end
```

```
permn = muzero*1*((2*os/us + 2*(ds-
os)*log(wsa/us)/(wsa-us) +
(5/6)*(hs/wsa)) ...
        + knssp*(os/us + (ds-
os)*log(wsa/us)/(wsa-us) + hs/(4*wsa)));
     % Lslot = na^2*permn/(2*ma*p);
     % Lslot =
(2*p*sum(nc))^2*mean(permn)/(2*ma*p);
Lslot =
(p*sum(nc))^2*mean(permn)/(2*ma*p);

% End Turn Leakage Inductance
% Lend = 0.5*(140/(4 * pi^2))*(3/2) *
muzero * r * na^2 * (alfa/pi - 0.3)/p^2;
% Estimate using mean 3/5/00
Lend = 0.5*(140/(4 * pi^2))*(3/2) *
muzero * r * na^2 * (mean(alfa)/pi -
0.3)/p^2;

% Harmonic Components: Belt Leakage
Inductance
% La5 = Lag * (ka5 / (ka * 5))^2;
% La7 = Lag * (ka7 / (ka * 7))^2;
% Estimate using mean 3/5/00
La5 = mean(Lag * (ka5 / (ka * 5))^2);
La7 = mean(Lag * (ka7 / (ka * 7))^2);

% Stator Zigzag Leakage Inductance
% Round rotor formulation
% Effective distribution is one 3/5/00
if (any(mac))>1,
  Lap = Lag * mean((kap ./ (ka *
np)).^2);
  Lam = Lag * mean((kam ./ (ka *
nm)).^2);
else,
    Lap = 0;
    Lam = 0;
end

% Salient Inductances
Laqm = Lag;
Ladt = Laqm*ratdtqm;
Ladc = Laqm*ratdcqm;
Ladm = Ladt + Ladc;

% Synchronous Reactances (Ohms)
Ll = Lslot + Lend + La5 + La7 + Lap +
Lam;
Ld = Ladm + Ll;
Lq = Laqm + Ll;
Lql=Lq;
xd = Ld*Ib/Lambda;
xq = Lq*Ib/Lambda;
Sr = xq/xd;

% Base torque
Tb = 3*p*Lambda*Ib;

% Saturable portion of IPM static design
```

```
lerror=0;
if(mflag==1)
    Iqx=linspace(.001,Ib);
    Lqy=Lq*linspace(1.001,.999);
    Lqy(1) = Lq;
elseif(mflag==3),
% New nonlinear model
    qaxmodel3;
else
% Slow nonlinear model
    qaxmodel4;
end
if(ismono(Iqx)==0);
   lerror = 1;
   return;
end
%   plot(Iqx,Lqy);
%   axis([0 500 0 1e-3]);
%   pause(1);
%   Iqx=linspace(1,501);
%   Lqy=Lq*ones(1,100);
[Lqmax,Indmax] = max(Lqy);
iqmax = Iqx(Indmax)/Ib;
Indmin = length(Lqy);
while((Lqy(Indmin) < Ld) & (Indmin >
Indmax))
   Indmin = Indmin - 1;
end
iqmin = min(1,Iqx(Indmin)/Ib);
%   if ((iqmax > 1) | (Lqmax < Ld))
if ((iqmax > 1) | (Indmin <= Indmax))
   Ia = 9e9;
   lerror = 1;
   return;
end

%
*****************************************
*************************
% *
*
% *                              SRPM.M
*
% * Synchronous Reluctance PM Machine,
Stator in Slots              *
% * Internal (Flux Concentrating) Magnets
*
% * Copyright 1995, James L. Kirtley Jr.
*
% * Modified 1997, Edward C. Lovelace
*
% *
% *
*
%
*****************************************
*************************
% Change History
```

```
% 10/5/99 - Added capability for three-
barrier machines
% srpm.m: main design program
% see 6.11s copyright statement for rules
of use
% Requires the following input variables:
% Rotational Speed
% Required Power
% Required power factor angle psi
% Outer diameter              dout
% Air-gap
% Magnet Depth Fraction       ratm
% Magnet Relative Depths      lamh
% Rotor Depth Fraction        lamrd
% Small Magnet Span Ratio     ratm1
% Large Magnet Span Ratio     ratm2
% Magnetizing Saliency Ratio  ratdtqm
% Circulating Saliency Ratio  ratdcqm
% Active length               l
% Pole pairs                  p
% Slots per pole per phase    ma
% Slots short pitched         nst
% Peripheral slot fraction    lams
% Slot height ratio           raths
% Slot depression depth       ds
% Slot opening fraction       lamus
% Back Iron depth             db
% Total armature turns        nat
% Armature parallel paths     nac
% Slot Fill Fraction          lama
% Magnet Remnant Flux Density Br
% Stator Conductivity         siga
% Iron Model Base Dissipation pb
% Base Frequency              omb
% Base Flux Density           bb
% Flux Exponent               epb
% Frequency Exponent          epf
% Steel Density               rhofe
% Magnet Density              rhom
% Conductor Density           rhos
% Air temperature rise        dtt
% Assumed fan efficiency      eft
%
% Power loop does not account for core or
winding losses.
% Core and winding losses are accounted
for, though, in efficiency.
% Can calculate motor or generator
conditions based on power factor input.
% Prat input should shaft output
(motoring), or electrical input
(generating).
% New input set

srpmlinear;
srpmsaturable;

% Speeds
% Electrical frequency
f = p*rpm/60;
```

```
om = 2*pi*p*rpm/60;
% Mechanical frequency
omegam = 2*pi*rpm/60;
% Tip (rotor peripheral) speed
stip = rro*om/p;

% Reactances
Xd = om*Ld;
Xq = om*Lq;
% RMS (!) Internal Voltage:
Ea = om*Lambda;

% Ok: now we go into a loop to see if we
can actually get
% terminal voltage and current
% This will probably crash here if the
rating is impossible
notdone = 1;
lerror = 0;
leg = 1;
nloop = 0;
Va = volt;
Ia = Prat/(3*Va*cos(pi/4));
% Now estimate losses
Pa = 3*Ia^2*Ra;

% Estimate of gap friction loss
% Reynold's Number in the gap
% ren = omegam*rro*g/nuair;
% that gives a friction factor
% ff = .0076/ren^.25;
% and that in turn leads to windage loss
% pwind =
2*pi*rro^4*omegam^3*l*rhoair*ff;
pwind = 0;

% fan pressure rise estimated from rotor
peripheral speed
% deltap = .5* rhoair * (omegam * rro)^2;
% mass flow based on temperature rise
% mdot = (Pc + Pa + pwind)/(cpair * dtt);
% then fan power is volume flow times
pressure drop
% pfan = mdot * deltap / (rhoair * etf);
pfan = 0;

while notdone == 1,
    nloop = nloop + 1;
    if (gen == 0),
%   fprintf('Motoring psi = %g\n',psi);
% Motoring
% Defined by ABB design 3/5/00
%   Ib = 5e7 * Aac;
    Tb = 3*p*Lambda*Ib;

%   plot(Iqx,Lqy);
%   axis([0 500 0 1e-3]);
%   pause(1);

    Tmax = Prat/omegam;
```

```
rpm
Pra

g
```

```
    te = Tmax/Tb;
% Find the iq that minimizes the phase
current ia
    iq = constr(['f = iqid(x);' 'g =
[];'],(iqmax+iqmin)/2,[],iqmax,iqmin);
%       iq = constr('f =
iqid(x);',iqmax*1.1,[],iqmax,1);
%       iq = fmin('iqid',Iqmax/Ib,1),
    Ia = ia*Ib;
    Id = id*Ib;
    Iq = iq*Ib;
    Lq = xq*Lambda/Ib;
    Tmax = Tb*(1 - (xq - xd)*id)*iq;
    Vq = om*Lambda + om*Ld*id*Ib +
Ra*iq*Ib;
    Vd = -om*Lq*iq*Ib + Ra*id*Ib;
    Va = sqrt(Vq^2 + Vd^2);
    delt = atan2(Vd,Vq);
    psi = atan2(id,iq) - delt;
    Sr = Lq/Ld;
    fprintf('Saliency Ratio = %g\n',Sr);
%   fprintf('Starting torque = %g Current
= %g\n',Tmax,Ia);
%   fprintf('Old Iq = %g  New Iq = %g
Torque = %g  Lq =
%g\n',iqold*Ib,iq*Ib,Tmax,xq*Lambda/Ib);
    if ((Va > mvolt) | (Ia > Ib))
        lerror = 1;
        break;
    else,
        notdone = 0;
     end
    else,
%   fprintf('Generating psi = %g\n',psi);
    % Generating
    Ia = Prat/(3*Va*cos(psi));
    delt = atan2(-Ia*(Xq*cos(psi)-
Ra*sin(psi)),...
                  (Va-
Ia*(Xq*sin(psi)+Ra*cos(psi))));
    E1 = sqrt((Va-
Ia*(Xq*sin(psi)+Ra*cos(psi)))^2 ...
               +(-Ia*(Xq*cos(psi)-
Ra*sin(psi)))^2);
    Eas = E1 - (Xd-Xq)*Ia*sin(psi+delt);

    if (nloop > 300)
        fprintf('Ea = %g\tEas = %g\tIa =
%g\tpsi = %g\n',Ea,Eas,Ia,psi);
        lerror = 1;
        break;
     end

    eratio = Eas/Ea;
    if (leg == 1),
        if (abs(eratio - 1) < tol),  % if
true we are done
            leg = 2;
            psi1 = psi;
            Ia1 = Ia;
```

```
            delt1 = delt;
            psi = psi + psistep;
            psistep = pi/10;
        elseif (eratio > 1),
            psi = psi + psistep;
        else,
            psi = psi - 0.9*psistep;
            psistep = psistep/10;
         end
        if (psi > psif)
            lerror = 1;
            break;
         end
%       fprintf('psi = %g eratio =
%g\n',psi,eratio);
    else,
        if (abs(eratio - 1) < tol),  % if
true we are done
            notdone = 0;
            if (Ia > Ia1),
                psi = psi1;
                Ia = Ia1;
                delt = delt1;
             end
        elseif (eratio < 1),
            psi = psi + psistep;
        else,
            psi = psi - 0.9*psistep;
            psistep = psistep/10;
         end
        if (psi > psif)
            if (Ia1 < 9e9),
                psi = psi1;
                Ia = Ia1;
                delt = delt1;
                notdone = 0;
            else,
                lerror = 1;
                break;
             end
         end
     end
    end
    % Coercive Force Estimate
    psidelt = atan(Xq/Ra) + gen*pi;
    Iashort = Ea/(Xd*sin(psidelt) +
Ra*cos(psidelt));
    Idshort = Iashort*sin(psidelt);
    Cf = Xd*Idshort*Br/Ea;
end        % end of power adjustment
loop

% RMS Air-gap Flux Density
% ABB 2-layer winding definition 3/5/00
% Bagv = Va*p/(om*2*rro*l*na*ka);
Bagv =
Va*p/(om*2*rro*l*(2*p)*sum(ka.*nc));
% Tooth Flux Density (RMS)
Bt = Bagv/lamt;
% Back Iron Flux Density (RMS)
```

```
Bb = Bagv*pi*rro/(2*p*db);
% Rotor Flux Density (RMS)
Brc = Bagv*pi*rro/(p*(rro-rri-sum(hm)));
% Flux Density Limit
% if ((Bt > 1.8) | (Bb > 1.8))
%   lerror = 1;
%   Ja = 9e9;
%   Tm = 0;
%   eff = 0;
%   Pin = 0;
%   return;
% end
% Core Iron Loss
Pcb =
mcore*pb*abs(Bb/bb)^epb*abs(om/omb)^epf;
% Teeth
Pct =
mtooth*pb*abs(Bt/bb)^epb*abs(om/omb)^epf;
% Rotor Iron Loss
Pcr =
mcorer*pb*abs(Brc/bb)^epb*abs(om/omb)^epf
;
Pc = Pcb+Pct;

if (lerror)
    Ja = 9e9;
    Tm = 0;
    eff = 0;
    Pin = 0;
    return;
end

% Performance Characterization
% dq Currents
Iq = Ia*cos(psi+delt);
Id = Ia*sin(psi+delt);
% Slot Current Density
Ja = 2*nc*Ia/(hs*wsa);

% Power, Torque, and Efficiency
Pa = 3*Ia^2*Ra;
if (gen == 0),
% Motoring
% Ignore Pc for motoring
    Pin = Prat+Pa+pwind+pfan;
    if (rpm == 0),
    Tm = 3*p*Lambda*Ia*cos(psi);
    else,
    Tm = Prat/omegam;
    end
    omcorner =
max(roots([Lambda^2+2*Ld*Id*Lambda+(Ld*Id
)^2+(Lq*Iq)^2,

2*Ra*Iq*(Lambda+Id*(Ld-Lq)),
                    Ra^2*Ia-mvolt^2]));
    ommax = sqrt((mvolt^2-
(Ra*Ia)^2)/(Lambda+Ld*Ia)^2);
    cpsr = ommax/omcorner;
    corpower = Tm*omcorner/p;
    corrpm = omcorner*30/pi/p;
else,
% Generating
    Pin = Prat-Pc-Pa-pwind-pfan;
    Tm = Pin/omegam;
end
eff = Prat/Pin;
% Average rotor shear stress
shear = abs(Tm)/(2*pi*rro^2*l);
% Power Factor
pfact = cos(psi);

return;

% srpmmg
% SRPM Motoring and Generating
global ia Ib Lambda xd xq id te mflag;

notdone = 1;
lerror = 0;
leg = 1;
nloop = 0;
Va = volt;

% Speeds
% Electrical frequency
f = p*rpm/60;
om = 2*pi*p*rpm/60;
% Mechanical frequency
omegam = 2*pi*rpm/60;
% Tip (rotor peripheral) speed
stip = rro*om/p;
% RMS (!) Internal Voltage:
Ea = om*Lambda;
% Reactances
Xd = om*Ld;
Xq = om*Lq;

% Estimate of gap friction loss
% Reynold's Number in the gap
% ren = omegam*rro*g/nuair;
% that gives a friction factor
% ff = .0076/ren^.25;
% and that in turn leads to windage loss
% pwind =
2*pi*rro^4*omegam^3*l*rhoair*ff;
pwind = 0;

% fan pressure rise estimated from rotor
peripheral speed
% deltap = .5* rhoair * (omegam * rro)^2;
% mass flow based on temperature rise
% mdot = (Pc + Pa + pwind)/(cpair * dtt);
% then fan power is volume flow times
pressure drop
% pfan = mdot * deltap / (rhoair * etf);
pfan = 0;

while notdone == 1,
    nloop = nloop + 1;
```

```
    if (gen == 0),
      % Motoring
      %     Tmax = Prat/omegam;
      %     te = Tmax/Tb;
      % Find the iq that minimizes the
phase current ia
      %     iq = constr(['f = iqid(x);'
'g =
[];'],(iqmax+iqmin)/2,[],iqmax,iqmin);
%      iq = constr(['f = iqte(x);' 'g =
[];'],(iqmax+iqmin)/2,[],iqmax,iqmin);
      ia = 1;
      iq = fmin('iqte',iqmax,iqmin);
      %     iq = constr('f =
iqid(x);',iqmax*1.1,[],iqmax,1);
      %     iq = fmin('iqid',Iqmax/Ib,1),
      Ia = ia*Ib;
      Id = id*Ib;
      Iq = iq*Ib;
      Lq = xq*Lambda/Ib;
      Tmax = Tb*(1 - (xq - xd)*id)*iq;
      Vq = om*Lambda + om*Ld*id*Ib +
Ra*iq*Ib;
      Vd = -om*Lq*iq*Ib + Ra*id*Ib;
      Va = sqrt(Vq^2 + Vd^2);
      % Beware valid range is -pi to pi
      delt = atan2(Vd,Vq);
      psi = atan2(id,iq) - delt;
      Sr = Lq/Ld;
      %     fprintf('Saliency Ratio =
%g\n',Sr);
      % fprintf('Starting torque = %g
Current = %g\n',Tmax,Ia);
      % fprintf('Old Iq = %g  New Iq = %g
Torque = %g  Lq =
%g\n',iqold*Ib,iq*Ib,Tmax,xq*Lambda/Ib);
      if ((Va > mvolt) | (Ia > Ib))
        lerror = 1;
        break;
    else,
        notdone = 0;
     end
    else,
%   fprintf('Generating psi = %g\n',psi);
% Generating
% Saturation model for generating
10/24/99

    global Prat Ia Va Ea Lq om Xq Xd Ra
delt;
      Ia1 = 9e9;
      Va = 0;
      while(Va < volt)
         Va = Va + volt/10;
         options = 0;
%         fprintf('Va = %g\n', Va);
% t1 = clock;
         [psi,options] = fmin('psigen',-
 .99*3*pi/2,-1.01*pi/2,options);
% fprintf('Elapsed time for fmin-psigen
is %g seconds\n',etime(clock,t1));
% fprintf('Number of evaluations is
%d\n',options(10));
        if (options(8) > 0.01)
           Ia = 9e9;
        elseif (Ia < Ia1)
           Ia1 = Ia;
           delt1 = delt;
           Lq1 = Lq;
           Xq1 = Xq;
           psi1 = psi;
           Va1 = Va;
    else
       Va = volt;
        end
     end
     if (Ia1 < 9e9)
        notdone = 0;
        Ia = Ia1;
        delt = delt1;
        Lq = Lq1;
        Xq = Xq1;
        psi = psi1;
        Va = Va1;
     else
         fprintf('Failed to find
generating point\n');
         lerror = 1;
         break;
     end
    end
    % Coercive Force Estimate
    psidelt = atan(Xq/Ra) + gen*pi;
    Iashort = Ea/(Xd*sin(psidelt) +
Ra*cos(psidelt));
    Idshort = Iashort*sin(psidelt);
    Cf = Xd*Idshort*Br/Ea;
end           % end of power adjustment
loop

% RMS Air-gap Flux Density
Bagv = Va*p/(om*2*rro*l*sum(ka.*nc));
% Change loss definitions from RMS to
Average 2/21/00
% Average Air-gap Flux Density
Bagva = 2*sqrt(2)*Bagv/pi;
% Tooth Flux Density (Average)
Bt = Bagva/lamt;
% Back Iron Flux Density (Average)
Bb = Bagva*pi*rro/(2*p*db);
% Rotor Flux Density (Average)
Brc = Bagva*pi*rro/(2*p*(rro-rri-
sum(hm)));
% Flux Density Limit
% if ((Bt > 1.8) | (Bb > 1.8))
%   lerror = 1;
%   Ja = 9e9;
%   Tm = 0;
%   eff = 0;
```

```
%   Pin = 0;
%   return;
% end
% Core Iron Loss
Pcb =
mcore*pb*abs(Bb/bb)^epb*abs(om/omb)^epf;
% Teeth Loss
Pct =
mtooth*pb*abs(Bt/bb)^epb*abs(om/omb)^epf;
% Total Loss
Pc = Pcb+Pct;

if (lerror)
    Ja = 9e9;
    Tm = 0;
    eff = 0;
    Pin = 0;
    return;
end

% Performance Characterization
% dq Currents
Iq = Ia*cos(psi+delt);
Id = Ia*sin(psi+delt);
% Slot Current Density
Ja = 2*(sum(nc)/ma)*Ia/(hs*wsa);

% Power, Torque, and Efficiency
Pa = 3*Ia^2*Ra;
if (gen == 0),
% Motoring
% Ignore Pc for motoring
    Pin = Prat+Pa+pwind+pfan;
    if (rpm == 0),
    Tm = 3*p*Lambda*Ia*cos(psi);
    else,
    Tm = Prat/omegam;
    end
else,
% Generating
    Pin = Prat-Pc-Pa-pwind-pfan;
    Tm = Pin/omegam;
end
eff = Prat/Pin;
% Average rotor shear stress
shear = abs(Tm)/(2*pi*rro^2*l);
% Power Factor
pfact = cos(psi);

return;

% srpmfeflex.m
% Builds finite element data points from
srpmspecs.m
% Assumes a flexible rubber magnet

if exist('allorone')
else
   allorone = input('Enter 0 to just draw
one pole: ')
```

```
end

if exist('roundb')
else
   roundb = input('Enter 1 for rounded
magnet tips: ')
end

fprintf('
RADIUS   ANGLE\n');
fprintf('DATUM NAME:
[mm]    [deg]\n');

% Stator Vertices
clf reset;
clear thetat rhot;
clear rhotc thetatc;
clear point1 point2 point3 point4;
thetatc = [];
rhotc = [];

grid off;
if(allorone)
    axis([-1 1 -1 1]*rco*1e3);
    axis('square','off');
else
    axis([rri*cos(pi/p) rco 0
rco*sin(pi/p)]*1e3);
    axis('image','off');
end
% title('Synchronous Reluctance PM
Machine')
xlabel('[mm]');
ylabel('[mm]');
hold on;

rhot =
[r,r,(r+os),(r+ds),(r+ds+hs),(r+ds+hs),(r
+ds),(r+os),r,r]*1e3;
thetat = [0,(0.5*(1-lamus))/ns,(0.5*(1-
lamus))/ns,(0.5*wt)/(2*pi*(r+ds))];
thetat =
[thetat,(0.5*wt)/(2*pi*(r+ds+hs)),(0.5*wt
+wsb)/(2*pi*(r+ds+hs))];
thetat =
[thetat,(0.5*wt+wst)/(2*pi*(r+ds)),(0.5*(
1+lamus))/ns];
thetat =
[thetat,(0.5*(1+lamus))/ns,1/ns]*2*pi;

if(allorone)
    temp = ns;
else
    temp = round(ns/(2*p));
end
for segt=1:temp,
    thetatc = [thetatc,thetat+(segt-
1)*2*pi/ns];
    rhotc = [rhotc,rhot];
end
```

```
if(allorone)
    fill(rco*1e3*cos(linspace(0,2*pi)),rc
o*1e3*sin(linspace(0,2*pi)),'c');
    fill(rhotc.*cos(thetatc),rhotc.*sin(t
hetatc),'k');
else
    fill([rco*1e3*cos(linspace(0,pi/p)),(
r+os)*1e3*cos(linspace(pi/p,0))],[rco*1e3
*sin(linspace(0,pi/p)),(r+os)*1e3*sin(lin
space(pi/p,0))],'k');
    fill([rco*1e3*cos(linspace(0,pi/p)),f
liplr(rhotc.*cos(thetatc))],[rco*1e3*sin(
linspace(0,pi/p)),fliplr(rhotc.*sin(theta
tc))],'c');
end

coiloff = 0;
midstr = 0.5*(rhot(6) + rhot(7));
midla = 0.5*(thetat(4) + thetat(5));
midra = 0.5*(thetat(6) + thetat(7));
botcoilr = [rhot(5)-coiloff,rhot(6)-
coiloff,midstr+0.5*coiloff,midstr+0.5*coi
loff,rhot(5)-coiloff];
topcoilr =
[rhot(7)+coiloff,rhot(4)+coiloff,midstr-
0.5*coiloff,midstr-
0.5*coiloff,rhot(7)+coiloff];
botcoila = [thetat(5)+coiloff/(rhot(5)-
coiloff),thetat(6)-coiloff/(rhot(6)-
coiloff)];
botcoila = [botcoila,midra-
coiloff/(midstr+0.5*coiloff),midla+coilof
f/(midstr+0.5*coiloff),thetat(5)+coiloff/
(rhot(6)-coiloff)];
topcoila = [thetat(7)-
coiloff/(rhot(7)+0.5*coiloff),thetat(4)+c
oiloff/(rhot(4)+0.5*coiloff)];
topcoila =
[topcoila,midla+coiloff/(midstr-
0.5*coiloff),midra-coiloff/(midstr-
0.5*coiloff),thetat(7)-
coiloff/(rhot(7)+0.5*coiloff)];
botcoila = botcoila*180/pi;
topcoila = topcoila*180/pi;

thetat = thetat*180/pi;
fprintf('Outer Stator Radius
%8.5g%8.5g\n',rco*1e3,0);
fprintf('Center Tooth Tip
%8.5g%8.5g\n',rhot(1),thetat(1));
fprintf('Right Tooth Tip
%8.5g%8.5g\n',rhot(2),thetat(2));
fprintf('Left Slot Opening
%8.5g%8.5g\n',rhot(3),thetat(3));
fprintf('Left Slot Top
%8.5g%8.5g\n',rhot(4),thetat(4));
fprintf('Left Slot Bottom
%8.5g%8.5g\n',rhot(5),thetat(5));
fprintf('Right Slot Bottom
%8.5g%8.5g\n',rhot(6),thetat(6));
fprintf('Right Slot Top
%8.5g%8.5g\n',rhot(7),thetat(7));
fprintf('Right Slot Opening
%8.5g%8.5g\n',rhot(8),thetat(8));
fprintf('Left Tooth Tip
%8.5g%8.5g\n',rhot(9),thetat(9));

fprintf('Mid Slot Bottom
%8.5g%8.5g\n',rhot(5),0);
fprintf('Right Slot Bottom
%8.5g%8.5g\n',rhot(6),thetat(6)-180/ns);
fprintf('Right Slot Top
%8.5g%8.5g\n',rhot(7),thetat(7)-180/ns);
fprintf('Right Slot Opening
%8.5g%8.5g\n',rhot(8),thetat(8)-180/ns);
fprintf('Left Tooth Tip
%8.5g%8.5g\n',rhot(9),thetat(9)-180/ns);
fprintf('Right Tooth Tip
%8.5g%8.5g\n',rhot(2),thetat(2)+180/ns);
fprintf('Left Slot Opening
%8.5g%8.5g\n',rhot(3),thetat(3)+180/ns);
fprintf('Left Slot Top
%8.5g%8.5g\n',rhot(4),thetat(4)+180/ns);
fprintf('Left Slot Bottom
%8.5g%8.5g\n',rhot(5),thetat(5)+180/ns);

for pt=1:4,
    fprintf('Bottom Coil Corner %d
%8.5g%8.5g\n',pt,botcoilr(pt),botcoila(pt
));
end
for pt=1:4,
    fprintf('Top Coil Corner %d
%8.5g%8.5g\n',pt,topcoilr(pt),topcoila(pt
));
end
   fprintf('Angle spanned by slot-tooth
pitch      %d%8.5g\n\n',0,360/ns);

% Rotor Vertices
% ang0 Angular delta from zero to
beginning of the magnet
% ang1 1/4th of the angular span of the
magnet
% rrem Radius to end of middle magnet
% len1 Length of the side magnet piece
% ang2 Angle included between the outer
radius of the magnet and the side magnet
length
% ang3 Angle included between the side
magnet length and the inner radius of the
magnet
% ang4 Half the angle between the side
and center magnet lengths
% len2 Length of the outer radius edge
% len3 Length from the inner corner to
the outer corner

% Each column is a different magnet
```

```
mang = [ang0+(pi-ang2)-
pi/2;pi/2/p*ones(1,nl);pi/p-ang0-(pi-
ang2)+pi/2];

if(any(crw))
   mrcoa = pol2comp((rro-brw),ang0)-
pol2comp(hm./(2*cos(ang2)),ang0-ang2);
   mrcia = pol2comp(rrm,pi/(2*p))-
pol2comp(crw+hm/2,pi/(2*p)+pi/2);
   mroc = pol2comp(rrem,ang0+ang1o) -
pol2comp(len3,pi/2/p+pi/2-ang4);
   mric = pol2comp(rrem,ang0+ang1o) +
pol2comp(len3,pi/2/p+pi/2-ang4);
   mlcoa = pol2comp((rro-brw),pi/p-ang0)-
pol2comp(hm./(2*cos(ang2)),pi/p-
ang0+ang2);
   mlcia =
pol2comp(rrm,pi/(2*p))+pol2comp(crw+hm/2,
pi/(2*p)+pi/2);
   mloc = pol2comp(rrem,pi/p-ang0-ang1o)
- pol2comp(len3,pi/2/p-pi/2+ang4);
   mlic = pol2comp(rrem,pi/p-ang0-ang1o)
+ pol2comp(len3,pi/2/p-pi/2+ang4);
   pointr = arc(mrcoa,hm/2,ang0-
ang2+pi/2,ang0-ang2-pi/2,-1);
   pointr = [pointr;mroc];
   pointr =
[pointr;arc(mrcia,hm/2,pi/(2*p)+pi*ones(1
,nl),pi/(2*p)*ones(1,nl),-1)];
   pointr = [pointr;mric];
   pointr = [pointr;pointr(1,:)]*1e3;
   pointl = arc(mlcoa,hm/2,pi/p-
ang0+ang2+pi/2,pi/p-ang0+ang2-pi/2,-1);
   pointl = [pointl;mlic];
   pointl =
[pointl;arc(mlcia,hm/2,pi/(2*p)*ones(1,nl
),pi/(2*p)+pi*ones(1,nl),-1)];
   pointl = [pointl;mloc];
   pointl = [pointl;pointl(1,:)]*1e3;
elseif(roundb)
   mrcoa = pol2comp((rro-brw),ang0)-
pol2comp(hm./(2*cos(ang2)),ang0-ang2);
   mroc = pol2comp(rrem,ang0+ang1o) -
pol2comp(len3,pi/2/p+pi/2-ang4);
   mric = pol2comp(rrem,ang0+ang1o) +
pol2comp(len3,pi/2/p+pi/2-ang4);
   mlcoa = pol2comp((rro-brw),pi/p-ang0)-
pol2comp(hm./(2*cos(ang2)),pi/p-
ang0+ang2);
   mloc = pol2comp(rrem,pi/p-ang0-ang1o)
- pol2comp(len3,pi/2/p-pi/2+ang4);
   mlic = pol2comp(rrem,pi/p-ang0-ang1o)
+ pol2comp(len3,pi/2/p-pi/2+ang4);
   pointm = arc(mrcoa,hm/2,ang0-
ang2+pi/2,ang0-ang2-pi/2,-1);
   pointm = [pointm;mroc];
   pointm = [pointm;mloc];
   pointm = [pointm;arc(mlcoa,hm/2,pi/p-
ang0+ang2+pi/2,pi/p-ang0+ang2-pi/2,-1)];
   pointm = [pointm;mlic];
   pointm = [pointm;mric];
   pointm = [pointm;pointm(1,:)]*1e3;
else
   pointm = [pol2comp((rro-brw),ang0) +
pol2comp(len2,ang0+pi/2);
              pol2comp((rro-brw),ang0) -
pol2comp(len2,ang0+pi/2);
              pol2comp(rrem,ang0+ang1o) -
pol2comp(len3,pi/2/p+pi/2-ang4);
              pol2comp(rrem,pi/p-ang0-
ang1o) - pol2comp(len3,pi/2/p-pi/2+ang4);
              pol2comp((rro-brw),pi/p-
ang0) + pol2comp(len2,pi/p-ang0+pi/2);
              pol2comp((rro-brw),pi/p-
ang0) - pol2comp(len2,pi/p-ang0+pi/2);
              pol2comp(rrem,pi/p-ang0-
ang1o) + pol2comp(len3,pi/2/p-pi/2+ang4);
              pol2comp(rrem,ang0+ang1o) +
pol2comp(len3,pi/2/p+pi/2-ang4);
              pol2comp((rro-brw),ang0) +
pol2comp(len2,ang0+pi/2)]*1e3;
end

% Plot and print rotor
if(allorone)
    fill(rro*1e3*cos(linspace(0,2*pi)),rr
o*1e3*sin(linspace(0,2*pi)),'c');
    fill(rri*1e3*cos(linspace(0,2*pi)),rr
i*1e3*sin(linspace(0,2*pi)),'k');
else
    fill([rro*1e3*cos(linspace(0,pi/p)),r
ri*1e3*cos(linspace(pi/p,0))],[rro*1e3*si
n(linspace(0,pi/p)),rri*1e3*sin(linspace(
pi/p,0))],'c');
end

if(allorone)
    temp = 2*p;
else
    temp = 1;
end

if(any(crw))
    for segm=1:temp,

    fill(abs(pointl).*cos(angle(pointl)+(
segm-
1)*pi/p),abs(pointl).*sin(angle(pointl)+(
segm-1)*pi/p),'w');

    fill(abs(pointr).*cos(angle(pointr)+(
segm-
1)*pi/p),abs(pointr).*sin(angle(pointr)+(
segm-1)*pi/p),'w');
    end
else
    for segm=1:temp,

    fill(abs(pointm).*cos(angle(pointm)+(
segm-
```

```
1)*pi/p),abs(pointm).*sin(angle(pointm)+(
segm-1)*pi/p),'w');
   end
end

fprintf('Rotor Outer Radius
%8.5g%8.5g\n',rro*1e3,0);
fprintf('Inner Rotor Radius
%8.5g%8.5g\n',rri*1e3,0);
fprintf('Angle spanned by pole
%8.5g%8.5g\n',0,180/p);

fprintf('\n
');
fprintf('Magnet #%d          ',1:nl);
if(any(crw))
   fprintf('\nMagnet Arc Radii
');
   fprintf('%8.5g%8.5g
',[hm*1e3/2;zeros(1,nl)]);
   fprintf('\nMagnet Right Center Outer
Arc   ');
   fprintf('%8.5g%8.5g
',[abs(mrcoa)*1e3;angle(mrcoa)*180/pi]);
   fprintf('\nMagnet Right Center Inner
Arc
',[abs(mrcia)*1e3;angle(mrcia)*180/pi]);
   fprintf('%8.5g%8.5g
',[abs(mrcia)*1e3;angle(mrcia)*180/pi]);
   fprintf('\nMagnet Right Inside Corner
',[abs(mric)*1e3;angle(mric)*180/pi]);
   fprintf('%8.5g%8.5g
',[abs(mric)*1e3;angle(mric)*180/pi]);
   fprintf('\nMagnet Right Outside Corner
',[abs(mroc)*1e3;angle(mroc)*180/pi]);
   fprintf('%8.5g%8.5g
',[abs(mroc)*1e3;angle(mroc)*180/pi]);
   fprintf('\nMagnet Left Center Outer
Arc
',[abs(mlcoa)*1e3;angle(mlcoa)*180/pi]);
   fprintf('%8.5g%8.5g
',[abs(mlcoa)*1e3;angle(mlcoa)*180/pi]);
   fprintf('\nMagnet Left Center Inner
Arc
',[abs(mlcia)*1e3;angle(mlcia)*180/pi]);
   fprintf('%8.5g%8.5g
',[abs(mlcia)*1e3;angle(mlcia)*180/pi]);
   fprintf('\nMagnet Left Inside Corner
',[abs(mlic)*1e3;angle(mlic)*180/pi]);
   fprintf('%8.5g%8.5g
',[abs(mlic)*1e3;angle(mlic)*180/pi]);
   fprintf('\nMagnet Left Outside Corner
',[abs(mloc)*1e3;angle(mloc)*180/pi]);
   fprintf('%8.5g%8.5g
',[abs(mloc)*1e3;angle(mloc)*180/pi]);
elseif(roundb)
   fprintf('\nMagnet Arc Radii
');
   fprintf('%8.5g%8.5g
',[hm*1e3/2;zeros(1,nl)]);
   fprintf('\nMagnet Right Center Outer
Arc   ');
   fprintf('%8.5g%8.5g
',[abs(mrcoa)*1e3;angle(mrcoa)*180/pi]);
   fprintf('\nMagnet Right Inside Corner
',[abs(mric)*1e3;angle(mric)*180/pi]);
   fprintf('%8.5g%8.5g
',[abs(mric)*1e3;angle(mric)*180/pi]);
   fprintf('\nMagnet Right Outside Corner
',[abs(mroc)*1e3;angle(mroc)*180/pi]);
   fprintf('%8.5g%8.5g
',[abs(mroc)*1e3;angle(mroc)*180/pi]);
   fprintf('\nMagnet Left Center Outer
Arc
',[abs(mlcoa)*1e3;angle(mlcoa)*180/pi]);
   fprintf('%8.5g%8.5g
',[abs(mlcoa)*1e3;angle(mlcoa)*180/pi]);
   fprintf('\nMagnet Left Inside Corner
',[abs(mlic)*1e3;angle(mlic)*180/pi]);
   fprintf('%8.5g%8.5g
',[abs(mlic)*1e3;angle(mlic)*180/pi]);
   fprintf('\nMagnet Left Outside Corner
',[abs(mloc)*1e3;angle(mloc)*180/pi]);
   fprintf('%8.5g%8.5g
',[abs(mloc)*1e3;angle(mloc)*180/pi]);
else
   for pt=1:length(pointm),
      fprintf('\nPoint #%d
',pt);
      for magnet=1:nl
         fprintf('%8.5g%8.5g
',abs(pointm(pt,magnet)),angle(pointm(pt,
magnet))*180/pi);
      end
   end
end
% for magnet=1:nl,
fprintf('\n\n
Right              Middle
Left\n');
%   for pt=1:3,
%   fprintf('\nDirection #%d
',pt);
    fprintf('Angle of Magnetization
');
    fprintf('
%8.3f',mang(:,1)*180/pi);
%   end
% end
fprintf('\n');

plot([(rro-brw) (rro-
brw);rro*ones(1,2*nl)].*1e3.*cos([alpm
(pi-alpm);alpm (pi-alpm)]/p),[(rro-brw)
(rro-
brw);rro*ones(1,2*nl)].*1e3.*sin([alpm
(pi-alpm);alpm (pi-alpm)]/p),'w');
hold off;
clear allorone;
```

```
% Nonlinear Iq and Lq Curves
t0 = clock;

clear global Bg Bry Bst Bsy;
clear global mmfg mmfry mmfst mmfsy;
clear global Bgq1 mmfq1 mmfq Iqx Lqy;
clear Bg Bry Bst Bsy;
clear mmfg mmfry mmfst mmfsy;
clear Bgq1 mmfq1 mmfq Iqx Lqy;
global Iqx Lqy Ib;
global Ag Aag lry Ab1 Ab2 Ab3 Ary Asy r p
db lamt geff muzero lry ds hs alp1 alp2;
global mmfqk lst lsy;

% Peak air-gap flux density on q-axis
% 'RMS-defined' q-axis current
VSIZE = 25;
% Scale for new Ib
% Iqx = linspace(1,500,VSIZE)';
Iqx = linspace(2*Ib/VSIZE,2*Ib,VSIZE)';
alp1 = [0 alphm/2];
alp2 = [alphm/2 pi/2];
% Resultant peak fundamental mmf
excitation
% ABB 2-layer winding definition 3/5/00
% mmfq1 = (3/2)*(4/pi)*(ka*na/p/2)  *
(sqrt(2)*Iqx);
mmfq1 =
(3/2)*(4/pi)*(sum(ka.*(p*nc))/p/2)  *
(sqrt(2)*Iqx);
% Average mmf for each parallel circuit
amplitude across half a pole
mmfq = mmfq1*((cos(alp1)-
cos(alp2))./(alp2-alp1));

X0 = ones(1,nl+1)*0.5/VSIZE;
options(5)=1;
for k=1:VSIZE,
    mmfqk = mmfq(k,:);
    X0 = fsolve('qcircuit4',X0,options);
    Bg(k,1:(nl+1)) = X0;
end

Bgq1 = Bg*(alp2-alp1)';
% Average rotor layer density
Bry = Bg.*(ones(VSIZE,1)*(Ag./Ary));
% Average stator tooth density
Bst = Bg/lamt;
% Average stator yoke density
% Bsy =
[Bg(:,1)+Bg(:,2)+Bg(:,3),Bg(:,2)+Bg(:,3),
Bg(:,3)]*(0.5*pi*r/(p*db));
% Bsy =
[Bg(:,1)*Ag(1)+Bg(:,2)*Ag(2)+Bg(:,3)*Ag(3
)+Bg(:,4)*Ag(4),Bg(:,2)*Ag(2)+Bg(:,3)*Ag(
3)+Bg(:,4)*Ag(4),Bg(:,3)*Ag(3)+Bg(:,4)*Ag
(4),Bg(:,4)*Ag(4)]/Asy;
Bsy =
flipud(cumsum(rot90(Bg.*(ones(VSIZE,1)*Ag
))))'/Asy;
```

```
% Corresponding average mmf components
mmfg = Bg*geff/muzero;
mmfry = [];
mmfst = [];
mmfsy = [];
for k=1:(nl+1)
    mmfry =
[mmfry,m19bh(Bry(:,k))*lry(k)];
    mmfst = [mmfst,m19bh(Bst(:,k))*lst];
    mmfsy =
[mmfsy,m19bh(Bsy(:,k))*lsy(k)];
end

% Q-axis synchronous inductance
% Lqy = (Bgq1./(Iqx*sqrt(2)))  *
(2*l*r*ka*na/p)  ...
%       + Lslot + Lend + La5 + La7 + Lap +
Lam;
% Corrected for separate windings 4/12/00
Lqy = (Bgq1./(Iqx*sqrt(2)))  *
(2*l*r*(sum((p*nc).*ka))/p)  ...
       + Lslot + Lend + La5 + La7 + Lap +
Lam;

etime(clock,t0),
if(Iqx(VSIZE) < Ib)
    Iqx(VSIZE+1) = Ib*1.1;
    Lqy(VSIZE+1) = Lqy(VSIZE);
end
Iqx = [0;Iqx];
Lqy = [Lqy(1);Lqy];

return;

Iin=max(find(Iqx<200));
x=linspace(0,90);
plot(x,mmfq1(Iin)*sin(x*pi/180));
hold on;
plot([alp1(1),alp1(2),alp1(2),alp1(3),alp
1(3),alp2(3)]*180/pi,...

[mmfq(Iin,1),mmfq(Iin,1),mmfq(Iin,2),mmfq
(Iin,2),mmfq(Iin,3),mmfq(Iin,3)]);
hold off;
axis([0 90 0 700])
xlabel('[Electrical Degrees]')
ylabel('[A.turns/m]')
title('Fundamental Component of 3 Segment
MMFs')
gtext(['Iq = ',num2str(Iqx(Iin)),'A'])

function fout = qcircuit4(x)
global Ag Aag lry Ary Asy r p db lamt
geff muzero lry ds hs alp1 alp2;
global mmfqk lst lsy;
global nl;

% Nonlinear q-axis rotor reluctance
network function
```

```
% (1,number of layers) row vector
Bg(1:nl+1)=x(1:nl+1);
% Average rotor layer density
Bry = Bg.*(Ag./Ary);
% Average stator tooth density
Bst = Bg/lamt;
% Average stator yoke density
Bsy = fliplr(cumsum(fliplr(Bg.*Ag')))/Asy;

% Corresponding average mmf components
% Torino material is ast3150bh()
mmfg = Bg*geff/muzero;
if (abs(version)*abs(version)'==92928)
   mmfry = m19bh(Bry)'.*lry;
   mmfst = m19bh(Bst)'*lst;
   mmfsy = m19bh(Bsy)'.*lsy;
else
   mmfry = m19bh(Bry).*lry;
   mmfst = m19bh(Bst)*lst;
   mmfsy = m19bh(Bsy).*lsy;
end


fout = cumsum(mmfsy)+mmfg-
mmfqk+mmfst+mmfry;

return;

% Nonlinear Iq and Lq Curves
%t0 = clock;

clear global Bg Bry Bst Bsy;
clear global mmfg mmfry mmfst mmfsy;
clear global Bgq1 mmfq1 mmfq Iqx Lqy;
clear Bg Bry Bst Bsy;
clear mmfg mmfry mmfst mmfsy;
clear Bgq1 mmfq1 mmfq Iqx Lqy;

global Iqx Lqy;
global Bg Bry Bst Bsy mmfg mmfry mmfst
mmfsy Bgq1 mmfq1 mmfq;
global Ag Ary Asy r p db lamt geff muzero
lry ds hs alp1 alp2;
global mmfqk lst lsy;

VSIZE=45;
% Peak air-gap flux density on q-axis
Bgq1 = linspace(.01,1.3,VSIZE)';
alp1 = [0 alphm/2];
alp2 = [alphm/2 pi/2];
% Average air-gap density for given rotor
layer
Bg = Bgq1*((cos(alp1)-cos(alp2))./(alp2-
alp1));
% Average rotor layer density
Bry = Bg.*(ones(VSIZE,1)*(Ag./Ary'));
% Average stator tooth density
Bst = Bg/lamt;
% Average stator yoke density
% Bsy =
[Bg(:,1)+Bg(:,2)+Bg(:,3),Bg(:,2)+Bg(:,3),
Bg(:,3)]*(0.5*pi*r/(p*db));
% Bsy =
[Bg(:,1)*Ag(1)+Bg(:,2)*Ag(2)+Bg(:,3)*Ag(3
)+Bg(:,4)*Ag(4),Bg(:,2)*Ag(2)+Bg(:,3)*Ag(
3)+Bg(:,4)*Ag(4),Bg(:,3)*Ag(3)+Bg(:,4)*Ag
(4),Bg(:,4)*Ag(4)]/Asy;
Bsy =
flipud(cumsum(rot90(Bg.*(ones(VSIZE,1)*Ag
))))'/Asy;
% Corresponding average mmf components
mmfg = Bg*geff/muzero;
mmfry = [];
mmfst = [];
mmfsy = [];
for k=1:(nl+1)
% Divide length by 2 for half-pole
   mmfry =
[mmfry,m19bh(Bry(:,k))*lry(k)];
   mmfst = [mmfst,m19bh(Bst(:,k))*lst];
   mmfsy =
[mmfsy,m19bh(Bsy(:,k))*lsy(k)];
end
% Average mmf for each parallel circuit
mmfq = mmfst + mmfsy + mmfry + mmfg;
% Resultant peak fundamental mmf
excitation
% Fourier decomposition
% mmfq1 = (4/pi)*mmfq*(sin(alp2)-
sin(alp1))';
% Average decomposition
mmfq1 = mmfq*(alp2-alp1)';
% 'RMS-defined' q-axis current
% ABB 2-layer winding definition 3/5/00
% Iqx = mmfq1 /
((3/2)*(ka*na/p/2)*(4/pi)*sqrt(2));
Iqx = mmfq1 /
((3/2)*(p*sum(ka.*nc)/p/2)*(4/pi)*sqrt(2)
);
% Q-axis synchronous inductance
% Lqy = (Bgq1./(Iqx*sqrt(2))) *
(2*l*r*ka*na/p) ...
%      + Lslot + Lend + La5 + La7 + Lap +
Lam;
Lqy = (Bgq1./(Iqx*sqrt(2))) *
(2*l*r*p*sum(ka.*nc)/p) ...
       + Lslot + Lend + La5 + La7 + Lap +
Lam;

% etime(clock,t0),
if(Iqx(VSIZE) < Ib)
   Iqx(VSIZE+1) = Ib*1.1;
   Lqy(VSIZE+1) = Lqy(VSIZE);
end
Iqx = [0;Iqx];
Lqy = [Lqy(1);Lqy];
return;

Iin=max(find(Iqx<200));
```

```
x=linspace(0,90);
plot(x,mmfq1(Iin)*sin(x*pi/180));
hold on;
plot([alp1(1),alp1(2),alp1(2),alp1(3),alp
1(3),alp2(3)]*180/pi,...

[mmfq(Iin,1),mmfq(Iin,1),mmfq(Iin,2),mmfq
(Iin,2),mmfq(Iin,3),mmfq(Iin,3)]);
hold off;
axis([0 90 0 700])
xlabel('[Electrical Degrees]')
ylabel('[A.turns/m]')
title('Fundamental Component of 3 Segment
MMFs')
gtext(['Iq = ',num2str(Iqx(Iin)),'A'])

% Chapter 5 Figures
while(0)

Va=mvolt;
close
wordfigs2;
plot(Iqx,Lqy,'w')
hold on
plot(Iqx,Lql*ones(size(Lqy)),'w-.')
plot(Iqx,Ld*ones(size(Lqy)),'w')
axis([0 25 0 .05]);
grid on;
xlabel('DQ Current [Amperes]')
ylabel('DQ Inductances [Henries]')
gtext('Ld (linear)')
gtext('Lq (linear "L")')
gtext('Lq (saturable "S")')

pause

% TORQUE-ANGLE PLOT
% Saturable
clf
gamm = linspace(-pi,pi);
Iq = Ia*cos(gamm);
Id = Ia*sin(gamm);
Te = 3*p*(Lambda - (Lqmodel(Iq)'-
Ld).*Id).*Iq;
plot(gamm*180/pi,Te,'w');
xlabel('Control Angle [Elec. Deg.]')
ylabel('Converted Torque [Nm]')
hold on;

% Linear
Te = 3*p*(Lambda - (Lql-Ld).*Id).*Iq;
plot(gamm*180/pi,Te,'w-.');
ylim = ceil(max(Te)/5);
axis([-180 180 -ylim*5 ylim*5]);
set(gca,'YTickMode','manual');
set(gca,'YTick',[5*(-ylim:ylim)]);
set(gca,'XTickMode','manual');
set(gca,'XTick',[-180 -135 -90 -45 0 45
90 135 180]);
grid on;
```

```
gtext('Motoring');
gtext('Generating');
gtext('L');
gtext('S');
pause

% DQ PLANE PLOT
% Saturated optimal torque curve
clf
clear Id Iq;
options = 0;
% options(1)=1;
options(18)=0.1;
for ia=linspace(0.02,1)
    iq = constr(['f = iqte(x);' 'g =
[];'],ia/1.1,options,0,ia);
    Iq = [Iq,iq*Ib];
    Id = [Id,id*Ib];
end
plot(Id,Iq,'w');
hold on;
ylim = ceil(max([Ib abs(Lambda/Ld)])/4);
Id = Id(100),
Iq = Iq(100),
plot(Id,Iq,'wo');
Lq = Lqmodel(Iq);

% Constant power region
voltlimop;
powergrad;
Ps0 = Ps;
Ptol = .01*Ps0;
Ps = 9e9;
om0 = om;
gamm0 = gamm;
dgamm = 0;
while(abs(Ps-Ps0) > Ptol)
    gamm = gamm + 1.1*dgamm;
    Ps = Ps0;
    while(Ps >= Ps0)
    dgamm = 0.5*(90+gamm);
    gamm = gamm-dgamm;
    Iq = Ia*cos(gamm*pi/180);
    Id = Ia*sin(gamm*pi/180);
    Lq = Lqmodel(Iq);
    voltlimop;
    powergrad;
    end
end
cpsr = om/om0,
pfact0s = cos(psi*pi/180),
om0s = om0,
Sr,
om0s*30/pi/p,
gamm0s = gamm0,
gamms = gamm;

% Rated torque hyperbola
te = (1 - id*(xq - xd))*iq;
Te = te*Tb,
```

```
Tmls = Te;
Iq = linspace(0,Ib);
Id = (Lambda-
Te./(3*p*Iq))./(Lqmodel(Iq)'-Ld);
plot(Id,Iq,'w');

% Current limit circle
gamm=linspace(-pi/2,0);
plot(Ia*sin(gamm),Ia*cos(gamm),'w--');

% Unsaturated Optimal Torque Curve
xq = Lql*Ib/Lambda;
ia = linspace(0.01,1);
id = -sqrt(ia.^2./2 + 2 .* (1./4./(xq-
xd)).^2 - sqrt((1./4./(xq-xd)).^2 +
ia.^2./2)./2./(xq - xd));
iq = sqrt(ia.^2./2 - 2 .* (1./4./(xq-
xd)).^2 + sqrt((1./4./(xq-xd)).^2 +
ia.^2./2)./2./(xq - xd));
plot(id*Ib,iq*Ib,'w-.');

% Rated torque hyperbola
Id = id(100)*Ib,
Iq = iq(100)*Ib,
plot(Id,Iq,'wo');
te = (1 - id(100)*(xq - xd))*iq(100);
Te = te*Tb,
Tml = Te;
id = linspace(-1,0);
iq = te./(1 - id*(xq - xd));
plot(id*Ib,iq*Ib,'w-.');
Lq = Lql;
voltlimop;

% Infinite speed point
plot(-Lambda/Ld,0,'wo');
axis([-ylim*4 0 0 ylim*4]);
axis('equal');
axis('square');
set(gca,'XTickMode','manual');
set(gca,'XTick',[-4*(ylim:-1:0)]);
set(gca,'YTickMode','manual');
set(gca,'YTick',[0 4 8 12 16]);
xlabel('Id [Amperes]');
ylabel('Iq [Amperes]');

gtext('L');
gtext('S');
gtext('I');

% Constant power region
powergrad;
Ps0 = Ps;
Ptol = .01*Ps0;
Ps = 9e9;
om0 = om;
gamm0 = gamm;
dgamm = 0;
while(abs(Ps-Ps0) > Ptol)
    gamm = gamm + 1.1*dgamm;
    Ps = Ps0;
    while(Ps >= Ps0)
    dgamm = 0.5*(90+gamm);
    gamm = gamm-dgamm;
    Iq = Ia*cos(gamm*pi/180);
    Id = Ia*sin(gamm*pi/180);
    Lq = Lql;
    voltlimop;
    powergrad;
    end
end
cpsr = om/om0,
pfact0 = cos(psi*pi/180),
Sr,
om0*30/pi/p,
pause;

% TORQUE-SPEED PLOT
% Linear torque curve
clf;
clear Tm2 rpm2;
for gamm = linspace(gamm0,gamm);
    Iq = Ia*cos(gamm*pi/180);
    Id = Ia*sin(gamm*pi/180);
    Lq = Lql;
    voltlimop;
    powergrad;
    Tm2 = [Tm2,Ps/(om/p)];
    rpm2 = [rpm2,rpm];
end
Tel = [Tm2(1),Tm2];
rpml = [0,rpm2];
plot(rpml/1e3,Tel,'w-.');
grid on;
hold on;
Psl = Tel.*rpml*(pi/30);
% Saturable torque curve
clear Tm2 rpm2 Pl2 eff2 Pc2 Ph2 Pa2;
for gamm = linspace(gamm0s,gamms);
    Iq = Ia*cos(gamm*pi/180);
    Id = Ia*sin(gamm*pi/180);
    Lq = Lqmodel(Iq);
    voltlimop;
    powergrad;
    Tm2 = [Tm2,Ps/(om/p)];
    rpm2 = [rpm2,rpm];
    Pl2 = [Pl2,Pl];
    eff2 = [eff2,eff];
    Pc2 = [Pc2,Pc];
    Ph2 = [Ph2,Ph];
    Pa2 = [Pa2,Pa];
end
Tes = [Tm2(1),Tm2];
rpms = [0,rpm2];
plot(rpms/1e3,Tes,'w');
xlabel('Speed [krpm]');
ylabel('Shaft Torque [Nm]');
gtext('L');
gtext('S');
pause;
```

```
% CONSTANT POWER-SPEED PLOT
% Linear
clf;
plot(rpml/1e3,Psl/1e3,'w-.');
grid on;
hold on;
plot(rpml/1e3,Tm1*(om0/p)*ones(size(Psl))
/1e3,'w-.');

% Saturable
Pss = Tes.*rpms*(pi/30);
plot(rpms/1e3,Pss/1e3,'w');
plot(rpms/1e3,Tm1s*(om0s/p)*ones(size(Pss
))/1e3,'w');
xlabel('Speed [krpm]');
ylabel('Shaft Power [kW]');
gtext('L');
gtext('S');

pause;

% LOSS-SPEED PLOT
% Saturable curve only
clf
% Mode II
plot(rpms(2:101)/1e3,Ph2,'w-.');
hold on;
plot(rpms(2:101)/1e3,Pa2,'w--');
plot(rpms(2:101)/1e3,Pc2,'w:');
plot(rpms(2:101)/1e3,Pl2,'w');
ylim=ceil(max(Pl2)/100);
xlim=ceil(rpms(101)/1e4);
axis([0 xlim*10 0 ylim*100]);
grid on;
% Mode I
om=linspace(0,om0s);
Iq = Ia*cos(gamm0s*pi/180);
Id = Ia*sin(gamm0s*pi/180);
Lq = Lqmodel(Iq);
Vq = om*Lambda + om*Ld*Id + Ra*Iq;
Vd = -om*Lq*Iq + Ra*Id;
Va = sqrt(Vq.^2 + Vd.^2);
delt = atan2(Vd,Vq)*180/pi;
psi = gamm0s - delt;
powergrad;
plot(rpm/1e3,Pa*ones(size(Pl)),'w--');
plot(rpm/1e3,Ph,'w-.');
plot(rpm/1e3,Pc,'w:');
plot(rpm/1e3,Pl,'w');
xlabel('Speed [krpm]');
ylabel('Losses [W]');
gtext('Psh')
gtext('Pc')
gtext('Pa')
gtext('Pa + Pc + Psh')
gtext('Saturable Only');

pause;
```

```
% EFFICIENCY-SPEED PLOT
% Saturable curve only
clf
plot(rpms(2:101)/1e3,eff2*100,'w');
% ylim=floor(min(eff2)*100/10);
xlim=ceil(rpms(101)/1e4);
axis([0 xlim*10 80 100]);
grid on;
hold on;
[meff,mind] = max(eff2);
plot([rpms(mind) rpms(mind)]/1e3,[.8
meff]*100,'w--');
plot(rpm/1e3,eff*100,'w');
gtext([num2str(meff*100),'%']);
xlabel('Speed [krpm]');
ylabel('Machine Efficiency [%]');
gtext('Saturable Only');

return;


% Efficiency contour plot
clf;
clear eff Zeff;
N=16;
om=linspace(0,om0s,N);
for te=linspace(Tm2(1)/Tb/N,Tm2(1)/Tb,N)
    clear Id Iq;
    options = 0;
    options(18)=0.1;
    iq = constr(['f = iqid(x);' 'g =
[];'],.9,options,0,1);
    Iq = iq*Ib;
    Id = id*Ib;
    Lq = Lqmodel(Iq);
    Vq = om*Lambda + om*Ld*Id + Ra*Iq;
    Vd = -om*Lq*Iq + Ra*Id;
    Va = sqrt(Vq.^2 + Vd.^2);
    delt = atan2(Vd,Vq)*180/pi;
    gamm = atan2(Id,Iq)*180/pi;
    psi = gamm - delt;
    powergrad;
    Zeff=[Zeff;eff];
end

% Iq = Ia*cos(gamm0s*pi/180);
% Id = Ia*sin(gamm0s*pi/180);
% Y1=linspace(0,Tm2(1),N);
cs=contour(rpm/1e3,linspace(Tm2(1)/Tb/N,T
m2(1),N),Zeff);
clabel(cs);

end

% FEA Inductance Comparison
Va=mvolt;
close;
wordfigs2
plot(Iqx,Lqy,'w')
hold on
```

```
plot(Iqx,Lql*ones(size(Lqy)),'w-.')
plot(Iqx,Ld*ones(size(Lqy)),'w')
IaFEA = [0
4
8
12
16];
LqFEA = [0.036062256
0.036062256
0.026104555
0.019474392
0.015564684];
LdFEA = [0.008237087
0.008237087
0.007584192
0.007204596
0.006930425];
plot(IaFEA,[LdFEA,LqFEA],'w--')
xlabel('DQ Current [Amperes]')
ylabel('DQ Inductances [Henries]')
% gtext('Ld (linear)')
% gtext('Lq (linear)')
% gtext('Lq (saturable)')
ylim=ceil(max(LqFEA)/.05);
xlim=floor(max(IaFEA)/5);
axis([0 xlim*5 0 ylim*.05]);
LEGEND=legend('w','Saturable LPM','w-
.','Linear LPM','--
','FEA','FontSize',10);
set(LEGEND,'Position',get(LEGEND,'Positio
n')*1.1);
set(LEGEND,'FontSize',10);
pause;


% TORQUE-ANGLE PLOT
% Saturable
clf
gamm = linspace(-pi/2,0);
Iq = Ia*cos(gamm);
Id = Ia*sin(gamm);
Te = 3*p*(Lambda - (Lqmodel(Iq)'-
Ld).*Id).*Iq;
plot(gamm*180/pi,Te,'w');
grid on;
xlabel('Control Angle [Elec. Deg.]')
ylabel('Converted Torque [Nm]')
ylim = ceil(max(Te)/5);
axis([-90 0 0 ylim*5]);
set(gca,'YTickMode','manual');
set(gca,'YTick',[5*(0:ylim)]);
set(gca,'XTickMode','manual');
set(gca,'XTick',[-90 -75 -60 -45 -30 -15
0]);
hold on;

Lambdat=Lambda;
Iqxt = Iqx;
Lqyt = Lqy;
global Idx Ldy;
Lambda = 0.1035;
Iqx = IaFEA;
Idx = Iqx;
Lqy = LqFEA;
Ldy = LdFEA;
Te = 3*p*(Lambda - (Lqmodel(Iq)'-
Ldmodel(abs(Id))').*Id).*Iq;
plot(gamm*180/pi,Te,'w-.');

Te=[0.1467028
5.26105
9.42049
12.46221
13.54416
13.58484
12.45662
11.3228
8.7729
7.34106];
gamm=[-90
-80
-70
-60
-50
-40
-30
-20
-10
0];
errorbar(gamm,Te,[0;0;0;0;Te(5)-
13.02249;0;0;0;0;0],[0;0;0;0;14.02709-
Te(5);0;0;0;0;0],'w--');
LEGEND=legend('w','Saturable LPM','w-
.','FEA Lumped Parameters','w--','FEA
Force','FontSize',10);
set(LEGEND,'Position',get(LEGEND,'Positio
n')*1.1);

pause;

clf;
Lqy = Lqyt;
Lambda = Lambdat;
Iqx = Iqxt;
plot(Iqx,Lqy,'w')
hold on
% plot(Iqx,Lql*ones(size(Lqy)),'w-.')
% plot(Iqx,Ld*ones(size(Lqy)),'w')
IaFEA = [0
4
8
12
16];
LqFEA = [0.03864995
0.03864995
0.02901001
0.021173519
0.016674038];
LdFEA = [0.016913299
0.016913299
```

```
0.012141383
0.010237366
0.009144461];
plot(IaFEA,LqFEA,'w--')
xlabel('DQ Current [Amperes]')
ylabel('DQ Inductances [Henries]')
% gtext('Ld (linear)')
% gtext('Lq (linear)')
% gtext('Lq (saturable)')
axis([0 14 0 0.05]);
LEGEND=legend('w','Saturable LPM','--
','FEA','FontSize',10);
set(LEGEND,'Position',get(LEGEND,'Positio
n')*1.1);
grid on;

% D-Axis Circuit Solutions
% Half Pole


% Inductance ratios
% Model bridge reluctance in parallel
with magnet cavities
rmp = par(rm,rb);
darmb = [zeros(1,nl+1);[diag(-1./rmp)
zeros(nl,1)]]+...
       [diag(1./rmp+1./rg+[0
1./rmp([1:nl-1])])
zeros(nl,1);zeros(1,nl+1)]+...
       [zeros(nl+1,1),[diag(-
1./rmp([1:nl]));zeros(1,nl)]];
darmb = darmb([1:nl],[1:nl]);
pur = (inv(darmb)*[puf./rg]')';
ratdcqm = 1 - (4/pi) *
sum(dalpm.*puf.^2);
ratdtqm = (4/pi) * sum(puf.*(puf-
pur).*dalpm);

pmfd = .000;
pmff = mean((hm-pmfd)./hm);
% Fundamental magnet field
% Assume bridges are a source so only
consider reluctance of magnet cavities
darm = [zeros(1,nl+1);[diag(-
1./(rm*pmff)) zeros(nl,1)]]+...

[diag(1./(rm*pmff)+1./(rg*(g+pmfd)/g)+[0
1./(pmff*rm([1:nl-1]))])
zeros(nl,1);zeros(1,nl+1)]+...
       [zeros(nl+1,1),[diag(-
1./(pmff*rm([1:nl])));zeros(1,nl)]];
darm = darm([1:nl],[1:nl]);

BA = (Br*0.5*Am - Bs*Ab);
Bg =
(1./(Rg*(g+pmfd)/g)).*(inv(((As*muzero)/g
eff)*darm)*((BA - [0,BA(1:nl-
1)])./Agd)')';
B1 = (4/pi) * sum(Bg.*(sin(pi/2-alpm) -
sin([0 pi/2-alpm(1:(nl-1))])));
```

```
function ia = iqid(iq)

global ia Ib Lambda xd xq id te;

xq = Lqmodel(iq*Ib)*Ib/Lambda;
id = (1 - te/iq)/(xq - xd);
%if (id < -1/xd),
%   ia = 9e9;
%   fprintf('id = %g  1/xd = %g\n',id, -
1/xd);
%else,
    ia = sqrt(id^2 + iq^2);
%end
return;

if (xq<=xd)
    ia = 9e9;
else,
    id = (1 - te/iq)/(xq - xd);
    ia = sqrt(id^2 + iq^2);
end

fprintf('iq = %g  xq = %g id = %g ia =
%g\n',iq,xq,id,ia);

function fout = iqte(iq)
% Finds torque for a given iq for a given
ia
% Output is -te to be minimized to find
maximum torque-per-amp

global ia Ib Lambda xd xq id te;

% ia = 1;
xq = Lqmodel(iq*Ib)*Ib/Lambda;
id = -sqrt(ia^2 - iq^2);
te = (1 - id*(xq - xd))*iq;
fout = -te;
return;

fprintf('iq = %g  xq = %g id = %g ia =
%g\n',iq,xq,id,ia);

function Ld = Ldmodel(Id)
% Nonlinear Id and Ld Curves

global Idx Ldy;
% Changed from spline to linear
interpolation because
% poorly space Idx data from the
qaxmodel3 was producing
% wildly inaccurate results
Ld = interp1(Idx,Ldy,abs(Id),'linear');

return;

function Lq = Lqmodel(Iq)
% Nonlinear Blmq, Iq, and Lq Curves
```

```
global Iqx Lqy;
% Changed from spline to linear
interpolation because
% poorly space Iqx data from the
qaxmodel3 was producing
% wildly inaccurate results
% Lq = interp1(Iqx,Lqy,abs(Iq),'linear');
Lq = interp1(Iqx,Lqy,abs(Iq),'spline');

return;

% M19 Steel B-H Curve
function hout = m19bh(bin)

muzero = pi*4e-7;
mur = 500000;
H_FIELD =
[0,23.08,31.04,38.2,46.96,54.128,61.29,70
.05,79.6,95.5,115.4,125,135.3,...

151.2,159.2,191.0,278.6,477.6,796,1114.4,
1631.8,3820.8,10746,18308,79600];
B_FIELD =
[0,.08,.16,.28,.4,.5,.6,.7,.8,.9,1,1.04,1
.08,1.12,1.14,1.2,1.3,1.4,1.46,...
          1.5,1.55,1.65,1.8,1.9,2.08];
hout =
interp1(B_FIELD,H_FIELD,bin,'spline');
% hout = (bin/(muzero*mur))';

return;

fprintf('[A.turns/m]       [Tesla]\n');
for k=1:length(H_FIELD)
    fprintf('%11g\t%11g\n',H_FIELD(k),B_F
IELD(k));
end

% Voltage limited conditions

Idreal=1;
Iq = 0;
Psmax = 0;
om = rpm*p*pi/30;
while(Idreal & (Iq<Ib))
   Iq = Iq + Ib/100;
   Lq=Lqmodel(Iq);
    C(1)=Ra^2 + (om*Ld)^2;
   C(2)=2*(om*Lambda+Ra*Iq)*om*Ld-
2*Ra*om*Lq*Iq;
   C(3)=(-
om*Lq*Iq)^2+(om*Lambda+Ra*Iq)^2-Va^2;
   Idr = min(roots(C));
   Idreal = isreal(Idr);
   if (Idreal)
      Id = Idr;
      Iqold = Iq;
      Ia = sqrt(Iq^2+Id^2);
    powergrad;
    if(Ps>Psmax)
       Psmax = Ps;
      end
   end
end
Iq=Iqold;
Lq=Lqmodel(Iq);
powergrad;
Vq = om*Lambda + om*Ld*Id + Ra*Iq;
Vd = -om*Lq*Iq + Ra*Id;
Va = sqrt(Vq^2 + Vd^2);
% Beware valid range is -pi to pi
delt = atan2(Vd,Vq)*180/pi;
gamm = atan2(Id,Iq)*180/pi;
psi = gamm - delt;
pfact = cos(psi*pi/180);
Sr = Lq/Ld;
rpm = (30/pi)*om/p;

% optfunc.m
% Cost optimization function for SRPM.M

function fout = optfunc(x)
srpmgvars;
global lowfout,SRPMGVAR;
raths = x(1);
lams = x(2);
lamus = x(3);
ratm = x(4);
lamh = x(5);
% ratm1 = x(6);
ratm2 = x(6);
l = x(7);
db = x(8);
Br = x(9);
lamrd = x(10);
lammd1 = x(11);
lammd2 = x(12);
srpmmap;
fout = tcsyst;
if (fout < lowfout)
    lowfout = fout
    eval(['save tempopt',SRPMGVAR]);
end;
return;

% Calculates losses and shaft
torque/power at given conditions
% Inputs: Va, Ia, om, Ll, psi
% Outputs: Pin, Ps, Pl, eff

% RMS Air-gap Flux Density
% Added effects of R and Ll 2/21/00
Bagv = (Va-
Ia*(Ra+om*Ll))*p/(om*2*rro*l*na*ka);
% Change loss definitions from RMS to
Average 2/21/00
% Average Air-gap Flux Density
Bagva = 2*sqrt(2)*Bagv/pi;
% Tooth Flux Density (Average)
Bt = Bagva/lamt;
```

```
% Back Iron Flux Density (Average)
Bb = Bagva*pi*rro/(2*p*db);
% Rotor Flux Density (Average)
Brc = Bagva*pi*rro/(2*p*(rro-rri-
sum(hm)));

% Core Iron Loss
Pcb =
mcore*pb*abs(Bb/bb).^epb*abs(om/omb).^epf
;
% Teeth Loss
Pct =
mtooth*pb*abs(Bt/bb).^epb*abs(om/omb).^ep
f;
% Total Loss
Pc = Pcb+Pct;

% Harmonic Loss
sigc = 1.46e6;
theta0 = us*ns/r;
Bh = Bagv*(2/pi)*sin(theta0/2);
omh = om*ns/p;
Ez = rro.*omh.*Bh/p;
B0 = 0.75*Bs;
deltc =
(3.79*B0./(sigc^2.*omh.*Ez)).^.3333;
Ph = 1.75.*rro.*l.*sigc.*deltc.*Ez.^2;

Pa = 3*Ra*Ia^2;

Te = 3*p*(Lambda - (Lq - Ld)*Id)*Iq;
rpm = (30/pi)*(om/p);
Ps = Te*om/p - Pc;
Pl = Pc+Ph+Pa;
Pin = 3.*Va.*Ia.*cos(psi.*pi/180);

eff = Ps./Pin;

% srpmcoils.m
% Given an rms current density, # poles,
and slot distribution
% calculates the current in each coil for
a two layer winding

Jb = Ja*cos(-2*pi/3);
Jc = Ja*cos(-4*pi/3);
Jorder = [Ja,-Jc,Jb,-Ja,Jc,-
Jb]*sqrt(2)/1e6;

fprintf('Current Densities [A/mm^2]:\n');
fprintf('Slot #  Bottom   Top\n');
for slotn=0:ns-1,
    coilb = round((rem(slotn,3*p)+1)/ma);
    coilt =
round((rem(slotn+nst,3*p)+1)/ma);
    Jbottom = Jorder(coilb);
    Jtop = Jorder(coilt);
    fprintf('%4d  %7.4g
%7.4g\n',slotn+1,Jbottom,Jtop);
end
```

```
% srpmcost

% Costs
ucsteel = 1.0;
uctape = 5.0;
uccopp = 5.0;
tcsteel = miron*ucsteel;
tccopp = massa*uccopp;
tcmagnet = mmagnet*ucmagnet;
tcmach = 2 * (tcsteel+tccopp) + tcmagnet
+ mmagnet*ucsteel;
tcconv = 402 + .4823*Imax/sqrt(2) +
21.18;
tcsyst = tcmach + tcconv;

% srpmpower.m
% I can't for the life of me remember
exactly what this calculates
% Perhaps the lowest current required for
a given speed and power

clf reset;
om = input('Input max speed [rpm]:
')*2*pi*p/60;
Pmax = input('Input power at max speed:
');
omegam = om/p;
Xd = Ld*om;
Xq = Lq*om;
Xqd = Xq-Xd;
Ea = Lambda*om;

a = -(Xd*Xqd)^2;
b = 2*Ea*Xd*Xqd*(Xd-Xqd);
c = Xqd^2*(volt^2-Ea^2)+4*Xqd*Ea^2*Xd-
(Xd*Ea)^2;
d = -2*Ea*(Xqd*(volt^2-Ea^2)+Xd*Ea^2);
e = Ea^2*(volt^2-Ea^2)-
(Xq*Pmax/omegam)^2;

id = roots([a,b,c,d,e]);

% srpmspecs.m
% Design specification output for srpm
machine

fprintf('STATOR SPECS:\n');
fprintf('Slots/pole/phase =  %12g  Pole
Pairs =        %12g\n', ma, p);
fprintf('Phases =            %12g  Slots
=        %12g\n', 3, ns);
fprintf('Series Turns =      %12g  #
Slots Shorted =   %12g\n', na, nst);
fprintf('Tooth Width =       %12g
Opening Width =      %12g\n', wt, us);
fprintf('Slot Bottom Width = %12g  Slot
Top Width =      %12g\n', wsb, wst)
fprintf('Opening Height =    %12g  Slot
Depression =    %12g\n', os, ds);
```

```
fprintf('Slot Height =        %12g  Back
Iron Depth =   %12g\n', hs, db);
fprintf('\nROTOR SPECS:\n');
fprintf('Rotor Outer Rad. =  %12g  Air
Gap =           %12g\n', r-g, g);
fprintf('Magnet Fraction =   %12g  Inner
Radius =      %12g\n', ratm, rri);
fprintf('Bridge Width =      %12g  Post
Width =        %12g\n', [brw; crw]);
fprintf('Magnet Depth =      %12g  Mag
Span [deg] =   %12g\n', [hm;
alphm*180/pi/p]);
fprintf('\nINDUCTANCES [Henries]:\n');
fprintf('d-Axis =            %12g  q-Axis
=           %12g\n',Ld,Lq);
fprintf('d-Magnetizing =     %12g  q-
Magnetizing =    %12g\n',Ladm,Laqm);
fprintf('d-Thru Over q-Mag = %12g  d-Thru
=           %12g\n',ratdtqm,Ladt);
fprintf('d-Circ Over q-Mag = %12g  d-
Circ. =          %12g\n',ratdcqm,Ladc);
fprintf('End Turn Leakage =  %12g  Slot
Leakage =      %12g\n',Lend,Lslot);
fprintf('5th Belt Leakage =  %12g  7th
Belt Leakage =  %12g\n',La5,La7);
fprintf('Forward Zig-Zag =   %12g
Backward Zig-Zag =  %12g\n',Lap,Lam);
fprintf('\nFIELD SPECS:\n');
fprintf('Magnet Remanence =  %12g  Fund
Field =          %12g\n',Br, B1);
fprintf('Max Core Density =  %12g  PM
Flux Linkage =   %12g\n',max([Bt Bb
Brc]), Lambda);
fprintf('\nMACHINE SPECS:\n');
fprintf('Diameter =          %12g  Total
Length =       %12g\n',dout,lout);
fprintf('Active Length =     %12g  Iron
Mass =         %12g\n',l,miron);
fprintf('Saliency Ratio =    %12g  Active
Rotor Vol. = %12g\n',Sr,pi*rro^2*l);
fprintf('Copper Mass =       %12g  Magnet
Mass =        %12g\n',massa,mmagnet);
fprintf('Total Mass =        %12g
Reflected Moment =
%12g\n',miron+massa+mmagnet,Jm*(dratio^2)
);
fprintf('Max RMS Sw. Curr. = %12g
Converter Cost =
%12g\n',Imax/sqrt(2),tcconv);
fprintf('Machine Cost =      %12g  Total
Cost =        %12g\n',tcmach,tcsyst);

% Solves for the corner speed where the
voltage Va intersects the given point
(Id,Iq)
% Inputs: Va, Id, Iq, Lq, Ld, and Lambda
% Outputs: om, Vd, Vq, psi, gamm, delt,
pfact, Sr, rpm

% Corner speed
C(1) = (Lambda+Ld*Id)^2+(Lq*Iq)^2;
C(2) = 2*((Lambda+Ld*Id)*(Ra*Iq)-
Lq*Iq*Ra*Id);
C(3) = (Ra*Iq)^2+(Ra*Id)^2-Va^2;
omr = roots(C);
if isreal(omr)
    if(abs(omr)==omr)
    om = min(omr);
    else
    om = max(omr);
    end
else
    printf('Calculated speed is
imaginary\n')
    break;
end
Vq = om*Lambda + om*Ld*Id + Ra*Iq;
Vd = -om*Lq*Iq + Ra*Id;
Va = sqrt(Vq^2 + Vd^2);
% Beware valid range is -pi to pi
delt = atan2(Vd,Vq)*180/pi;
gamm = atan2(Id,Iq)*180/pi;
psi = gamm - delt;
pfact = cos(psi*pi/180);
Sr = Lq/Ld;
rpm = (30/pi)*om/p;

% Checks the trigonometric addition of
vectors
Idc = Id*sin(delt) - i*Id*cos(delt);
Iqc = Iq*cos(delt) + i*Iq*sin(delt);
Iac = Ia*cos(-psi) + i*Ia*sin(-psi);
Eac = Va - Iac*Ra - (i*Xd*Idc) -
(i*Xq*Iqc);
% fprintf('Check Trigonomtry of Salient
Machine\n');
% fprintf('Ea = %g\t Check =
%g\n',Ea,abs(Eac));
% fprintf('delt = %g\t Check =
%g\n',delt*180/pi,angle(Eac)*180/pi);
vectorplot([Eac,Iac*Ra,i*Xd*Idc,i*Xq*Iqc]
)

function vectorplot(vectors)

hold on;
vectorsum=0+0i;
N = length(vectors);
xmin = 0;
xmax = 0;
ymin = 0;
ymax = 0;
for n=1:N;
    vectorsum = vectorsum + vectors(n);
    xmin = min(real(vectorsum),xmin);
    xmax = max(real(vectorsum),xmax);
    ymin = min(imag(vectorsum),ymin);
    ymax = max(imag(vectorsum),ymax);
end
```

```
xysize =
max([abs(xmin),abs(xmax),abs(ymin),abs(ym
ax)]);
axis([-xysize,xysize,-xysize,xysize]);
axis('image');
vectorsum=0+0i;
for n=1:N;
    oldsum = vectorsum;
    vectorsum = vectorsum + vectors(n);
    arrowfill(oldsum,vectorsum);
%
    plot([real(oldsum),real(vectorsum)],[
imag(oldsum),imag(vectorsum)],'wo');
%
    plot([real(oldsum),real(vectorsum)],[
imag(oldsum),imag(vectorsum)],'w-');
end
arrowfill(0,vectorsum,0);
hold off;


% abc2qd0.m Instantaneous Park
transformation
% Takes 3-phase vector 'abc' and
transforms it into 'qd0' vector

function qd0 = abc2qd0(abc,the)

qd0 = (2/3)*[cos(the) cos(the - 2*pi/3)
cos(the + 2*pi/3); ...
             sin(the) sin(the - 2*pi/3)
sin(the + 2*pi/3); ...
             0.5 0.5 0.5]*abc;

return;

% arc(X,Y,R,S,F)
% Create an arc
% XC,YC are the cartesian coordinates of
the center
% R is the radius
% S is the start angle in radians
% F is the finish angle
% Zero is at 3 oclock
% D=1 for counterclockwise, and D=-1 for
clockwise
% The function returns a column vector of
complex cartesian coordinates
% spaced a maximum of 1 degree apart
function C=arc(CTR,R,S,F,D)

if(any(abs(F-S)<pi/180))
   fprintf('Span must be at least 1
degree');
   return
end
% X = [real(CTR)+R*cos(S)];
% Y = [imag(CTR)+R*sin(S)];
X = [];
Y = [];
```

```
if(all((F-S>0) & (D==-1)))
   S=S+2*pi;
elseif(all((S-F>0) & (D==1)))
   F=F+2*pi;
end
% for angle=S+D*pi/180:D*pi/180:F,
for k=1:length(S),
%
angle(:,k)=linspace(S(k),F(k),round(abs(F
(k)-S(k))/(pi/180)))';
   angle(:,k)=linspace(S(k),F(k))';
end
X =
ones(100,1)*real(CTR)+(ones(100,1)*R).*co
s(angle);
Y =
ones(100,1)*imag(CTR)+(ones(100,1)*R).*si
n(angle);

% if (angle~=F),
%   X = [X,real(CTR)+R*cos(F)];
%   Y = [Y,imag(CTR)+R*sin(F)];
% end

C = X + Y*i;
return

function arrow(start,stop,scale)

% ARROW(start,stop,scale)  draw a line
with an arrow pointing from
%                          start to stop
% Draw a line with an  arrow at the end
of a line
% start is the x,y point where the line
starts
% stop is the x,y point where the line
stops
% Scale is an optional argument that
will scale the size of the arrows
% It is assumed that the axis limits are
already set

%       8/4/93    Jeffery Faneuff
%       Copyright (c) 1988-93 by the
MathWorks, Inc.

if nargin==2
  xl = get(gca,'xlim');
  yl = get(gca,'ylim');
  xd = xl(2)-xl(1);         % this sets
the scale for the arrow size
  yd = yl(2)-yl(1);         % thus
enabling the arrow to appear in correct
  scale = (xd + yd) / 2;    % proportion
to the current axis
end

hold on
axis(axis)
```

```
xdif = stop(1) - start(1);
ydif = stop(2) - start(2);

theta = atan(ydif/xdif);  % the angle has
to point according to the slope

if(xdif>=0)
  scale = -scale;
end

xx = [start(1),
stop(1),(stop(1)+0.02*scale*cos(theta+pi/
8)),(stop(1)+0.02*scale*cos(theta-
pi/8)),stop(1)]';
yy = [start(2), stop(2),
(stop(2)+0.02*scale*sin(theta+pi/8)),(sto
p(2)+0.02*scale*sin(theta-
pi/8)),stop(2)]';

plot(xx,yy,'w')

hold off

function arrowfill(start,stop,scale)

%  ARROW(start,stop,scale)  draw a line
with an arrow pointing from
%                          start to stop
%  Draw a line with an  arrow at the end
of a line
%  start is the x,y point where the line
starts
%  stop is the x,y point where the line
stops
%  Scale is an optional argument that
will scale the size of the arrows
%  It is assumed that the axis limits are
already set

%       8/4/93    Jeffery Faneuff
%       Copyright (c) 1988-93 by the
MathWorks, Inc.

if nargin==2
  xl = get(gca,'xlim');
  yl = get(gca,'ylim');
  xd = xl(2)-xl(1);        % this sets
the scale for the arrow size
  yd = yl(2)-yl(1);        % thus
enabling the arrow to appear in correct
  scale = (xd + yd) / 2;   % proportion
to the current axis
end

hold on

if(length(start)==1)
    start = [real(start),imag(start)];
end
```

```
if(length(stop)==1)
    stop = [real(stop),imag(stop)];
end

xdif = stop(1) - start(1);
ydif = stop(2) - start(2);

theta = atan(ydif/xdif);  % the angle has
to point according to the slope

if(xdif>=0)
  scale = -scale;
end

xx = [start(1), stop(1)]';
yy = [start(2), stop(2)]';

plot(xx,yy,'w')

for fill=1:10,
    xx =
[stop(1),(stop(1)+0.02*scale*cos(theta+pi
/(8*fill))),(stop(1)+0.02*scale*cos(theta
-pi/(8*fill))),stop(1)]';
    yy =
[stop(2),(stop(2)+0.02*scale*sin(theta+pi
/(8*fill))),(stop(2)+0.02*scale*sin(theta
-pi/(8*fill))),stop(2)]';

    plot(xx,yy,'w')
end

hold off

function beep(kHz)

x=linspace(0,kHz*1000*2*pi,8192);
y=sin(x);
sound(y,8192);

return;

function [r,th] = comp2pol(c)
% [r,th] = COMP2POL(c)
% COMP2POL transforms a complex number
into the polar coordinates [r,th]
%   See also CART2SPH, SPH2CART,
POL2CART.

x = real(c);
y = imag(c);
th = atan2(y,x);
r = sqrt(x.^2+y.^2);

function yesno = ismono(xdata)

yesno = 1;
k = 1;
while(xdata(k+1) == xdata(k))
    k = k+1;
```

```
end
if (xdata(k+1) > xdata(k))
    for k = k:(length(xdata)-1)
    if (xdata(k+1) < xdata(k))
        yesno = 0;
     end
    end
elseif (xdata(2) < xdata(1))
    for k = k:(length(xdata)-1)
    if (xdata(k+1) > xdata(k))
        yesno = 0;
     end
    end
end

function A = locangle(a,b,c)

% Find side a using the law of cosines
% A = acos((b^2 + c^2 - a^2)/(2*b*c))

A = acos((b.^2 + c.^2 - a.^2)./(2*b.*c));

return;

function a = locside(A,b,c)

% Find side a using the law of cosines
% a = sqrt(b.^2 + c.^2 - 2*b.*c.*cos(A))

a = sqrt(b.^2 + c.^2 - 2*b.*c.*cos(A));

return;

function B = losangle(a,A,b)

% Law of Sines - find angle
%
% B = asin((b./a).*sinA)

B = asin((b./a).*sin(A));

return;

function b = losside(a,A,B)

% Law of Sines - find side
%
% b = a.*sin(B)./sin(A)

b = a.*sin(B)./sin(A);

return;

function c = pol2comp(r,th);
% c = POL2COMP(r,th)
% POL2COMP transforms the polar form to a
cartesian complex number
%   See also CART2SPH, CART2POL,
SPH2CART.
```

```
x = r.*cos(th);
y = r.*sin(th);
c = x+y*i;

function Z = par(a, b)
Z = a .* b ./ (a + b);

% qd02abc.m Instantaneous inverse Park
transformation
% Takes 'qd0' vector and transforms it
into the 3-phase 'abc' vector

function abc = qd02abc(qd0,the)

abc = [cos(the) sin(the) 1; ...
       cos(the - 2*pi/3) sin(the -
2*pi/3) 1; ...
       cos(the + 2*pi/3) sin(the +
2*pi/3) 1]*qd0;

return;

function y = randi(min,max)
y = round((1+max-min)*rand + min-.5);

function y = randr(min,max)
y = (max-min)*rand + min;
```

Chapter 10 Appendix B

MATLAB ISG OPTIMIZATION SOFTWARE

This appendix contains the MATLAB scripts and functions that are particular to the optimization of the ISG including both Monte Carlo and local gradient optimization scripts.

```
%
*****************************************
*************************
% *
*
% *                             SRPM.M
*
% * Synchronous Reluctance PM Machine,
Stator in Slots            *
% * Internal (Flux Concentrating) Magnets
*
% * Copyright 1995, James L. Kirtley Jr.
*
% * Modified 1997, Edward C. Lovelace
*
% * Modified 1999, for new partition of
rounded, posted cavities    *
% * Modified 1999, for saturated
generation                         *
% *
*
%
*****************************************
*************************
% srpm.m: main design program
% see 6.11s copyright statement for rules
of use
% Requires the following input variables:
% Rotational Speed
% Required Power
% Required power factor angle psi
% Outer diameter              dout
% Air-gap
% Magnet Depth Fraction       ratm
% Magnet Relative Depths      lamh
% Rotor Depth Fraction        lamrd
% Small Magnet Span Ratio     ratm1
% Large Magnet Span Ratio     ratm2
% Magnetizing Saliency Ratio  ratdtqm
% Circulating Saliency Ratio  ratdcqm
% Active length               l
% Pole pairs                    p
% Slots per pole per phase      ma
% Slots short pitched           nst
% Peripheral slot fraction      lams
% Slot height ratio             raths
% Slot depression depth         ds
% Slot opening fraction         lamus
% Back Iron depth               db
% Total armature turns          nat
% Armature parallel paths       nac
% Slot Fill Fraction            lama
% Magnet Remnant Flux Density Br
% Stator Conductivity           siga
% Iron Model Base Dissipation pb
% Base Frequency                omb
% Base Flux Density             bb
% Flux Exponent                 epb
% Frequency Exponent            epf
% Steel Density                 rhofe
% Magnet Density                rhom
% Conductor Density             rhos
% Air temperature rise          dtt
% Assumed fan efficiency        eft
%
% Power loop does not account for core or
winding losses.
% Core and winding losses are accounted
for, though, in efficiency.
% Can calculate motor or generator
conditions based on power factor input.
% Prat input should shaft output
(motoring), or electrical input
(generating).
% New input set

global ia Ib Lambda xd xq id te mflag;
clear angle;

% Here are a few constants
muzero=pi*4e-7;     % free-space
permeability
```

```
tol=1e-6;              % error tolerance in
power loop
cpair = 1005.7;        % mass heat capacity
of air
rhoair = 1.1774;       % density of air
nuair = 1.56e-5;       % kinematic viscosity
of air
psistep = pi/10;
nac = 10;              % parallel paths
os = .0005;            % slot opening
depression
% Defaults for mechanical losses
dtt = 100;
etf = 1;

% Stator Geometry
% Number of stator slots
ns = 6*ma*p;
% Slot opening
% Minimum opening is 2x20gage diameter
usl = .032*25.4*.001;
% Stator radius from outside diameter
% r = (dout/2 - ds*(1+raths*lams*2*pi/ns)
- db)/(1+raths*lams*2*pi/ns);
r = (dout/2 - db)/(1+raths*lams*2*pi/ns +
(1+raths*lams*2*pi/ns)*pi*(lams-
lamus)/ns);
us = lamus*2*pi*r/ns;
if (us < usl),
    us = usl;
    r = (dout/2
+0.5*us*(1+raths*lams*2*pi/ns) -
db)/(1+raths*lams*2*pi/ns +
(1+raths*lams*2*pi/ns)*pi*lams/ns);
end

% Coil depression
ds = pi*r*lams/ns - us/2;
% Number of total armature turns
nat = na*nac;
% Turns per coil
nc = na/(2*ma*p);
nct = nat/(2*ma*p);
% Tooth fraction
lamt = 1 - lams;
% Slot height
hs = raths*lams*2*pi*(r+ds)/ns;
% tooth width
wt = 2*pi*(r+ds)*lamt/ns;
% slot top width
wst = 2*pi*(r+ds)*lams/ns;
% slot bottom width
% Old Formula
% wsb = wst*(r+ds+hs)/(r+ds);
% Corrected Formula
wsb = 2*pi*(r+ds+hs)/ns - wt;
% average
wsa = 0.5*(wsb+wst);
% Stator Core Inside Radius
rci = r+ds+hs;
% Stator Core Outside Radius
rco = rci + db;
% full-pitched coil throw
nsfp = ns/(2*p);
% actual coil throw
nsct = nsfp - nst;
% estimate of end cone length
% coil angle
thetae = acos(lams);
% azimuthal travel (half end)
laz = pi*(r+ds+.5*hs)*nsct/ns;
% end length (axial)
le1 = laz/tan(thetae);
% Overall machine length
lout = l+2*le1;
% end length (half coil)
le2 = laz/sin(thetae);
% Armature Conductor Length
Lac = 2*na*(l+2*le2);
% Armature Conductor Area
Aac = hs*wsa*lama/(2*nc);
% Armature Resistance
Ra = Lac/(siga*Aac);

% Rotor Geometry
% Average air gap radius
rag = r - g/2;
% Rotor Outer Radius
rro = r - g;
% Rotor Inner Radius
rri = lamrd*rro;
% Rotor Magnet Dimensions
hm = ratm*(rro-rri);
hm1 = lamh*hm;
hm2 = (1-lamh)*hm;
% Radius at the half magnet height on the
line of symmetry
rrm1 = rri + hm2 + 0.5*hm1 +
(lammd1+lammd2)*(1-ratm)*(rro-rri);
rrm2 = rri + 0.5*hm2 + lammd2*(1-
ratm)*(rro-rri);

% Rotor Vertices for Drawing

% Start with wider magnet
% Magnet pole span [elect. rad]
```

```
alphm2 = ratm2*pi;
% Angular distance from Q-Axis to End of
Magnet [elect. rad]
alpm2 = (1-ratm2)*pi/2;
% Angular delta from zero ref to
beginning of the magnet
ang02 = alpm2/p;
% 1/4th of the angular span of the magnet
% Angles defined to intersections of
magnet midline with radii rro-brw and
rrem
ang12 = alphm2/(4*p);
% Radius to end of middle magnet
rrem2 = rrm2/cos(ang12);
% Length of the side magnet piece
len12 = locside(ang12,(rro-brw),rrem2);
% Angle included between the outer radius
of the magnet and the side magnet length
ang22 = locangle(rrem2,(rro-brw),len12);
% Angle included between the side magnet
length and the inner radius of the magnet
ang32 = pi - ang22 - ang12;
% Half the angle between the side and
center magnet lengths
ang42 = 0.5*(pi/2 + ang22 + 2*ang12);
% Length of the outer radius edge
len22 = hm2/cos(ang22)/2;
% Length from the inner corner to the
outer corner
len32 = hm2/sin(ang42)/2;
% Modified equivalent circuit partion
endpoint 9/19/99
% alpm1 is angle at rro-brw and minimum
bridge width 'pinch point' 9/19/99
alpm2 = angle(pol2comp((rro-brw),ang02)-
pol2comp(hm2/(2*cos(ang22)),ang02-
ang22))*p;

% Repeat for narrower magnet fixed to
parallel
% ang11 = alphm1/(4*p);
ang11i = atan((rrm2*tan(ang12)-(rrm1-
rrm2)/tan(ang42))/rrm1);
rrem1 = rrm1/cos(ang11i);
% ang31 = pi - ang21 - ang11o;
ang31 = 2*pi-2*ang42-(pi/2-ang11i);
% ang21 = locangle(rrem1,(rro-
brw),len11);
ang21 = losangle(rro-brw,ang31,rrem1);
% ang11o = alphm1/(2*p) - ang11i;
ang11o = pi - ang31 - ang21;
% alphm1 = alphm2 - 2*p*(asin((rrm1-
rrm2)/(rro-brw) - sin(ang22)) + ang22);
```

```
alphm1 = 2*p*(ang11o+ang11i);
len11 = locside(ang11o,(rro-brw),rrem1);
ratm1 = alphm1/pi;
% Change for rounded geometry 9/19/99
% alpm1 = (1-ratm1)*pi/2
% ang01 = alpm1/p;
ang01 = (1-ratm1)*pi/(2*p);
% alpm2 is angle at rro-brw and minimum
bridge width 'pinch point' 9/19/99
alpm1 = angle(pol2comp((rro-brw),ang01)-
pol2comp(hm1/(2*cos(ang21)),ang01-
ang21))*p;
% Change for parallelism precision
% ang41 = 0.5*(pi/2 + ang21 + 2*ang11);
% ang41 = 0.5*(pi/2 + ang21 + ang11o +
ang11i);
ang41 = ang42;
len21 = hm1/cos(ang21)/2;
len31 = hm1/sin(ang41)/2;

% Continue with both
% Angular distance from End of Magnet #1
to D-Axis [elect. rad]
dalpm1 = pi/2 - alpm1;
% Angular distance from End of Magnet #2
to End of Magnet #1
dalpm2 = alpm1 - alpm2;
% Nonlinear Magnetic Circuit Areas and
Lengths
% Length of magnet assuming three
straight segments
% and middle portion is half the magnets
angular span
% does not include length of post or
bridges 9/19/99
% lm1 = 2*(rrm1*tan(ang11i) ...
%       + sqrt(rrm1^2 + (rro - brw)^2 -
2*rrm1*(rro - brw)*cos(ang11o))) - crw;
% lm2 = 2*(rrm2*tan(ang12) ...
%       + sqrt(rrm2^2 + (rro - brw)^2 -
2*rrm2*(rro - brw)*cos(ang12)));
% Estimates magnet side length assuming
round cavities effect is about 1.5%
length 9/19/99
% lm1 = 2*(rrm1*tan(ang11i) ...
%       + sqrt(rrm1^2 + (rro - brw)^2 -
2*rrm1*(rro - brw)*cos(ang11o)) - crw);
% lm2 = 2*(rrm2*tan(ang12) ...
%       + sqrt(rrm2^2 + (rro - brw)^2 -
2*rrm2*(rro - brw)*cos(ang12)) - crw);
% Can't recall what this factor,  +
(hm2/2)*(1-1/cos(ang22)), was for 10/7/99
% Corrected rrm to rrem 9/19/99
```

```
lm1 = 2*(rrm1*tan(angl1i) - crw ...
     + sqrt(rrem1^2 + (rro - brw)^2 -
2*rrem1*(rro - brw)*cos(angl1o)));
lm2 = 2*(rrm2*tan(angl2) - crw ...
     + sqrt(rrem2^2 + (rro - brw)^2 -
2*rrem2*(rro - brw)*cos(angl2)));
% lry(1) estimate is average of rotor
surface and magnet length
% lry(2) estimate is average of both
magnet lengths
% lry(3) estimate is 2 times average
radial length from rotor surface to
average rotor yoke radius
% plus circumferential length at average
rotor yoke radius
% lry =
[0.5*(lm1+rro*alphm1/p),0.5*(lm1+lm2),2*(
rro-0.5*(rrm2-hm2/2+rri))+0.5*(rrm2-
hm2/2+rri)*pi/p];
% Half-pole lengths
% lry =
0.5*[0.5*(lm1+2*brw),0.5*(lm1+lm2+4*brw),
2*rrm2*tan(alphm2/(4*p))]
% Corrected for center posts 9/19/99
lry =
0.5*[0.5*(lm1+2*(brw+crw)),0.5*(lm1+lm2+4
*(brw+crw)),2*rrm2*tan(alphm2/(4*p))];
lst = hs+ds+db/2;
% Corrected for rounded cavities 9/19/99
% lsy =
(r+ds+hs+0.5*db)*[alphm1,alphm2,pi-
alphm1]/(4*p);
lsy =
(r+ds+hs+0.5*db)*[2*dalpm1,2*(dalpm2+dalp
m1),pi-2*dalpm1]/(4*p);
% Cross-sectional areas
% Full pole
Asy = db*l;
Am1 = (lm1+2*(crw+brw))*l;
Am2 = (lm2+2*(crw+brw))*l;
Aag = rro*l*pi/p;
% Corrected for rounded cavities 9/19/99
% Ag1 = rro*l*alphm1/p;
Ag1 = rro*l*2*dalpm1/p;
% Ag2 = rro*l*(alphm2-alphm1)/p;
Ag2 = rro*l*2*dalpm2/p;
% Half pole
% Ag = 0.5*[Ag1,Ag2,rro*l*(pi-alphm2)/p];
Ag = 0.5*[Ag1,Ag2,rro*l*(pi-
2*(dalpm1+dalpm2))/p];
Ast = lamt*Ag;
% Ary = l*[0.5*(rro-rrm1-hm1/2),(rrm1-
rrm2-hm1/2-hm2/2),locside((pi-
alphm2)/(2*p)+alphm2/(4*p),rrm2-
hm2/2,rri)];
% Changed third rotor area 10/19/99
% Ary = l*[(rro-rrm1-hm1/2),(rrm1-rrm2-
hm1/2-hm2/2),(rrem2-rri-hm2/2)]
Ary = l*[(rro-rrm1-hm1/2),(rrm1-rrm2-
hm1/2-hm2/2),(rrm2-rri-hm2/2)];
% Saturating bridge dimensions
% Corrected for center posts 9/19/99
% Ab1 = brw*l;
% Ab2 = brw*l;
Ab1 = (brw+crw)*l;
Ab2 = (brw+crw)*l;
% Bridge length is not terribly useful
for rounded cavities
lb1 = len21;
lb2 = len22;
% Area of one slot pitch
As = 2*pi*r*l/ns;
% Electrical angle spanned by one slot
pitch
dalps = 2*pi*p/ns;

% Masses
% Armature Conductor
massa = 3*Lac*Aac*rhos;
% Stator Mass
% Back Iron
mcore = rhofe*l*pi*(rco^2-rci^2);
% Teeth
mtooth = rhofe*l*(ns*wt*hs+2*pi*r*ds-
ns*ds*us);
% Tapered opening
mtooth = rhofe*l*ns*(wt*(hs+ds) +
(ds+os)*(2*pi*r/ns-wt-us));
% Rotor Magnet Mass
marea = 2*p*(lm1*hm1+lm2*hm2);
mmagnet = l*marea*rhom;
% Rotor Core Mass
mcorer = rhofe*l*(pi*(rro^2-rri^2)-
marea);
% Iron Mass
miron = mcore+mtooth+mcorer;
% Rotational Inertia
Jm = (mcorer+mmagnet)*(rro^2+rri^2)/2;

% Carter Coefficient
% only using stator extension
% Extension of the air-gap because of
slot openings
% slot top is depression width
sts = us;
% str = hm/2;
```

```
% tooth width is the rest:
tws = 2*pi*r/ns - sts;
% twr = 2*pi*(r-g)/(8*p) - str;
alphas = atan(sts/(2*g));
% alphar = atan(str/(2*g));
ccs = g*(alphas*tan(alphas) - log
(1/cos(alphas)));
% Ignore rotor effects for now
% ccr = g*(alphar*tan(alphar) - log
(1/cos(alphar)));
% geff = g*(sts+tws)/(sts+tws-
ccs)*(str+twr)/(str+twr-ccr);
geff = g*(sts+tws)/(sts+tws-ccs);

% Calculation of d-axis inductance ratios
using
% per-unit circuit elements (Vagati, et
al)
% Corrected all pu reluctances by
inverting 4/12/98
% Corrected to include bridge width which
is assumed saturated 9/19/99
% Corrected to assume that bridges don't
saturate over the full depth of the
magnet with rounded cavities 10/20/99
rm1 = hm1*As/(geff*0.5*Am1);
rm1 = par(hm1*As/(geff*(0.5*Am1-
(brw+crw)*l)),0.5*(brw+crw)*As/(geff*Ab1)
);
rm2 = hm2*As/(geff*0.5*Am2);
rm2 = par(hm2*As/(geff*(0.5*Am2-
(brw+crw)*l)),0.5*(brw+crw)*As/(geff*Ab2)
);
rg1 = dalps/dalpm1;
rg2 = dalps/dalpm2;

puf1 = (cos(alpm1) - 0)/dalpm1;
puf2 = (cos(alpm2) - cos(alpm1))/dalpm2;

% Corrected misplaced parenth 4/12/98
% New element deleted - does not
contribute to pur calculations 9/19/99
pur1 =
((rm1+par(rm2,rg2))/(rm1+rg1+par(rm2,rg2)
))*puf1 ...
        +
(rm2*rg1/(rm2+rm1+rg1)/(rg2+par(rm2,rm1+r
g1)))*puf2;
pur2 =
(par(rm2,rg2)/(rm1+rg1+par(rm2,rg2)))*puf
1 ...
        +
(par(rm2,rm1+rg1)/(rg2+par(rm2,rm1+rg1)))
*puf2;
ratdcqm = 1 - (4/pi) * (dalpm1*puf1^2 +
dalpm2*puf2^2);
ratdtqm = (4/pi) * (puf1*(puf1-
pur1)*dalpm1 + puf2*(puf2-pur2)*dalpm2);

% Magnetic circuit elements
% Considering various options 10/19/99
% PM reluctance based on full length of
magnets plus bridge
% based on parallel combo of reduced
depth bridge and magnets
% based on magnet length alone (current
choice)
Rm1 = hm1/(muzero*Am1);
Rm1 = par(hm1/(muzero*(Am1-
2*(brw+crw)*l)),(brw+crw)/(muzero*2*Ab1))
;
Rm1 = hm1/(muzero*(Am1-2*(brw+crw)*l));
Rm2 = hm2/(muzero*Am2);
Rm2 = par(hm2/(muzero*(Am2-
2*(brw+crw)*l)),(brw+crw)/(muzero*2*Ab2))
;
Rm2 = hm2/(muzero*(Am2-2*(brw+crw)*l));
Rg1 = geff/(muzero*Ag1);
Rg2 = geff/(muzero*Ag2);

Areq1 =
(hm2*Rg2+hm1*(Rm2+Rg1))/(Rm2*Rg2+(Rm2+Rg2
)*(Rm1+Rg1))/muzero;
Areq2 = (hm2*(Rm1+Rg1)-
hm1*Rm2)/(Rm2*Rg2+(Rm2+Rg2)*(Rm1+Rg1))/mu
zero;
Aseq1 = (-
Rm2*Rg2/(Rm2*(Rg2+Rg1+Rm1)+Rg2*(Rg1+Rm1))
)*Ab2 ...
        + (-
(Rg2+Rm2)*Rm1/(Rg2*Rm2+(Rm1+Rg1)*(Rm2+Rg2
)))*Ab1;
Aseq2 = (-
Rm2*(Rm1+Rg1)/(Rm2*(Rg2+Rg1+Rm1)+Rg2*(Rg1
+Rm1)))*Ab2 ...
        +
(Rm2*Rm1/(Rg2*Rm2+(Rm1+Rg1)*(Rm2+Rg2)))*A
b1;

% Calculation of magnetic field
% Bg1 = (Br*Areq1 + Bs*Aseq1)/Ag1;
% Bg2 = (Br*Areq2 + Bs*Aseq2)/Ag2;
Bg1 = (Br*Areq1 + Bs*2*Aseq1)/Ag1;
Bg2 = (Br*Areq2 + Bs*2*Aseq2)/Ag2;
```

```
% Fundamental magnet field
% Corrected to use electrical angles
% Average composition
% B1 = 0.5 * (Bg1*alphm1 + Bg2*(alphm2 -
alphm1));
% B1 = (4/pi) * (Bg1*sin(alphm1) +
Bg2*(sin(alphm1) - sin(alphm2)));
% Corrected again for rounded cavities
9/19/99
% B1 = (4/pi) * (Bg1*sin(alphm1/2) +
Bg2*(sin(alphm2/2) - sin(alphm1/2)));
B1 = (4/pi) * (Bg1*sin(dalpm1) +
Bg2*(sin(dalpm1+dalpm2) - sin(dalpm1)));

% Stator winding factors
% Stator slot pitch (in electrical
radians)
gama = 2*pi*p/ns;
% Coil throw (in electrical radians)
nssp = nsct/nsfp;
alfa = pi*nssp;

% Breadth or distribution
kb = sin (0.5 * ma * gama) / (ma * sin (
0.5 * gama));
kb5 = sin (2.5 * ma * gama) / (ma * sin
(2.5 * gama));
kb7 = sin (3.5 * ma * gama) / (ma * sin
(3.5 * gama));

% Pitch
kp = sin (alfa/2.0);
kp5 = sin (5.0 * alfa/2.0);
kp7 = sin (7.0 * alfa/2.0);

% Skew of one slot pitch
ks = sin (gama/2.0) / (gama/2.0);
ks5 = sin (5*gama/2.0) / (5*gama/2.0);
ks7 = sin (7*gama/2.0) / (7*gama/2.0);

% Total
ka = kb * kp * ks;
ka5 = kb5 * kp5 * ks5;
ka7 = kb7 * kp7 * ks7;

% Zig-zag Factors
np = ns/p+1;
nm = ns/p-1;
% if ma>1 we need to compute a separate
zigzag component
% np and nm are the positive and negative
zigzag harmonic orders
if ma>1,
  kbp = sin (0.5 * ma * np * gama) / (ma
* sin ( 0.5 * np * gama));
  kbm = sin (0.5 * ma * nm * gama) / (ma
* sin ( 0.5 * nm * gama));
  kpp = sin (np * alfa/2.0);
  kpm = sin (nm * alfa/2.0);
    ksp = sin (gama * np/2.0) / (gama *
np/2.0);
    ksm = sin (gama * nm/2.0) / (gama *
nm/2.0);
  kap = kbp * kpp * ksp;
  kam = kbm * kpm * ksm;
end

% Calculation of internal voltage
lambda = 2*rro*l*B1*na*ka/p;
% RMS Air-gap flux linkage
Lambda=lambda/sqrt(2);

% Calculation of reactances: only two
count here!
% Air-gap inductance: basic round rotor
Lag =
(3/2)*(4/pi)*muzero*na^2*ka^2*l*r/(p^2*ge
ff);

% Stator Leakage Inductance Calculation
% Slot leakage
% FIX
perm = muzero*l*(ds/us+(1/3)*hs/wst);
Lslot = 2*p*nc^2*perm*(4*ma-nst);
if (nssp > (2/3)),
    knssp = 1.5*nssp - 0.5;
elseif (nssp < (1/3)),
    knssp = 1.5*nssp - 1;
else,
    knssp = 3*nssp - 1.5;
end
permn = muzero*l*((2*os/us + 2*(ds-
os)*log(wsa/us)/(wsa-us) +
(5/6)*(hs/wsa)) ...
         + knssp*(os/us + (ds-
os)*log(wsa/us)/(wsa-us) + hs/(4*wsa)));
Lslot = na^2*permn/(2*ma*p);

% End Turn Leakage Inductance
Lend = 0.5*(140/(4 * pi^2))*(3/2) *
muzero * r * na^2 * (alfa/pi - 0.3)/p^2;

% Harmonic Components: Belt Leakage
Inductance
La5 = Lag * (ka5 / (ka * 5))^2;
La7 = Lag * (ka7 / (ka * 7))^2;
```

```
% Stator Zigzag Leakage Inductance
% Round rotor formulation
if ma>1,
  Lap = Lag * (kap / (ka * np))^2;
  Lam = Lag * (kam / (ka * nm))^2;
else,
    Lap = 0;
    Lam = 0;
end

% Salient Inductances
Laqm = Lag;
Ladt = Laqm*ratdtqm;
Ladc = Laqm*ratdcqm;
Ladm = Ladt + Ladc;

% Synchronous Reactances (Ohms)
% Added leakage definition 2/21/00
Ll = Lslot + Lend + La5 + La7 + Lap +
Lam;
Ld = Ladm + Ll;
Lq = Laqm + Ll;
Lql = Lq;
Sr = Lq/Ld;

% Ok: now we go into a loop to see if we
can actually get
% terminal voltage and current
% This will probably crash here if the
rating is impossible

% Speeds
% Electrical frequency
f = p*rpm/60;
om = 2*pi*p*rpm/60;
% Mechanical frequency
omegam = 2*pi*rpm/60;
% Tip (rotor peripheral) speed
stip = rro*om/p;
% RMS (!) Internal Voltage:
Ea = om*Lambda;
% Reactances
Xd = om*Ld;
Xq = om*Lq;

notdone = 1;
lerror = 0;
leg = 1;
nloop = 0;
Va = volt;
Ia = Prat/(3*Va*cos(pi/4));
% Now estimate losses
Pa = 3*Ia^2*Ra;

% Estimate of gap friction loss
% Reynold's Number in the gap
% ren = omegam*rro*g/nuair;
% that gives a friction factor
% ff = .0076/ren^.25;
% and that in turn leads to windage loss
% pwind =
2*pi*rro^4*omegam^3*l*rhoair*ff;
pwind = 0;

% fan pressure rise estimated from rotor
peripheral speed
% deltap = .5* rhoair * (omegam * rro)^2;
% mass flow based on temperature rise
% mdot = (Pc + Pa + pwind)/(cpair * dtt);
% then fan power is volume flow times
pressure drop
% pfan = mdot * deltap / (rhoair * etf);
pfan = 0;

% Consistent set of definitions for psi,
delt, and gam
% Power Angle delt is: -pi < delt <= pi
% Power Factor angle psi is: 3*pi/2 > psi
>= -5*pi/2
% Q-Axis Angle gam = psi + delt is: pi/2
> gam >= -3*pi/2

while notdone == 1,
    nloop = nloop + 1;
    if (gen == 0),
%   fprintf('Motoring psi = %g\n',psi);
    % Motoring
    Ib = 5e7 * Aac;
    Tb = 3*p*Lambda*Ib;
    xd = Ld*Ib/Lambda;
      % New nonlinear model
      if (mflag==1)
         Iqx = linspace(.001, Ib);
         Lqy = Lq*linspace(1.001,.999);
         Lqy(1) = Lq;
      elseif (mflag==3)
% Fast, Imprecise nonlinear model
         qaxmodel3;
      else
% Slow, Accurate nonlinear model
         qaxmodel4;
      end
    if(ismono(Iqx)==0);
       lerror = 1;
       break;
```

```
    end
%   plot(Iqx,Lqy);
%   axis([0 500 0 1e-3]);
%   pause(1);
%   Iqx=linspace(1,501);
%   Lqy=Lq*ones(1,100);
    [Lqmax,Indmax] = max(Lqy);
      iqmax = Iqx(Indmax)/Ib;
    Indmin = length(Lqy);
    while((Lqy(Indmin) < Ld) & (Indmin >
Indmax))
        Indmin = Indmin - 1;
     end
    iqmin = min(1,Iqx(Indmin)/Ib);
%   if ((iqmax > 1) | (Lqmax < Ld))
    if ((iqmax > 1) | (Indmin <= Indmax))
        Ia = 9e9;
    else,
        Tmax = Prat/omegam;
        te = Tmax/Tb;
% Find the iq that minimizes the phase
current ia
%       iq = constr(['f = iqid(x);' 'g =
[];'],(iqmax+iqmin)/2,[],iqmax,iqmin);
        iq = fmin('iqid',iqmax,iqmin);
%       iq = constr('f =
iqid(x);',iqmax*1.1,[],iqmax,1);
%       iq = fmin('iqid',Iqmax/Ib,1),
        Ia = ia*Ib;
        Id = id*Ib;
        Iq = iq*Ib;
        Lq = xq*Lambda/Ib;
        Tmax = Tb*(1 - (xq - xd)*id)*iq;
        Vq = om*Lambda + om*Ld*id*Ib +
Ra*iq*Ib;
        Vd = -om*Lq*iq*Ib + Ra*id*Ib;
        Va = sqrt(Vq^2 + Vd^2);
        delt = atan2(Vd,Vq);
        psi = fixgam(atan2(id,iq)) -
delt;
        Sr = Lq/Ld;
%       fprintf('Saliency Ratio =
%g\n',Sr);
    %   fprintf('Starting torque = %g
Current = %g\n',Tmax,Ia);
    %   fprintf('Old Iq = %g  New Iq = %g
Torque = %g  Lq =
%g\n',iqold*Ib,iq*Ib,Tmax,xq*Lambda/Ib);
     end
    if ((Va > mvolt) | (Ia > Ib))
        lerror = 1;
        break;
    else,
```

```
            notdone = 0;
         end
        else,
%   fprintf('Generating psi = %g\n',psi);
% Generating
% Saturation model for generating
10/24/99

    global Prat Ia Va Ea Lq om Xq Xd Ra
delt;
      Ia1 = 9e9;
      % Start searching for a generating
solution with minimal terminal voltage
      % Results in quick solution at
lower speeds generally
      Va = 0;
      while(Va < volt)
         Va = Va + volt/10;
         options = 0;
%         fprintf('Va = %g\n', Va);
%         [psi,options] =
fmin('psigen',1.01*pi/2,.99*3*pi/2,option
s);
        [psi,options] = fmin('psigen',-
.99*3*pi/2,-1.01*pi/2,options);
         if (options(8) > 0.01)
            Ia = 9e9;
%            fprintf('Failed to find
psi\n');
         elseif (Ia < Ia1)
            Ia1 = Ia;
            delt1 = delt;
            Lq1 = Lq;
            Xq1 = Xq;
            psi1 = psi;
            Va1 = Va;
         else
% Terminate when current reqt starts
increasing
%           clf;
%           ytemp = [];
%           for psi=linspace((-
.99*3*pi/2),(-1.01*pi/2));
%               ytemp =
[ytemp,psigen(psi)];
%           end
%           plot(linspace(-.99*3*pi/2,-
1.01*pi/2),ytemp);
%           pause;
            Va = volt;
         end
       end
       if (Ia1 < 9e9)
```

```
         notdone = 0;
         Ia = Ia1;
         delt = delt1;
         Lq = Lq1;
         Xq = Xq1;
         psi = psi1;
         Va = Va1;
      else
%         fprintf('Failed to find
generating point\n');
         lerror = 1;
         break;
      end
    end
    % Coercive Force Estimate
    psidelt = atan(Xq/Ra) + gen*pi;
    Iashort = Ea/(Xd*sin(psidelt) +
Ra*cos(psidelt));
    Idshort = Iashort*sin(psidelt);
    Cf = Xd*Idshort*Br/Ea;
end        % end of power adjustment
loop

% RMS Air-gap Flux Density
% Added effects of R and Ll 2/21/00
Bagv =
(Va+Ia*(Ra+om*Ll))*p/(om*2*rro*l*na*ka);
% Change loss definitions from RMS to
Average 2/21/00
% Average Air-gap Flux Density
Bagva = 2*sqrt(2)*Bagv/pi;
% Tooth Flux Density (Average)
Bt = Bagva/lamt;
% Back Iron Flux Density (Average)
Bb = Bagva*pi*rro/(2*p*db);
% Rotor Flux Density (Average)
Brc = Bagva*pi*rro/(2*p*(rro-rri-hm1-
hm2));
% Flux Density Limit
% if ((Bt > 1.8) | (Bb > 1.8))
%   lerror = 1;
%   Ja = 9e9;
%   Tm = 0;
%   eff = 0;
%   Pin = 0;
%   return;
% end
% Core Iron Loss
Pcb =
mcore*pb*abs(Bb/bb)^epb*abs(om/omb)^epf;
% Teeth Loss
Pct =
mtooth*pb*abs(Bt/bb)^epb*abs(om/omb)^epf;
```

```
% Harmonic Loss
sigc = 1.46e6;
theta0 = us*ns/r;
Bh = Bagv*(2/pi)*sin(theta0/2);
omh = om*ns/p;
Ez = rro.*omh.*Bh/p;
B0 = 0.75*Bs;
deltc =
(3.79*B0./(sigc^2.*omh.*Ez)).^.3333;
Ph = 1.75.*rro.*l.*sigc.*deltc.*Ez.^2;
% Total Loss
Pc = Pcb+Pct;

if (lerror)
    Ja = 9e9;
    Tm = 0;
    eff = 0;
    Pin = 0;
    return;
end

% Performance Characterization
% dq Currents
Iq = Ia*cos(psi+delt);
Id = Ia*sin(psi+delt);
% Slot Current Density
Ja = 2*nc*Ia/(hs*wsa);

% Power, Torque, and Efficiency
Pa = 3*Ia^2*Ra;
if (gen == 0),
% Motoring
% Ignore Pc for motoring
    Pin = Prat+Pa+pwind+pfan;
    if (rpm == 0),
    Tm = 3*p*Lambda*Ia*cos(psi);
    else,
    Tm = Prat/omegam;
    end
else,
% Generating
    Pin = Prat-Pc-Pa-pwind-pfan;
    Tm = Pin/omegam;
end
eff = Prat/Pin;
% Average rotor shear stress
shear = abs(Tm)/(2*pi*rro^2*l);
% Power Factor
pfact = cos(psi);

return;
% srpmcost
%
```

```
% Costs
ucsteel = 1.0;
uctape = 5.0;
uccopp = 5.0;
tcsteel = miron*ucsteel;
tccopp = massa*uccopp;
tcmagnet = mmagnet*ucmagnet;
tcmach = 2 * (tcsteel+tccopp) + tcmagnet
+ mmagnet*ucsteel;
tcconv = 402 + .4823*Imax/sqrt(2) +
21.18;
tcsyst = tcmach + tcconv;
% srpmmap.m
% Automotive Starter/Generator Rating Map
% Uses srpm.m and input parameters
dvars.m to find
% correct power factor and terminal
voltage to acheive rating
% Added variable generating voltage
10/21/99

clf reset

mflag = input('Type 1 for linear, 3 for
fast nonlinear, and 4 for accurate
nonlinear model: ');

fprintf('INTERIOR PM MACHINE\n');

% Initialize constants
nogood = 0;
Imax = -9e9;
tcsyst = 9e9;
mvolt = 19.3;
% vstep = 0.5;
vstep = mvolt/40;
speedm = [10,600,1500,6000];

t1=clock;
for spind=1:4,
    speed = speedm(spind);
    if (speed < 600),
    gen = 0;
      % volt = 0.5;
       volt = vstep;
    rpm = speed*mratio;
    Prat = Trat*speed*pi/30;
    psi = -.95*pi/2;
    psif = psi + pi;
    srpm;
%   while ((Ja/lama > 5e7) & (volt <
mvolt)),
%       psi = -.95*pi/2;
%       volt = volt + vstep;
%       srpm;
%    end
    if ((Ja/lama > 5e7) | (volt >
mvolt)),
        fprintf('Machine does not meet
spec at %g rpm\n',speed);
        fprintf('Lratio = %12g, B1 =
%12g\n',Lq/Ld,B1);
        nogood = 1;
        break;
    else,
        srpmout;
        subplot(2,2,spind);
        title([num2str(speed),' rpm']);
        xlabel('Re')
        ylabel('Im')
        syntrig;
     end
    else,
      gen = 1;
%       psistep = pi/40;
    if (speed==1500),
%       Prat = -(1+3/42)*3000;
        Prat = -(1+3/42)*(6000 - (6000-
4000)*(6000-speed)/(6000-600))*0.75;
    else,
        Prat = -(1+3/42)*(6000 - (6000-
4000)*(6000-speed)/(6000-600));
     end
    volt = mvolt;
%   volt = vstep;
      rpm = speed*dratio;
%       lerror = 1;
%       while ((volt < mvolt) & ((lerror)
| (Ja/lama > 2e7) | ((speed == 1500) &
(eff < .804)) | (Ea > volt*55/42)))
        psi = 1.05*pi/2;
         psif = psi + pi;
%          volt = volt + vstep;
         srpm;
%        end
    if ((lerror) | (Ja/lama > 2.0e7) |
((speed == 1500) & (eff < .804)) | (Ea >
volt*55/42))
        nogood = 1;
        fprintf('Machine does not meet
spec at %g rpm\n',speed);
        fprintf('lerror = %d  Ja/lama =
%g  eff = %g  Ea =
%g\n',lerror,Ja/lama,eff,Ea);
        fprintf('Lratio = %12g, B1 =
%12g\n',Lq/Ld,B1);
```

```
        break;
    else,
        srpmout;
        subplot(2,2,spind);
        title([num2str(speed),' rpm']);
        xlabel('Re')
        ylabel('Im')
        syntrig;
     end
    end
    if(Imax < Ia)
    Imax = Ia;
    end
end
if (nogood==0)
    srpmcost;
    srpmspecs;
end
% fprintf('Elapsed time is %g
seconds\n',etime(clock,t1));


% srpmmap.m
% Automotive Starter/Generator Rating Map
% Uses srpm.m and input parameters
dvars.m to find
% correct power factor and terminal
voltage to acheive rating
% Added variable generating voltage
10/21/99

% Initialize constants
nogood = 0;
Imax = -9e9;
tcsyst = 9e9;
mvolt = 19.3;
vstep = mvolt/40;
speedm = [10,600,1500,6000,6000];

for spind=1:4,
% t1=clock;
    speed = speedm(spind);
    if (speed < 600),
      gen = 0;
       % volt = 0.5;
    volt = vstep;
    rpm = speed*mratio;
    Prat = Trat*speed*pi/30;
    psi = -.95*pi/2;
    psif = psi + pi;
    srpm;
%   while ((Ja/lama > 5e7) & (volt <
mvolt)),
%       psi = -.95*pi/2;
%       volt = volt + vstep;
%       srpm;
%    end
    if ((Ja/lama > 5e7) | (volt >
mvolt)),
%       fprintf('Machine does not meet
spec at %g rpm\n',speed);
%       fprintf('Lratio = %12g, B1 =
%12g\n',Lq/Ld,B1);
        nogood = 1;
        break;
     end
    else,
    gen = 1;
    if (speed==1500),
        Prat = -(1+3/42)*3000;
    else,
        Prat = -(1+3/42)*(6000 - (6000-
4000)*(6000-speed)/(6000-600));
      end
       volt = mvolt;
%   volt = vstep;
      rpm = speed*dratio;
%       lerror = 1;
%       while ((volt < mvolt) & ((lerror)
| (Ja/lama > 2e7) | ((speed == 1500) &
(eff < .804)) | (Ea > volt*55/42)))
        psi = 1.05*pi/2;
         psif = psi + pi;
%          volt = volt + vstep;
         srpm;
%       end
    if ((lerror) | (Ja/lama > 2.0e7) |
((speed == 1500) & (eff < .804)) | (Ea >
volt*55/42))
        nogood = 1;
%       fprintf('Machine does not meet
spec at %g rpm\n',speed);
%       fprintf('lerror = %d  Ja/lama =
%g  eff = %g  Ea =
%g\n',lerror,Ja/lama,eff,Ea);
%           fprintf('Lratio = %12g, B1 =
%12g\n',Lq/Ld,B1);
        break;
     end
    end
    if(Imax < Ia)
    Imax = Ia;
    end
% fprintf('Elapsed time is %g
seconds\n',etime(clock,t1));
end
```

```
if (nogood==0)
   srpmcost;
end
% srpmmc.m
% Monte Carlo SRPM Designer
global mctype;

designct = 0;
if(exist('savedtc')==0)
   savedtc = 9e9;
end
mctype = input('Type 1 for system and 2
for machine optimization: ');

ndes=0;
t0 = clock;
while(1)
   ndes=ndes+1;
%   fprintf('\nDesign Number %d\n',ndes);
% Length
   l = randr(.04,.075);
%  l = .055;
% Outside diameter
%  dout = randr(.23,.3);
   dout = .28;
%   dout = .3;
% Back iron depth
   db = randr(.01,.020);
% Magnet remanence
   Br = randr(.025,.45);
% Stator slot dimensions
   raths = randr(.75,3.0);
   lams = randr(.35,.65);
%  lamus = randr(.35,lams);
   lamus = 0.5*lams;
% Poles & slots
   p = randi(3,6);
%  p = 6;
   if (p >= 5)
     ma = 2;
  elseif (p == 4)
     ma = randi(2,3);
  else
     ma = randi(2,4);
  end
% Armature turns
   na = 2*ma*p;
% Short pitch
   nst = randi(0,ma);
%  nst = 1;

% Calculation of stator inner radius
   ns = 6*ma*p;
```

```
     usl = .032*25.4*.001;
     % Stator radius from outside diameter
     r = (dout/2 -
db)/(1+raths*lams*2*pi/ns +
(1+raths*lams*2*pi/ns)*pi*(lams-
lamus)/ns);
     us = lamus*2*pi*r/ns;
     if (us < usl),
     us = usl;
     r = (dout/2
+0.5*us*(1+raths*lams*2*pi/ns) -
db)/(1+raths*lams*2*pi/ns +
(1+raths*lams*2*pi/ns)*pi*lams/ns);
    end
%  lamrd = randr(.5,.82);
   if (.0825/(r-g) < .85)
      lamrd = randr(.0825/(r-g),.85);
 %      lamrd = .0825/(r-g);
      % Rotor slot dimensions
      ratm = randr(.1,.8);
      lamh = randr(.25,.75);
      %ratm1 = randr(.20,.75);
       ratm1 = 0.50;
      ratm2 = randr(ratm1,.80);
      lammd1 = randr(.15,.4);
      lammd2 = randr(.15,.4);
       if (ratm2*(r-g)*pi/p >
(2*lammd1*(1-ratm)+(1+lamh)*ratm)*(r-
g)*(1-lamrd));
       % Run machine design code
          srpmmap;
       else
          nogood = 1;
       end
   else
      nogood = 1;
    end
    time = fix(clock);
    if (nogood == 0)
       designct = designct+1;
     if (tcsyst < savedtc)
          eval([sprintf('save
tempmc%d',designct),SRPMGVAR]);
%            eval(['save
tempmc',SRPMGVAR]);
           if(mctype==1)
             savedtc = tcsyst;
           else
              savedtc = tcmach;
           end
          fprintf('Saved design number
%d\n',ndes);
           srpmfeflexnew;
```

```
          destime=clock;
          title(sprintf('Cost = %g,
Designed at %d:%.2d,
%s',tcsyst,time(4),time(5),date));
          pause(2);
      end
%       if(mctype==1)
%         fprintf('\nCost = %g, Best Cost
= %g\n',tcsyst,savedtc);
%       else
%          fprintf('\nCost = %g, Best
Cost = %g\n',tcmach,savedtc);
%       end
    end
%   fprintf('Elapsed time is
%g\n',etime(clock,t0));
    desrate =
ndes*24*60*60/etime(clock,t0);
    hitrate = 100*designct/ndes;
%   fprintf('Time is
%d:%.2d:%.2d\n',time(4),time(5),time(6));
end

% srpmopt.m
% SRPM optimization script uses optfunc.m

global lowfout;
lowfout = 9e9;
options = [];
ratm1 = 0.5*ratm2;
X0 =
[raths,lams,lamus,ratm,lamh,ratm2,l,db,Br
,lamrd,lammd1,lammd2];
VLB = X0*.96;
VLB(8) = .010;
VUB = X0*1.04;
VUB(10) = 0.85;
x = constr(['f = optfunc(x);' 'g = x(3)
- 0.51*x(2);'],X0,options,VLB,VUB);
%
****************************************
************************ %
%
%
%                            SRPMOUT.M
%
%
%
%
****************************************
************************ %
% srpmout.m: output of major attributes
% requires srpm to be run first!
```

```
% Output Section:
% clc
fprintf('PERFORMANCE DATA [rms]:\n');
fprintf('Rating [W] =        %12g  Speed
[RPM] =        %12g\n', Prat, rpm);
fprintf('Armature Cur Den =  %12g
Current =            %12g\n', Ja/lama,
Ia);
fprintf('Id =                %12g  Iq =
%12g\n', Id, Iq);
fprintf('Vd =                %12g  Vq =
%12g\n', Vd, Vq);
fprintf('Terminal Voltage =  %12g  Field
Voltage =      %12g\n', Va, Ea);
fprintf('B RMS Air Gap =     %12g  B RMS
Teeth =        %12g\n', Bagv, Bt);
fprintf('B RMS Back Iron =   %12g  B RMS
Rotor =        %12g\n', Bb, Brc);
fprintf('Core Loss =         %12g
Armature Loss =      %12g\n', Pc, Pa);
fprintf('Total Loss =        %12g
Harmonic Loss =      %12g\n', Pc+Pa+Ph,
Ph);
fprintf('S.C. Current =      %12g
Coercive Force =     %12g\n', Iashort,
Cf);
fprintf('Shear [psi] =       %12g  delta
[deg] =        %12g\n', shear/6.9e3,
delt*180/pi);
fprintf('psi [deg] =         %12g  gamma
[deg] =        %12g\n', psi*180/pi,
(psi+delt)*180/pi);
fprintf('Efficiency =        %12g  Power
Factor =       %12g\n\n', eff, pfact);
% srpmspecs.m
% Design specification output for srpm
machine

fprintf('STATOR SPECS:\n');
fprintf('Slots/pole/phase =  %12g  Pole
Pairs =        %12g\n', ma, p);
fprintf('Phases =            %12g  Slots
=              %12g\n', 3, ns);
fprintf('Series Turns =      %12g  #
Slots Shorted =  %12g\n', na, nst);
fprintf('Tooth Width =       %12g
Opening Width =      %12g\n', wt, us);
fprintf('Slot Bottom Width = %12g  Slot
Top Width =      %12g\n', wsb, wst)
fprintf('Opening Height =    %12g  Slot
Depression =     %12g\n', os, ds);
```

```
fprintf('Slot Height =        %12g  Back
Iron Depth =   %12g\n', hs, db);
fprintf('\nROTOR SPECS:\n');
fprintf('Rotor A.G. Radius = %12g  Air
Gap =            %12g\n', r-g, g);
fprintf('Bridge Width =      %12g  Inner
Radius =      %12g\n', brw, rri);
fprintf('Sm. Magnet Depth =  %12g  Lg.
Magnet Depth =  %12g\n', hm1, hm2);
fprintf('Sm Mag Span [deg] = %12g  Lg Mag
Span [deg] = %12g\n', alphm1*180/pi/p,
alphm2*180/pi/p);
fprintf('\nINDUCTANCES [Henries]:\n');
fprintf('d-Axis =            %12g  q-Axis
=           %12g\n',Ld,Lq);
fprintf('d-Magnetizing =     %12g  q-
Magnetizing =     %12g\n',Ladm,Laqm);
fprintf('d-Thru Over q-Mag = %12g  d-Thru
=           %12g\n',ratdtqm,Ladt);
fprintf('d-Circ Over q-Mag = %12g  d-
Circ. =           %12g\n',ratdcqm,Ladc);
fprintf('End Turn Leakage =  %12g  Slot
Leakage =      %12g\n',Lend,Lslot);
fprintf('5th Belt Leakage =  %12g  7th
Belt Leakage =  %12g\n',La5,La7);
fprintf('Forward Zig-Zag =   %12g
Backward Zig-Zag =  %12g\n',Lap,Lam);
fprintf('\nFIELD SPECS:\n');
fprintf('Magnet Remanence =  %12g  Fund
Field =         %12g\n',Br, B1);
fprintf('Air-Gap Field 1 =   %12g  Air-
Gap Field 2 =   %12g\n',Bg1, Bg2);
fprintf('Max Core Density =  %12g  PM
Flux Linkage =   %12g\n',max([Bt Bb
Brc]), Lambda);
fprintf('\nMACHINE SPECS:\n');
fprintf('Diameter =          %12g  Total
Length =      %12g\n',dout,lout);
fprintf('Active Length =     %12g  Iron
Mass =          %12g\n',l,miron);
fprintf('Saliency Ratio =    %12g  Active
Rotor Vol. = %12g\n',Sr,pi*rro^2*l);
fprintf('Copper Mass =       %12g  Magnet
Mass =        %12g\n',massa,mmagnet);
fprintf('Total Mass =        %12g
Reflected Moment =
%12g\n',miron+massa+mmagnet,Jm*(dratio^2)
);
fprintf('Max RMS Sw. Curr. = %12g
Converter Cost =
%12g\n',Imax/sqrt(2),tcconv);
fprintf('Machine Cost =      %12g  Total
Cost =         %12g\n',tcmach,tcsyst);
```

Chapter 11 Appendix C

MATLAB SPECIAL PURPOSE SOFTWARE

This appendix contains MATLAB scripts and functions for three purposes:

1. optimization for maximum torque or maximum CPSR
2. creation of DXF AutoCAD ASCII files
3. creation of MagNet solid models for EM FEA

```
% srpmmap.m
% Automotive Starter/Generator Rating Map
% Uses srpm.m and input parameters
dvars.m to find
% correct power factor and terminal
voltage to acheive rating
% Added variable generating voltage
10/21/99
clf reset

mflag = input('Type 1 for linear, 3 for
fast nonlinear, and 4 for accurate
nonlinear model: ');

fprintf('INTERIOR PM MACHINE\n');

% Initialize constants
nogood = 0;
Imax = -9e9;
tcsyst = 9e9;
mvolt = Vb;
% Changed rated current and voltage from
460/15 to 480/12.4 2/26/00
vstep = Vb/40;
speedm = [10,5000];

t1=clock;
volt = Vb;
srpmlinear;
srpmsaturable;
if (lerror)
   nogood = 1;
   fprintf('Saturable model error\n');
else
   for spind=1:2,
      speed = speedm(spind);
      if (speed < 6000),
         gen = 0;
         volt = vstep;
         rpm = speed*mratio;
         % Prat = Trat*speed*pi/30;
         psi = -.95*pi/2;
         psif = psi + pi;
         srpmmg;
         Prat = Tmax*speed*pi/30;
         Trat = Tmax;
         % while ((Ja/lama > 5e7) &
(volt < Vb)),
         %      psi = -.95*pi/2;
         %      volt = volt + vstep;
         %      srpm;
         %   end
         if ((Ja/lama > 5e7) | (volt >
Vb) | (lerror)),
            fprintf('Machine does not
meet spec at %g rpm\n',speed);
            fprintf('Lratio = %12g, B1 =
%12g\n',Lq/Ld,B1);
            nogood = 1;
            break;
         else,
            srpmout;
            subplot(2,2,spind);
            title([num2str(speed),'
rpm']);
            xlabel('Re')
            ylabel('Im')
            syntrig;
         end
      else,
         gen = 1;
         %      psistep = pi/40;
```

```
        if (speed==1500),
           Prat = -(1+3/42)*3000;
        else,
           Prat = -(1+3/42)*(6000 -
(6000-4000)*(6000-speed)/(6000-600));
        end
        volt = Vb;
        % volt = vstep;
        rpm = speed*dratio;
        %      lerror = 1;
        %      while ((volt < Vb) &
((lerror) | (Ja/lama > 2e7) | ((speed ==
1500) & (eff < .804)) | (Ea >
volt*55/42)))
        psi = 1.05*pi/2;
        psif = psi + pi;
        %          volt = volt + vstep;
        srpm;
        %      end
        if ((lerror) | (Ja/lama > 2.0e7)
| ((speed == 1500) & (eff < .804)) | (Ea
> volt*55/42))
           nogood = 1;
           fprintf('Machine does not
meet spec at %g rpm\n',speed);
           fprintf('lerror = %d  Ja/lama
= %g  eff = %g  Ea =
%g\n',lerror,Ja/lama,eff,Ea);
           fprintf('Lratio = %12g, B1 =
%12g\n',Lq/Ld,B1);
           break;
        else,
           srpmout;
           subplot(2,2,spind);
           title([num2str(speed),'
rpm']);
           xlabel('Re')
           ylabel('Im')
           syntrig;
        end
     end
     if(Imax < Ia)
        Imax = Ia;
     end
   end
end
if (nogood==0)
    srpmcost;
    srpmspecs;
end
% fprintf('Elapsed time is %g
seconds\n',etime(clock,t1));

% srpmmap.m
% Automotive Starter/Generator Rating Map
% Uses srpm.m and input parameters
dvars.m to find
% correct power factor and terminal
voltage to acheive rating
% Added variable generating voltage
10/21/99
clf reset

mflag = input('Type 1 for linear, 3 for
fast nonlinear, and 4 for accurate
nonlinear model: ');

fprintf('INTERIOR PM MACHINE\n');

% Initialize constants
nogood = 0;
Imax = -9e9;
tcsyst = 9e9;
% Changed rated current and voltage from
460/15 to 480/12.4 2/26/00
mvolt = 460/sqrt(3);
Ib = 12.4*(84/na);
vstep = mvolt/40;
speedm = [5500/7,5500];
t1=clock;
volt = mvolt;
srpmlinear;
srpmsaturable;
if (lerror)
   nogood = 1;
else
   for spind=1:length(speedm),
      speed = speedm(spind);
      if (speed < 5000),
         gen = 0;
         volt = vstep;
         rpm = speed*mratio;
         psi = -.95*pi/2;
         psif = psi + pi;
         srpmmg;
         Prat = Tmax*speed*pi/30;
         Trat = Tmax;
         if ((Ja/lama > 5e7) | (volt >
mvolt) | (lerror)),
            fprintf('Machine does not
meet spec at %g rpm\n',speed);
            fprintf('Lratio = %12g, B1 =
%12g\n',Lq/Ld,B1);
            nogood = 1;
            break;
         else,
            srpmout;
            subplot(2,2,spind);
            title([num2str(speed),'
rpm']);
            xlabel('Re')
            ylabel('Im')
            syntrig;
         end
      elseif (speed==5500)
         % Find corner speed point
         Va=mvolt;
         voltlimop;
         powergrad;
```

```
      Ps0 = Ps;
      rpm0 = rpm;
      % Check that 5500 is still in
constant power region
      rpm = speed;
      mode3op;
      fprintf('Shaft power at corner
speed %f is %f and power at 5500rpm is
%f\n',rpm0,Ps0,Ps);
      if (Ps < Ps0)
        nogood=1;
      end
    end
    if(Imax < Ia)
      Imax = Ia;
    end
  end
end
if (nogood==0)
  srpmcost;
  srpmspecs;
end
% fprintf('Elapsed time is %g
seconds\n',etime(clock,t1));
% srpmmap.m
% Automotive Starter/Generator Rating Map
% Uses srpm.m and input parameters
dvars.m to find
% correct power factor and terminal
voltage to acheive rating
% Added variable generating voltage
10/21/99

% Initialize constants
nogood = 0;
Imax = -9e9;
tcsyst = 9e9;
% Changed rated current and voltage from
460/15 to 480/12.4 2/26/00
mvolt = 460/sqrt(3);
Ib = 12.4*(84/na);
vstep = mvolt/40;
speedm = [5500/7,5500];
opttype=0;
t1=clock;
volt = mvolt;
srpmlinear;
srpmsaturable;
if (lerror)
  nogood = 1;
else
  for spind=1:2,
    speed = speedm(spind);
    if ((speed < 5000) | (opttype >
0)),
      gen = 0;
      volt = vstep;
      % Prat = Trat*speed*pi/30;
      psi = -.95*pi/2;
      psif = psi + pi;
      rpm = speed*mratio;
      srpmmg;
      Prat = Tmax*speed*pi/30;
      Trat = Tmax;
      if(opttype)
      while(Prat > 12.5*speed*pi/30)
        speed=speed+500,
        rpm = speed*mratio;
        srpmmg;
        Prat = Tmax*speed*pi/30;
        Trat = Tmax;
      end
      end
      speedmax = speed;
      % while ((Ja/lama > 5e7) &
(volt < mvolt)),
      %     psi = -.95*pi/2;
      %     volt = volt + vstep;
      %     srpm;
      %  end
      if ((Ja/lama > 5e7) | (volt >
mvolt) | (lerror) | (Prat==9e9)),
        fprintf('Machine does not
meet spec at %g rpm\n',speed);
        fprintf('Lratio = %12g, B1 =
%12g\n',Lq/Ld,B1);
        nogood = 1;
        break;
      end
    elseif (speed==5500)
      % Find corner speed point
      Va=mvolt;
      voltlimop;
      powergrad;
      Ps0 = Ps;
      rpm0 = rpm;
      % Check that 5500 is still in
constant power region
      rpm = speed;
      mode3op;
      fprintf('Shaft power at corner
speed %f is %f and power at 5500rpm is
%f\n',rpm0,Ps0,Ps);
      if (Ps < Ps0)
        nogood=1;
      end
    end
    if(Imax < Ia)
      Imax = Ia;
    end
  end
end
if (nogood==0)
  srpmcost;
end
% fprintf('Elapsed time is %g
seconds\n',etime(clock,t1));
% srpmmc.m
% Monte Carlo SRPM Designer
% Kollmorgen Goldline Stator
```

```
global mctype;

designct = 0;
if(exist('savedtc')==0)
   %   savedtc = 9e9;
   savedTmax = 0;
   savedspeed = 0;
end
% mctype = input('Type 1 for system and 2
for machine optimization: ');
opttype = 0;

ndes = 0;
while(1)
    ndes=ndes+1;
%   t0 = clock;
    fprintf('\nDesign Number %d\n',ndes);
% Length
%   l = randr(.04,.075);
    l = 6.36*25.4*1e-3;
% Outside diameter
%   dout = randr(.23,.3);
    dout = 0.5*(.108039+.107988);
% Back iron depth
%   db = randr(.01,.020);
    db = 0.5*(dout-.09246);
% Magnet remanence
%   Br = randr(.025,.56);
    Br = .56;
% Stator slot dimensions
%   raths = randr(.75,3.0);
    raths = (0.5*.09246-.02893)/.00549;
%   lams = randr(.35,.65);
    lams = .00549/((2*pi*.02893)/18);
%   lamus = randr(.35,lams);
    lamus = .002795/((2*pi*.02893)/18);
% Poles & slots
%   p = randi(3,6);
    p = 2;
    if (p >= 5)
      ma = 2;
    elseif (p == 4)
      ma = randi(2,3);
    else
%     ma = randi(2,4);
    ma = 18/(2*p*3);
    end
% Armature turns
%   na = 2*ma*p;
    nc = randi(14,4*14);
    nc = [2*nc nc];
% Short pitch
%   nst = randi(0,ma);
    nst = 0.5;

% Calculation of stator inner radius
    ns = round(6*ma*p);
% Rotor dimensions
    g = .014*25.4*1e-3;
% Fix the rotor ID 2/26/00
%   lamrd = randr(.1,.50);
%   lamrd =
(.025159+.025133)/(.054445+.054343);
   lamrd = .990/2.1135;
% Rotor slot dimensions
   ratm = randr(.1,.8);
   lamh = randr(.25,.75);
%   ratm1 = randr(.20,.75);
   ratm1 = 0.50;
   ratm2 = randr(ratm1,.80);
   lammd1 = randr(.15,.4);
   lammd2 = randr(.15,.4);
% Reject rotors that don't leave enough
room for bends in magnets
        % Run machine design code
   srpmmapK2;
   time = fix(clock);
   if (nogood == 0)
      designct = designct+1;
    if ((Tmax > savedTmax) & (Tmax > 0))
%   if ((speedmax > savedspeed) & (Tmax >
0))
         eval(['save
tempmca',SRPMGVAR(1:99)]);
         eval(['save tempmcb
',SRPMGVAR(100:length(SRPMGVAR))]);
%          if(mctype==1)
%             savedtc = tcsyst;
%          else
%             savedtc = tcmach;
%          end
        savedTmax = Tmax;
        savedspeed = speedmax;
        fprintf('Saved design number
%d\n',ndes);
     allorone=0;
          srpmfeflexnew;
          destime=clock;
          title(sprintf('Torque = %g Nm,
Designed at %d:%.2d,
%s',Tmax,time(4),time(5),date));
%          title(sprintf('Speed = %g RPM,
Designed at %d:%.2d,
%s',speedmax,time(4),time(5),date));
          pause(2);
      end
%      if(mctype==1)
%         fprintf('\nCost = %g, Best Cost
= %g\n',tcsyst,savedtc);
%      else
%         fprintf('\nCost = %g, Best Cost
= %g\n',tcmach,savedtc);
%      end
         fprintf('\nTmax = %g, Best Tmax
= %g\n',Tmax,savedTmax);
%         fprintf('\nspeedmax = %g, Best
speedmax = %g\n',speedmax,savedspeed);
    end
```

```
%   fprintf('Elapsed time is
%g\n',etime(clock,t0));

    fprintf('Time is
%d:%.2d:%.2d\n',time(4),time(5),time(6));
end


function
dxfarc(fid,arccenter,arcradius,arcstartan
gle,arcendangle)
% Define a 2D DXF arc

fprintf(fid,'0\n');
fprintf(fid,'ARC\n');
fprintf(fid,'8\n');
fprintf(fid,'0\n');
fprintf(fid,'10\n');
fprintf(fid,'%g\n',real(arccenter));
fprintf(fid,'20\n');
fprintf(fid,'%g\n',imag(arccenter));
fprintf(fid,'30\n');
fprintf(fid,'0\n');
fprintf(fid,'40\n');
fprintf(fid,'%g\n',arcradius);
fprintf(fid,'50\n');
fprintf(fid,'%g\n',arcstartangle);
fprintf(fid,'51\n');
fprintf(fid,'%g\n',arcendangle);

return;
function
dxfcircle(fid,circlecenter,circleradius)
% Define a 2D DXF circle

fprintf(fid,'0\n');
fprintf(fid,'CIRCLE\n');
fprintf(fid,'8\n');
fprintf(fid,'0\n');
fprintf(fid,'10\n');
fprintf(fid,'%g\n',real(circlecenter));
fprintf(fid,'20\n');
fprintf(fid,'%g\n',imag(circlecenter));
fprintf(fid,'30\n');
fprintf(fid,'0\n');
fprintf(fid,'40\n');
fprintf(fid,'%g\n',circleradius);

return;
function dxfendpolyline(fid)

fprintf(fid,'0\n');
fprintf(fid,'SEQEND\n');
% DXF Export Machine Design

% Open a file to write to
name = input('Input export file name:
','s');
fid = fopen(strcat(name,'.dxf'),'w');
```

```
oneorall = input('\nInput number of poles
to plot: ');
if(oneorall~=1)
   oneorall = 2*p;
end

% Write DXF entities (i.e. objects)
fprintf(fid,'0\n');
fprintf(fid,'SECTION\n');
fprintf(fid,'2\n');
fprintf(fid,'ENTITIES\n');

% Write object definitions using group
code, value pairs
% Each on separate lines
% It takes 16 lines of code to draw one
line
% Default coordinates are cartesian
% Default units are centimeters and
degrees
% Primary point: start of a line, center
of a circle/arc
% Other points: end of a line,
% Group code  Definition
Values
% 0           Object type           text
(SECTION, ENDSEC, EOF, LINE)
% 2           Name                  text
(ENTITIES)
% 8           Layer name            text
(0)
% 10          X-value primary point
number
% 20          Y-value primary point
number
% 30          Z-value primary point
number
% 11-18       X-value other points
number
% 21-28       Y-value other points
number
% 31-38       Z-value other points
number
% 40          Radius of arc/circle
number
% 50          Start angle arc
number
% 51          End angle arc
number
% Stator OD
if(oneorall)
   dxfpolyline(fid,1);
   dxfvertex(fid,pol2comp(rci*1e3,0),0);
   dxfvertex(fid,pol2comp(rco*1e3,0),0);

dxfvertex(fid,pol2comp(rco*1e3,pi/p),180/
p);
else
    dxfcircle(fid,0,rco*1e3);
end
```

```
dxfendpolyline(fid);

% Stator ID
% Radii and angle in mm and deg
% 10 points make a tooth pitch
dxfr = rhotc;
dxfa = thetatc*180/pi;
dxfpolyline(fid,1);
% Starting point
dxfvertex(fid,pol2comp(dxfr(1),thetatc(1)
),0);
for k=0:(oneorall*ns/(2*p)),
% First half of tooth tip
    dxfvertex(fid,pol2comp(dxfr(2+10*k),t
hetatc(2+10*k)),dxfa(2+10*k)-
dxfa(1+10*k));
% Slot right opening
    dxfvertex(fid,pol2comp(dxfr(3+10*k),t
hetatc(3+10*k)),0);
% Slot right top
    dxfvertex(fid,pol2comp(dxfr(4+10*k),t
hetatc(4+10*k)),0);
% Slot right side
    dxfvertex(fid,pol2comp(dxfr(5+10*k),t
hetatc(5+10*k)),0);
% Bottom of slot
    dxfvertex(fid,pol2comp(dxfr(6+10*k),t
hetatc(6+10*k)),dxfa(6+10*k)-
dxfa(5+10*k));
% Slot left side
    dxfvertex(fid,pol2comp(dxfr(7+10*k),t
hetatc(7+10*k)),0);
% Slot left top
    dxfvertex(fid,pol2comp(dxfr(8+10*k),t
hetatc(8+10*k)),0);
% Slot left opening
    dxfvertex(fid,pol2comp(dxfr(9+10*k),t
hetatc(9+10*k)),0);
% Second half of tooth tip
    dxfvertex(fid,pol2comp(dxfr(10+10*k),
thetatc(10+10*k)),dxfa(10+10*k)-
dxfa(9+10*k));
end
if(oneorall~=1)

dxfvertex(fid,pol2comp(dxfr(1),thetatc(1)
),0);
end
dxfendpolyline(fid);

if(allorone)
   dxfpolyline(fid,1);
   dxfvertex(fid,pol2comp(rro*1e3,0),0);

dxfvertex(fid,pol2comp(rro*1e3,pi/p),180/
p);

dxfvertex(fid,pol2comp(rri*1e3,pi/p),0);
   dxfvertex(fid,pol2comp(rri*1e3,0),-
180/p);
   dxfvertex(fid,pol2comp(rro*1e3,0),0);
   dxfendpolyline(fid);
else
   % Rotor OD
   dxfcircle(fid,0,rro*1e3);
   % Rotor ID
   dxfcircle(fid,0,rri*1e3);
end

% Magnets
for segm=1:oneorall,
    dxfpt=[point1;point2;point3;point4]*e
xp(i*(segm-1)*pi/p);
   for k=1:4,
      % Start magnet
      dxfpolyline(fid,1);
      % Outer arc
      dxfvertex(fid,dxfpt(k,180),0)
      dxfvertex(fid,dxfpt(k,1),180);
      % Inside lines
      dxfvertex(fid,dxfpt(k,362),0);
      dxfvertex(fid,dxfpt(k,361),0)
      % Inner arc
      dxfvertex(fid,dxfpt(k,182),180);
      % Outside lines
      dxfvertex(fid,dxfpt(k,181),0);
      % End magnet
      dxfvertex(fid,dxfpt(k,180),0)
      dxfendpolyline(fid);
   end
end
% End of entities and end of file
fprintf(fid,'0\n');
fprintf(fid,'ENDSEC\n');
fprintf(fid,'0\n');
fprintf(fid,'EOF\n');
fclose(fid);
function dxfpline(fid,linestart,lineend)
% Define a 2D DXF line

fprintf(fid,'0\n');
fprintf(fid,'LINE\n');
fprintf(fid,'8\n');
fprintf(fid,'0\n');
fprintf(fid,'10\n');
fprintf(fid,'%g\n',real(linestart));
fprintf(fid,'20\n');
fprintf(fid,'%g\n',imag(linestart));
fprintf(fid,'30\n');
fprintf(fid,'0\n');
fprintf(fid,'11\n');
fprintf(fid,'%g\n',real(lineend));
fprintf(fid,'21\n');
fprintf(fid,'%g\n',imag(lineend));
fprintf(fid,'31\n');
fprintf(fid,'0\n');

return;
function dxfpolyline(fid,closed)
% Define a 2D DXF line
```

```
fprintf(fid,'0\n');
fprintf(fid,'POLYLINE\n');
fprintf(fid,'8\n');
fprintf(fid,'0\n');
fprintf(fid,'66\n');
fprintf(fid,'1\n');
fprintf(fid,'70\n');
fprintf(fid,'%d\n',closed);

return;
function
dxfvertex(fid,vertex,includedangle)
% Define a 2D DXF line

fprintf(fid,'42\n');
fprintf(fid,'%g\n',tan(includedangle*pi/(
180*4)));
fprintf(fid,'0\n');
fprintf(fid,'VERTEX\n');
fprintf(fid,'8\n');
fprintf(fid,'0\n');
fprintf(fid,'10\n');
fprintf(fid,'%g\n',real(vertex));
fprintf(fid,'20\n');
fprintf(fid,'%g\n',imag(vertex));
fprintf(fid,'30\n');
fprintf(fid,'0\n');

return;

function magnetarc(fid,z1,z2,z3)
% Make An Arc In MagNet

fprintf(fid,'CALL
getDocument.newConstructionSliceArc(%f,%f
,%f,%f,%f,%f)\n',[real(z1);imag(z1);real(
z2);imag(z2);real(z3);imag(z3)]);
return;
function magnetcomp(fid,d1,z1,c1,c2)
% Make A Component In MagNet

fprintf(fid,'CALL
getDocument.selectAtWithObjectCode (%f,
%f, infoSetSelection,
infoSliceSurface)\n',[real(z1);imag(z1)])
;
fprintf(fid,'REDIM ArrayOfValues(0)\n');
fprintf(fid,'ArrayOfValues(0)=
"%s"\n',c1);
fprintf(fid,'CALL
getDocument.makeComponentInALine(%f,
ArrayOfValues, "Name=%s")\n',d1,c2);

return;
function magnetline(fid,z1,z2)
% Make A Line In MagNet

fprintf(fid,'CALL
getDocument.newConstructionSliceLine(%f,%
f,%f,%f)\n',[real(z1);imag(z1);real(z2);i
mag(z2)]);
return;
% Make straight segment magnets

fid = fopen('makemagnets.vbs','w');
for magnet=1:nl,
    magnetline(fid,rot90(pointm(:,magnet)
),rot90([pointm(2:length(pointm'),magnet)
;pointm(1,magnet)]));
end
fclose(fid);
% Make a rotor

fid = fopen('makerotor.vbs','w');
magnetarc(fid,zeros(1,2),[rri
rro]*1e3,[rri
rro]*1e3*(cos(pi/p)+sin(pi/p)*i));
magnetline(fid,rri*1e3*[1
(cos(pi/p)+sin(pi/p)*i)],rro*1e3*[1
(cos(pi/p)+sin(pi/p)*i)]);
magnetcomp(fid,1*1e3,mean([rri*1e3,rro*1e
3*(cos(pi/p)+sin(pi/p)*i)]),'Rotor','M19
Custom');
fclose(fid);
% Make a stator

fid = fopen('makestator.vbs','w');
for magnet=1:nl,
    magnetline(fid,rot90(pointm(:,magnet)
),rot90([pointm(2:length(pointm'),magnet)
;pointm(1,magnet)]));
end
fclose(fid
```

Bibliography

[1] MIT/Industry Consortium on Advanced Automotive Electronic/Electrical Components and Systems, "Discussions with Automotive OEMs Regarding Component Costs," 1996.

[2] G. Robert Bosch, *Automotive Electrical Systems Handbook.* Cambridge, MA: Robert Bentley, 1996.

[3] MIT/Industry Consortium on Advanced Automotive Electronic/Electrical Components and Systems, "Discussions with Automotive OEMs About Typical Future Vehicle Requirements," 1996.

[4] J. Miller, D. Kaminski, T. Jahns, D. Goel, and H.-P. Schoener, "Making the Case for a Next Generation Automotive Electrical System," *in Proc. Convergence '98*, Dearborn, MI, 1998

[5] J. G. Kassakian, J. M. Miller, and N. Traub, "Automotive Electronics Power Up," in *IEEE Spectrum*, vol. May, 2000, pp. 34-39.

[6] T. Sebastian and G. R. Slemon, "Operating Limits of Inverter-Driven Permanent Magnet Motor Drives," *IEEE IAS Trans.*, vol. IA-23, pp. 327-333, 1987.

[7] W. Soong, "*Design and Modelling of Axially-Laminated Interior Permanent Magnet Motor Drives for Field-Weakening Applications*," in *Department of Electronics and Electrical Engineering*: University of Glasgow, 1993.

[8] W. L. Soong and T. J. E. Miller, "Theoretical Limitations to the Field-Weakening Performance of the Five Classes of Brushless Synchronous AC Motor Drive," *in Proc. IEE Electric Machines and Drives Conf.*, 1993, pp. 127-132.

[9] W. L. Soong and T. J. E. Miller, "Practical Field-Weakening Performance of the Five Classes of Brushless Synchronous AC Motor Drive," *in Proc. European Power Electronics Association Conf.*, 1993, pp. 303-310.

[10] MIT/Industry Consortium on Advanced Automotive Electronic/Electrical Components and Systems, "Discussions with Automotive OEMs about the Limitations of Lundell Automotive Alternators," 1996.

[11] T. J. E. Miller, *Brushless Permanent-Magnet and Reluctance Motor Drives.* Oxford: Clarendon Press, 1989.

[12] R. H. Park, "Two-Reaction Theory of Synchronous Machines - Generalized Method of Analysis - Part I," *AIEE Trans.*, vol. 48, pp. 716-727, 1929.

[13] B. K. Bose, *Power Electronics and AC Drives*. Englewood Cliffs: Prentice-Hall, 1986.

[14] P. C. Krause, *Analysis of Electric Machinery*. New York: McGraw-Hill, 1986.

[15] S. Morimoto, Y. Takeda, T. Hirasa, and K. Taniguchi, "Expansion of Operating Limits for Permanent Magnet Motor by Current Vector Control Considering Inverter Capacity," *IEEE IAS Trans.*, vol. 26, pp. 866-871, 1990.

[16] S. Morimoto, M. Sanada, and Y. Takeda, "Wide-Speed Operation of Interior Permanent Magnet Synchronous Motors with High-Performance Current Regulator," *IEEE IAS Trans.*, vol. 30, pp. 920-926, 1994.

[17] W. L. Soong and T. J. E. Miller, "Field-Weakening Performance of Brushless Synchronous AC Motor Drives," *IEE Proceedings - Elec. Power Appl.*, vol. 141, pp. 331-339, 1994.

[18] T. M. Jahns, "Flux Weakening Regime Operation of an IPM Synchronous Motor Drive," *IEEE Transactions on Industry Applications*, vol. IA-23, pp. pp. 681-689, 1987.

[19] R. Schiferl and T. A. Lipo, "Power Capability of Salient Pole P.M. Synchronous Motors in Variable Speed Drive," *in Proc. IEEE IAS Annual Meeting*, 1988, pp. 23-31.

[20] V. Honsinger, "The Fields and Parameters of Interior Type AC Permanent Magnet Machines," *IEEE Power Apparatus and Systems Trans.*, vol. PAS-101, pp. 867-876, 1982.

[21] Y. Honda, T. Nakamura, T. Higaki, and Y. Takeda, "Motor Design Considerations and Test Results of an Interior Permanent Magnet Synchronous Motor for Electric Vehicles," *in Proc. IEEE IAS Annual Meeting*, 1997, pp. 75-.

[22] I. Boldea, *Reluctance Synchronous Machines and Drives*. Oxford: Clarendon Press, 1996.

[23] A. Fratta, A. Vagati, and F. Villata, "On the Evolution of A.C. Machines for Spindle Drive Applications," *in Proc. IEEE IAS Annual Meeting*, 1989, pp. 699-704.

[24] A. Fratta, A. Vagati, and F. Villata, "Design Criteria of an IPM Machine Suitable for Field-Weakened Operation," *in Proc. ICEM*, 1990, pp. 1059-1065.

[25] A. Fratta, R. Grassi, and A. Vagati, "High Performance Spindle Drives Adopting IPM Synchronous Machines: Theoretical Goals and a Practical Solution," *in Proc. EPE Proc.*, Firenze, 1991, vol. 3, pp. 476-481.

[26] A. Vagati, A. Fratta, G. Franceschini, and P. M. Rosso, "A.C. Motors for High-Performance Drives: A Design-Based Comparison," *in Proc. IEEE IAS Annual Meeting*, 1995, pp. 725-733.

[27] A. Vagati, M. Pastorelli, and G. Franceschini, "Effect of Magnetic Cross-coupling in Synchronous Reluctance Motors," *in Proc. Intelligent Motion*, 1997, pp. pp. 279-285.

[28] A. E. Fitzgerald, J. C. Kingsley, and S. D. Umans, *Electric Machinery*. New York: McGraw-Hill Book Company, 1983.

[29] T. A. Lipo, *Introduction to AC Machine Design*. UW-Madison: WisPERC, 1997.

[30] H. W. Beaty and J. L. Kirtley Jr., *Electric Motor Handbook*. New York: McGraw-Hill, 1998.

[31] T. A. Lipo, T. J. E. Miller, A. Vagati, I. Boldea, L. Malesani, and T. Fukao, "Synchronous Reluctance Drives Tutorial," *in Proc. IEEE IAS Annual Meeting*, 1994

[32] "Carpenter Alloy Steel Product Selection Guide," Carpenter Steel, 1997.

[33] "Non-oriented Electrical Steel Guide," Armco Incorporated, 1998.

[34] G. Kliman, "High-speed Induction Machine," *in Proc. IEEE IAS Annual Meeting*, Phoenix, 1999

[35] "Hard Magnetic Material Characteristics and Selection," Arnold Engineering, 1998.

[36] B. J. Chalmers, "Influence of Saturation in Brushless Permanent-Magnet Motor Drives," *in Proc. IEE Proc., Pt. B*, 1992, vol. 139, pp. 51-52.

[37] L. Xu, X. Xu, T. A. Lipo, and D. W. Novotny, "Vector Control of a Synchronous Reluctance Motor Including Saturation and Iron Loss," *IEEE IAS Trans.*, vol. 27, pp. 977-985, 1991.

[38] R. E. Betz, M. Jovanovic, R. Lagerquist, and T. J. E. Miller, "Aspects of the Control of Synchronous Reluctance Machines including Saturation and Iron Losses," *in Proc. IEEE IAS Annual Meeting*, 1992, pp. 456-463.

[39] H. Murakami, Y. Honda, H. Kiriyama, S. Morimoto, and Y. Takeda, "The Performance Comparison of SPMSM, IPMSM and SynRM in Use as Air-conditioning Compressor," *in Proc. IEEE IAS Annual Meeting*, 1999, pp. 840-845.

[40] Y. Honda, T. Higaki, S. Morimoto, and Y. Takeda, "Rotor Design Optimization of a Multi-layer Interior Permanent-Magnet Synchronous Motor," *IEE Electric Power Applications Proc.*, vol. 145, pp. 119-124, 1998.

[41] S. Kawano, H. Murakami, N. Nishiyama, Y. Ikkai, Y. Honda, and T. Higaki, "High Performance Design of an Interior Permanent Magnet Synchronous Reluctance Motor for Electric Vehicles," *in Proc. IEEE Power Conversion Conf.*, Nagaoka, 1997, pp. 33-36.

[42] H. Kiriyama, S. Kawano, Y. Honda, and T. Higaki, "High Performance Synchronous Reluctance Motor with Multi-flux Barrier for the Appliance Industry," *in Proc. IEEE*, 1998, pp. 111-117.

[43] L. Ma, M. Sanada, S. Morimoto, Y. Takeda, and N. Matsui, "High Efficiency Adjustable Speed Control of IPMSM with Variable Permanent Magnet Flux Linkage," *in Proc. IEEE IAS Annual Meeting*, 1999, pp. 881-887.

[44] S. Morimoto, T. Ueno, and M. Sanada, "Variable Speed Drive System of Interior Permanent Magnet Synchronous Motors for Constant Power Operation," *in Proc. IEEE Power Conversion Conf.*, Yokohama, 1993, pp. 402-407.

[45] S. Morimoto, M. Sanada, and Y. Takeda, "Effects and Compensation of Magnetic Saturation in Flux-Weakening Controlled Permanent Magnet Synchronous Motor Drives," *IEEE IAS Trans.*, vol. 30, pp. 1632-1637, 1994.

[46] S. Morimoto, M. Sanada, and Y. Takeda, "Performance of PM/Reluctance Hybrid Motor with Multiple Flux-Barrier," *in Proc. IEEE Power Conversion Conf.*, Nagaoka, 1997, pp. 649-654.

[47] B. Sneyers, D. W. Novotny, and T. A. Lipo, "Field Weakening in Buried Permanent Magnet AC Motor Drives," *IEEE IAS Trans.*, vol. IA-21, pp. 398-407, 1985.

[48] B. C. Mecrow and A. G. Jack, "Operation of highly-rated permanent magnet synchronous machines," *in Proc. IEE Electrical Machines and Drives Conference*, 1991, pp. 26-30.

[49] A. Vagati and G. Franceschini, "Cross-Saturation in Synchronous Reluctance Motors of the Transverse-Laminated Type," *in Proc. IEEE IAS Annual Meeting*, 1998, pp. 127-135.

[50] "Nonoriented Sheet Steel for Magnetic Applications," United States Steel, Pittsburgh, PA: USS, 1978.

[51] W. L. Soong, D. A. Staton, and T. J. E. Miller, "Validation of Lumped-Circuit and Finite-Element Modelling of Axially-Laminated Brushless Motors," *in Proc. IEE Electric Machines and Drives Conf.*, 1993, pp. 85-90.

[52] Mathworks, "MATLAB v5 Users Guide," , 1998.

[53] Infolytica_Corporation, "MagNet v6.5 Online Help," , 2000.

[54] W. Soong, "Design and Test Data for Three and Four Layer IPM and Synchronous Reluctance Machines," : University of Adelaide, Australia, 2000.

[55] T. J. E. Miller, D. A. Staton, and S. E. Wood, "Maximising the Saliency Ratio of the Synchronous Reluctance Motor," *in Proc. IEE Proceedings, Electric Power Applications*, 1993, vol. 140, No. 4, pp. 249-259.

[56] T. M. Jahns and V. Caliskan, "Uncontrolled generator operation of interior PM synchronous machines following high-speed inverter shutdown," *IEEE IAS Trans.*, vol. 35, pp. 1347-1357, 1999.

[57] J. Kassakian, *Fundamentals of Power Electronics*, 1994.

[58] F. R. Laboratory, "Cost Analysis of Three-Phase Full Bridge MOSFET-based Converters," , 1997.

[59] T. Wilson, "Power Converter Cost Trends, Zytec Inc.," *in Proc. MIT-Industry Automotive Consortium on Elcctronics/Electrical Systems June 1997 Meeting*, 1997

[60] D. E. Cameron, J. H. Lang, and D. Belanger, "The Computer-aided Design of High-speed Variable-reluctance Generators," *in Proc. APEC*, Boston, MA, 1992, pp. 114-119.

[61] L. S. Marks and T. Baumeister, *Marks' standard handbook for mechanical engineers*. New York,: McGraw-Hill., 1986.

[62] J. E. Shigley and C. R. Mischke, *Mechanical engineering design*, 5th ed. New York: McGraw-Hill, 1989.

[63] ANSYS Corporation, "ANSYS Multiphysics," 1999.

[64] P. Campbell, *Permanent magnet materials and their application*. Cambridge [England] ; New York: Cambridge University Press, 1994.

[65] Armco Steel, "Discussion of Alloy Steel Lamination Products," 1999.

[66] W. L. Soong, D. A. Staton, and T. J. E. Miller, "Design of a New Axially-Laminated Interior Permanent Magnet Motor," *IEEE IAS Trans.*, vol. 31, pp. 358-367, 1995.

[67] A. Vagati, A. Fratta, G. Franceschini, and P. Rosso, "AC Motors for High-Performance Drives: A Design-Based Comparison," *IEEE IAS Trans.*, vol. 32, pp. 1211-1219, 1996.

[68] A. Fratta, A. Vagati, and F. Villata, "On the Evolution of ac Machines for Spindle Drive Applications," *IEEE IAS Trans.*, vol. 28, pp. 1081-1086, 1992.

[69] T. Matsuo and T. A. Lipo, "Rotor Design Optimization of Synchronous Reluctance Machine," *IEEE Transaction on Eneergy Conversion*, vol. 9, pp. 359-365, 1994.